Application of full-waveform inversion to shallow-seismic Rayleigh waves on 2D structures

Zur Erlangung des akademischen Grades eines

DOKTORS DER NATURWISSENSCHAFTEN

von der Fakultät für Physik des
Karlsruher Instituts für Technologie (KIT)

genehmigte

DISSERTATION

von

Dipl.-Geophys. Martin Schäfer
aus Tuttlingen

Tag der mündlichen Prüfung:	04. Juli 2014
Referent:	Prof. Dr. Thomas Bohlen
Korreferent:	Prof. Dr. Wolfgang Rabbel

Contents

Chapter I

Introduction

A key challenge for various applications like lithological sediment characterization, risk analysis or archeology is the quantitative imaging of the topmost meters of the subsoil. The inversion of shallow-seismic surface waves is very attractive for these applications primarily for two reasons. Firstly, surface waves are easily excited in particular by hammer blows and provide excellent signal-to-noise ratio. Secondly, they have a high sensitivity to the shear-wave velocity in the topmost meters of the subsurface. Furthermore, they may reveal properties of so-called hidden layers which cannot be studied as easily as with refracted body waves, among others. In general, the penetration depth of shallow-seismic surface waves is around 10 m to 60 m for wave fields in the frequency range from 10 Hz to 100 Hz and geophone profile lengths of 50 m to 200 m.

Conventional surface-wave inversion methods
Surface wave analysis is widely adopted for generating near-surface S-wave velocity models and it is under continuous development. Socco et al. (2010) present a literature review of previous studies as well as a detailed discussion of established approaches and new perspectives. Established methods to invert surface waves are the inversion of dispersion curves (Wathelet et al., 2004) or wave-field expansion coefficients (Forbriger, 2003, Part I and II). However, these methods assume 1D subsurface structures (material properties vary only with depth) because they require phase coherent signals along the receiver profile. This condition is not satisfied in many applications of practical relevance. Miller et al. (1999) and Bohlen et al. (2004) investigate sites with dispersion curves of Rayleigh and Scholte waves, respectively, where lateral variations of the elastic material properties along the receiver profile are present. The pseudo 2D subsurface models are obtained by joining adjacent 1D subsurface models. Nevertheless, these concepts are only applicable for rather smooth lateral variations of elastic material properties. For stronger lateral variations or even 3D structures (e.g. sediment lenses) the concept breaks down because no continuous dispersion curves can be extracted (Forbriger, 2001, Lerchenberg p. 190).

Elastic full-waveform inversion
To overcome the 1D limitation elastic full-waveform inversion (FWI) can be applied to infer 2D and 3D structural earth models from shallow-seismic surface waves. In application of practical relevance the realistic subsurface is characterized by 3D structures, which should

consider 3D wave propagation. However, the application of a 3D elastic FWI is still difficult due to excessive computational demands (Butzer et al., 2013). Therefore today, 2D FWI is preferential for code development and gaining experience for synthetic case studies and field-data application, because it allows for frequent repeat runs of inversion tests. However, one important prerequisite for a successful application of 2D FWI to field data is to perform accurate spreading transformations for 2D media.

The aim of full-waveform inversion is to extract information from observed seismograms on model parameters describing the Earth's interior and to exploit the full richness of the broad-band waveforms. Among other conventional imaging methods, such as first-arrival travel-time tomography, FWI has the potential to infer subsurface structures smaller than a wavelength. The objective of FWI is to reduce the misfit between observed and synthetic seismograms and deduce a subsurface model that predicts the observed seismograms accurately. In the adjoint approach, the gradient of the misfit function is calculated by interaction of the forward and adjoint wave field in particular a zero-lag cross-correlation. The latter is generated by back-propagation of adjoint sources based on data (Tromp et al., 2005). Possible choice are residuals between observed and synthetic seismograms (Tarantola, 1984). In this work the forward problem and the back-propagation of the adjoint sources are solved using a parallel time-domain finite-difference scheme (Bohlen, 2002). A steepest-descent or preconditioned conjugate gradient method is used to solve the non-linear inverse problem iteratively. The full-waveform inversion scheme is introduced by Tarantola (1984) for acoustic wave propagation in the time domain. Further developments comprise elastic (Mora, 1987) and even viscoelastic (Tarantola, 1988) wave propagation. Later Pratt and Worthington (1990) and Pratt (1990, 1999) established the frequency-domain FWI. I apply a 2D elastic full-waveform inversion code which was originally developed by Köhn (2011) and represents a pure time-domain approach.

Previous studies
There are already a few applications which show the high potential of 2D elastic FWI being applied to shallow-seismic surface waves. Romdhane et al. (2011) present a numerical study of the inversion with Rayleigh waves where they apply a 2D elastic frequency-domain FWI algorithm to image a realistic landslide model with complex geology and topography. Furthermore, they report that restricting the inversion to vertical component data may lead to acceptable reproduction capability compared to two-component data. In the context of field data application this is of great significance because single-component data is commonly used in practical applications. Tran and McVay (2012) apply a 2D elastic FWI in the time domain and they investigate two synthetic data sets with and without noise as well as one field data application. Furthermore, they suggest that it is possible to characterize both high- and low-velocity layers, latter even in the field data application. A comparison with a ground truth (standard penetration test) confirms that the results are consistent. Bretaudeau et al. (2013) present an application to synthetic and physical modeling data sets with a 2D FWI scheme in the frequency domain where viscoelastic wave propagation is considered. They perform a small-scale seismic experiment with a laser-ultrasonic measurement bench to produce controlled seismic data with surface waves. Main problems occur at very shallow depths where strong artifacts are present in the reconstructed subsurface models due to inappropriate source signature inversion and singularities of the gradient in the vicinity of the sources. Nevertheless, the main target, a high-velocity inclusion, is inferred by the

inversion. Tran et al. (2013) present an application of elastic full-waveform inversion of surface waves for detection of embedded voids. The inversion of the field data shows that the algorithm is able to infer an embedded concrete culvert, an embedded void, and highly variable bedrock. They verify their inversion results with an independent invasive test (standard penetration test). Groos (2013) applies a 2D time-domain FWI algorithm where she considers viscoelastic wave propagation. She presents an application to recorded shallow-seismic surface waves on a predominantly depth-dependent structure in unconsolidated sediments. Although the differences between the inital and inferred S-wave velocity model are small, the misfit can be reduced significantly which shows the strong influence of the S-wave velocity on the shallow-seismic wave fields. Furthermore, a comparison of the FWI results with a joint inversion of first arrival P-wave travel times and Fourier-Bessel expansion coefficients is discussed. Basically, current applications of FWI to recorded shallow-seismic surface waves are in an early stage and so far no general approach emerged.

Main objective and outline of this thesis
The main objective of my thesis is the application of 2D elastic full-waveform inversion to shallow-seismic Rayleigh waves recorded on 2D structures. Firstly, I focus on one important prerequisite for a successful application of 2D FWI to field data which is the application of accurate spreading transformations for 2D media. To make 2D FWI applicable to field data (point source), recordings must be preprocessed to simulate the response to a line source. After the point-source wave fields are filtered, the wave fields can be inverted by a 2D full-waveform inversion. Furthermore, the unknown source signature of the hammer impacts and viscoelastic wave propagation have to be considered. Secondly, I apply the 2D FWI scheme to a field data set recorded on a significant 2D subsurface structure.

This thesis is organized as follows.

Chapter 2 - Basic principles and inversion strategies
Chapter 2 discusses the basic principles of the used forward solver, the adjoint approach and the numerical implementation of FWI as well as inversion strategies in particular for field data inversion. I use a 2D P-SV finite-difference scheme in the time domain to solve the elastic and viscoelastic wave equation. The gradient of the misfit function is calculated by the adjoint approach. The numerical implementation is introduced via a workflow chart. Furthermore, I discuss preconditioning and scaling of the gradients and suggest inversion strategies like multi-scale inversion with frequency filtering, controlled v_p/v_s ratio and regularized updates.

Chapter 3 - Line-source simulation for shallow-seismic data
Field data are commonly gained with a point source such as a hammer blow or an explosion which produces wave fields with 3D geometrical spreading. However, the applied inversion-code uses Cartesian 2D forward modeling and hence implicitly uses a line source in 3D space. Therefore, I discuss in this chapter the differences of geometrical spreading of 3D and 2D wave propagation and investigate possible artifacts produced by a line-source simulation for 2D FWI of shallow-seismic surface waves. I introduce an integral Fourier-Bessel transformation and a single-trace transformation derived by an approximation from the acoustic homogeneous full-space solution. Synthetic 3D/2D-transformed point-source wave fields are used as observed data in a 2D FWI. In these so-called reconstruction tests I investigate the reproduction capability by assuming the true subsurface structure.

Chapter 4 - Feasibility study of a line-source simulation in the field
Among the numerical line-source simulations in Chapter 3 I focus in this chapter again on a line-source simulation technique, however, in a more practical point of view. I present a feasibility study of a line-source simulation in the field where a line source can be expressed as a superposition of seismograms excited by a vast number of point sources along the line source.

Chapter 5 - Inversion of field data on a 2D structure – test-site Mammolshain
Chapter 5 deals with the application of FWI to recorded shallow-seismic surface waves. The data sets were acquired on a fault system of the southern rim of the Taunus which is a significantly 2D-heterogeneous structure. Main topics are preparatory investigations to verify the 2D assumption, generation of starting models with first-arrival travel-time tomography and comparison of FWI results for parallel seismic profiles set up perpendicular to the fault.

Chapter 6 - Summary and conclusion
Finally, Chapter 6 summarizes and concludes the main results of this thesis.

The TOAST project
This thesis is embedded in the framework of the TOAST (Toolbox for Applied Seismic Tomography) project (Forbriger et al., 2014a). The project pursues the goal to collect and improve algorithms available in academia with different inversion strategies implemented (global search, conjugate gradient, waveform sensitivity kernels) as well as preparation of these approaches for application to field recordings. The developed software programs, results of benchmark tests and field-cases are published online by the `OpenTOAST.de` initiative. The field data in this thesis was also acquired with TOAST project partners from Ruhr-University of Bochum (RUB), Geophysics and Geotechnique Leipzig GmbH (GGL), German Research Centre for Geosciences of Potsdam (GFZ) and Karlsruhe Institute of Technology (KIT).

Chapter II

Basic principles and inversion strategies

II.1 Seismic forward problem

Linear stress-strain relation
The physical principle to describe seismic wave propagation is based on the linear theory of elasticity which investigates behavior between stress and strain. The following reflects the script of Müller (2007). For ideal elasticity and infinitesimal deformations, the relation between stress σ and strain ϵ is given by Hooke's law:

$$\sigma_{ij} = c_{ijkl} \cdot \epsilon_{kl} \tag{II.1}$$

$$\text{with } c_{ijkl} = \text{stiffness tensor.} \tag{II.2}$$

The theory of linear elasticity investigates the elastic behavior of bodies under following assumptions:

1. The deformations are infinitesimal.
2. The stress-strain relations are linear.

For an isotropic elastic body, which means uniformity in all directions, only two elastic constants are required. In this case the stress-strain relation can be written as:

$$\sigma_{ij} = \lambda\theta\delta_{ij} + 2\mu\epsilon_{ij} \tag{II.3}$$

with

λ and μ: Lamé parameters,

$$\epsilon_{ij} = \left(\frac{\partial u_i}{\partial x_j} + \frac{\partial u_j}{\partial x_i} \right) \text{ strain tensor,} \tag{II.4}$$

$$\theta = \epsilon_{11} + \epsilon_{22} + \epsilon_{33} \quad \text{cubic dilatation,} \tag{II.5}$$

$$\delta_{ij} = \begin{cases} 1 & \text{for i = j} \\ 0 & \text{for i} \neq \text{j} \end{cases} \quad \text{Kronecker's delta.} \tag{II.6}$$

The relation between λ and μ as well as other elastic parameters is given by:

$$\text{Young's modulus } E = \frac{\mu(3\lambda + 2\mu)}{\lambda + \mu}, \tag{II.7}$$

$$\text{Poisson number } \nu = \frac{\lambda}{2(\lambda + \mu)}. \tag{II.8}$$

For an isothermal and isotropic viscoelastic medium the stress-strain relation is described by

$$\sigma_{ij} = (\dot{\Psi}_p - 2\dot{\Psi}_s) * \epsilon_{ll}\delta_{ij} + 2\dot{\Psi}_s * \epsilon_{ij} \tag{II.9}$$

where Ψ_p and Ψ_s are the relaxation functions of the medium for P- and S-waves, respectively (Bohlen, 1998). $*$ denotes a convolution. The forward solver applied in the FWI scheme uses a generalized standard linear solid (GSLS) as rheological model (Blanch et al., 1995). Hereby, the relaxation functions of the L relaxation mechanisms have the form of

$$\Psi_p(t) = \pi\left\{1 + \sum_{l=1}^{L}\left(\frac{\tau_{\epsilon l}^p}{\tau_{\sigma l}} - 1\right)e^{-t/\tau_{\sigma l}}\right\}\mathrm{H}(t), \tag{II.10}$$

$$\Psi_s(t) = \mu\left\{1 + \sum_{l=1}^{L}\left(\frac{\tau_{\epsilon l}^s}{\tau_{\sigma l}} - 1\right)e^{-t/\tau_{\sigma l}}\right\}\mathrm{H}(t), \tag{II.11}$$

where π is the relaxed P-wave modulus, μ the relaxed shear modulus. $\tau_{\epsilon l}^p$ and $\tau_{\epsilon l}^s$ are the retardation times of the strain of the l-th relaxation mechanism for P- and S-waves, respectively, and $\tau_{\sigma l}$ are the corresponding relaxation times for the stress (Liu et al., 1976; Carcione et al., 1988; Robertsson et al., 1994). H(t) is the Heaviside step function.

Blanch et al. (1995) suggest the so-called τ method to approximate a frequency-independent quality factor Q (at least in a limited frequency interval) and to reduce the number of variables describing the GSLS. Hereby, the L retardation times $\tau_{\epsilon l}$ can be described by a dimensionless and frequency-independent variable τ:

$$\tau = \frac{\tau_{\epsilon l}}{\tau_{\sigma l}} - 1. \tag{II.12}$$

The frequency interval for the frequency-independent quality factor Q is approximated by the relaxation frequencies $f_l = 1/(2\pi\tau_{\sigma l})$. Bohlen (1998) suggests that this frequency interval is equal for P- and S-waves. The quality factor Q is given by (Blanch et al., 1995)

$$Q(w) = \frac{1 + \sum_{l=1}^{L}\frac{\omega^2\tau_{\sigma l}^2}{1+\omega^2\tau_{\sigma l}^2}\tau}{\sum_{l=1}^{L}\frac{\omega\tau_{\sigma l}}{1+\omega^2\tau_{\sigma l}^2}\tau}. \tag{II.13}$$

For Q_p one has to substitute $\tau_{\epsilon l} = \tau_{\epsilon l}^p$ in eq. II.12 and eq. II.13 and $\tau_{\epsilon l} = \tau_{\epsilon l}^s$ for Q_s. For the field data application in Chapter V (Section V.6), where viscoelastic wave propagation is considered, the quality factor is approximated by three relaxation mechanisms.

For convenience, the following considerations are related to the elastic approximation. For viscoelastic wave propagation I refer to Bohlen (1998) and Groos (2013).

Elastic wave equation
The momentum equation (Müller, 2007, eq. 2.12) for infinitesimal deformations (non-linear terms vanish), the linear isotropic stress-strain relation (eq. II.3) as well as the strain tensor (eq. II.4) yield to

$$\begin{aligned} \rho \frac{\partial^2 u_i}{\partial t^2} &= \frac{\partial \sigma_{ij}}{\partial x_j} + f_i, \\ \sigma_{ij} &= \lambda \theta \delta_{ij} + 2\mu \epsilon_{ij}, \\ \epsilon_{ij} &= \left(\frac{\partial u_i}{\partial x_j} + \frac{\partial u_j}{\partial x_i} \right). \end{aligned} \tag{II.14}$$

with mass density ρ in kg/m^3, particle displacement u_i in m, stresses σ_{ij} in N/m^2 and volume force density f_i in N/m^3. This system of second order partial differential equations describes the propagation of seismic waves in an elastic medium. This expression is called stress-displacement formulation.
Since a stress-velocity formulation is implemented in the forward solver of the FWI scheme, eq. II.14 can be rewritten by replacing $\partial u_i / \partial t$ with v_i and taking the time derivatives of the stress-strain relation and the strain tensor:

$$\begin{aligned} \rho \frac{\partial v_i}{\partial t} &= \frac{\partial \sigma_{ij}}{\partial x_j} + f_i, \\ \frac{\partial \sigma_{ij}}{\partial t} &= \lambda \frac{\partial \theta}{\partial t} \delta_{ij} + 2\mu \frac{\partial \epsilon_{ij}}{\partial t}, \\ \frac{\partial \epsilon_{ij}}{\partial t} &= \left(\frac{\partial v_i}{\partial x_j} + \frac{\partial v_j}{\partial x_i} \right). \end{aligned} \tag{II.15}$$

Solving eq. II.14 and eq. II.15 for complex geological problems requires numerical solutions. In the following I briefly describe a scheme where the partial derivatives are replaced by finite-difference (FD) operators.

2D finite-difference scheme
The full-waveform inversion code `DENISE` uses a 2D P-SV finite-difference (FD) scheme in the time domain to solve the elastic wave equation. It was originally developed by Bohlen (1998, 2002). It is based on the stress-velocity formulation and uses a Standard Staggered Grid (SSG) (Virieux, 1986; Levander, 1988; Robertsson et al., 1994).

A 2D Cartesian coordinate system is used in the forward solver. The y component denotes the vertical direction. The origin of the coordinate system is located in the upper left corner of the model. The wave equation is discretized at discrete Cartesian coordinates $x = i\,\Delta h$, $y = j\,\Delta h$ as well as discrete times $t = n\,\Delta t$. Δh indicates the spatial grid spacing and Δt denotes the sampling interval between two time steps. The partial derivatives are approximated by finite-difference operators. An exemplary system of 1D first order partial differential equations might have the following continuous

$$\frac{\partial f(x,t)}{\partial t} \sim \frac{\partial g(x,t)}{\partial x} \tag{II.16}$$

$$\frac{\partial g(x,t)}{\partial t} \sim \frac{\partial f(x,t)}{\partial x} \tag{II.17}$$

and discrete

$$\frac{f_i^{n+1} - f_i^n}{\Delta t} \sim \frac{g_{i+1/2}^{n+1/2} - g_{i-1/2}^{n+1/2}}{\Delta x} \tag{II.18}$$

$$\frac{g_{i+1/2}^{n+1/2} - g_{i+1/2}^{n-1/2}}{\Delta t} \sim \frac{f_{i+1}^n - f_i^n}{\Delta x} \tag{II.19}$$

form, which requires a staggered grid formulation. The arbitrary wave field variables $f(x,t)$ and $g(x,t)$ are shifted by half a time sample and half a grid point to each other in the FD scheme. In the case of the elastic wave equation this principle is assigned to the stress and velocity field. For the FD solution of the elastic and viscoelastic wave propagation I refer to Bohlen (1998). The presented time and spatial derivatives are related to Taylor coefficients of second order. However, the latter are implemented up to eight order.

Free surface with image technique
The interface between the elastic medium and the atmosphere is called free surface. The free surface has a significant influence on the accuracy of modeling surface waves and multiple reflections. Therefore, a numerical exact and stable implementation of the free surface is important. From a physical point of view all stresses in the normal direction at the free surface vanish:

$$\sigma_{iy} = 0 \, , \, i = x, y. \tag{II.20}$$

I apply an imaging technique after Levander (1988) which leads to stable and accurate solutions for plain interfaces (Groos, 2013). The stress component σ_{yy} is set explicitly to zero at the free surface and the stress components σ_{iy} with $i = x, y$ are imaged with an inverse sign.

Boundary conditions with CPML
A numerical problem of modeling seismic waves on a finite grid is that the waves are reflected at the boundaries of the model and infer with the waves of interest. To avoid this problem absorbing boundary conditions have to be applied. This is done by extending the model grid by a few grid points (typically 20-30 grid points) in each direction. Cerjan et al. (1985) suggest to multiply the stress and velocity field with an exponential damping factor within the absorbing boundary frame. However, Groos (2013) reports that this approach is inappropriate for surface waves even for very large absorbing boundaries of 100 grid points. Therefore, I use convolutional perfectly matched layers (CPML) after Komatitsch and Martin (2007) and Martin and Komatitsch (2009) to avoid most effectively boundary reflections.

Choice of discretization parameters Δh and Δt
In the following two criteria of spatial and temporal sampling are discussed to avoid numerical artifacts and instabilities during finite-difference modeling.
For too large spatial discretization numerical dispersion occurs (Bohlen, 1998). This numerical

artifact is called grid dispersion. To minimize the grid dispersion following criterion for spatial grid spacing Δh has to be fulfilled:

$$\Delta h \leq \frac{\lambda_{\min}}{n} = \frac{c_{\min}(f_{\max})}{n\, f_{\max}} \tag{II.21}$$

with the minimum wavelength $\lambda_{\min}$, the minimum phase velocity (of shear waves) $c_{\min}(f_{\max})$ present in the model and the maximum frequency $f_{\max}$ of the wave field. The parameter n depends on the used order of Taylor operators. For second-order and fourth-order Taylor operators it is $n = 12$ and $n = 8$, respectively (e.g. Doblain, 1986).

The second criterion is the so-called Courant instability. The temporal discretization has to satisfy a sampling criteria which ensures the stability of the finite-difference modeling. This means that the sampling interval Δt has to be less than the travel time of a wave (in particular P-wave) between two adjacent grid points with spatial grid spacing Δh. In case of Taylor operator of second order the Courant-Friedrichs-Lewy criterion (Courant et al., 1928, 1967) is defined by

$$\Delta t \leq \frac{\Delta h}{\sqrt{2}\, c_{\max}(f_{\max})} \tag{II.22}$$

with the maximum phase velocity (of P-wave) $c_{\max}(f_{\max})$ (Bohlen, 1998).

II.2 The adjoint approach

The aim of full-waveform inversion is to extract information from observed seismograms on model parameters describing the Earth's interior. By minimizing a chosen measure of misfit between observed and synthetic seismograms, the model parameters $\boldsymbol{m}(\lambda, \mu, \rho)$ are updated. In the adjoint approach, the gradient of the misfit function is calculated by interaction of the forward and adjoint wave field, in particular a zero-lag cross-correlation. The latter is generated by back-propagation of adjoint sources based on data (Tromp et al., 2005) like e.g. residuals between observed and synthetic seismograms (Tarantola, 1984). A preconditioned conjugate gradient method is used to solve the non-linear inverse problem iteratively.

To find a minimum of the residual energy the model parameters $\boldsymbol{m}_n(\lambda_n, \mu_n, \rho_n)$ are updated along the search direction $\delta \boldsymbol{m}_n$ at iteration n:

$$\boldsymbol{m}_{n+1} = \boldsymbol{m}_n + \alpha \delta \boldsymbol{m}_n \tag{II.23}$$

with the step length α which is discussed in detail in Section II.4.2.
The residual energy $E(\boldsymbol{m}_n + \delta \boldsymbol{m}_n)$ is expanded in a Taylor series to find the search direction $\delta \boldsymbol{m}_n$:

$$E(\boldsymbol{m}_n + \delta \boldsymbol{m}_n) \approx E(\boldsymbol{m}_n) + \delta \boldsymbol{m}_n \left(\frac{\partial E}{\partial m}\right)_n + \frac{1}{2} \boldsymbol{m}_n \left(\frac{\partial^2 E}{\partial m^2}\right)_n \delta \boldsymbol{m}_n^{\mathrm{T}}. \tag{II.24}$$

Subsequently, the derivative of eq. II.24 with respect to $\boldsymbol{m}_n$ is set to zero:

$$\frac{\partial E(\boldsymbol{m}_n + \delta \boldsymbol{m}_n)}{\partial \boldsymbol{m}_n} = \left(\frac{\partial E}{\partial m}\right)_n + \boldsymbol{m}_n \left(\frac{\partial^2 E}{\partial m^2}\right)_n = 0. \tag{II.25}$$

Eq. II.25 can be written in the form

$$\delta \boldsymbol{m}_n = -\left(\frac{\partial^2 E}{\partial m^2}\right)_n^{-1} \left(\frac{\partial E}{\partial m}\right)_n = -\boldsymbol{H}_n^{-1} \left(\frac{\partial E}{\partial m}\right)_n \tag{II.26}$$

where $-\left(\partial E/\partial m\right)_n$ denotes the steepest-descent direction of the misfit function and $\boldsymbol{H}_n^{-1}$ the inverse Hessian matrix. The calculation of the inverse Hessian matrix is difficult due to excessive computational demands and is therefore often approximated by a preconditioning operator $\boldsymbol{P}$. Different approaches for applying a preconditioning to the gradients are discussed in Section II.4.1.

Inserting eq. II.26 into eq. II.23 leads to

$$\boldsymbol{m}_{n+1} = \boldsymbol{m}_n - \alpha \boldsymbol{P}_n \left(\frac{\partial E}{\partial m}\right)_n . \tag{II.27}$$

The misfit function E is defined by

$$E(m) = \sum_{r=1}^{n_r} \sum_{i=1}^{n_c} \int_0^T g[d_i(\boldsymbol{x_r}, t), s_i(\boldsymbol{x_r}, t, \boldsymbol{m})] \, \mathrm{d}t \tag{II.28}$$

where g may be any kind of misfit definition to quantifies the discrepancy between the observed $d_i(\boldsymbol{x_r}, t)$ and synthetic $s_i(\boldsymbol{x_r}, t, \boldsymbol{m})$ particle displacement at a receiver r at point $\boldsymbol{x_r}$ of the i-th component. n_r and n_c denote the number of receivers and components, respectively, and T is the recording time.
With the chain rule the gradient of the misfit function is calculated by

$$\frac{\partial E}{\partial m_n} = \sum_{r=1}^{n_r} \sum_{i=1}^{n_c} \int_0^T \partial_{s_i} g \, \frac{\partial s_i(\boldsymbol{x_r}, t, \boldsymbol{m})}{\partial m_n} \, \mathrm{d}t \tag{II.29}$$

where $\partial_{s_i} g$ is the Fréchet derivative (Tromp et al., 2005). In seismic waveform tomography, where multiple earthquake or rather active sources like hammer blows are present, the Fréchet derivatives are simply summed up. However, for convenience, I consider data with only one source. To avoid clutter I omit the dependence of the synthetic displacement $s_i(\boldsymbol{x_r}, t, \boldsymbol{m})$ on the model $\boldsymbol{m}$ from here on.

According to Tromp et al. (2005) the partial derivatives of the synthetic seismograms with respect to the model parameters may be expressed by using the Born approximation (Hudson, 1977; Wu and Aki, 1985) as

$$\begin{aligned} \frac{\partial}{\partial m_n} s_i(\boldsymbol{x_r}, t) = -\int_0^T \int_V [&\delta\rho(\boldsymbol{x}') G_{ij}(\boldsymbol{x}, \boldsymbol{x}'; t - t') \partial_{t'}^2 s_j(\boldsymbol{x}', t') \\ &+ \delta c_{jklm}(\boldsymbol{x}') \partial_k' G_{ij}(\boldsymbol{x}, \boldsymbol{x}'; t - t') \partial_l' s_m(\boldsymbol{x}', t')] \mathrm{d}^3\boldsymbol{x}' \mathrm{d}t', \end{aligned} \tag{II.30}$$

where ρ is the density, c_{jklm} is the fourth-order elastic tensor and $\delta\rho$ and δc_{jklm} are their corresponding perturbations, respectively. Inserting the partial derivatives into eq. II.29

yields

$$\frac{\partial E}{\partial m_n} = -\sum_{r=1}^{n_r} \int_0^T \partial_{s_i} g \int_0^t \int_V [\delta\rho(\boldsymbol{x}') G_{ij}(\boldsymbol{x}, \boldsymbol{x}'; t-t') \partial_{t'}^2 s_j(\boldsymbol{x}', t') + \delta c_{jklm}(\boldsymbol{x}') \partial_k' G_{ij}(\boldsymbol{x}, \boldsymbol{x}'; t-t') \partial_l' s_m(\boldsymbol{x}', t')] \mathrm{d}^3\boldsymbol{x}' \mathrm{d}t' \mathrm{d}t. \tag{II.31}$$

Making usage of the reciprocity of the Green's Tensor (Aki and Richards, 1980),

$$G_{ik}(\boldsymbol{x}_r, \boldsymbol{x}'; t-t') = G_{ki}(\boldsymbol{x}', \boldsymbol{x}_r; t-t'), \tag{II.32}$$

and reversing time by substituting $t \rightarrow T - t$, Tromp et al. (2005) define the adjoint wave field $\boldsymbol{s}^\dagger$ by

$$s_k^\dagger(\boldsymbol{x}', t') = \int_0^{t'} \int_V G_{ki}(\boldsymbol{x}', \boldsymbol{x}_r; t'-t)\, f_i^\dagger(\boldsymbol{x}, t)\, \mathrm{d}^3\boldsymbol{x}\, \mathrm{d}t, \tag{II.33}$$

where $f_i^\dagger$ is the adjoint source given by

$$f_i^\dagger(\boldsymbol{x}, t) = \sum_{r=1}^{n_r} \partial_{s_i} g(\boldsymbol{x}_r, T-t, \boldsymbol{m}) \delta(\boldsymbol{x} - \boldsymbol{x}_r). \tag{II.34}$$

For an isotropic elastic medium and in the 2D case the gradient of the misfit function with respect to the different model parameters is

$$\frac{\partial E}{\partial \rho_n} = \int_0^T \left(\frac{\partial s_1}{\partial t} \frac{\partial s_1^\dagger}{\partial t} + \frac{\partial s_2}{\partial t} \frac{\partial s_2^\dagger}{\partial t} \right) \mathrm{d}t, \tag{II.35}$$

$$\frac{\partial E}{\partial \lambda_n} = -\int_0^T \left(\frac{\partial s_1^\dagger}{\partial x_1} + \frac{\partial s_2^\dagger}{\partial x_2} \right) \cdot \left(\frac{\partial s_1}{\partial x_1} + \frac{\partial s_2}{\partial x_2} \right) \mathrm{d}t, \tag{II.36}$$

$$\frac{\partial E}{\partial \mu_n} = -\int_0^T \left(\frac{\partial s_1^\dagger}{\partial x_2} + \frac{\partial s_2^\dagger}{\partial x_1} \right) \cdot \left(\frac{\partial s_1}{\partial x_2} + \frac{\partial s_2}{\partial x_1} \right) + 2 \left(\frac{\partial s_1^\dagger}{\partial x_1} \frac{\partial s_1}{\partial x_1} + \frac{\partial s_2^\dagger}{\partial x_2} \frac{\partial s_2}{\partial x_2} \right) \mathrm{d}t \tag{II.37}$$

with $s := s(\boldsymbol{x}_r, t, \boldsymbol{m})$ and $s^\dagger := s^\dagger(\boldsymbol{x}_r, t, \boldsymbol{m})$ for convenience. The gradient may be obtained by two numerical simulations, one for the forward propagated and one for the adjoint wave field. Finally, the gradient can be calculated by a zero-lag cross-correlation of both wave fields.

Köhn et al. (2012) studied the influence on reproduction capability for different parametrizations in a 2D FWI. They recommended to invert for P- and S-wave velocities as well as density rather than for Lamé parameters and density. Therefore, I decided to use density and seismic velocities in the inversion tests of my thesis. The gradients for these parameters are calculated with the chain rule based on Mora (1987) and are given by Köhn et al. (2012) and Groos (2013):

$$\frac{\partial E}{\partial v_p} = 2\rho v_p \frac{\partial E}{\partial \lambda}, \tag{II.38}$$

$$\frac{\partial E}{\partial v_s} = -4\rho v_s \frac{\partial E}{\partial \lambda} + 2\rho v_s \frac{\partial E}{\partial \mu}, \tag{II.39}$$

$$\frac{\partial E}{\partial \rho} = (v_p^2 - 2v_s^2)\frac{\partial E}{\partial \lambda} + v_s^2 \frac{\partial E}{\partial \mu} + \frac{\partial E}{\partial \rho} \tag{II.40}$$

with

$$\lambda = \rho(v_p^2 - 2v_s^2), \tag{II.41}$$

$$\mu = \rho v_s^2. \tag{II.42}$$

For the derivation of the gradient for viscoelastic media the reader is referred to Groos (2013) and Groos et al. (2014).

II.3 Misfit definitions and corresponding adjoint sources

II.3.1 L2 norm

The L2 or rather least-squares norm is defined by

$$E = \sum_{r=1}^{n_r} \sum_{i=1}^{n_c} \int_0^T \left(d_i(\boldsymbol{x_r}, t) - s_i(\boldsymbol{x_r}, t, \boldsymbol{m})\right)^2 \, \mathrm{d}t \tag{II.43}$$

and has a special physical meaning as it represents the residual elastic energy which is contained in the data residuals. This misfit definition is widely used in FWI.
The gradient is calculated by the derivative of the misfit function with respect to the model parameters (see eq. II.29) which yields

$$\frac{\partial E}{\partial m_n} = \sum_{r=1}^{n_r} \sum_{i=1}^{n_c} \int_0^T -2\left(d_i(\boldsymbol{x_r}, t) - s_i(\boldsymbol{x_r}, t, \boldsymbol{m})\right) \frac{\partial s_i(\boldsymbol{x_r}, t, \boldsymbol{m})}{\partial m_n} \, \mathrm{d}t. \tag{II.44}$$

With eq. II.34 the adjoint source is

$$f_i^\dagger(\boldsymbol{x}, t) = \sum_{r=1}^{n_r} 2\left(s_i(\boldsymbol{x}, T-t, \boldsymbol{m}) - d_i(\boldsymbol{x}, T-t)\right) \delta(\boldsymbol{x} - \boldsymbol{x}_r). \tag{II.45}$$

II.3.2 L2 norm of normalized wave fields

Choi and Alkhalifah (2012) recommended a least-squares norm of normalized wave fields as objective function

$$E = \sum_{r=1}^{n_r} \sum_{i=1}^{n_c} \int_0^T \left(\frac{s_i(\boldsymbol{x_r}, t, \boldsymbol{m})}{\left(\frac{1}{T} \int_0^T s_i^2(\boldsymbol{x_r}, t', \boldsymbol{m}) \, \mathrm{d}t' \right)^{1/2}} - \frac{d_i(\boldsymbol{x_r}, t)}{\left(\frac{1}{T} \int_0^T d_i^2(\boldsymbol{x_r}, t') \, \mathrm{d}t' \right)^{1/2}} \right)^2 \mathrm{d}t \tag{II.46}$$

where each seismogram is normalized by its RMS value. Therefore, near and far-offset traces contribute equally to the misfit and it is not sensitive to residuals in the amplitude decay with offset. It is, however, sensitive to relative amplitude differences within one seismogram. The misfit function can be also expressed as a zero-lag cross-correlation between normalized observed and synthetic data (Choi and Alkhalifah, 2012)

$$E = 2\frac{n_r \cdot n_c}{\frac{1}{T}} - 2 \sum_{r=1}^{n_r} \sum_{i=1}^{n_c} \int_0^T \frac{s_i(\boldsymbol{x_r}, t, \boldsymbol{m}) \cdot d_i(\boldsymbol{x_r}, t)}{\left(\frac{1}{T} \int_0^T s_i^2(\boldsymbol{x_r}, t', \boldsymbol{m}) \, \mathrm{d}t' \right)^{1/2} \left(\frac{1}{T} \int_0^T d_i^2(\boldsymbol{x_r}, t') \, \mathrm{d}t' \right)^{1/2}} \, \mathrm{d}t. \tag{II.47}$$

The gradient is calculated by the derivative of the misfit function with respect to the model parameters (see eq. II.29 and Choi and Alkhalifah, 2012; Groos, 2013) which yields

$$\begin{aligned} \frac{\partial E}{\partial m_n} = \sum_{r=1}^{n_r} \sum_{i=1}^{n_c} \int_0^T 2 \Bigg[& \frac{d_i(\boldsymbol{x_r}, t)}{\left(\frac{1}{T} \int_0^T s_i^2(\boldsymbol{x_r}, t', \boldsymbol{m}) \, \mathrm{d}t' \right)^{1/2} \left(\frac{1}{T} \int_0^T d_i^2(\boldsymbol{x_r}, t') \, \mathrm{d}t' \right)^{1/2}} \\ & - \frac{\left(\frac{1}{T} \int_0^T s_i(\boldsymbol{x_r}, t, \boldsymbol{m}) d_i(\boldsymbol{x_r}, t') \, \mathrm{d}t' \right) s_i(\boldsymbol{x_r}, t, \boldsymbol{m})}{\left(\frac{1}{T} \int_0^T s_i^2(\boldsymbol{x_r}, t', \boldsymbol{m}) \, \mathrm{d}t' \right)^{3/2} \left(\frac{1}{T} \int_0^T d_i^2(\boldsymbol{x_r}, t') \, \mathrm{d}t' \right)^{1/2}} \Bigg] \frac{\partial s_i(\boldsymbol{x_r}, t, \boldsymbol{m})}{\partial m_n} \, \mathrm{d}t. \end{aligned} \tag{II.48}$$

With eq. II.34 the adjoint source is

$$\begin{aligned} f_i^\dagger(\boldsymbol{x}, t) = \sum_{r=1}^{n_r} 2 \Bigg(& - \frac{d_i(\boldsymbol{x}, T-t)}{\left(\frac{1}{T} \int_0^T s_i^2(\boldsymbol{x}, t', \boldsymbol{m}) \, \mathrm{d}t' \right)^{1/2} \left(\frac{1}{T} \int_0^T d_i^2(\boldsymbol{x}, t') \, \mathrm{d}t' \right)^{1/2}} \\ & + \frac{\left(\frac{1}{T} \int_0^T s_i(\boldsymbol{x}, t, \boldsymbol{m}) d_i(\boldsymbol{x}, t') \, \mathrm{d}t' \right) s_i(\boldsymbol{x}, T-t, \boldsymbol{m})}{\left(\frac{1}{T} \int_0^T s_i^2(\boldsymbol{x}, t', \boldsymbol{m}) \, \mathrm{d}t' \right)^{3/2} \left(\frac{1}{T} \int_0^T d_i^2(\boldsymbol{x}, t') \, \mathrm{d}t' \right)^{1/2}} \Bigg) \delta(\boldsymbol{x} - \boldsymbol{x}_r). \end{aligned} \tag{II.49}$$

Since I use this misfit function for the synthetic reconstruction tests in Chapter III and the field data application in Chapter V I give the misfit function additionally in time discrete notation which can be expressed by

$$E = \frac{\sum_i^{n_c} \sum_r^{n_r} \sum_j^{n_s} |\hat{\boldsymbol{s}}_{i,r,j} - \hat{\boldsymbol{d}}_{i,r,j}|^2}{\sum_i^{n_c} \sum_r^{n_r} \sum_j^{n_s} |\hat{\boldsymbol{d}}_{i,r,j}|^2} = \frac{\sum_i^{n_c} \sum_r^{n_r} \sum_j^{n_s} |\hat{\boldsymbol{s}}_{i,r,j} - \hat{\boldsymbol{d}}_{i,r,j}|^2}{n_s n_r n_c} \tag{II.50}$$

where the vectors $\boldsymbol{s}_{i,r,j}$ and $\boldsymbol{d}_{i,r,j}$ are the synthetic and observed displacement seismograms which contain all time samples. $\hat{\boldsymbol{s}}_{i,r,j} = \boldsymbol{s}_{i,r,j}/|\boldsymbol{s}_{i,r,j}|$ and $\hat{\boldsymbol{d}}_{i,r,j} = \boldsymbol{d}_{i,r,j}/|\boldsymbol{d}_{i,r,j}|$ are the corresponding normalized displacement seismograms, respectively. Additionally, the misfit function is normalized by the energy of the normalized observed data (Groos, 2013).

II.3.3 Envelope-based misfit definition

Chi et al. (2013) suggested an envelope-based objective function which compares the difference between the envelopes of observed and synthetic wave fields. Such a misfit definition might reduce the non-linearity of the misfit function. The envelope of a seismogram is less sensitive to the oscillating waveform and therefore the risk of cycle-skipping (Virieux and Operto, 2009) can be reduced dramatically. Furthermore, the long wavelength components are amplified which is in particular important by a lack of low frequencies in field data application (see Section V.8.1).

Hilbert transform
Following the work of Bozdag et al. (2011) a signal constructed from a real signal $f(t)$ and its Hilbert transform $\mathcal{H}$(f(t)) is called an analytical signal:

$$\tilde{f}(t) = f(t) - i\mathcal{H}\left\{f(t)\right\}. \tag{II.51}$$

The definition of a Hilbert transformed signal is

$$\mathcal{H}\left\{f(t)\right\} = -\frac{1}{\pi}\, P \int_{-\infty}^{+\infty} \frac{f(\tau)}{t-\tau}\, d\tau, \tag{II.52}$$

where P represents for the Cauchy principal value. The analytical signal can be formulated in terms of phase $\phi(t)$ and amplitude $A(t)$

$$\tilde{f}(t) = A(t)\, e^{i\phi(t)}, \tag{II.53}$$

where

$$\phi(t) = \frac{\Im\left\{\tilde{f}(t)\right\}}{\Re\left\{\tilde{f}(t)\right\}} \tag{II.54}$$

and

$$A(t) = \sqrt{\Re\left\{\tilde{f}(t)\right\}^2 + \Im\left\{\tilde{f}(t)\right\}^2}. \tag{II.55}$$

Finally, $A(t)$ is also known as the envelope of the real signal $f(t)$ and is indicated in the following by env().

Misfit function and corresponding adjoint source
The misfit function is defined by

$$E = \frac{1}{2} \sum_{r=1}^{n_r} \sum_{i=1}^{n_c} \int_0^T \left(\mathrm{env}(s_i(\boldsymbol{x_r}, t, \boldsymbol{m})) - \mathrm{env}(d_i(\boldsymbol{x_r}, t))\right)^2 \, \mathrm{d}t. \tag{II.56}$$

The gradient is calculated by the derivative of the misfit function with respect to the model parameters (see eq. II.29) which yields

$$\frac{\partial E}{\partial m_n} = \sum_{r=1}^{n_r} \sum_{i=1}^{n_c} \int_0^T \left(\mathrm{env}(s_i(\boldsymbol{x_r}, t, \boldsymbol{m})) - \mathrm{env}(d_i(\boldsymbol{x_r}, t))\right) \frac{\partial \mathrm{env}(s_i(\boldsymbol{x_r}, t, \boldsymbol{m}))}{\partial s_i(\boldsymbol{x_r}, t, \boldsymbol{m})} \frac{\partial s_i(\boldsymbol{x_r}, t, \boldsymbol{m})}{\partial m_n} \, \mathrm{d}t. \tag{II.57}$$

Comparison with eq. II.29 yields

$$\partial_{s_i} g(\boldsymbol{x}_r, t, \boldsymbol{m}) = \left(\mathrm{env}(s_i(\boldsymbol{x_r}, t, \boldsymbol{m})) - \mathrm{env}(d_i(\boldsymbol{x_r}, t))\right) \frac{\partial \mathrm{env}(s_i(\boldsymbol{x_r}, t, \boldsymbol{m}))}{\partial s_i(\boldsymbol{x_r}, t, \boldsymbol{m})} \tag{II.58}$$

for the Fréchet derivative. In the following I omit the dependence of $s_i(\boldsymbol{x_r}, t, \boldsymbol{m})$ and $d_i(\boldsymbol{x_r}, t)$ on time and place as well as the component i to avoid clutter.
With $\mathrm{env}(s) = \sqrt{s^2 + \mathcal{H}\{s\}^2}$ (see eq. II.55) I get

$$\begin{aligned}
\partial_{s_i} g &= \left(\mathrm{env}(s) - \mathrm{env}(d)\right) \frac{\partial \sqrt{s^2 + \mathcal{H}\{s\}^2}}{\partial s} && \text{(II.59)} \\
&= \left(\mathrm{env}(s) - \mathrm{env}(d)\right) \frac{1}{2} \frac{2s\partial s + 2\mathcal{H}\{s\}\,\partial\mathcal{H}\{s\}}{\sqrt{s^2 + \mathcal{H}\{s\}^2}} && \text{(II.60)} \\
&= \left(\mathrm{env}(s) - \mathrm{env}(d)\right) \frac{s\partial s + \mathcal{H}\{s\}\,\partial\mathcal{H}\{s\}}{\mathrm{env}(s)} && \text{(II.61)} \\
&= \left(\mathrm{env}(s) - \mathrm{env}(d)\right) \frac{s\partial s}{\mathrm{env}(s)} + \left(\mathrm{env}(s) - \mathrm{env}(d)\right) \frac{\mathcal{H}\{s\}\,\partial\mathcal{H}\{s\}}{\mathrm{env}(s)}. && \text{(II.62)}
\end{aligned}$$

A solution how to handle $\partial\mathcal{H}(s)$ is given by Bozdag et al. (2011). Let us define the Hilbert transform of $s(t)$ as

$$\mathcal{H}\{s(t)\} = h(t) \, * \, s(t), \tag{II.63}$$

where

$$h(t) \equiv -\frac{1}{\pi t}. \tag{II.64}$$

Note that $h(-t) = -h(t)$.
According to Bozdag et al. (2011) one obtains

$$\begin{aligned}
\int f(t)\partial\mathcal{H}\{s(t)\}\,dt &= \int f(t) \int h(t - t')\partial s(t')dt'dt && \text{(II.65)} \\
&= -\int \mathcal{H}\{f(t)\}\,\partial s(t)dt. && \text{(II.66)}
\end{aligned}$$

With eq. II.66 I get

$$\partial_{s_i} g = (\mathrm{env}(s) - \mathrm{env}(d)) \frac{s \partial s}{\mathrm{env}(s)} - \mathcal{H} \left\{ \frac{(\mathrm{env}(s) - \mathrm{env}(d))\, \mathcal{H}(s)}{\mathrm{env}(s)} \right\} \partial s \quad \text{(II.67)}$$

$$= \left((\mathrm{env}(s) - \mathrm{env}(d)) \frac{s}{\mathrm{env}(s)} - \mathcal{H} \left\{ \frac{(\mathrm{env}(s) - \mathrm{env}(d))\, \mathcal{H}(s)}{\mathrm{env}(s)} \right\} \right) \partial s. \quad \text{(II.68)}$$

Finally, the adjoint source is together with eq. II.34

$$f_i^\dagger(\boldsymbol{x}, t) = \left((\mathrm{env}(s_i(\boldsymbol{x}, T-t, \boldsymbol{m})) - \mathrm{env}(d_i(\boldsymbol{x}, T-t))) \frac{s_i(\boldsymbol{x}, T-t, \boldsymbol{m})}{\mathrm{env}(s_i(\boldsymbol{x}, T-t, \boldsymbol{m}))} - \right.$$
$$\left. \mathcal{H} \left\{ \frac{(\mathrm{env}(s_i(\boldsymbol{x}, T-t, \boldsymbol{m})) - \mathrm{env}(d_i(\boldsymbol{x}, T-t)))\, \mathcal{H}(s_i(\boldsymbol{x}, T-t, \boldsymbol{m}))}{\mathrm{env}(s_i(\boldsymbol{x}, T-t, \boldsymbol{m}))} \right\} \right) \delta(\boldsymbol{x} - \boldsymbol{x_r}). \quad \text{(II.69)}$$

At time samples t where the envelope of the synthetics $\mathrm{env}(s)$ becomes small with respect to the noise of the observed data $\mathrm{env}(d)$, the adjoint source in eq. II.69 develops a singularity (for $\mathrm{env}(s) \to 0$). A finite water-level ϵ is used to keep the division regular. The water-level ϵ is estimated about the smallest signal amplitude of the observed data which is considered in the misfit. I introduce a stabilizing water-level ϵ to the denominator of eq. II.69:

$$f_i^\dagger(\boldsymbol{x}, t) = \left((\mathrm{env}(s_i(\boldsymbol{x}, T-t, \boldsymbol{m})) - \mathrm{env}(d_i(\boldsymbol{x}, T-t))) \frac{s_i(\boldsymbol{x}, T-t, \boldsymbol{m})}{\mathrm{env}(s_i(\boldsymbol{x}, T-t, \boldsymbol{m})) + \epsilon} - \right.$$
$$\left. \mathcal{H} \left\{ \frac{(\mathrm{env}(s_i(\boldsymbol{x}, T-t, \boldsymbol{m})) - \mathrm{env}(d_i(\boldsymbol{x}, T-t)))\, \mathcal{H}(s_i(\boldsymbol{x}, T-t, \boldsymbol{m}))}{\mathrm{env}(s_i(\boldsymbol{x}, T-t, \boldsymbol{m})) + \epsilon} \right\} \right) \delta(\boldsymbol{x} - \boldsymbol{x_r}). \quad \text{(II.70)}$$

I implemented the envelope-based misfit function (eq. II.56) and the corresponding adjoint source (eq. II.70) to the FWI code `DENISE`.

II.4 Numerical implementation of FWI

In my thesis I apply the 2D elastic full-waveform inversion code `DENISE` which was originally developed by Köhn (2011). The FWI scheme is based on the adjoint approach (Tarantola, 1986; Mora, 1987) where the parallelized elastic finite-difference forward modeling (Bohlen, 2002) and the gradient calculation are performed in the time domain. The code is freely available under the terms of GNU public license and references to the source code are provided at `http://www.opentoast.de`. Fig. II.1 shows a workflow of the main steps implemented in the 2D elastic full-waveform inversion code `DENISE` (Groos, 2013).

Input parameters
The input parameters are the observed data and the acquisition geometry as well as the initial model or rather the model of the previous iteration step. Furthermore, a source wavelet is required which is either an arbitrary force time function (e.g., the first period of a $sin^3(t)$ where t is the time) or an optimal source wavelet estimated by inversion (see Section II.4.4).

Calculation of the gradient
The gradient calculation is performed with a loop over all shots. Firstly, a forward simulation on the current model is computed and the wave fields of stress as well as particle velocities are saved in memory. Secondly, the adjoint sources are calculated with the observed and synthetic data at the receiver positions. Thirdly, a back-propagation of the adjoint sources from the receiver positions is simulated. Finally, the gradient of the misfit function is calculated on the fly with a zero-lag cross-correlation within the same loop over time steps that is used for the back-propagation. The single-shot gradients are summed for all shots.

Preconditioning
Subsequently, a preconditioning is applied to the gradients (Section II.4.1). Possible choices are 1) semi-circular taper at source locations to avoid high-amplitude artifacts, 2) median filter to remove unrealistic components within the gradient or 3) sharpening or focusing filter (e.g. approximated Hessian matrix, Sheen et al., 2006). Furthermore, a conjugate gradient method is applied due to higher convergence compared to a simplistic steepest descent method.

Step length estimation
For the model update an appropriate step length α is required (see eq. II.23). For the step length estimation a parabolic line search method suggested by Nocedal and Wright (1999) is used. Basically, only two further test forward modelings are needed. However, there is a more enhanced algorithm implemented in `DENISE` to estimate a preferably large but still appropriate step length (Köhn et al., 2013). Not all shots of the acquisition geometry were used for the step length estimation to save computing time. For the synthetic reconstruction tests in Chapter III I used three test shots (left, middle and right side of the profile), whereas I used every second shot for the field data inversion in Chapter V. Finally, the model is updated with the calculated conjugate gradient and the optimal step length which is found for the current iteration step.

II.4.1 Preconditioning of gradients

The application of preconditioning to the gradients in elastic full-waveform inversion of shallow-seismic surface waves is a basic prerequisite. I apply three different approaches for preconditioning:

1) In the presence of shallow-seismic surface waves the gradients have high-amplitude artifacts in the vicinity of the source locations. If these artifacts are not damped the model parameters are only updated near the sources or more precisely, the inversion fails. In general, it is not possible to mitigate the high gradient amplitudes in a depth up to few meters, because in the context of surface waves the shallow subsoil is the region of most interest. Therefore, I apply a semi-circular taper around each source location of the single gradients before they were summed up. This way a model update is also obtained at the source locations in the final gradient. This preconditioning approach is used for every inversion test of my work.

2) Newton and Gauss-Newton methods are effective and robust techniques for numerical optimization of non-linear problems (Sheen et al., 2006). Pratt et al. (1998) suggested to apply a preconditioning using the inverse Hessian (see eq. II.26), or an approximation of the inverse Hessian which can yield improved convergence rates of iterative solutions like

steepest descent or conjugate gradient method (Section II.2). The Newton method (Tarantola, 1987) is given by (compare eq. II.23 and eq. II.26):

$$\boldsymbol{m}_{n+1} = \boldsymbol{m}_n - \boldsymbol{H}_n^{-1} \left(\frac{\partial E}{\partial m} \right)_n \tag{II.71}$$

with eq. II.29

$$\boldsymbol{m}_{n+1} = \boldsymbol{m}_n - \boldsymbol{H}_n^{-1} \partial_{s_i} g \frac{\partial s_i(\boldsymbol{x}_r, t, \boldsymbol{m})}{\partial m_n} \tag{II.72}$$

and the transpose of the Jacobian matrix $\boldsymbol{J}^t = \partial s_i(\boldsymbol{x}_r, t, \boldsymbol{m}) / \partial m_n$

$$\boldsymbol{m}_{n+1} = \boldsymbol{m}_n - \boldsymbol{H}_n^{-1} \partial_{s_i} g \boldsymbol{J}^t. \tag{II.73}$$

Each element of the Hessian matrix can be expressed as

$$\boldsymbol{H} = \left(\frac{\partial}{\partial m} \right)_n [\partial_{s_i} g \boldsymbol{J}^t] = \boldsymbol{J}^t \boldsymbol{J} + \left(\frac{\boldsymbol{J}^t}{\partial m} \right)_n \partial_{s_i} g. \tag{II.74}$$

After Tarantola (1987) the second term of eq. II.74 is usually small and negligible. Finally, the Gauss-Newton formula is given by

$$\boldsymbol{m}_{n+1} = \boldsymbol{m}_n - [\boldsymbol{J}^t \boldsymbol{J}]^{-1} \boldsymbol{J}^t \partial_{s_i} g = \boldsymbol{m}_n - [\boldsymbol{H}_a]^{-1} \boldsymbol{J}^t \partial_{s_i} g, \tag{II.75}$$

where $\boldsymbol{H}_a$ is the approximated Hessian matrix (Sheen et al., 2006). $\boldsymbol{H}_a$ is calculated from a zero-lag cross-correlation of the partial derivative wave fields and in particular the diagonal elements of the matrix from a zero-lag auto-correlation of the derivatives. The partial derivatives are mostly uncorrelated to each other and therefore, the approximated Hessian matrix is diagonally dominant due to auto-correlation. Furthermore, the approximated Hessian matrix is known that it acts like a sharpening or focusing filter (Sheen et al., 2006).

Daniel Köhn has implemented the calculation of the diagonal elements of the Hessian in the 2D elastic FWI code `DENISE`. Currently, the approximated Hessian matrix is only computed for the P- and S-wave model and for vertical sources. For the density model the Hessian matrix of the P-wave model is used. The estimation of the approximated Hessian requires the solution of the forward problem for each shot location and of the back-propagation for each receiver location. The wave fields have to be saved in memory and convolved with each other which is done as multiplication in the frequency domain (personal communication with Daniel Köhn, Kiel University). The approximated Hessian matrix is computed for the initial model and is unaltered during inversion. Finally, the inverse of the matrix is used as a preconditioning filter (see eq. II.26) to the gradients. The inversion of the Hessian matrix is done with an application of a Marquardt-Levenberg regularization, where the water-level has to be estimated empirically.

I use the inverse approximated Hessian matrix as a preconditioning filter for the reconstruction tests in Chapter III. Fig. II.2 shows the true and initial subsurface structure for the S-wave velocity, the corresponding gradient of the first iteration step, the calculated inverse approximated Hessian matrix as well as the preconditioned gradient (see eq. II.26). The

inverse approximated Hessian equals a predominantly depth dependent structure due to the initial subsurface structure. In the shallow part of the model small values are present whereas the values become larger with depth. This behavior may be slightly changed with different water-levels used in the inversion of the Hessian matrix. The original gradient of the first iteration shows periodic artifacts in the first meters of the model which correspond to source and receiver locations. These artifacts are mitigated by the preconditioning with the approximated Hessian matrix. Furthermore, the values of deeper structures are amplified. Obviously, the Hessian acts as a depth-dependent amplifier and, furthermore, yields to stronger convergence rates (not shown here).

3) Appropriate smoothing of gradients is a key point for successful full-waveform inversions. On the one hand, I observe instabilities during forward simulations due to very small-scale heterogeneities in the subsurface models inferred by the inversion. To avoid these artifacts very small filter lengths (around 0.5 m) are required. The filter lengths are still smaller than half of the minimum wavelength. On the other hand, a smooth inferred subsurface model is preferred over a rather rough model as long as the waveform fit is similar, because it shows the ambiguity of the inversion problem and the inferred small-scale structures of the rough model aren't reliable. Therefore, I implemented a 2D median filter in the elastic 2D FWI code `DENISE` to apply smoothing to the gradients.

II.4.2 Scaling of gradients

The calculation of the gradient of the misfit function is divided into three parts: a gradient for the S-wave velocity, a gradient for the P-wave velocity and a gradient for the density (see Section II.2). Therefore, the gradient may be written as

$$\frac{\partial E}{\partial m_n} = \begin{pmatrix} \partial E/\partial \boldsymbol{v}_p \\ \partial E/\partial \boldsymbol{v}_s \\ \partial E/\partial \boldsymbol{\rho} \end{pmatrix} = \begin{pmatrix} \boldsymbol{g}_{v_p} \\ \boldsymbol{g}_{v_s} \\ \boldsymbol{g}_{\rho} \end{pmatrix}. \tag{II.76}$$

Furthermore, the model update is divided by using

$$\begin{aligned} \Delta \boldsymbol{v}_p &= \alpha_{v_p} \boldsymbol{g}_{v_p} \quad \text{with} \quad \alpha_{v_p} = \epsilon \frac{\max[\boldsymbol{v}_p]}{\max[\boldsymbol{g}_{v_p}]} \\ \Delta \boldsymbol{v}_s &= \alpha_{v_s} \boldsymbol{g}_{v_s} \quad \text{with} \quad \alpha_{v_s} = \epsilon \frac{\max[\boldsymbol{v}_s]}{\max[\boldsymbol{g}_{v_s}]} \\ \Delta \boldsymbol{\rho} &= \alpha_{\rho} \boldsymbol{g}_{\rho} \quad \text{with} \quad \alpha_{\rho} = \epsilon \frac{\max[\boldsymbol{\rho}]}{\max[\boldsymbol{g}_{\rho}]} \end{aligned} \tag{II.77}$$

where $\max[\boldsymbol{a}]$ is the maximum absolute value of the vector $\boldsymbol{a}$ and ϵ is a scalar factor (Groos, 2013). In the `DENISE` code the absolute maximum of the gradient is scaled to the maximum value of the corresponding model parameter. Therefore, the largest update of each model parameter $\boldsymbol{v}_p$, $\boldsymbol{v}_s$ and $\boldsymbol{\rho}$ is ϵ times the maximum value of this model parameter in the current model. More precisely, $\epsilon = 0.01$ equals a model update of 1 % of the maximum model parameter. Nevertheless, this update is independent of the original absolute value of the single gradient due to the normalization in eq. II.77.

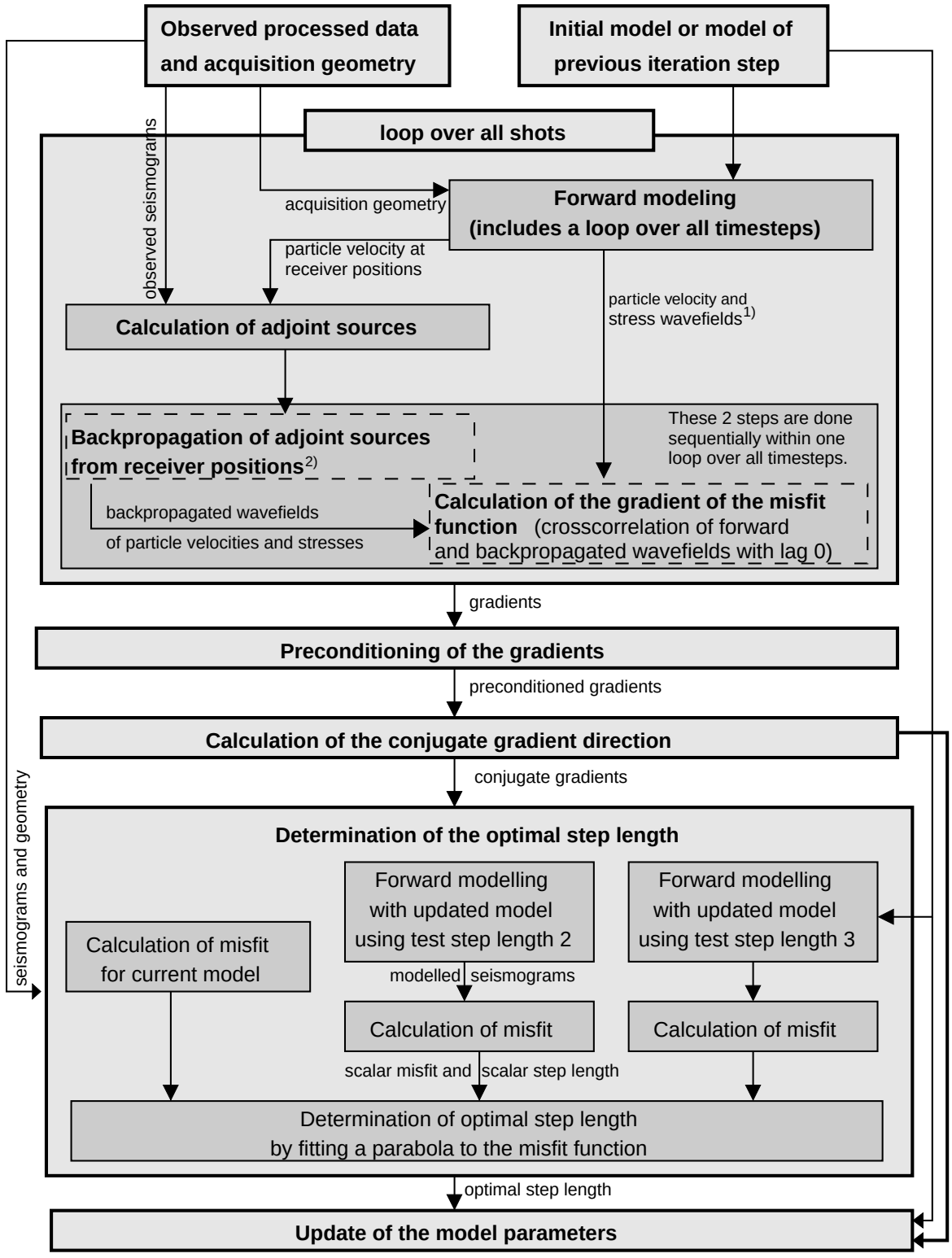

1) The whole process is realized in one binary program. Therefore, the wavefields remain in memory for one shot.
2) Corresponds to a forward modelling with time reversed adjoint sources which act as sources at the receiver positions.

Figure II.1: Workflow of the 2D FWI code `DENISE` for one iteration step from Groos (2013).

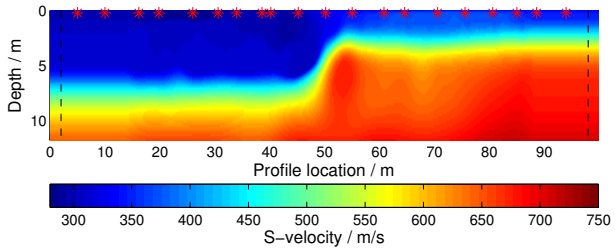

(a) 2D subsurface structure

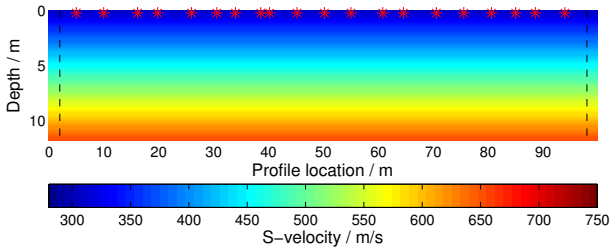

(b) initial subsurface structure

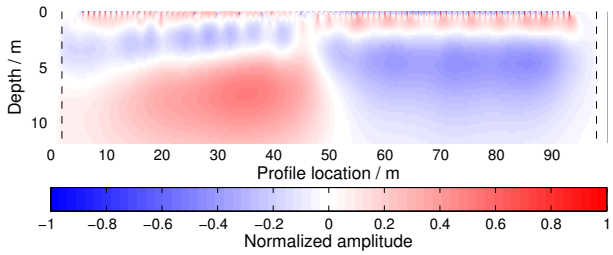

(c) Gradient of first iteration

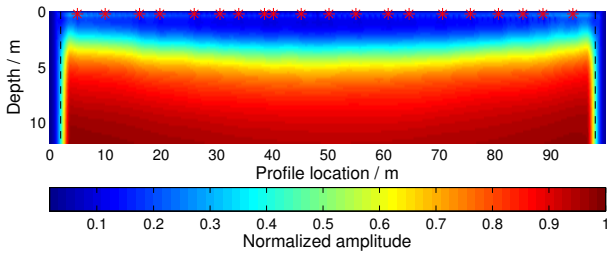

(d) inverse approximated Hessian matrix

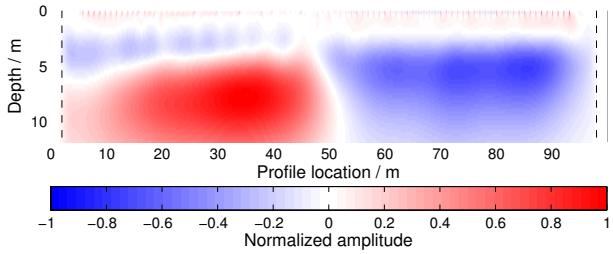

(e) preconditioned gradient of first iteration

Figure II.2: (a) and (b) display the true and initial subsurface structure for the S-wave velocity used for the reconstruction tests in Chapter III. (c) shows the corresponding S-wave velocity gradient of the first iteration. (d) is the inverse approximated Hessian matrix which is used as an unaltered preconditioning filter (see eq. II.26) during inversion. (e) displays the preconditioned S-wave velocity gradient used for the model update in the first iteration step. The absorbing boundary with convolutional perfectly matched layers (CPML) is indicated with black dashed lines. The red stars denote the source locations.

II.4.3 Multi-scale inversion with frequency filtering

Non-linear inverse problems, such as FWI, suffer from the presence of numerous local minima in the misfit function. The multi-scale approach is a technique which improves the performance of iterative inversions by decomposing the problem by scale (Bunks et al., 1995). The convergence of an iterative method to the global minimum or rather a local minimum strongly depends on the initial model. Bunks et al. (1995) suggested that at long scales the inversion may get closer to the neighborhood of the global minimum (see Fig. II.3). Starting with the inversion of strongly low-pass filtered data establishes the long wavelength components of the subsurface model first. Gradually higher frequencies are added to deduce the smaller scale distribution of the material properties in the subsurface subsequently. I implemented in the elastic full-waveform inversion code `DENISE` an automatic multi-scale inversion with frequency filtering (Butterworth low-pass filter). After an appropriate convergence of low frequencies, the corner frequency of the low-pass filter is increased automatically with an arbitrary frequency increment. If a given stop criterion is fulfilled, the frequency content will be increased. It is based on a threshold value of 1 % calculated between the relative change of the data misfit of the current iteration with respect to the next to last iteration.

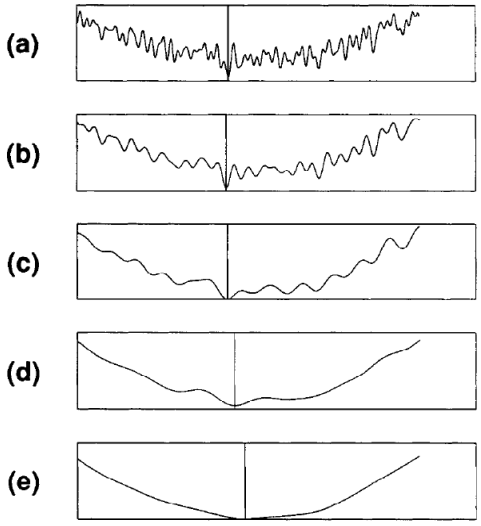

Figure II.3: (a) displays an illustration of a 1D misfit function and (b-e) show the same misfit function at ever increasing scale lengths (Bunks et al., 1995).

II.4.4 Source wavelet correction filter

For an inversion of field data it is necessary to estimate the unknown source time functions of the hammer impacts for each single shot. This is done by solving a damped, linear least-squares optimization problem (Groos et al., 2014, Appendix A). It can be formulated as a stabilized deconvolution of the recorded wave field with the synthetics. The suggested approach is similar to the method proposed by Pratt (1999). The shot-wise obtained source-wavelet correction filters are unaltered within a frequency interval and they are recalculated

for each single shot when the frequency interval is increased (Section II.4.3). This approach requires an additional forward simulation for every single shot. Therefore, I implemented in the loop of the gradient calculation (Section II.4) a second forward simulation for every shot to estimate an optimal source-wavelet correction filter which is then used in the original inversion scheme shown in Fig. II.1. The second forward simulation is only calculated when an optimal source-wavelet correction filter estimation is required (in particular first iteration, increase of frequency interval). Furthermore, it is possible to use a weighting with offset for the optimization problem (not used in this work) and to apply a trace killing so that not all traces are used (in particular far-offset traces, see Section V.6 preprocessing of field data).

II.4.5 Further inversion strategies for field data inversion

v_p/v_s ratio

After Bachrach et al. (2000) reasonable v_p/v_s ratios are expected for seismic material properties of shallow sediments between 1.56 (i.e., a Poisson number of $\nu = 0.15$) and values larger than 10 (i.e. $\nu > 0.495$). Stümpel et al. (1984) report even $\nu = 0$ (v_p/v_s ratio of 1.41) for dry and partially saturated sand. Material with $\nu < 0$ is physically not intuitive, because the material will actually contract in the transverse direction when compressed or expand when stretched. For shallow-seismic surveys known values lie between (Forbriger, 2003, Part II)

$$0.1 < \nu < 0.49, \tag{II.78}$$

$$1.5 < v_p/v_s < 10. \tag{II.79}$$

Up to now no regularization (expect smoothing of the gradients) is applied in the elastic full-waveform inversion code `DENISE`. However, I observe unrealistic small v_p/v_s ratios ($<$ 1.41) in the shallow subsoil in the field data inversion (Chapter V). Therefore, I implemented an automatic checking of the v_p/v_s ratio after every model update. It requires a minimum v_p/v_s ratio of 1.5 to ensure physically feasible subsurface models. This is done by checking the v_p/v_s ratio at every grid point after every model update and if it is less than 1.5 the P-wave velocity will be increased.

Regularized update of density

For the field data inversion in Chapter V the parameter range of density is limited between 1200 kg/m^3 and 3100 kg/m^3 to avoid unrealistic density values (in particular, $\rho < 1000$ kg/m^3). Furthermore, I observe large variations in the density model which haven't an influence to the waveforms at all. Therefore, I constrain the density update by scaling the step length α_ρ of the density parameter with an additional scalar factor of 30 % (see eq. II.77). This approach has neither an influence on convergence properties nor on the total data misfit. However, it ensures that the density model keeps closer to the initial values which is a reasonable assumption.

Chapter III

Line-source simulation for shallow-seismic data: a synthetic 2D case study

In this chapter I discuss the differences of geometrical spreading of 3D and 2D wave propagation and investigate possible artifacts produced by a line-source simulation for 2D FWI of shallow-seismic surface waves. A companion contribution and this study are also published with the title *Line-source simulation for shallow-seismic data. Part 1: Theoretical background, Part 2: Full-waveform inversion - a synthetic 2D case study* (Forbriger et al., 2014b; Schäfer et al., 2014).

Statement of the problem
Field data are commonly gained with a point source such as a hammer blow or an explosion which produces wave fields with 3D geometrical spreading. However, the applied inversion-code uses Cartesian 2D forward modeling and hence implicitly uses a line source in 3D space. Only 3D forward modeling would account appropriately for the point-source wave propagation like present in field data recordings. Unfortunately, the application of a 3D FWI to surface waves is still difficult due to excessive computational demands (Butzer et al., 2013). Therefore today, 2D FWI is preferential for code development and gaining experience because it allows for frequent repeat runs of inversion tests. One important prerequisite for a successful application of 2D FWI to field data is to perform accurate spreading transformations for 2D media.

Previous studies
Previous studies have shown the high potential of 2D elastic FWI being applied to surface waves (Romdhane et al., 2011; Tran and McVay, 2012; Tran et al., 2013; Bretaudeau et al., 2013). They all use a Cartesian 2D solver. Romdhane et al. (2011) investigate the inversion of 2D synthetic surface wave data and thus require no 3D/2D spreading correction because they use the same 2D forward solver for the pseudo-observed data and within the inversion scheme. Tran and McVay (2012) limit the discrepancy of 3D wave propagation of the field

data and 2D forward modeling in FWI by removing near offset traces. Tran et al. (2013) use an offset-dependent correction factor to account for the different amplitude-decay of waves excited by a point and a line source (Schäfer et al., 2012). Additionally a phase transformation is applied by convolving the point-source waveforms with $\sqrt{t^{-1}}$, where t is the traveltime. Bretaudeau et al. (2013) convert the 3D geometrical spreading into 2D spreading by applying a factor $\sqrt{t}$ to each sample. Additionally, they infer a source wavelet with appropriate phase by inversion. We demonstrate in a companion contribution that a scaling with $\sqrt{t^{-1}}$ is superior for the case of shallow-seismic data (Forbriger et al., 2014b). Amplitude scaling with $\sqrt{t}$ is unsatisfactory when applied to waves propagating with different phase velocities (e.g. P-, S- and Rayleigh waves) as are all present in shallow-seismic recordings.
Auer et al. (2013) assess the validity of the widely used 3D/2D data transformation derived from asymptotic ray theory (Bleibstein, 1986). They investigate the performance by comparing transformed waveforms with 2D reference waveforms and by reconstruction tests. For the latter a crosshole transmission geometry for acoustic and elastic data as well as a marine reflection geometry is used. They report that the filter performs well in simple acoustic transmission geometry in particular for random media, while substantial errors occur in more complex elastic models and reflection geometry. The study does not compare different filter approaches as we do, nor does it investigate the shallow-seismic configuration with dominant surface waves.

To make 2D FWI applicable to field data, recordings must be preprocessed to simulate the response to a line source. After the point-source wave fields are filtered, the wave fields can be inverted by a 2D full-waveform inversion. A simulation of a line source in the field may be also possible. In Chapter IV I present a feasibility study of a line-source simulation in a field survey. We present in a companion contribution a survey of previous studies and a detailed discussion and theory of line-source simulation procedures tested in the current study (Forbriger et al., 2014b).

Structure of this study
This chapter is organized as follows. To investigate the significance of the different geometrical spreading of line-source and point-source wave fields, we firstly investigate the accuracy of different numerical transformation techniques and discuss the waveform fit of transformed point-source seismograms in comparison to reference line-source seismograms for a 2D test structure. The 2D structure is designed to resemble a transverse section of a vertical fault located on the southern rim of the Taunus (near Frankfurt on the Main, Hesse, Germany) which is one of our field test sites with a significantly 2D heterogeneous structure (Chapter V). Secondly, we use the transformed point-source wave fields in a 2D full-waveform inversion as observed data to investigate possible artifacts produced by a line-source simulation for a 2D FWI of shallow-seismic surface waves. We compare results for 1) a line-source simulation by the *hybrid* transformation which is derived by approximation for the homogeneous-space acoustic case, 2) a line-source simulation by the *Fourier-Bessel* transformation which is exact for wave propagation on 1D structures, and 3) the original point-source seismograms with no correcting applied.

III.1 Line-source simulation for shallow-seismic surface waves

Several different 3D/2D transformation techniques are proposed in the literature. Some of them use an integral-transformation approach which requires a complete common source gather. Other transformation techniques have the benefit of being applicable to single traces. I refer to a detailed discussion of the theoretical background of appropriate line-source simulation procedures for shallow-seismic field data to our companion contribution (Forbriger et al., 2014b). Here I just summarize those approaches which are used in the current study. Their accuracy when applied to the 2D test scenario is presented in Section III.2.

III.1.1 Integral-transformation approach using wave-field expansion for 1D-structures

For laterally homogeneous structures (model parameters are only changing with depth) Wapenaar et al. (1992) and Amundsen and Reitan (1994) present an exact transformation. For a cylindrically symmetric source (vertical point force or explosive point source) in the origin of the coordinate system and a receiver profile along the horizontal y-axis, this kind of transformation uses a Fourier-Bessel expansion to express the Fourier transform of the vertical component $\tilde{u}_P$ of the wave field at offset r along the surface by

$$\tilde{u}_P(r,\omega) = \int_0^\infty G(\omega,p) J_0(\omega p r) \omega^2 p \,\mathrm{d}p \tag{III.1}$$

with the expansion coefficients G, the phase slowness p, the source to receiver distance r, the Bessel function J_0 of order zero, and the angular frequency ω. If the line source is aligned with the x-axis, the generated wave motion at a distance y to the line source can be expressed as a superposition of seismograms excited by an infinite number of point sources along the line source (see Figs III.1 and III.2). This way we obtain

$$\tilde{u}_L(y,\omega) = \int_{-\infty}^\infty \tilde{u}_P(\sqrt{x^2+y^2},\omega)\,\frac{\mathrm{d}x}{[x]} \tag{III.2}$$

for the Fourier coefficients of a seismogram $\tilde{u}_L(y,\omega)$ excited by a line source along the x-axis. The transformation provides correct magnitude and physical units for a definition of the line source appropriate for 2D Cartesian solvers (Forbriger et al., 2014b), if $[x]$ is the physical unit of length (commonly $[x] = 1\,\mathrm{m}$). Inserting eq. (III.1) into eq. (III.2) we obtain after some lines of calculus

$$\tilde{u}_L(y,\omega) = 2\int_0^\infty G(\omega,p)\cos(\omega p y)\,\omega\,\mathrm{d}p \tag{III.3}$$

for the line-source seismograms. Summarizing this transformation one first has to derive the expansion coefficients G from the point-source seismograms by the inverse transformation to

eq. (III.1) via

$$G(\omega, p) = \int_0^\infty \tilde{u}_p(r, \omega) J_0(\omega p r)\, r\, \mathrm{d}r. \tag{III.4}$$

In eq. (III.3) they produce the equivalent line-source generated Fourier coefficients. For sampled data a discrete approximation is given by Forbriger (2003 Part I; eq. 19). The transformation for the radial component can be derived in a similar way (Forbriger et al., 2014b). We call this the *Fourier-Bessel* transformation.

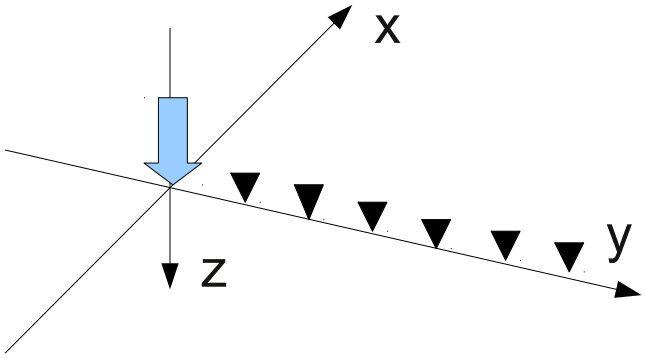

Figure III.1: The arrow denotes a point source located at the origin of the coordinate system. The triangles mark the location of receivers at $y = y_R$ with offset $r = y_R$.

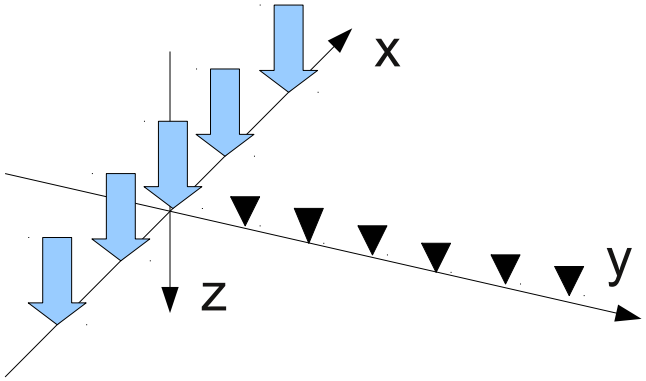

Figure III.2: A line source is located at $y = z = 0$ and extends along the x-axis of the coordinate system. The line source is sketched as an arrangement of point sources along the x-axis. The triangles mark the location of receivers at $y = y_R$ with offset $r = \sqrt{x_i^2 + y_R^2}$ to a single point source at $x = x_i$.

III.1.2 Single-trace transformations for non 1D-structures

The *Fourier-Bessel* transformation is limited to 1D structures and cannot properly handle waves propagating in laterally heterogeneous structures. In reflection seismics a single-trace transformation has been suggested by Pica et al. (1990) and Crase et al. (1990) which is adapted for reflected waves and is commonly applied today. In this approach the wave

fields are first convolved with $\sqrt{t^{-1}}$ and then tapered with $\sqrt{t}$. Amplitude correction of 3D/2D single-trace transformations are adapted to a certain group of wave types, but not to others. The $\sqrt{t}$ taper is appropriate for wave propagating with approximately the same phase velocity along an unknown propagation path. Therefore, this transformation is not able to scale amplitudes appropriately if waves with different phase velocities (e.g. P-, S- and Rayleigh waves) are present at the same time. For shallow-seismic Rayleigh waves we recommend to scale with $r\sqrt{2}\sqrt{t^{-1}}$ with offset r. The latter taper is appropriate for waves with unknown phase velocity propagating more or less along a direct wave path, such that offset r approximately equals propagation distance. Both scaling rules can be derived as an approximation for acoustic waves in homogeneous full-space and expressed by a simple factor in the Fourier domain (Forbriger et al., 2014b). We define the Fourier transform as follows.
If

$$u(t) = \int_{-\infty}^{\infty} \tilde{u}(\omega)\, e^{-i\omega t}\, \frac{\mathrm{d}\omega}{2\pi} \tag{III.5}$$

is the time history of quantity u, then $\tilde{u}$ is its Fourier transform.

If we take the Fourier transform of Green's functions $g_k^{2D}(r)$ and $g_k^{3D}(r)$ for the acoustic wave equation in 2D and 3D, respectively, we obtain the conversion factor

$$\lim_{r\to\infty} \frac{g_k^{2D}(r)}{g_k^{3D}(r)} \approx \sqrt{\frac{2\pi r}{k}} \cdot e^{i\pi/4} \tag{III.6}$$

in the far-field, where $k = \omega/v_{ph}$ is the wave number, v_{ph} the phase velocity of the wave, ω the angular frequency and r is the distance to the source. Forbriger et al. (2014b) show that this approach is also appropriate in the viscoelastic case (both vertical and radial component) for 1D structures with source and receiver at the free surface.

The conversion factor in eq. (III.6) applies a phase shift of $\pi/4$ to the waves and a spreading correction to the amplitudes, depending on offset r and wave number k. With phase velocity $v_{ph} = \omega/k$ eq. (III.6) can be factorized to

$$\sqrt{\frac{2\pi r}{k}} \cdot e^{i\pi/4} = \underbrace{\sqrt{2rv_{ph}}}_{F_{amp}} \cdot \underbrace{\sqrt{\frac{\pi}{\omega}}\, e^{i\pi/4}}_{\tilde{F}_{\sqrt{t^{-1}}}}. \tag{III.7}$$

The factor

$$\tilde{F}_{\sqrt{t^{-1}}}(\omega) = \sqrt{\frac{\pi}{\omega}}\, e^{i\pi/4} = \sqrt{\frac{\pi}{|\omega|}}(1 + \mathrm{i}\,\mathrm{sign}(\omega)) \tag{III.8}$$

applies the phase shift of $\pi/4$ and essentially is a convolution with $\sqrt{t^{-1}}$ in the time domain. This equals a fractional (half) integration.

The amplitude factor F_{amp} can be handled in different ways for shallow-seismic surface waves. Assuming a known single-phase velocity v_{ph} e.g. for homogeneous full-space

$$F_{amp} = \sqrt{2rv_{ph}}. \tag{III.9}$$

We call this the *single-velocity* transformation.

Commonly surface waves are strongly dispersive and comprise a large range of phase velocities. For surface waves and direct waves the offset is identical with the wave propagation distance. For waves travelling at shallow depth, offset almost equals propagation distance. We therefore estimate the phase velocity $v_{ph} = r/t$ from the offset r and the travel time t and recommend

$$F_{amp} = r \sqrt{\frac{2}{t}}. \tag{III.10}$$

We call this the *direct-wave* transformation.

Results can be improved by delaying the taper by the centroid delay of the source signal. At small receiver offsets this can shift the singularity of $\sqrt{t^{-1}}$ into the signal resulting in strong artifacts. In such cases the *direct-wave* transformation is used at larger offsets and is gradually replaced by the *single-velocity* transformation for small offsets with a smooth transition between both transformations (Forbriger et al., 2014b). We call this *hybrid* transformation and use it as single-trace transformation in the current study.

In the next part of the chapter I use the *Fourier-Bessel* and the *hybrid* transformation to simulate equivalent line-source generated waveforms from point-source wave fields calculated for a 2D heterogeneous structure.

III.2 Comparison with reference solution for a 2D structure

I demonstrate the accuracy of the *Fourier-Bessel* and the *hybrid* transformation by a synthetic 2D test case. The 2D test structure consists of a layer over half space with a step in the interface between them (see Fig. III.3). The transition zone of the layer to the half space is smooth. The velocity and density range is typical for the shallow subsoil. The 2D structure is designed to resemble a transverse section of a vertical fault located on the southern rim of the Taunus (near Frankfurt on the Main, Hesse, Germany) which is one of our field test sites with a significantly 2D heterogeneous structure (Chapter V). I calculate wave fields excited by point and line sources, respectively, with a 3D and 2D finite-difference forward modeling code in the time domain (Bohlen, 2002). We use a single vertical force

$$\vec{F}(t) = -\hat{z} \begin{cases} \sin^3(\pi t/0.032\,\mathrm{s}) & \text{if } 0 \le t \le 32\,\mathrm{ms} \text{ and} \\ 0 & \text{otherwise,} \end{cases} \tag{III.11}$$

where $\hat{z}$ is the unit vector in z-direction. This source produces seismic energy in a frequency bandwidth from 0 Hz to about 100 Hz. The finite-difference forward modeling parameters are shown in Tables D.1 and D.2 in the Appendix D. The actual computation time for the 3D modeling is enormously larger (factor of about 300) than for 2D simulations.

I use vertical point forces at 20 locations resembling hammer blows and record the waves with 88 receivers (vertical and radial component) with 1 m spacing. For discussing the transformation accuracy I show three exemplary shots at a profile location of 5 m (very left part of the model), of 45 m (middle of the model) and of 94 m (very right part of the model). In

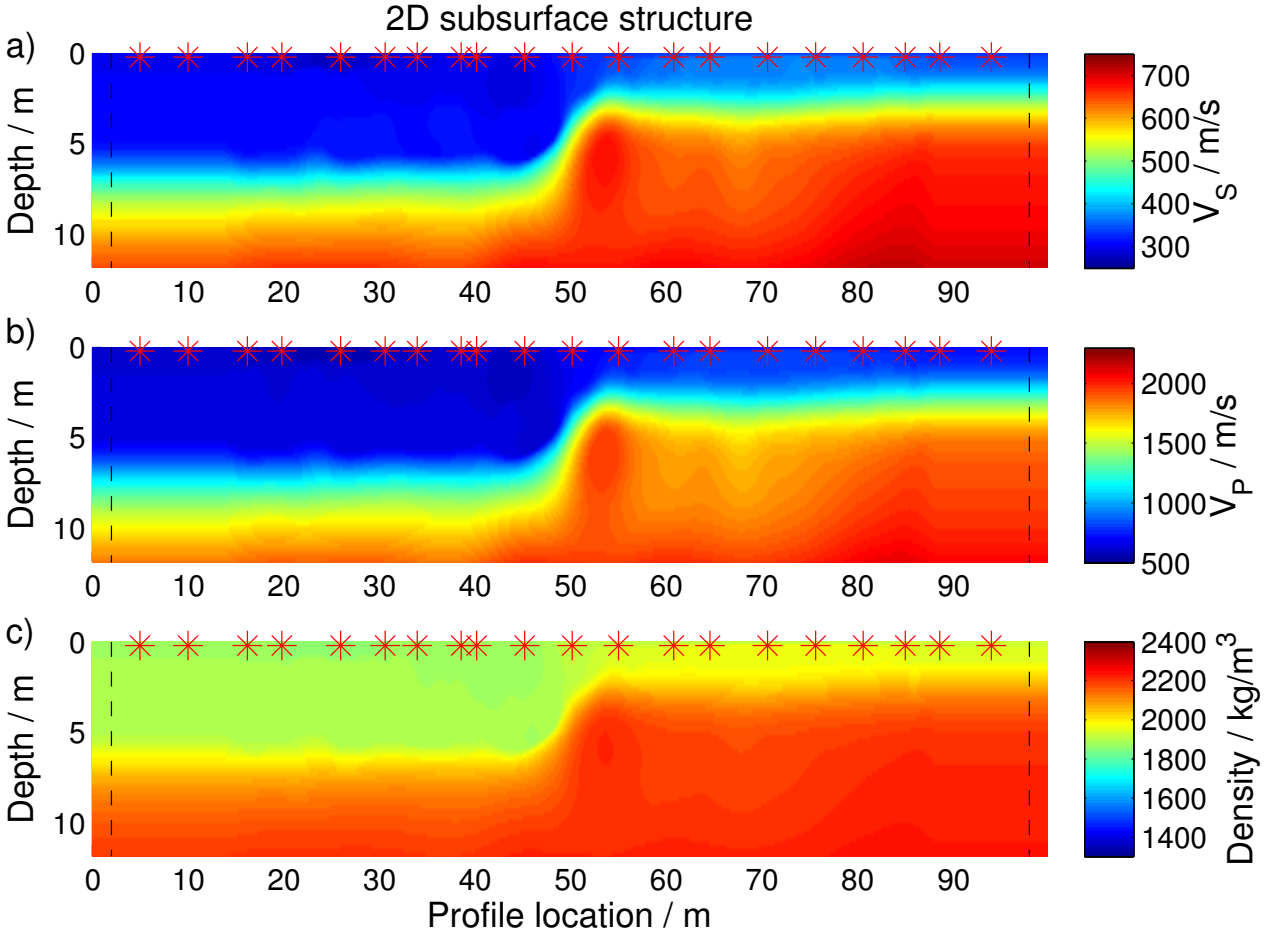

Figure III.3: 2D test structure for 2D and 3D modeling as well as for the reconstruction tests. For point-source simulations (3D) the structure is uniformly extended over 40 m in the third spatial dimension. a) displays the S-velocity, b) the P-velocity and c) the density model. For a better visualization the model is cut off in a depth of 12 m. The FD-grid extends to a depth of 20 m. The absorbing boundary with convolutional perfectly matched layers (CPML) is indicated with black dashed lines. The red stars denote the source locations. The colorbars are chosen to cover this and following figures.

all figures in Section III.2 the line-source seismograms are displayed as a reference with a thick grey line while the seismograms derived from point-source seismograms are displayed by a thin black line. In the following I show comparisons of line-source seismograms with original and transformed point-source seismograms with *Fourier-Bessel* and *hybrid* transformation.

In Fig. III.4 original line-source and point-source seismograms are displayed. Seismograms are normalized to their maximum, such that amplitude decay with offset is not apparent. For a shot at profile location of 5 m (very left part of the model, Fig. III.4a) for near offsets we observe Rayleigh waves with lower phase velocities than for offsets larger than 40 m due to the change of layer thickness in the right part of the subsurface model. Additionally Rayleigh waves reflected at the step of the layer occur. Waves excited by a shot at profile location of 45 m show different phase velocities in the left and right part of the profile (Fig. III.4b). Furthermore, a shot at profile location of 94 m produces signals (Fig. III.4c) with different waveform and phase velocity when compared to the wave field excited by a shot of profile location of 5 m. The radial component shows similar features and is therefore not displayed and discussed in detail (except for the *hybrid* transformation).

III.2.1 Original point-source seismograms

Fig. III.4 displays the differences between wave fields excited by line and point sources for the vertical component. The traces are normalized to their maximum so we cannot compare true amplitudes. However, the wave fields excited by a point source are advanced in phase with respect to the wave field excited by a line source. A comparison of the different amplitude-decay with offset is displayed in Fig. III.5 for an exemplary shot at profile location of 5 m (very left part of the model).

III.2.2 *Fourier-Bessel* transformation

The *Fourier-Bessel* transformation is exact for 1D media (model properties only vary with depth). Here I test its applicability to waves on a 2D structure (lateral heterogeneity). Comparison of line-source and transformed point-source seismograms with *Fourier-Bessel* transformation are plotted in Fig. III.6 for the vertical component. The seismograms in Figs III.6a, b and c are not trace normalized but amplitudes are scaled by an offset dependent factor $(r/1\,\mathrm{m})^{0.3}$ due to a better visualization within the figure. By doing this far-offset traces can be observed with the same amplitudes than near-offset traces. The factor approximately compensates the effect on wave amplitudes caused by geometrical spreading and anelastic dissipation. Other than displays where each trace is normalized to its maximum amplitude, this scaling still supports a comparison of amplitudes of different signals. However, the factor is not used in the misfit and therefore has no effect on the inversion later on. For a shot location of 5 m the transformation works quite well for the surface waves controlled by the 1D structures in the left and right part of the subsurface model. However, the *Fourier-Bessel* transformation neither reproduces amplitudes nor phases of the reflected surface waves as this transformation cannot handle waves originating at a location other than the origin. A shot at profile location of 45 m (middle of the model) is located on the fault in the subsurface

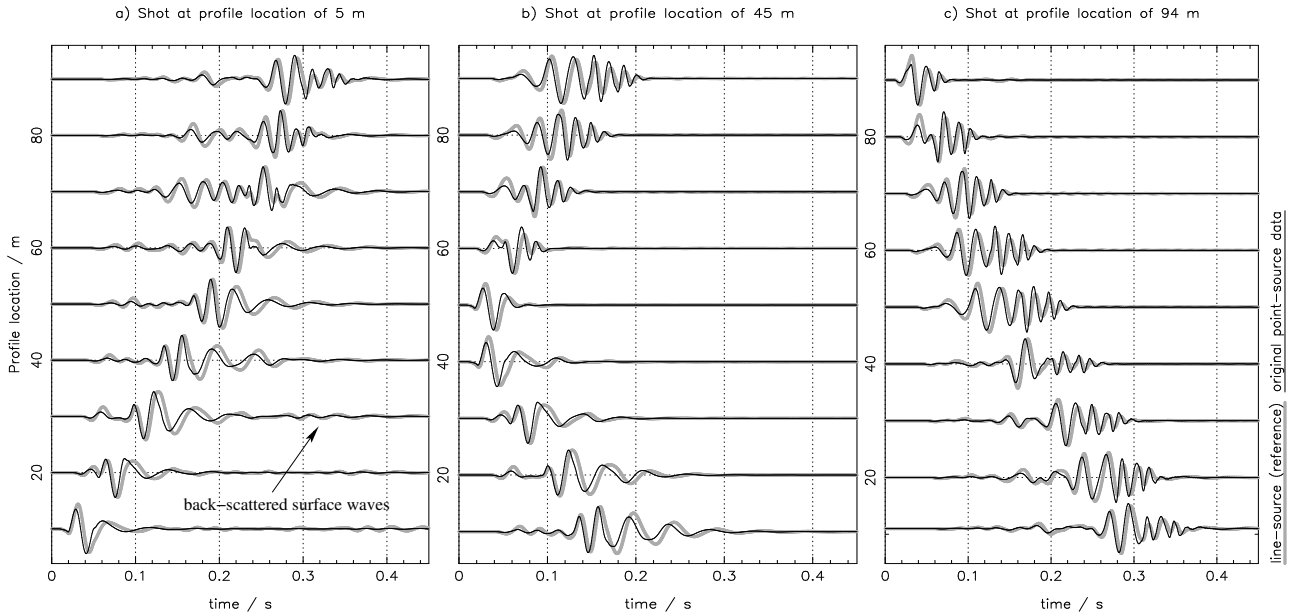

Figure III.4: Comparison of line-source seismograms and point-source seismograms (vertical particle velocity) for the true model in Fig. III.3; only every 10th trace is displayed. Seismogram a) shows a shot at profile location of 5 m (very left part of the model), seismogram b) of 45 m (middle of the model) and seismogram c) of 94 m (very right part of the model). The seismograms are trace normalized otherwise comparison would not be possible due to different decay of amplitudes.

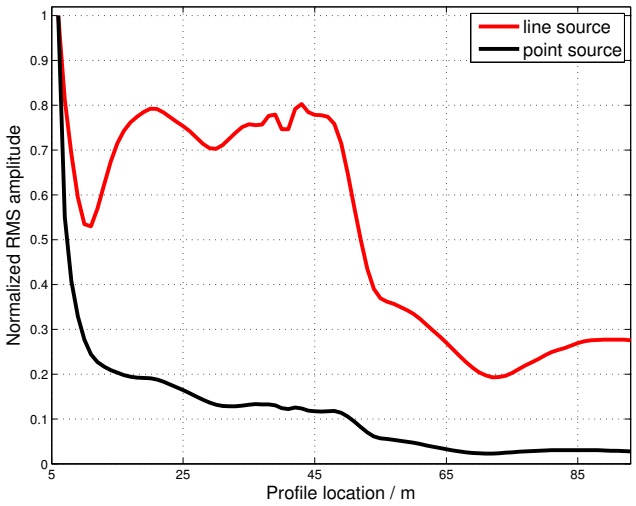

Figure III.5: Comparison of amplitude-decay with offset of waves excited by a line source (red line) and a point source (black line) for a shot at profile location of 5 m (vertical component). RMS amplitude is normalized to nearest offset trace.

model and the structure produces a significantly different dispersion to the left and to the right of the source. This cannot be handled by the *Fourier-Bessel* transformation which produces waves for a kind of pseudo 1D medium and has not the ability to explain the different dispersion in the left and right part of the model. We can clearly observe this behavior in Fig. III.6b. Waves for a shot in the right part of the model (Fig. III.6c) don't contain strong 2D characteristics. The transformation performs quite well in this case except for larger receiver offsets, where a cut-off is apparent in the reduced amplitude of the transformed signals. It appears due to the concept of superposition of limited number of point sources (Forbriger et al., 2014b).

III.2.3 *Hybrid* transformation

While the *Fourier-Bessel* transformation derives propagation velocity by integration over the entire profile and consequently becomes inconsistent on 2D structures, this is not the case for the *hybrid* transformation which can be applied to a single trace. The latter estimates propagation velocity from offset and sample time and produces reasonable results for shallow-seismic surface waves. As the *hybrid* transformation is a combination of the *single-velocity* and *direct-wave* transformation one has to select the single phase velocity v_{ph} at small offsets and the transition from offset r_1 to r_2. For the current test case I choose $v_{ph} = 200\,\mathrm{m/s}$, $r_1 = 10\,\mathrm{m}$ and $r_2 = 20\,\mathrm{m}$ for all shots and components. The single phase velocity is estimated from the phase velocity of the Rayleigh waves in the region near to the source. The values of the transition zone are based on the consideration of the dominant wavelength of the Rayleigh waves which is about 10 m. Comparison of line-source and transformed point-source seismograms with *hybrid* transformation are plotted in Figs III.7 and III.8 for the vertical and radial component, respectively. The seismograms in Figs III.7a, b and c and III.8a, b and c are not trace normalized but amplitudes are scaled by an offset dependent factor $(r/1\,\mathrm{m})^{0.3}$. The fit of the phases as well as the amplitudes for all shots and components (vertical and radial) are very accurate. The *hybrid* transformation performs excellent in this case. Exceptions are the signals of the back-scattered surface waves, which have too small amplitudes.

III.3 Reconstruction tests

On account of the observations described in the previous section, I expect artifacts produced in a 2D FWI when applied to point-source seismograms or signals obtained by *Fourier-Bessel* transformation. Therefore, I do not consider this transformation for the reconstruction tests. Artefacts due to conceptual inconsistencies should be least for a 2D FWI of signals derived by the *hybrid* transformation. For this reason I carry out reconstruction tests for original point-source and *hybrid* transformed data and investigate the ability to reproduce the original subsurface model in comparison to the reconstruction provided by 2D FWI of reference line-source data.

Before I present and discuss the reconstruction tests, I briefly introduce our inversion parameters and strategies used for FWI. For a detailed description of the theory the reader is

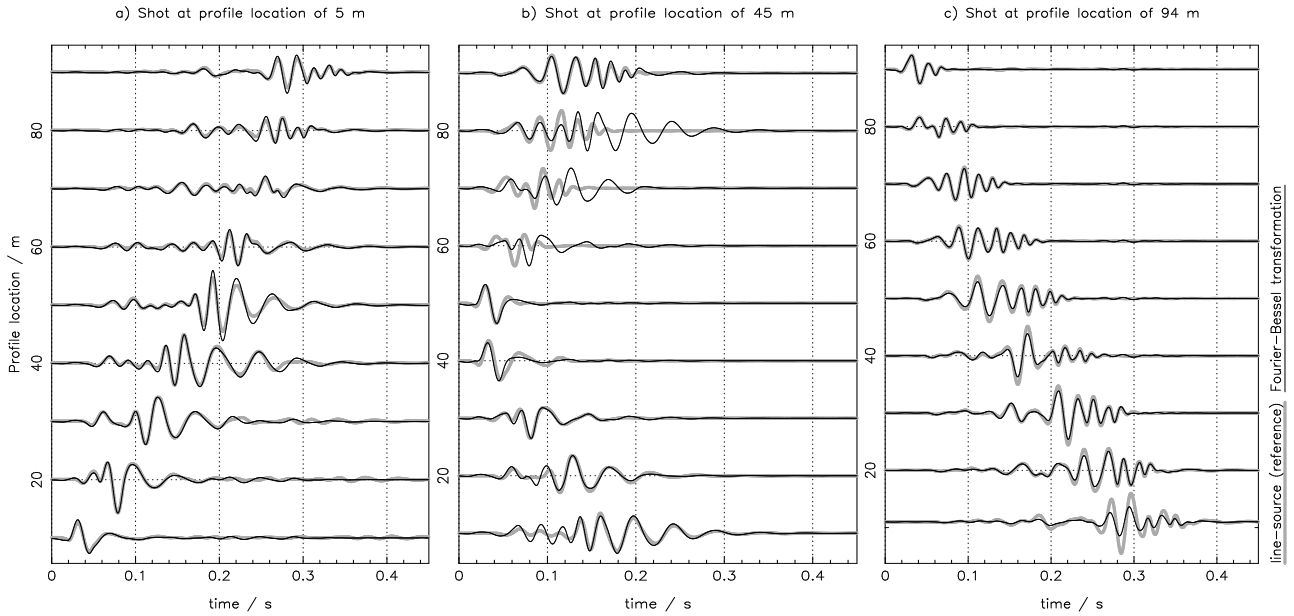

Figure III.6: Result of *Fourier-Bessel* transformation for the vertical component: Comparison of line-source seismograms and transformed point-source seismograms (vertical particle velocity) with the *Fourier-Bessel* transformation for the true model in Fig. III.3; only every 10th trace is displayed. Seismogram a) shows a shot at profile location of 5 m (very left part of the model), seismogram b) of 45 m (middle of the model) and seismogram c) of 94 m (very right part of the model). The seismograms are not trace normalized but scaled by an offset dependent factor $(r/1\,\mathrm{m})^{0.3}$.

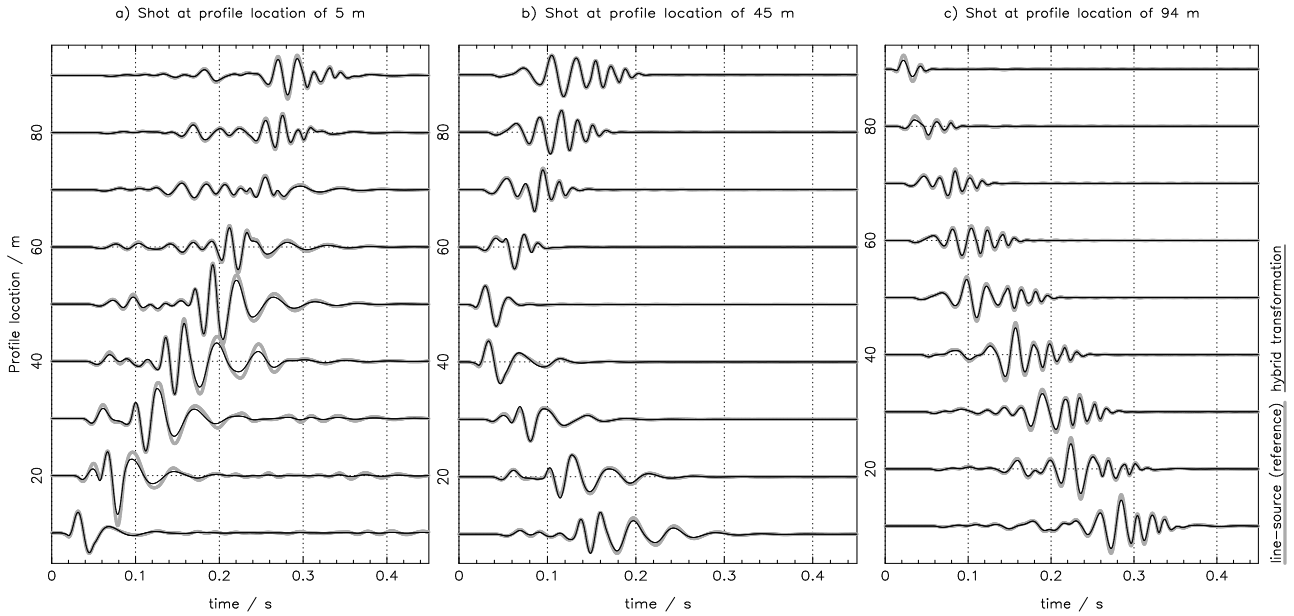

Figure III.7: Result of *hybrid* transformation for the vertical component: Comparison of line-source seismograms and transformed point-source seismograms (vertical particle velocity) with the *hybrid* transformation for the true model in Fig. III.3; only every 10th trace is displayed. Seismogram a) shows a shot at profile location of 5 m (very left part of the model), seismogram b) of 45 m (middle of the model) and seismogram c) of 94 m (very right part of the model). The seismograms are not trace normalized but scaled by an offset dependent factor $(r/1\,\mathrm{m})^{0.3}$.

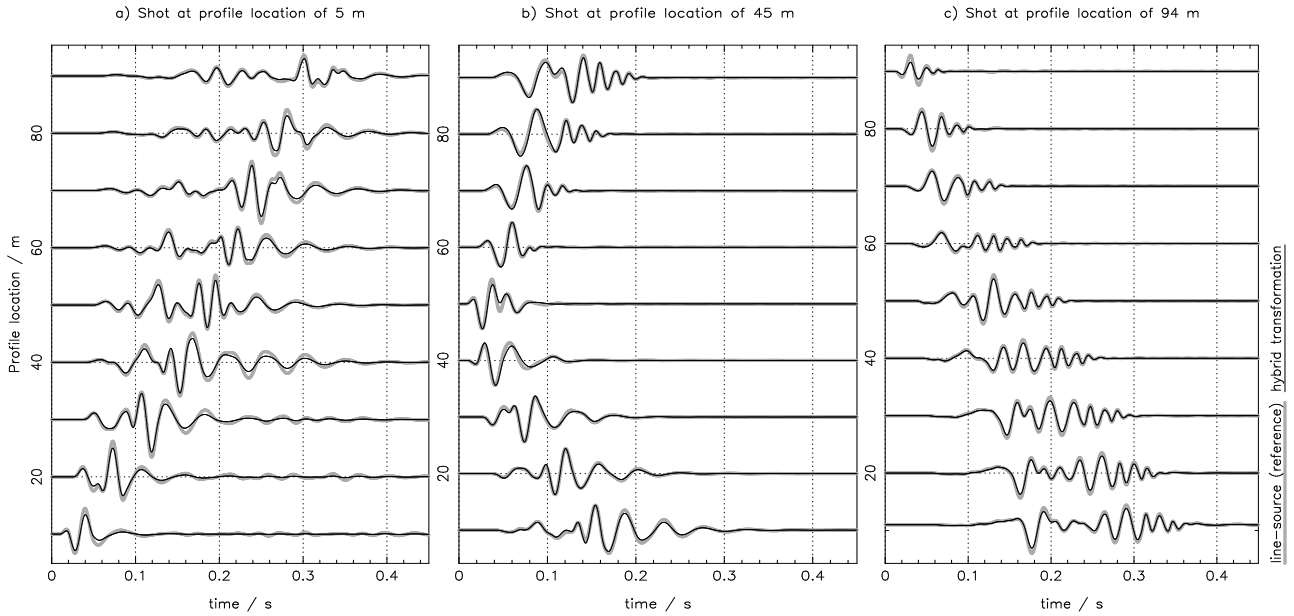

Figure III.8: Result of *hybrid* transformation for the radial component: Comparison of line-source seismograms and transformed point-source seismograms (radial particle velocity) with the *hybrid* transformation for the true model in Fig. III.3; only every 10th trace is displayed. Seismogram a) shows a shot at profile location of 5 m (very left part of the model), seismogram b) of 45 m (middle of the model) and seismogram c) of 94 m (very right part of the model). The seismograms are not trace normalized but scaled by an offset dependent factor $(r/1\,\mathrm{m})^{0.3}$.

referred to the Chapter II (Basic principles and inversion strategies). I apply a 2D elastic full-waveform inversion. The FWI method is based on the adjoint method (Tarantola, 1984; Mora, 1987) where the parallelized elastic finite-difference forward modeling (Bohlen, 2002) and the gradient calculation are performed in the time domain. The code was originally developed by Köhn (2011) and is called `DENISE`[1].

For inversion a preconditioned conjugate gradient method is applied. We use the least square misfit of normalized seismograms as objective function (see eq. II.50). I have mentioned in the previous section that point- and line-source generated waves differ in the amplitude-decay with offset. As this objective function contains normalized seismograms near and far-offset traces contribute equally to the misfit and it is not sensitive to residuals in the amplitude decay with offset. It is, however, sensitive to relative amplitude differences within one seismogram.

As preconditioning taper of the gradients I use the approximate Hessian matrix after Sheen et al. (2006) (see Section II.4.1). Additionally, I taper the gradients per shot semi-circularly at the source location to reduce artifacts. For the force time function I use the first period of a $\sin^3(t)$ as given in eq. (III.11) with a frequency bandwidth from 0 Hz to about 100 Hz. Since the source wavelet is known, it is not estimated during inversion. Furthermore, I use a multi-scale approach for inversion with frequency filtering to reduce the non-linearity of the misfit function (Bunks et al., 1995; Sirgue and Pratt, 2004). Starting at low frequencies initially produces a smooth subsurface model and prevents the FWI to get stuck in a local minimum. I start at a low-pass frequency of 10 Hz. After the inversion converges within this frequency bandwidth we increase the low-pass frequency in steps of 10 Hz. The number of iterations in each frequency range is different and depends on the achieved convergence. We invert for the S-velocity, the P-velocity and the density but due to the high sensitivity of the Rayleigh waves to the shear-wave velocity I discuss the reconstructed S-velocity model in more detail.

In Fig. III.3 the true 2D subsurface model is displayed. It is composed of a layer with a step in the interface to the half space. The layer and half space are not completely homogeneous and have a smooth gradient which peaks at the transition zone of layer and half space. I intentionally avoid strong contrasts in the model since the FWI is not able to reconstruct discontinuities accurately. The velocity and density range is realistic for shallow subsoil.

The initial model I use in all reconstruction tests is a linear gradient for each parameter (Fig. III.9). The parameter values of the inital model comprise the parameter range of the true model which turned out to be essential for the inversion not to get stuck in a local minimum. I apply vertical point forces at 20 locations resembling hammer blows and record the wave fields with 88 receivers (vertical and radial component) with spacing of 1 m. I calculate synthetic point-source seismograms for the 2D structure, using a 3D FD solver. Each of the different line-source simulation techniques are applied to these simulated observed data. We then apply the 2D FWI to each of these pseudo-observed transformed data sets and investigate the ability to reproduce the known subsurface structure and call this *reconstruction tests*.

[1] References to the source code are provided at `http://www.opentoast.de`

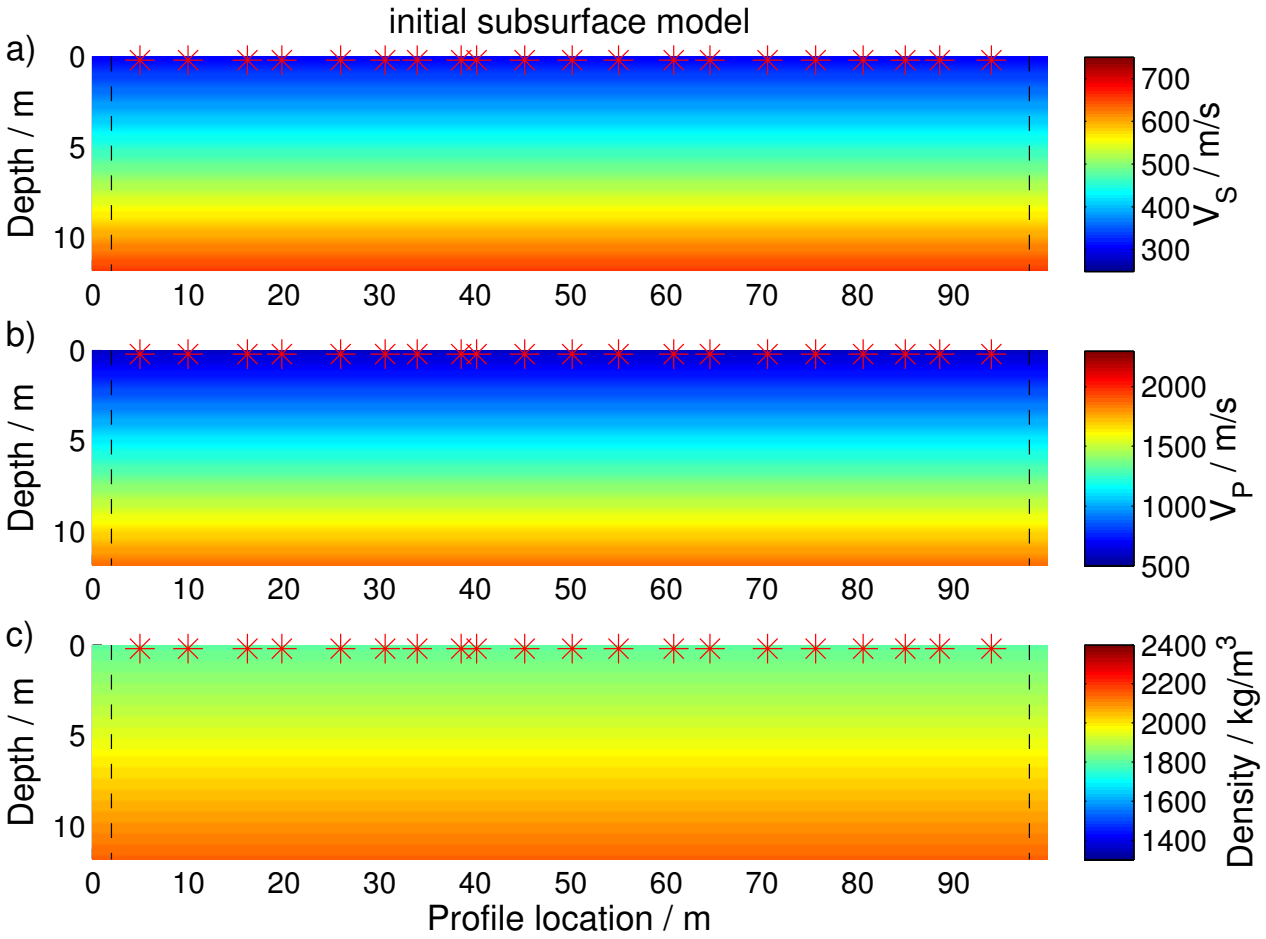

Figure III.9: Layered initial model for all reconstruction tests. The absorbing boundary with convolutional perfectly matched layers (CPML) is indicated with black dashed lines. a) displays the S-velocity, b) the P-velocity, and c) the density model.

III.3.1 Reconstruction test for line-source seismograms

In order to obtain a reference FWI result I use line-source seismograms calculated by a 2D FD solver as observed data. The objective is to find a reference for optimal resolution obtainable by FWI of surface waves on the test structure. Hence, all FWI results in Section III.3.2 with transformed point-source seismograms will then be compared with this consistent 2D FWI result. In the following we call this inversion result *reference inversion*.

In Figs III.3 and III.9 the true subsurface and FWI initial models are plotted, respectively. Fig. III.10 shows the comparison of seismograms of the true subsurface and of the reconstructed model for the vertical component. Residuals are smaller than artifacts that would be produced by the *hybrid* transformation of the observed data (Figs III.7 and III.8) and are therefore not significant in the current context. Judging from the waveform only we apparently have estimated an appropriate subsurface model during inversion. The misfit is reduced from an initial error of 55 % to around 3 % of total signal energy. In Fig. III.11 the FWI results of the S-velocity, P-velocity and density, respectively, are plotted with the same colorbar as in Figs III.3 and III.9. Indeed we obtain a satisfactory subsurface model by inversion at least for the S-velocity. Remaining model errors are underestimated parameter values in the half space due to insufficient penetration depth of the Rayleigh wave with the dominant wave length of about 10 m and a smoother transition zone than in the true model. The S-velocity errors are smaller than the P-velocity and density errors because of the high sensitivity of surface waves to the shear-wave velocity. We use the S-velocity model displayed in Fig. III.11 as a reference for the subsequent reconstruction tests.

III.3.2 Reconstruction tests for point-source seismograms

In this section I discuss 2D FWI results with point-source seismograms as pseudo-observed data which were on the one hand not transformed and on the other hand transformed with the *hybrid* transformation. We expect the strongest artifacts for a 2D inversion of raw point-source data, since the signals have inappropriate phase and relative amplitudes for being fit by line-source generated waves (Fig. III.4). The inversion of data obtained by a *hybrid* transformation is expected to represent the best result achievable by 2D inversion.

All inversion tests run with the same parameter settings like frequency filtering, inital models and so on as used for the *reference inversion* in the previous section. The number of iterations can differ due to different convergence properties. I obtain misfit values for the final seismograms in the FWI of 7.96 % for the *hybrid* transformation and 23.18 % for the original point-source data (Table III.1 - first line). If I regard the misfit as a measure of how successful an inversion is, it is clear that the inversion of the *hybrid* transformation should be more reliable than the inversion of the original point-source data. However, it is essential how well the inversion could reconstruct the subsurface model. In Figs III.12 and III.13 the FWI results of S-velocity, P-velocity and density are plotted for original point-source data and after *hybrid* transformation, respectively.

Due to the high sensitivity of surface waves to the shear-wave velocity we firstly discuss the S-velocity models to investigate the effects of geometrical spreading corrections in an FWI

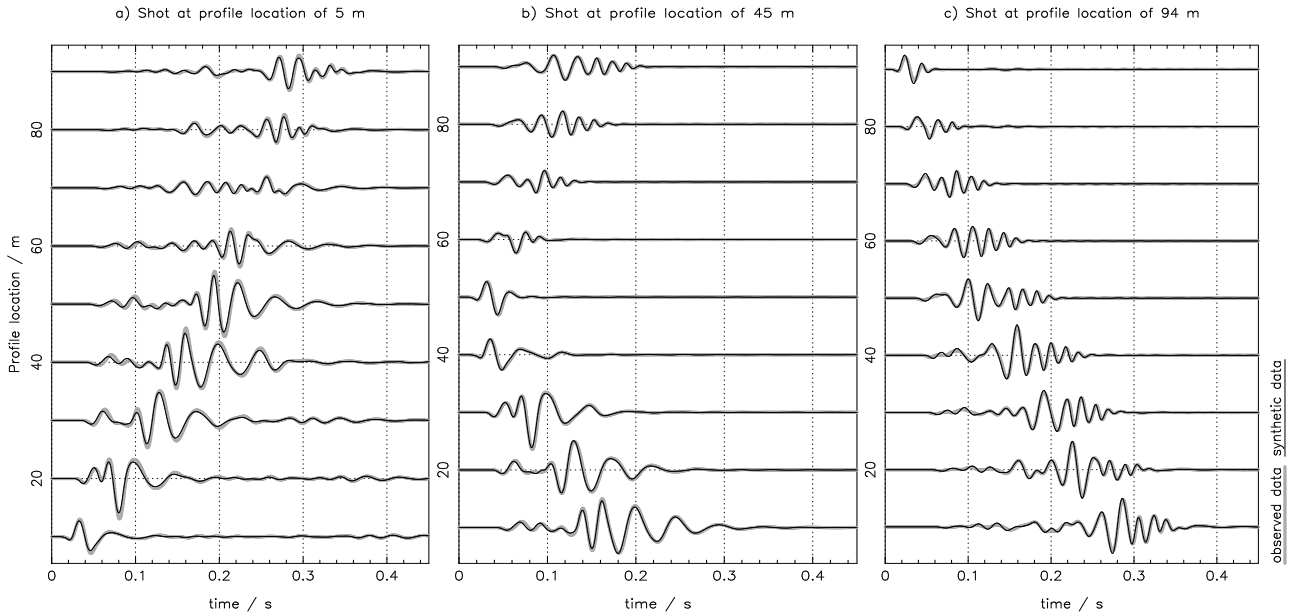

Figure III.10: Result of *reference inversion* for the vertical component: Comparison of observed data and synthetic data (vertical particle velocity) for the reconstructed model for the *reference inversion* test with perfect line-source seismograms as observed data; only every 10th trace is displayed. Seismograms a) show a shot at profile location of 5 m (very left part of the model), seismograms b) of 45 m (middle of the model), and seismograms c) of 94 m (very right part of the model). The seismograms are not trace normalized but scaled by an offset dependent factor $(r/1\,\mathrm{m})^{0.3}$.

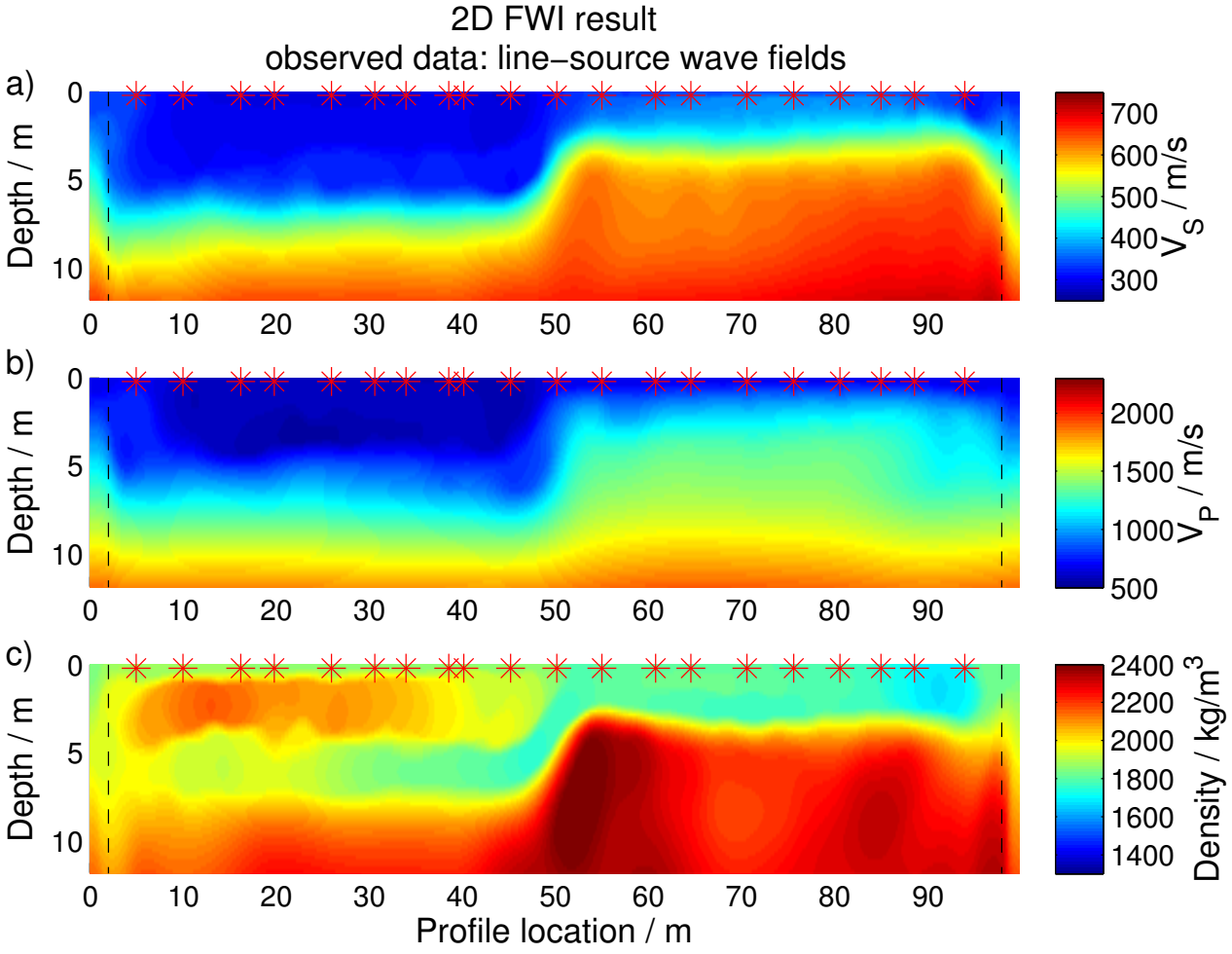

Figure III.11: 2D FWI result using perfect line-source wave fields as observed data. The absorbing boundary with convolutional perfectly matched layers (CPML) is indicated with black dashed lines. a) displays the S-velocity, b) the P-velocity, and c) the density model.

Pseudo-observed data in 2D FWI:	line-source seismograms	point-source seismograms original	point-source seismograms *hybrid* transformation	point-source seismograms source-wavelet correction
Final data misfit in 2D FWI	2.99 %	23.18 %	7.96 %	9.38 %
Number of iterations	156	146	156	130
S-velocity RMS final model error RMS of starting model: 14.5 %	2.19 %	8.41%	2.4 %	4.88 %
P-velocity RMS final model error RMS of starting model: 22 %	11.5 %	16.63 %	9.7 %	15.95 %
Density RMS final model error RMS of starting model: 3.9 %	4.6 %	14.72 %	4.8 %	9.2 %
Data misfit for point-source seismograms	-	53.39 %	5.67 %	12.14 %

Table III.1: Final data misfit of the full-waveform inversion, the number of iterations and the final RMS model errors for different pseudo-observed data and the parameters S-velocity, P-velocity and density. Additionally the RMS model error of the starting model is displayed. I calculate point-source seismograms (3D solver) for the final model and present the data misfit with respect to the original point-source seismograms of the true model in the sixth row. The vertical and radial components are considered in a joint misfit. We use the least square misfit of normalized wave fields as defined in eq. (II.50).

of surface waves. In Fig. III.14 the inversion results for original point-source seismograms and after *hybrid* transformation are plotted together with the reference result obtained by inversion of line-source seismograms. The inversion results for the original point-source data and the *hybrid* transformation both reproduce the gross features of the true model and are in this respect comparable with the *reference inversion* result. Surprisingly the result after inversion of original point-source data contains no strong artifacts and is able to produce the required $\pi/4$ phase shift of the signals through the model structure. The RMS model errors vary from 2.19 % (*reference inversion*), 2.4 % (*hybrid* transformation) to 8.41 % (original point-source data). A single error value appears to be insufficient to describe the inversion results completely. Because of this I display in Fig. III.15 a relative error between the true and the reconstructed S-velocity model

$$\text{relative error}(x,z) = \frac{m_{true}(x,z) - m_{syn}(x,z)}{m_{true}(x,z)} \tag{III.12}$$

where x and z are the spatial coordinates, m_{true} the true subsurface and m_{syn} the reconstructed model. For the *reference inversion* result in Figs III.14a and III.15a, it is obvious that the velocities in the half space for the right part of the model are underestimated and that they are overestimated in the transition zone between the layer and the half space. It would be not reasonable to expect better reconstruction for the other two tests. The reproduction capability of the 2D inversion after *hybrid* transformation indeed is not inferior when compared with the *reference inversion* result. It is reasonable that the inversion with the original point-source data produces too large S-velocity in an area above the transition zone and in the half space of the right part. Line-source seismograms in the inversion must be advanced by $\pi/4$ to match the original point-source signals used as observed data (Fig. III.4). The velocity in the resulting model is therefore expected to be larger than in the true model. In the difference between true model and final model (Fig. III.15b) the expected artifacts which result from the conceptual mistake when fitting line-source seismograms to point-source seismograms become obvious. The reproduction capability of the 2D inversion after *hybrid* transformation (Fig. III.15c) is not inferior when compared with the *reference inversion* result (Fig. III.15a). In this sense the correction applied by the *hybrid* transformation was fully successful.

Figs III.12b and c and III.13b and c show the inversion result for the P-wave velocity and density for original point-source data and after *hybrid* transformation, respectively. Again I compare with the *reference inversion* in Figs III.11b and c. The P-velocity is only vaguely imaged in all results and is worst for the inversion of original point-source data (Fig. III.12b). In this case the density reconstruction entirely fails (Fig. III.12c), while the density structure is reasonably imaged in the *reference inversion* (Fig. III.11c) as well as for the inversion after *hybrid* transformation (Fig. III.13c). This is also reflected by the RMS model errors in Table III.1 - fourth and fifth line. Remaining model errors for the density are mainly underestimated and overestimated parameter values resulting in the RMS model error being larger than for the initial model. I conclude that after *hybrid* transformation the reproduction capability for all three model parameters (S-velocity, P-velocity and density) is similar to the *reference inversion*. The insufficient reconstruction capability for the P-velocity and the surprisingly well reconstruction of the density structure is a property of the observed data and not of the line-source simulation procedure.

Amplitude corrections of 3D/2D single-trace transformations are adapted to a certain wave

group (e.g. reflected, refracted or Rayleigh waves) or propagation path. The *hybrid* transformation, particularly the *direct-wave* transformation, is adapted to waves with a travel path along the receiver profile and therefore mainly appropriate for direct body and Rayleigh waves. Considering that the penetration depth of the observed waves is not larger than 10 m while the profile length is 100 m it becomes comprehensible that the propagation distance also for most body wave signals is similar to the source to receiver offset. This is reflected by the reasonable amplitude transformation for practical all direct signals contributing to the inversion (Figs III.7 and III.8). For this reason the *hybrid* transformation provides useful data for the reconstruction by 2D FWI. The only signal obviously not properly handled by the *hybrid* transformation is due to back-scattered Rayleigh waves produced at the fault zone, which are apparent in Fig. III.7a. However, this conceptual error doesn't yield traceable artifacts in the reconstructed models with the *hybrid* transformation (Fig. III.13) when compared to the *reference inversion* (Fig. III.12).

During inversion the misfit between line-source generated seismograms for the current model and equivalent line-source seismograms simulated from original recorded point-source seismograms is reduced. A small misfit value in this sense not necessarily means that the inferred subsurface model would produce point-source seismograms matching the original point-source data well. On account of this I extended the reconstructed 2D models (Figs III.12 and III.13) into the third spatial dimension. For the such obtained 3D models I calculate point-source seismograms. Comparison of the original point-source seismograms of the true subsurface and point-source seismograms of the 3D-extended reconstructed models are plotted in Figs III.16a and III.16b. Fig. III.16a displays the signals for the model in Fig. III.12, which was obtained by inversion of the original point-source data. We observe a good fit for near-offset traces but a significant phase mismatch for far-offset traces. This yields a huge misfit of around 53 % (Table III.1 - sixth line). Fig. III.16b shows the equivalent comparison for the result of inversion after *hybrid* transformation. We observe a very good fit over the full offset range and for all shot locations (misfit of about 6 %). We conclude that the 3D-extended reconstructed model for the *hybrid* transformation has the ability to produce nearly identical point-source seismograms as the original seismograms. This approach to line-source simulation therefore is appropriate for an inversion with 2D FWI.

III.3.3 Phase correction by source-wavelet inversion

For synthetic reconstruction tests the source wavelet is known in contrast to an inversion of field data where a source-correction filter must be inferred from the data as part of the FWI. Pratt (1999) shows that the source-wavelet estimation can at least partly account for a phase advance of point-source data with respect to line-source data. I carried out additional reconstruction tests to investigate the consequences of the effect reported by Pratt for a 2D FWI of original point-source seismograms. In this FWI shot-wise source-correction filters were derived for each frequency range. I obtain a source-wavelet correction by a stabilized deconvolution of the recorded seismograms with the simulated seismograms (Groos et al., 2014). Data misfit (2D as well as 3D) and model error for the results then become smaller than without source-wavelet correction. The misfit between original point-source seismograms and such calculated for a 3D extension of the final model is about 12 % of total signal energy. This is less than without source-wavelet inversion, but still larger than with the *hybrid* transformation (Table III.1 - fourth row).

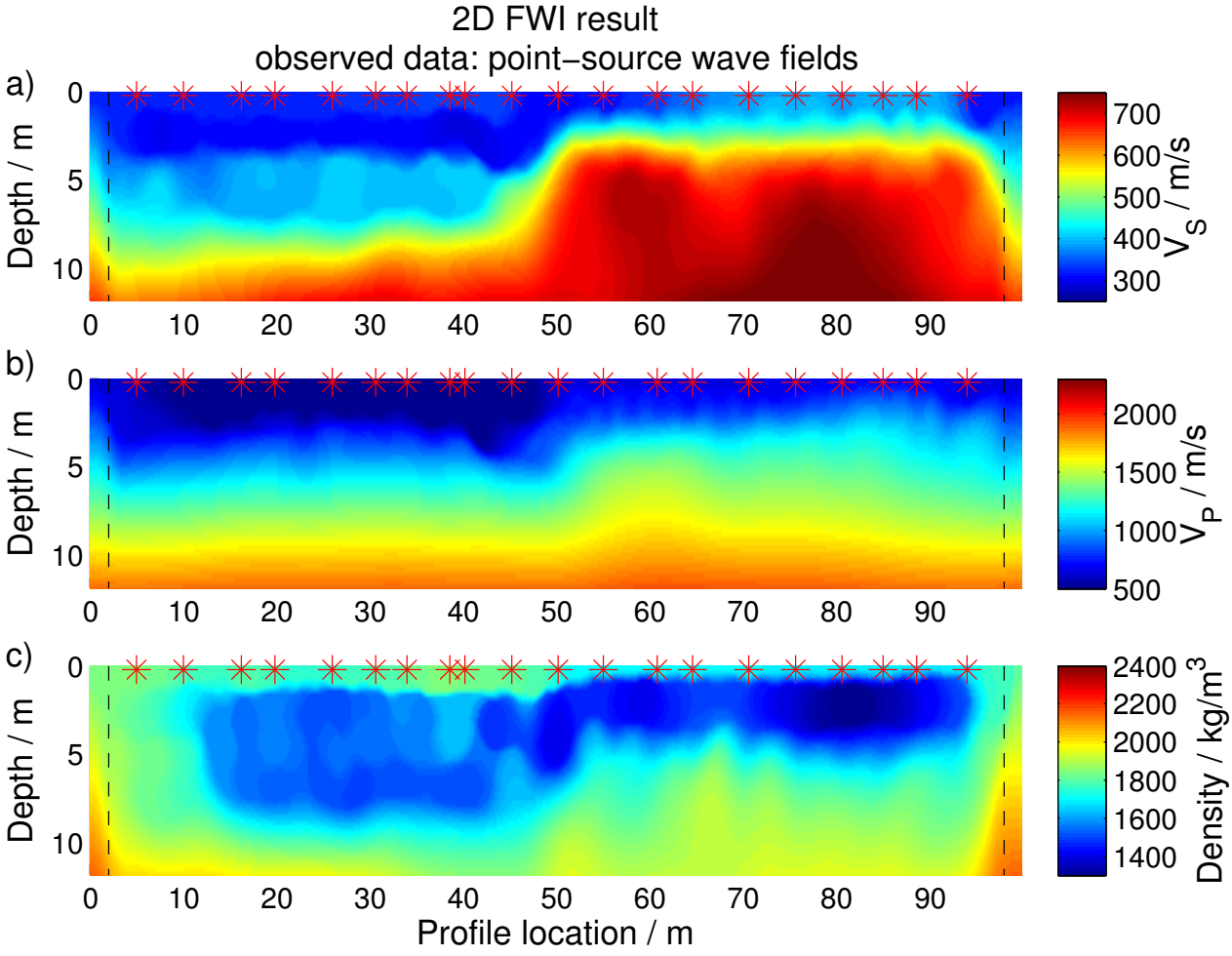

Figure III.12: 2D FWI result using point-source wave fields as observed data. The absorbing boundary with convolutional perfectly matched layers (CPML) is indicated with black dashed lines. a) displays the S-velocity, b) the P-velocity, and c) the density model.

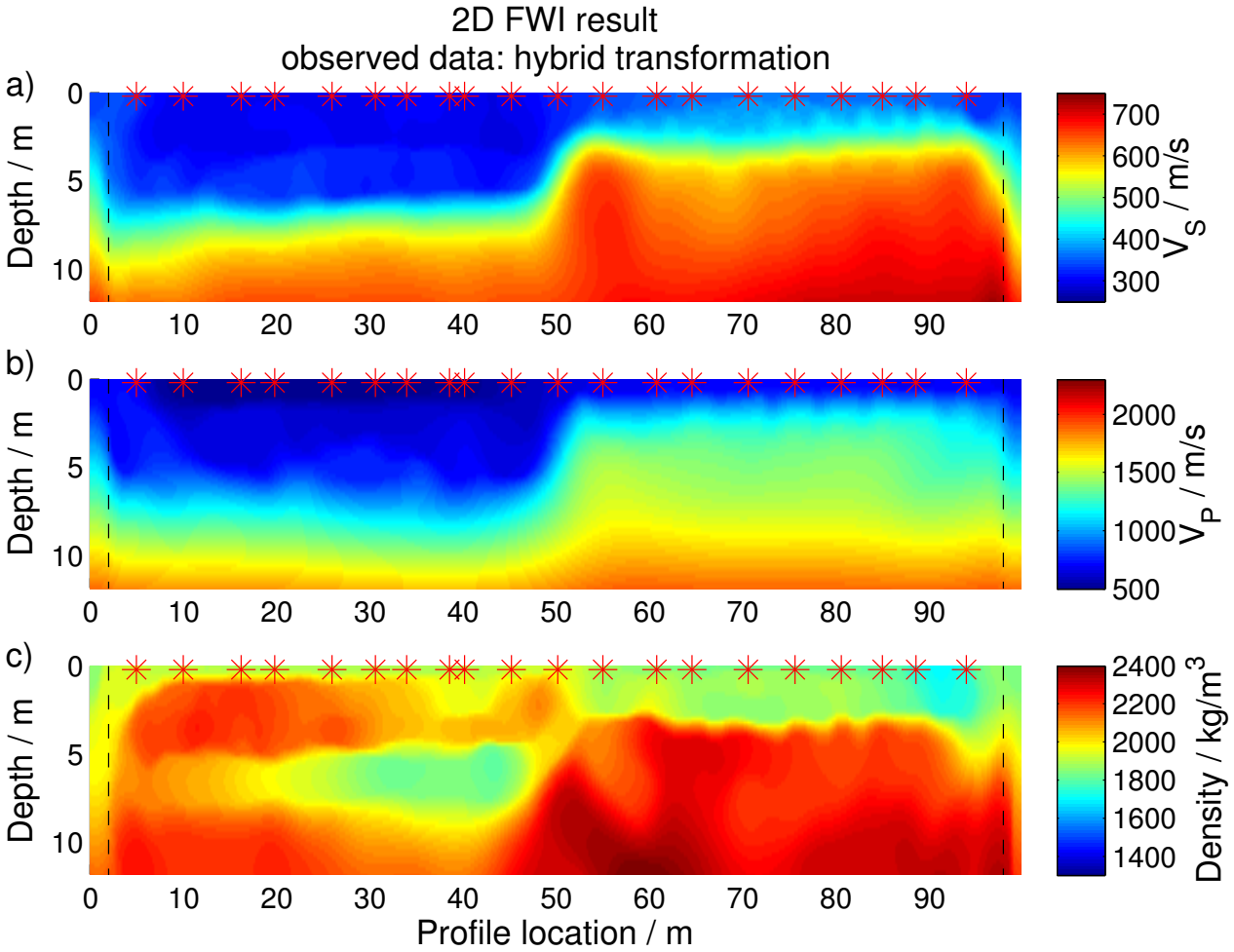

Figure III.13: 2D FWI result using transformed point-source seismograms with *hybrid* transformation as observed data. The absorbing boundary with convolutional perfectly matched layers (CPML) is indicated with black dashed lines. a) displays the S-velocity, b) the P-velocity, and c) the density model.

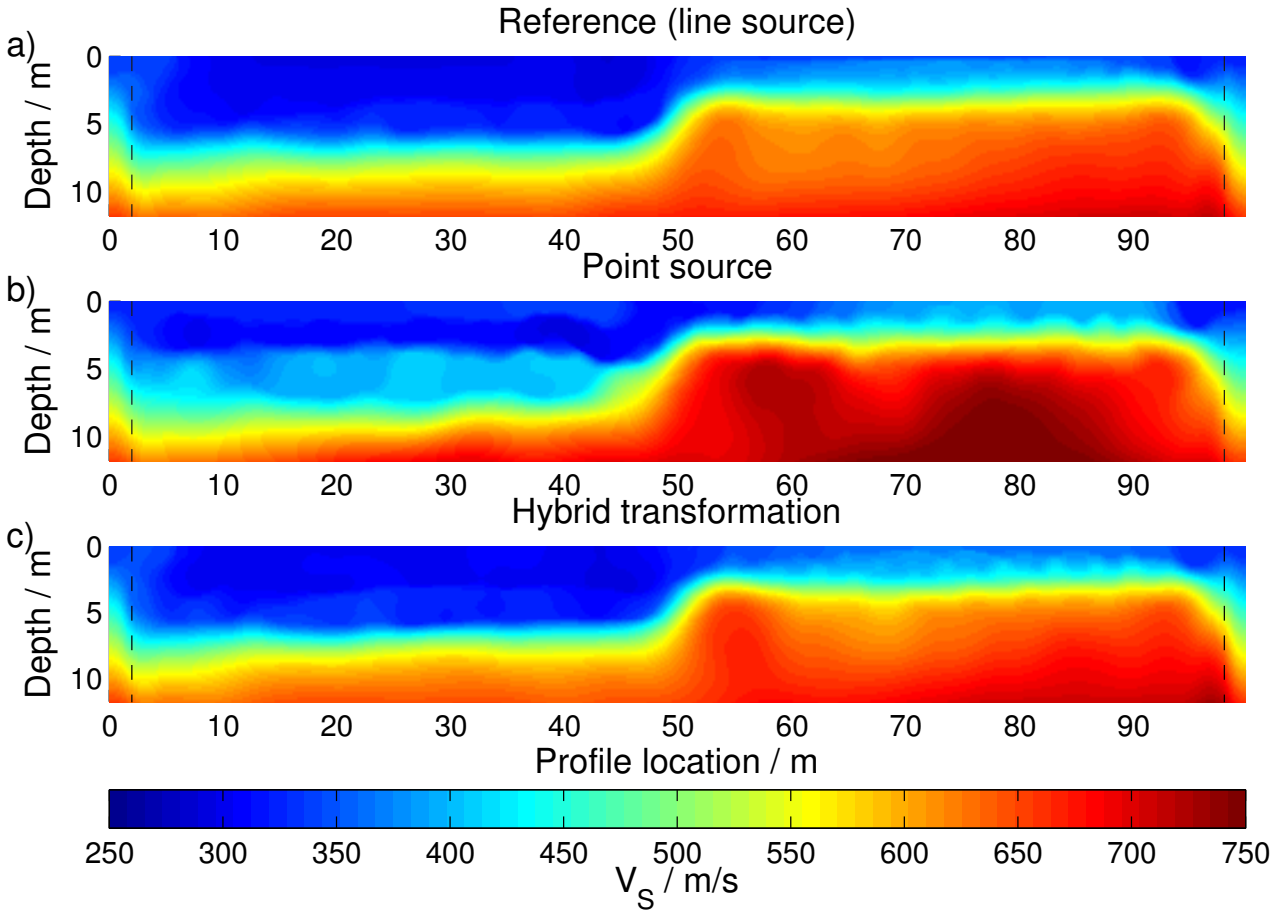

Figure III.14: Comparison of 2D FWI result (S-velocity model only) using perfect line-source and transformed point-source wave fields as observed data. a) displays the reconstructed S-velocity model using line-source seismograms, b) original point-source seismograms and c) transformed point-source seismograms with *hybrid* transformation. The absorbing boundary with convolutional perfectly matched layers (CPML) is indicated with black dashed lines.

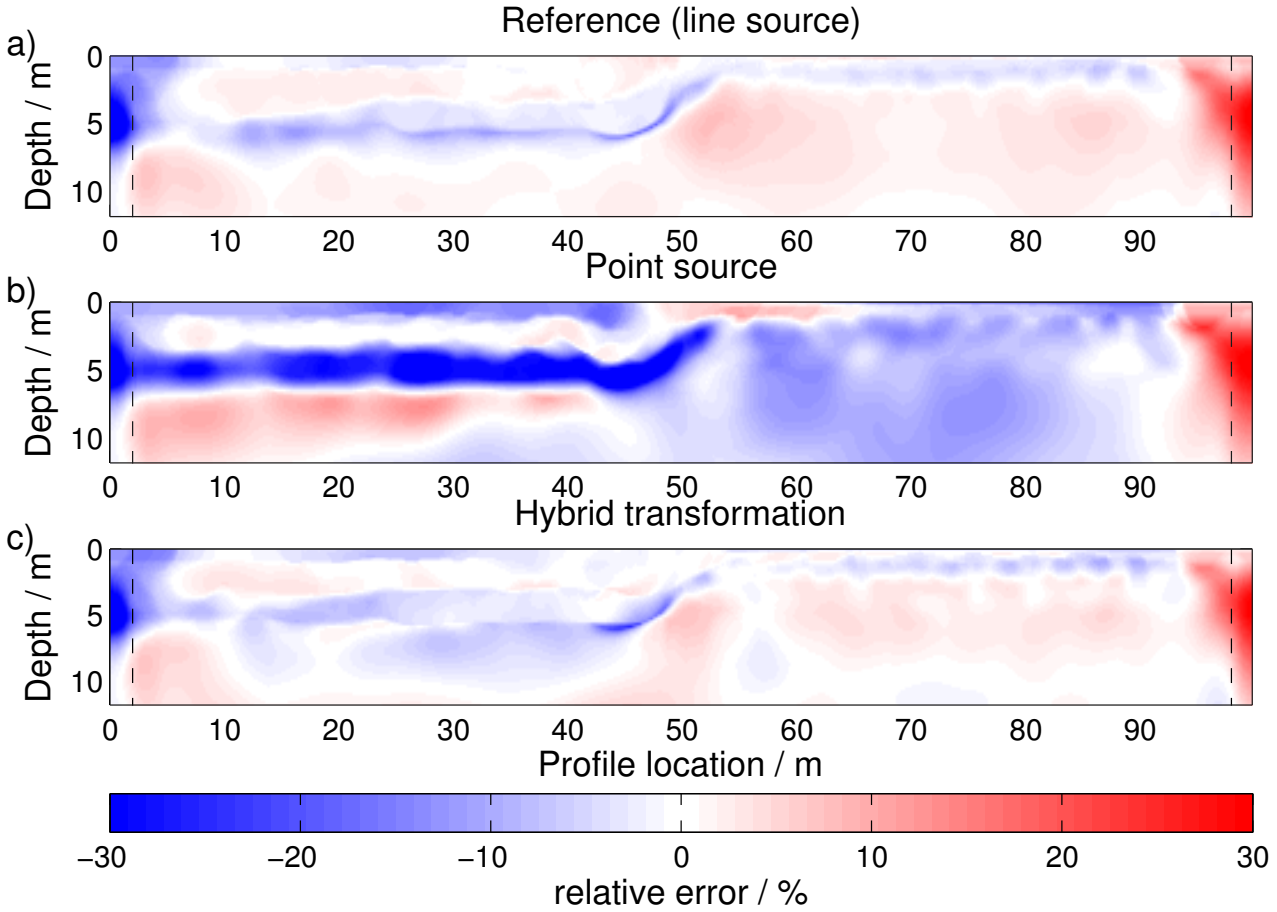

Figure III.15: Relative error between true and reconstructed S-velocity models. a) displays the relative error by using line-source seismograms, b) original point-source seismograms and c) transformed point-source seismograms with *hybrid* transformation. Due to a better visualization the colorbar is clipped from -30 % to 30 %. The absorbing boundary with convolutional perfectly matched layers (CPML) is indicated with black dashed lines.

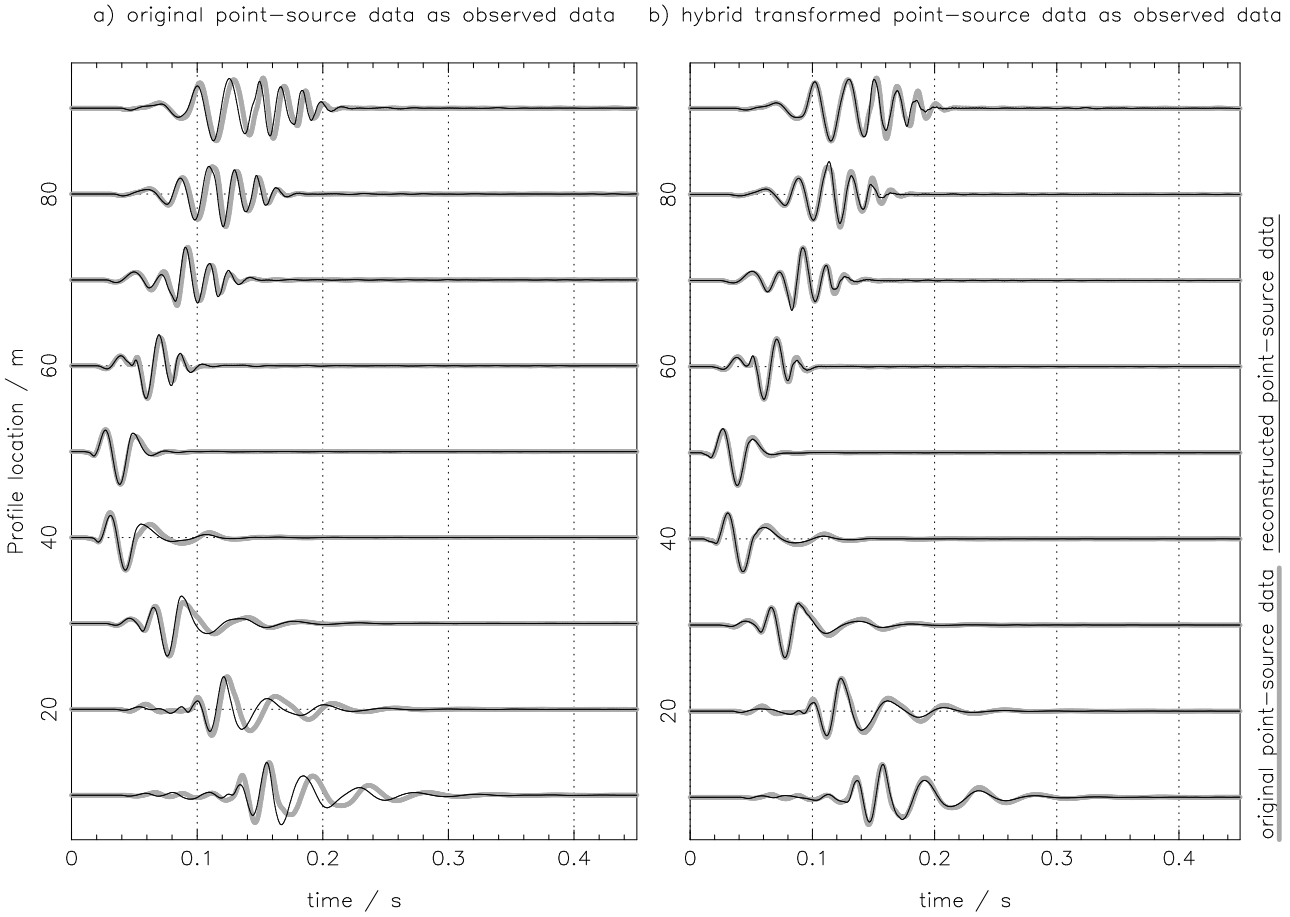

Figure III.16: Comparison of original point-source data and point-source data for the reconstructed model of a) original point-source seismograms (Fig. III.14b) and b) *hybrid* transformed point-source seismograms as observed data (Fig. III.14c); only every 10th trace is displayed. Seismograms show a shot at profile location of 45 m (vertical particle velocity). The seismograms are trace normalized.

III.4 Conclusion

2D full-waveform inversion of field data must account for the different spreading of recorded and computed waves. I summarized an integral *Fourier-Bessel* transformation and a single-trace *hybrid* transformation which are able to produce equivalent line-source seismograms from point-source recordings (Forbriger et al., 2014b). The first requires a complete common source gather and is exact for wave propagation in 1D structures. The latter is derived by approximation from the acoustic homogeneous full-space solution, but nevertheless performs surprisingly well with near-surface elastic waves in 2D structures. It has the benefit of being applicable to individual traces. By testing the accuracy for shallow-seismic surface waves produced on a 2D test structure I show that the most appropriate correction filter is the single-trace *hybrid* transformation as it is applicable to waves produced on 2D structures and it adjusts both the amplitude-decay as well as the signal's phase. The *Fourier-Bessel* transformation produces significant artifacts in the same test.

If the conceptual difference is ignored and point-source recordings are inverted by a 2D Cartesian FWI (implicitly using line-source waveforms) the resulting subsurface model suffers from a bias to larger S-velocity. The final model, after extension to three spatial dimensions, is not well able to reproduce the original point-source data. Nevertheless, the inversion result contains all gross features of the true subsurface structure. I demonstrate this by reconstruction tests. If a *hybrid* transformation is applied to the point-source data prior to inversion, the results are fully satisfactory in the sense that the reproduction capability is as strong as for the *reference inversion* of line-source data and that the final model when extended to 3D is able to reproduce the original data. For this reason I recommend the application of a *hybrid* transformation to field data prior to 2D Cartesian FWI.

Chapter IV

Feasibility study of a line-source simulation in the field

In the previous chapter I discussed theory and accuracy of numerical line-source simulations for shallow-seismic data and investigated possible artifacts produced by these transformation techniques for a 2D FWI. In this chapter I focus again on the line-source simulation, however, in a more practical point of view. I present a feasibility study of a line-source simulation in the field.

A line source can be expressed as a superposition of a continuous arrangement of point sources along the x-axis (see Figs III.1 and III.2). The seismogram u_L of a line source is defined by

$$u_L(y,t) = \int_{-\infty}^{\infty} u_P(\sqrt{x^2+y^2},t)\,\frac{\mathrm{d}x}{[x]} \tag{IV.1}$$

with the seismograms u_P of point sources (see eq. III.2). This transformation provides correct magnitude and physical units for a definition of the line source appropriate for 2D Cartesian solvers (Forbriger et al., 2014b), if $[x]$ is the physical unit of length (commonly $[x] = 1\,\mathrm{m}$). From a theoretical point of view it is possible to simulate a line source in the field survey by exciting a vast number of dense shot locations of point sources perpendicular to the seismic profile. For this approach the integral in eq. IV.1 is approximated by a finite sum over the number of used point sources N_{u_P} in the field survey

$$u_L(y,t) = \sum_{i=1}^{N_{u_P}} u_P(\sqrt{x_i^2+y^2},t)\,\frac{\Delta x}{[x]} \tag{IV.2}$$

with the spacing of the discrete point sources Δx.

To test this approach I did a feasibility study in a field survey. The chapter is organized as follows. Firstly, I present a shallow-seismic field survey at the gliding airfield in Rheinstetten near Karlsruhe where we have excited point sources perpendicular to the seismic profile to simulate a line-source in the field. Secondly, I show a synthetic case study to investigate the question how long a line-source profile should be or rather how many single point sources

are required to obtain appropriate simulated line-source seismograms. Finally, I discuss and conclude the results for line-source simulations in the field.

IV.1 Field survey Rheinstetten and 1D subsurface model

The field data set was acquired near Karlsruhe at the gliding airfield of Rheinstetten. The subsurface structure is mainly made up of layered fluviatile sediments of the Late Pleistocene (Hüttner et al., 1986). We used a hammer blow as vertical sources at 11 shot locations and recorded the wave fields with 35 vertical component geophones (4.5 Hz eigenfrequency) with 2 m spacing. The acquisition geometry is displayed in Fig. IV.1(a). One shot location is located in-line of the receiver profile and additionally there are five shot locations perpendicular to each side of the profile with 1 m spacing. This amounts a line-source profile of 10 m.
Former investigations show the predominantly depth dependent structure of the site (e.g. Stelzer, 2010). I obtain a 1D subsurface model from joint inversion of first arrival P-wave travel times and Fourier-Bessel expansion coefficients (Forbriger, 2003) of the shot which was excited in-line of the receiver profile. The inversion result is shown in Fig. IV.1(b). The S-wave velocity model is characterized by two gradients over a homogeneous half-space and the P-wave velocity model is described by a homogeneous layer over a homogeneous half-space. Density is not well constrained by the data. The density model consists of a homogeneous layer (1700 $\mathrm{kg/m^{-3}}$, 6.3 m depth) over a homogeneous half-space (2000 $\mathrm{kg/m^{-3}}$) and the values are estimated based on common density values for unconsolidated sediments (Schön, 1996). The discontinuity in 6.3 m depth is interpreted as the water-ground table.

IV.2 Synthetic case study

In a first step I investigate the approach of simulating a line source in the field by a synthetic case study. The synthetic seismograms are computed with the reflectivity method (Fuchs and Müller, 1971) using an implementation by Ungerer (1990). For the subsurface structure I use the obtained inversion result of the previous section (see Fig. IV.1) and I use a single vertical force as shown in eq. III.11. The wave fields are recorded with 35 vertical component geophones with 2 m spacing as in the field survey (Section IV.1). I calculate synthetics on the one hand with a line source for reference and on the other hand with point sources. In total I excite 80 single point sources perpendicular to the receiver profile with 1 m spacing. More precisely I excite 40 point sources on the left side and 40 point sources on the right side of the receiver profile. To obtain the simulated line-source seismograms I use eq. IV.2 which equals a superposition of single point sources. Different numbers of used point sources N_{up} result in a different size of the line-source profile length. The largest possible line-source profile length amounts 80 m. In the following I compare the reference line source with different number of point sources or rather different line-source profile lengths. Therefore, I calculate the L2 norm (see eq. II.43) between the wave fields of a line source and simulated line sources (number of point sources depends on the profile length). The result is shown in Fig. IV.2(a). A line-source profile length of 0 m corresponds to a single point source located in-line with the receiver profile. The misfit value is large for small line-source profile lengths, however, it decreases

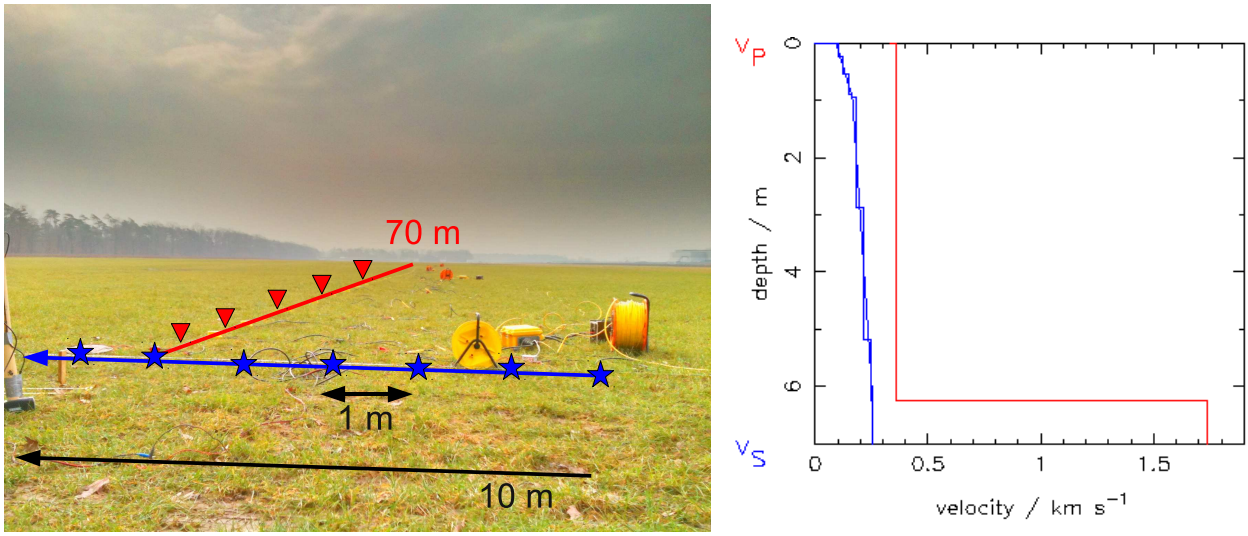

(a) Field site Rheinstetten (b) 1D subsurface model

Figure IV.1: (a) shows an impression of the field site Rheinstetten and a sketch of the acquisition geometry. The red triangles denote the position of vertical geophones (eigenfrequency of 4.5 Hz, receiver spacing of 2 m) and the blue stars indicate the shot locations (vertical hammer blow, shot distance of 1 m). Total line-source length is 10 m. (b) displays a 1D subsurface model obtained from joint inversion of first arrival P-wave travel times and Fourier-Bessel expansion coefficients (Forbriger, 2003) of the shot which was excited in-line of the receiver profile.

significantly for increasing line-source profile lengths. It is obvious that the misfit depends on the size of the line-source profile. This reflects the approximation of the infinite integral by a finite sum in eq. IV.2. Therefore, it is a question of accuracy and time requirements how many point sources one excites in a field survey to simulate a line source with single point sources. As expected the smallest misfit in this test is observed for the largest tested line-source profile length of 80 m. This line-source is built up of 81 point sources. However, please note that for 1D and 2D (additional lateral variations in the direction perpendicular to the line source) media only one side of the line-source profile must be excited due to symmetry of the subsurface structure. Therefore, the number of single point sources can be halved. E.g. 40 point sources perpendicular on the left side of the receiver profile are required for a 80 m line-source profile length.

The misfit displayed in Fig. IV.2(a) describes the sum of the misfit values for all used receivers. In Fig. IV.2(b) I additionally study single-misfit values of every single receiver for different number of point sources or rather different line-source profile lengths. For small line-source profile lengths the misfit increases significantly for larger offsets, because the later contributions to the line source response are due to point sources at larger distance to the origin. However, this later contributions are missing for small line-source profiles. Only larger line-source profiles account appropriate for this effect which is observable in Fig. IV.2(b). In other words far-offset receivers notice a small line-source profile in the origin rather as a point source then as an appropriate line-source simulation.

For the line-source simulation in the field we excited a line-source profile of 10 m. With the knowledge of Fig. IV.2(b) I expect only an observable adaptation of the line-source simulation for near-offset receivers.

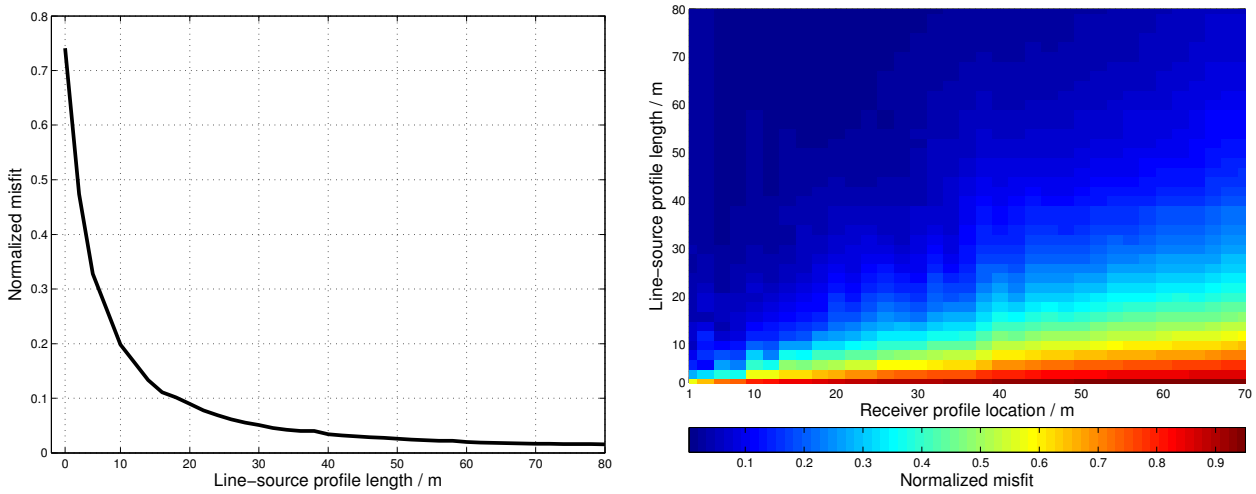

(a) L2 norm misfit with different line-source profile length.

(b) L2 norm misfit of single receivers with different line-source profile length.

Figure IV.2: (a) shows the L2 norm of original line-source seismograms and simulated line-source seismograms with different line-source profile lengths for all receivers. (b) displays the L2 norm for single receivers. A line-source profile length of 0 m corresponds to a single point-source located in-line with the receiver profile. The misfit is normalized to the energy of the original line-source seismograms.

IV.3 Line-source simulation in the field

We acquired 11 single point sources perpendicular to the receiver profile in the field survey on the gliding airfield of Rheinstetten (Section IV.1). By superposition of the point sources (eq. IV.2) I calculate simulated line-source wave fields with a 10 m line-source profile. To obtain a reference for a line-source wave field I apply the *Fourier-Bessel* transformation to the point-source wave field of the in-line shot (Section III.2.2) as this transformation is exact for wave propagation on 1D structures. For comparison I show in Fig. IV.3 the wave fields of the original point source, the reference line source (*Fourier-Bessel*) and the simulated line source in the field. I observe a good adjustment of the reference line source and the simulated line source wave fields for near-offset traces (offset between 1-20 m). For larger offsets the wave fields of the simulated line source are gradually shifted to the original point source wave field. This is exactly what I expected from the experience of the synthetic case study in Section IV.2. Only near-offset receivers notice a small line-source profile of 10 m as an appropriate line source, but for larger offsets it appears more like a point source.

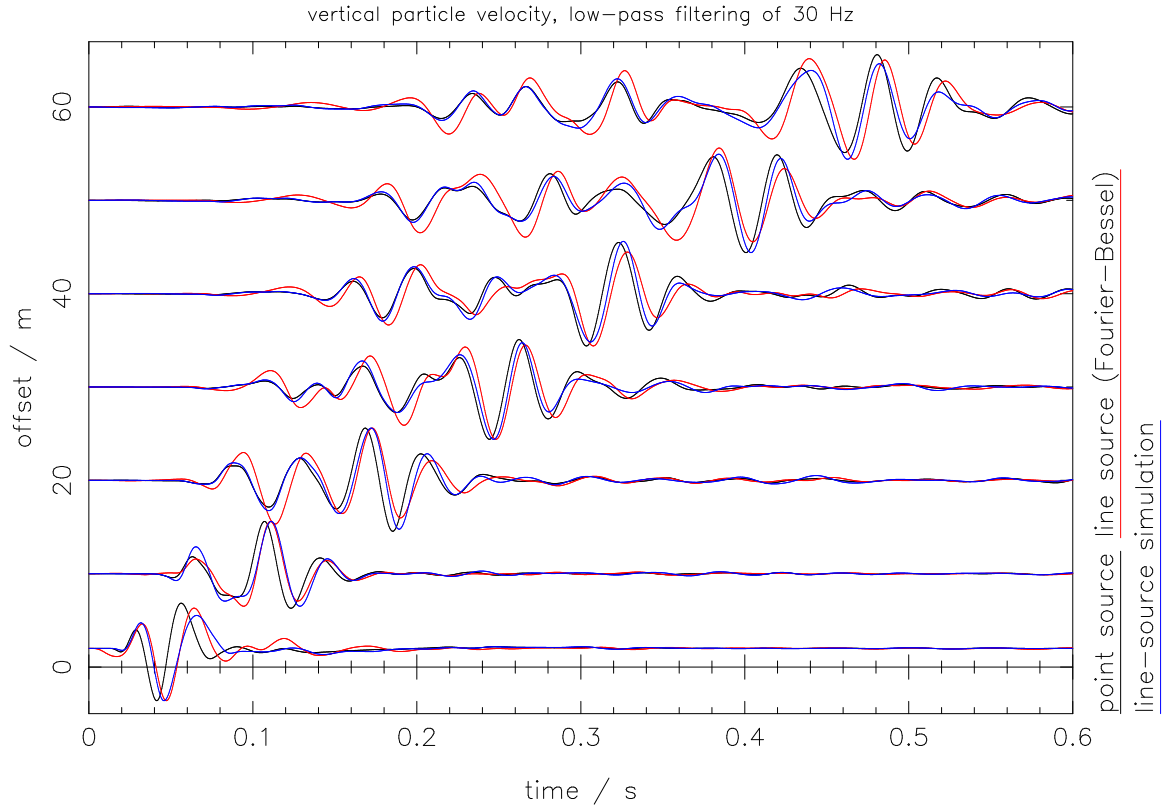

Figure IV.3: Comparison of point source and different line-source simulations: Original point source (black), line source obtained by *Fourier-Bessel* transformation as reference (red) and line-source simulation in the field with 10 m line-source profile (blue). Only every 5th trace is plotted. The seismograms are normalized to their maximum due to different amplitude-decay with offset.

IV.4 Discussion and conclusion

I presented in this chapter the approach for simulating a line source in the field by superposition of single point sources perpendicular to the receiver profile. This transformation provides correct magnitude and physical units. For practical application one has to approximate the infinite integral by a finite sum over the number of used single point sources in the field survey. I showed for a synthetic case study that the approach is in principle applicable for the simulation of a line source in the field. However, a vast number of point sources is required. Furthermore, I presented that the approach is also valid for field data within the expected limits of an appropriate line-source simulation which depend on the line-source profile length and the offset of the receiver. I conclude that a simulation of a line source in the field survey is meaningful, however, it is inefficient due to the vast number of required point sources in particular for far-offset traces. Please note that this investigation is only done for one shot location. In the framework of FWI several shot locations within the receiver profile are required which will multiply the effort dramatically. Therefore, the numerical transformations of the previous chapter are superior to the approach introduced here.

Chapter V

Inversion of field data on a 2D structure – test-site Mammolshain

In this chapter I am dealing with the application of 2D FWI to recorded shallow-seismic Rayleigh waves on a 2D structure which we have acquired in the vicinity of Mammolshain (Taunus). 2D FWI is reasonably applicable to field data acquired on 2D structures since scattering at 3D structures cannot be explained by 2D forward solver within the inversion scheme. Therefore, I am looking for a dominant 2D nature of the subsoil which is a challenging task. I selected a 2D test-site on a fault system of the southern rim of the Taunus. With preparatory investigations (geoelectric and seismics) we confirmed the predominantly 2D nature of the subsoil. In collaboration with the Bauhaus-University Weimar we acquired ground-truth data such as a dynamic probing light (DPL) investigation as well as seismic velocities and density values measured in the laboratory of collected samples. Perpendicular to this 2D fault we carried out a shallow-seismic 2D survey in summer of 2011. To obtain suitable starting models first arrivals of the P- and S-Waves for a travel-time tomography are used. Finally, I apply the 2D FWI to the recorded shallow-seismic field data acquired in Mammolshain (Taunus).

V.1 Taunus - Location Mammolshain

The Taunus is a mountain range in Hesse near Frankfurt (Main) and it is part of the Rhenish Slate Mountains (Winkelmann, 1997). Surface weathering and erosion degraded the mountains in the age of Mesozoic. Therefore today, it is characterized by relatively low range, with smooth and rounded mountains that are mainly covered with forest. For geographical, ecological and geological purposes the Taunus is divided in Pre-Taunus (Vortaunus), the High-Taunus (Hochtaunus, Taunuskamm) and the Back-Taunus (Hintertaunus). Our region of interest is located in the Pre-Taunus (see Fig V.1). This section is mainly made up of metamorphic volcanic rocks with phyllite, greenschist and sericite-gneiss (Kümmerle and Seidenschwann, 2009). The test-site Mammolshain is located on a fault system of the southern rim of the Taunus (see Fig. V.2). In the northwestern part of the fault sericite-gneiss is met at shallow depth, while it is covered by large sedimentary layers southeast of the

fault. This is confirmed by exploratory drillings in Fig. V.3. At the exploratory drilling site "Theodorusquelle" (No. 36) on the northwest of the fault the sericite-gneiss is met in a depth of 9 m while the drilling of "Kronthal" (No. 37) shows no sericite-gneiss up to a depth of 21 m. Furthermore, the annual field practical course of the University of Frankfurt takes place in this region. Fig. V.4 displays a DC geoelectric investigation from students of this field lab. It is obvious that the electric resistance values are suddenly changing along the profiles. The geological formation and the investigations of the students are a strong indication for a 2D structure in the subsoil.

Table V.1 gives a small overview of velocities of elastic waves and density in unconsolidated sediments as well as in metamorphic rocks which are present in the subsoil of the test-site Mammolshain. Therefore, these seismic velocities can be expected during the field-data inversion in Section V.8.

Rock type	v_p in m/s	v_s in m/s	ρ in kg/m^3
Unconsolidated sediments	550...1950	150...400	1200...2000
Quartzite	1900...5300	1500...2900	2600...2700
Gneiss	3000...5200	1900...3000	2500...3100
Schist	2400...4900	1800...3100	2800...3000

Table V.1: Mean-value range of P-wave (v_p) and S-wave (v_s) velocities as well as density ρ in unconsolidated sediments and rocks (Schön, 1996).

V.2 Preparatory investigations

With the information of the geological formation and the hint of the geophysical field course of the University of Frankfurt, I decided to consider the location Mammolshain as our test-site for the 2D shallow-seismic field survey. As we are using a 2D inversion with a 2D forward modeling code, the 2D assumption of the test-site is a indispensable requirement which we should verify as precise as possible. If the 2D assumption is largely fulfilled, the material properties won't change parallel to the fault. Therefore, predominant 1D media should be present on both sides of the fault system. To prove this we acquired two shallow-seismic field data sets: one profile located in the northwestern part of the assumed fault and the other profile in the southeast of the fault system (Section V.2.1). But even when the 2D assumption is satisfied, we only obtain a 2D data set if the profile is set up perpendicular to the 2D fault. Because of this we did another shallow-seismic survey to estimate the strike direction of the 2D fault (Section V.2.2).

V.2.1 Shallow-seismic profiles parallel to the 2D fault

We acquired two shallow-seismic field data sets at the location Mammolshain to verify the 2D assumption of this test-site. The Profile P1 was set up parallel to the assumed fault in the northwestern part and Profile P2 was located in the southeast of the fault (see Fig. V.5). The

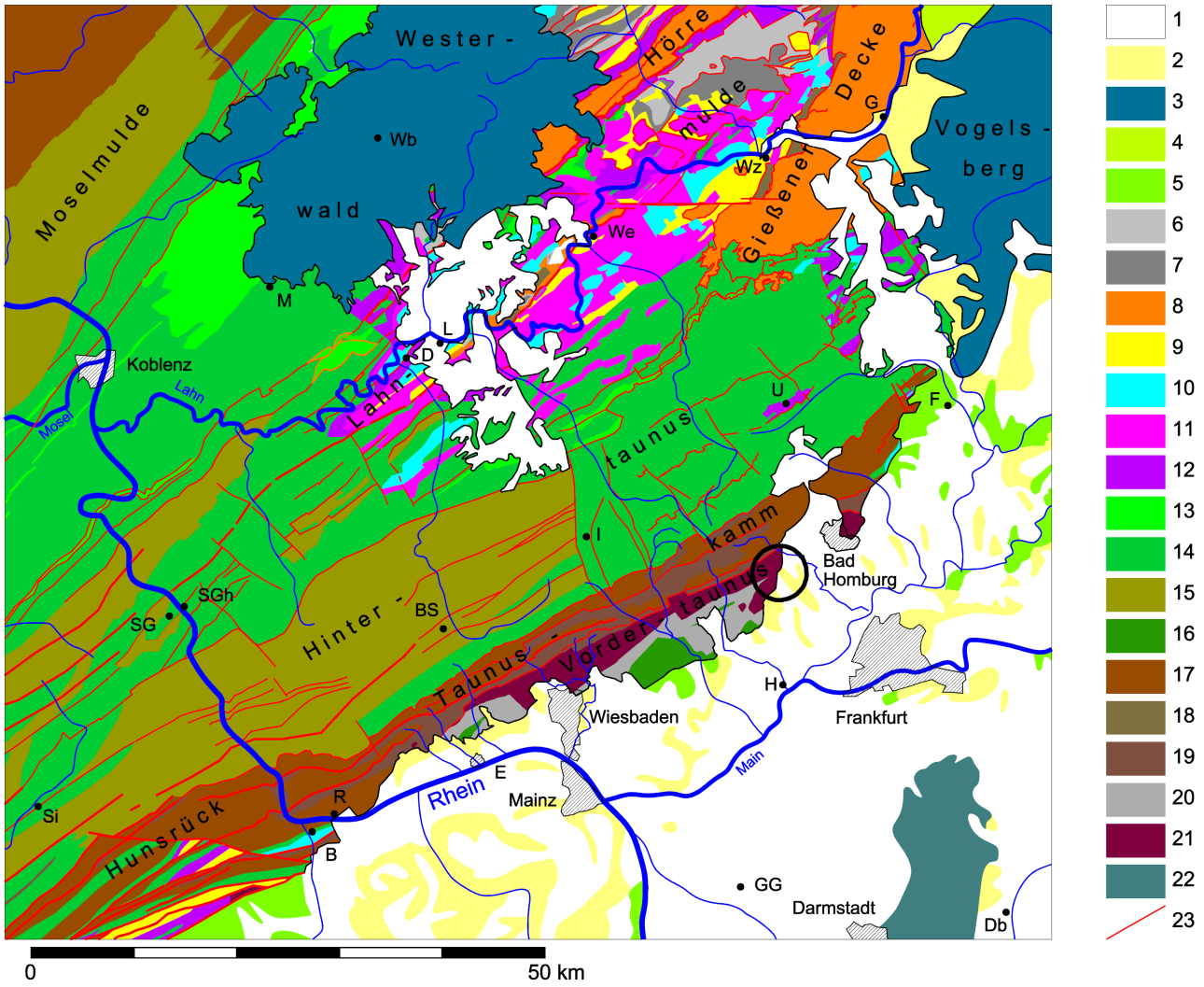

Figure V.1: Overview of the geological map of the Taunus region. The black circle indicates the vicinity of Mammolshain. In Fig. V.2 the region of interest is displayed in more detail. Legend: 1: Quaternary; 2: Tertiary; 3: Tertiary, vulcanite; 4: Trias, bunter; 5: Permian, Rotliegendes; 6: Lower Carboniferous; 7: Lower Carboniferous; 8: Late Devonian - Lower Carboniferous; 9: Late Devonian; 10: Middle Devonian - Late Devonian; 11: Middle Devonian, Givet; 12: Middle Devonian; 13: Late Devonian, Ems; 14: Late Devonian, Ems; 15: Late Devonian, Siegen-Ems; 16: Late Devonian, Ems; 17: Late Devonian, Siegen; 18: Late Devonian (structureless); 19: Late Devonian, Gedinne; 20: Silurian; 21: Ordovician (metavulcanite); 22: Crystalline of Odenwald; 23: faults; Source: Jo Weber (modified Geological map of Hesse GK25; URL: http://commons.wikimedia.org/wiki/File:Geologische_Karte_Taunus.png, March 2014).

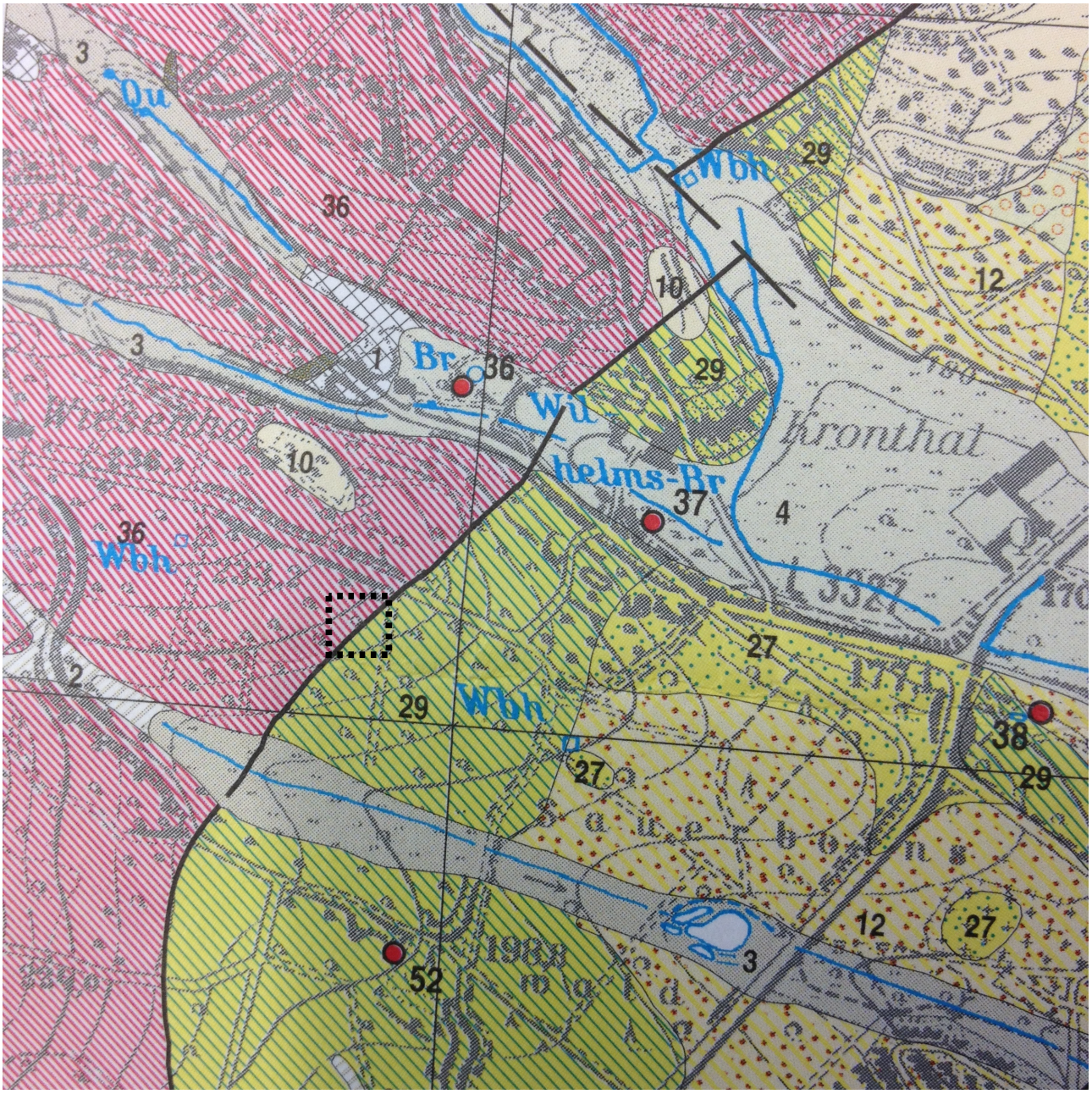

Figure V.2: Extraction of the geological map of Hesse 1:25000 GK25 No. 5817 Frankfurt a.M. West. The red color indicates Wiesbaden-Metarhyolith with sericite-gneiss while the green color denotes lime-free border facies with gravel, sand and clay. The black square sketchs the shallow-seismic field survey of Mammolshain and the DC geoelectric investigations during a field lab (see Fig. V.4). Borehole profiles of two exploratory drillings (No. 36 and 37) are displayed in Fig. V.3.

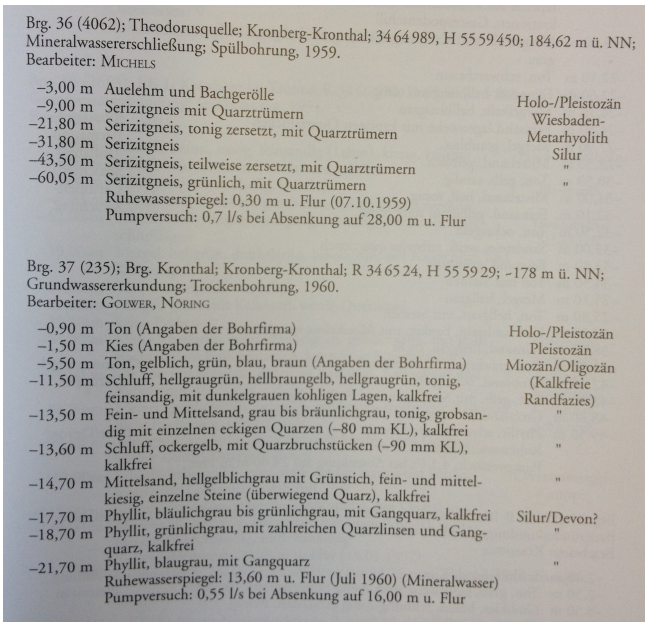

Brg. 36 (4062); Theodorusquelle; Kronberg-Kronthal; 34 64 989, H 55 59 450; 184,62 m ü. NN; Mineralwassererschließung; Spülbohrung, 1959.
Bearbeiter: MICHELS

–3,00 m	Auelehm und Bachgerölle	Holo-/Pleistozän
–9,00 m	Serizitgneis mit Quarztrümern	Wiesbaden-Metarhyolith
–21,80 m	Serizitgneis, tonig zersetzt, mit Quarztrümern	Silur
–31,80 m	Serizitgneis	"
–43,50 m	Serizitgneis, teilweise zersetzt, mit Quarztrümern	"
–60,05 m	Serizitgneis, grünlich, mit Quarztrümern	
	Ruhewasserspiegel: 0,30 m u. Flur (07.10.1959)	
	Pumpversuch: 0,7 l/s bei Absenkung auf 28,00 m u. Flur	

Brg. 37 (235); Brg. Kronthal; Kronberg-Kronthal; R 34 65 24, H 55 59 29; ~178 m ü. NN; Grundwassererkundung; Trockenbohrung, 1960.
Bearbeiter: GOLWER, NÖRING

–0,90 m	Ton (Angaben der Bohrfirma)	Holo-/Pleistozän
–1,50 m	Kies (Angaben der Bohrfirma)	Pleistozän
–5,50 m	Ton, gelblich, grün, blau, braun (Angaben der Bohrfirma)	Miozän/Oligozän
–11,50 m	Schluff, hellgraugrün, hellbraungelb, hellgraugrün, tonig, feinsandig, mit dunkelgrauen kohligen Lagen, kalkfrei	(Kalkfreie Randfazies)
–13,50 m	Fein- und Mittelsand, grau bis bräunlichgrau, tonig, grobsandig mit einzelnen eckigen Quarzen (–80 mm KL), kalkfrei	"
–13,60 m	Schluff, ockergelb, mit Quarzbruchstücken (–90 mm KL), kalkfrei	"
–14,70 m	Mittelsand, hellgelblichgrau mit Grünstich, fein- und mittelkiesig, einzelne Steine (überwiegend Quarz), kalkfrei	"
–17,70 m	Phyllit, bläulichgrau bis grünlichgrau, mit Gangquarz, kalkfrei	Silur/Devon?
–18,70 m	Phyllit, grünlichgrau, mit zahlreichen Quarzlinsen und Gangquarz, kalkfrei	"
–21,70 m	Phyllit, blaugrau, mit Gangquarz	"
	Ruhewasserspiegel: 13,60 m u. Flur (Juli 1960) (Mineralwasser)	
	Pumpversuch: 0,55 l/s bei Absenkung auf 16,00 m u. Flur	

Figure V.3: Extraction of the geological map of Hesse 1:25000 GK25 (Explanation of No. 5817 Frankfurt a.M. West, Kümmerle and Seidenschwann, 2009). In the upper part the borehole profile of No. 36 is displayed and in the lower part the borehole profile of No. 37. Both profiles are in near vicinity of the field survey (see Fig. V.2).

acquisition geometries consisted of linear profiles with 72 vertical geophones (eigenfrequency of 4.5 Hz) with an equidistant geophone spacing of 1 m for both profiles. We chose a sampling interval of 0.125 ms and the record length was 1 s. 18 shots were excited along the profiles where a hammer blow was used as vertical source.

Fig. V.6 displays shot08 which is located in the middle of Profile P1 and P2, respectively. The fundamental mode as well as most of the higher modes coincide for both profiles. Therefore, we can assume that the material properties are only depth dependent and there are less lateral variations. Such a subsurface is called 1D medium or 1D structure. In Fig. V.7 I show a comparison of shot01 (southeast end of profile; profile meter 74 m) of Profile P1 and P2, respectively. It is clearly observable that the phase velocities of the seismograms of Profile P1 are significantly higher than of Profile P2. This observation supports the geological formation: I expect high phase velocities for the sericite-gneiss at shallow depth in the northwestern part of the fault system and lower phase velocities for the large sedimentary layers southeast of the fault.

For laterally homogeneous structures (material properties are only changing with depth) the wave field excited by a cylindrically symmetric source (e.g. vertical point force such as a vertical hammer blow) can be expanded by Fourier-Bessel functions. Therefore, I additionally calculated Fourier-Bessel expansion coefficients for a better characterization of Profile P1 and P2, respectively. This comprises a modified Fourier-Bessel-Transformation after Forbriger (2003, Part I, Section 5.1 and 5.2). The Fourier-Bessel expansion coefficients G_z (vertical

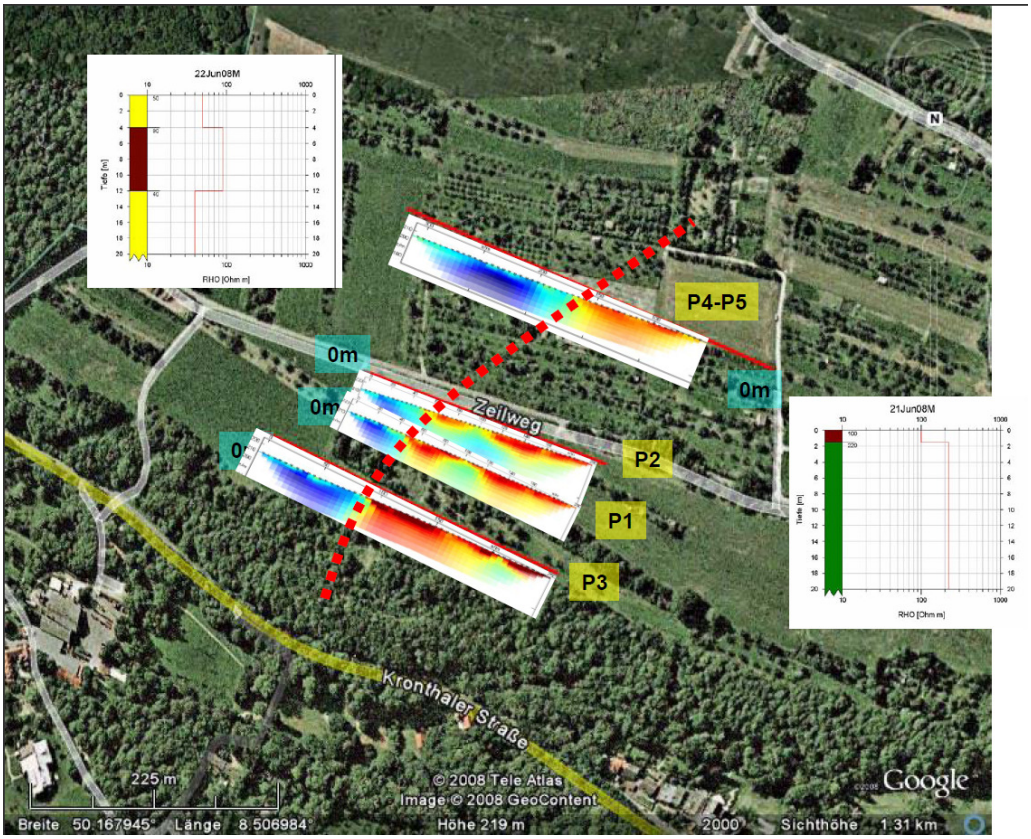

Figure V.4: Extraction of a DC geoelectric investigation during the annual field practical course of the University of Frankfurt. The blue color indicates low electric resistance values whereas the red color denotes high values. The red dashed line indicates the location of the faulting interpreted by the students of the field lab. Source: University of Frankfurt, Institute of Geophysics.

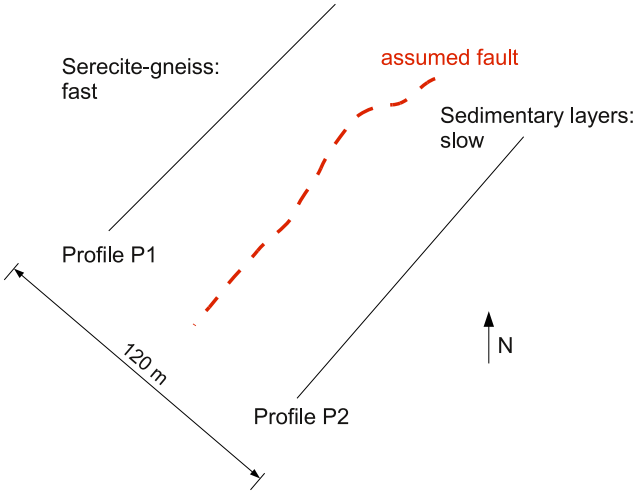

Figure V.5: Sketch of the 2D fault and locations of Profile P1 and P2. The dashed red line indicates the assumed fault location.

component) can by calculated by

$$G_z(\omega, p) = \frac{\omega^2}{2} \sum_{l=1}^{N} \tilde{u}_z(\omega, r) H_0^{(2)}(\omega p r_l) r_l \Delta r_l \tag{V.1}$$

$$\text{with} \quad \Delta r_l = \frac{1}{2} \begin{cases} r_2 - r_1 & \text{for } l = 1, \\ r_N - r_{N-1} & \text{for } l = N, \\ r_{l+1} - r_{l-1} & \text{otherwise} \end{cases} \tag{V.2}$$

with the phase slowness $p = k/\omega$, the wavenumber k, the angular frequency ω, the discrete offsets r_l, the Hankel function $H_0^{(2)}$ of order zero, the Fourier transform of the vertical component $\tilde{u}_z$ of the wave field and the number N of receivers.

Fig. V.8 displays the Fourier-Bessel expansion coefficients G_z for the wave fields of shot01 (profile meter 74 m) for Profile P1 and P2, respectively. I observe for both dispersion analyses coherent fundamental and even one coherent higher mode. For the Profile P1 I get slowness values between 1 - 4 s km^{-1} which corresponds to phase velocities of 250 - 1000 m s^{-1} and for Profile P2 I observe slowness values between 3 - 7 s km^{-1} which corresponds to seismic velocities of 150 - 300 m s^{-1} for both observed modes.

To summarize we acquired two seismic Profiles P1 and P2 which were set up parallel on each side of the fault system to verify the 2D assumption of the selected test-site in Mammolshain. I observe for each Profile P1 and P2, individually, phase coherent signals and different seismic velocities which correspond to the geological formation. I conclude that this is a strong indication for a 2D structure in the subsoil. As I already mentioned, we only acquire an appropriate 2D data set if, on the one hand, the 2D assumption is fulfilled and, on the other hand, we set up the profile perpendicular to the 2D fault.

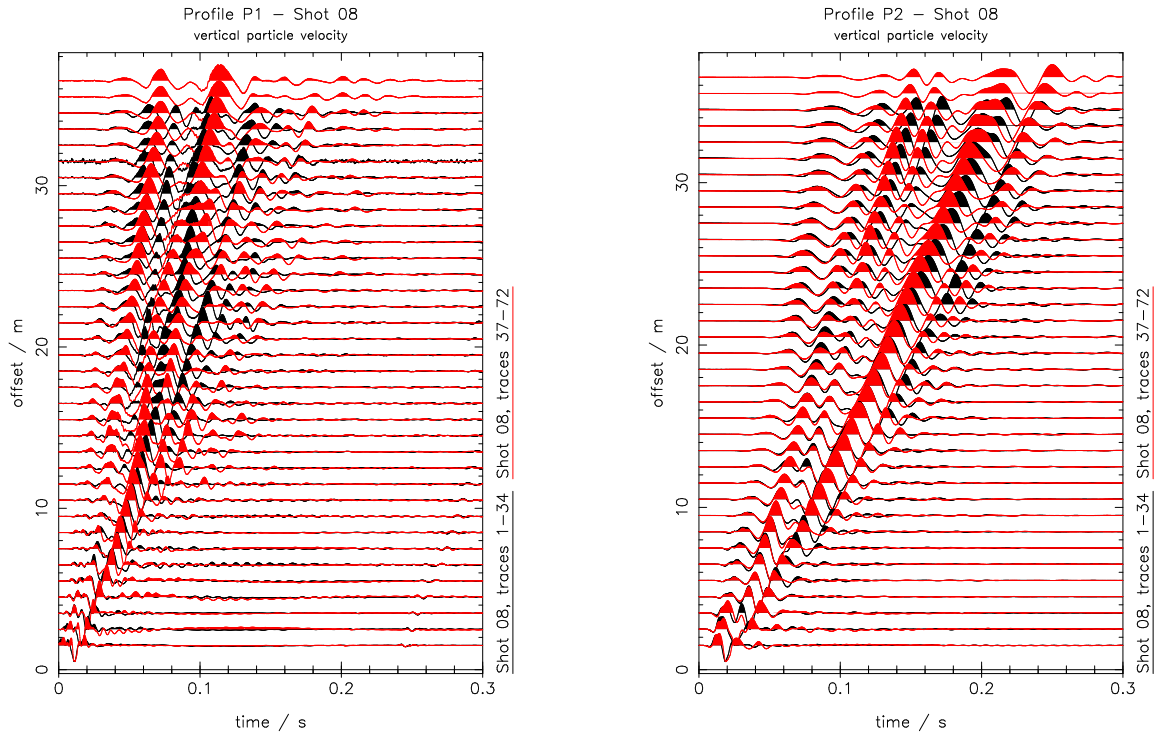

(a) Profile P1 - northwest of the fault

(b) Profile P2 - southeast of the fault

Figure V.6: Vertical particle velocity of Profile P1 and P2 of shot08 (profile meter 37.5 m). Traces 1-34 are plotted in black while traces 37-72 are plotted in red. Clipped traces 35 and 36 are not displayed. Each trace is normalized to its maximum amplitude.

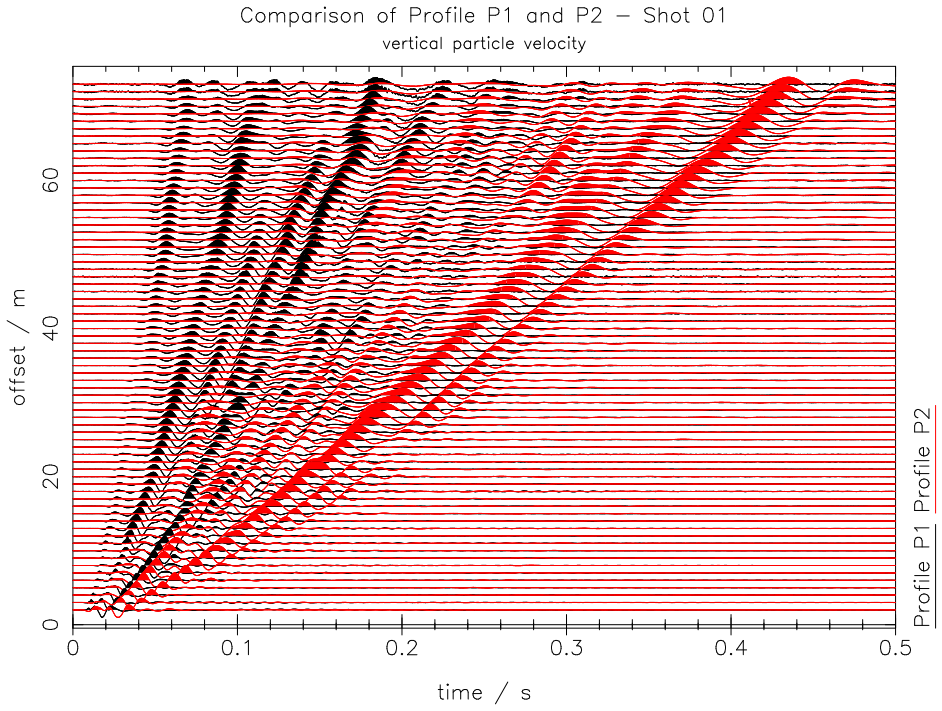

Figure V.7: Vertical particle velocity of shot01 (southeast end of the profile; profile meter 74 m) for Profile P1 (black) and Profile P2 (red). Each trace is normalized to its maximum amplitude.

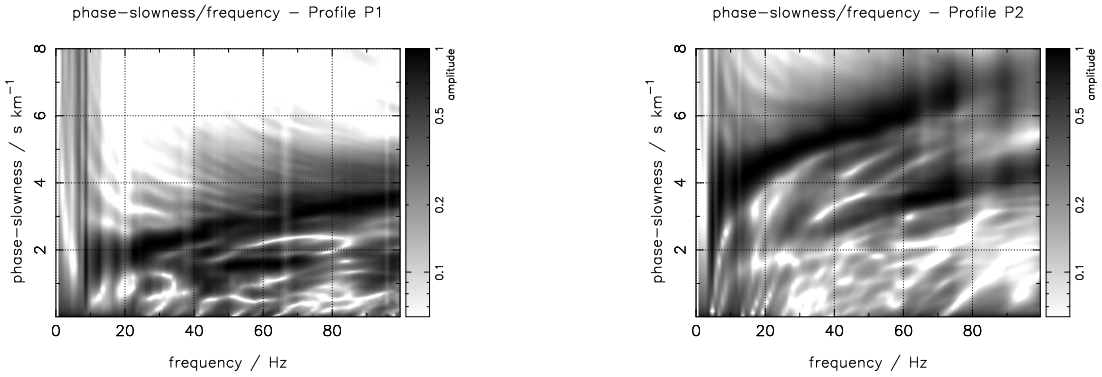

(a) Profile P1 - northwest of the fault

(b) Profile P2 - southeast of the fault

Figure V.8: Amplitudes of complex Fourier-Bessel expansion coefficients of shot01 (southeast end of the profile; profile meter 74 m) for Profile P1 and P2 (see Fig. V.7). The expansion coefficients are scaled for each frequency individually using the maximum amplitude value.

V.2.2 Estimation of the strike direction α of the 2D fault

It is an essential requirement that the shallow-seismic profile for the 2D data set is set up perpendicular to the 2D faulting. So far I have investigated strong indications for the dominant 2D nature of the subsoil like the geological formation and 1D seismic profiles on both sides of the fault system. In this section I attempt to estimate the strike direction α of the 2D fault in the test-site Mammolshain because the exact run of the faulting is unknown. This seismic survey distinguishes from other surveys in this thesis because the locations of the receiver profiles and shot profiles differ. The acquisition geometry is shown in Fig. V.9(a). The receiver profile consisted of a linear profile in east-west direction with 43 vertical geophones (eigenfrequency of 4.5 Hz) with an equidistant geophone spacing of 2 m. We chose a sampling rate of 0.25 ms and the record length was 1 s. The shot profiles are set up parallel to the receiver profile with an offset of 20 m. We excited 10 shots along the shot profile a and 10 shots along the shot profile b where a hammer blow was used as vertical source. So in total 20 single-shots are acquired. As the shots are not inline with the receiver profile I call them offline shots in the following.

We have seen in Section V.2.1 that the material properties are mostly changing in northwest-southeast direction and less in northeast-southwest direction. This is a strong indication that the material properties are mostly changing perpendicular to the fault and are largely unvaried parallel to the fault. I attempt to use this characteristic to estimate the strike direction of the faulting. For this purpose I compare waveforms of offline shots of the two shot profiles a and b for certain shot/geophone combinations. I show in the following two exemplary shot/geophone groups (*case 1* and *2*) to constitute the estimation of the strike direction. In the Appendix A all used combinations are displayed.

For *case 1* I use the shot/geophone groups displayed in Fig. V.9(b) and Tab. V.2. In this case I compare the shot01 of shot profile a with the shot01 of shot profile b and shot02 (shot profile a) with shot02 (shot profile b) and so on. For the waveform comparison I only use the geophones in the shortest direct distance of the two shots (within in one ellipse). In Fig. V.10(a) the waveform comparison of *case 1* is displayed. The red traces are shots (01-10) of shot profile a and the blue traces are of shot profile b. The numbers of shot/geophone groups displayed in Fig. V.9(b) and Tab. V.2 are also plotted in Fig. V.10(a) to ease the belonging. All seismograms are filtered with a fourth-order Butterworth low-pass filter with a corner frequency of 20 Hz. Indeed I observe that the waveforms are quite similar to each other (within the shot/geophone group) but it exists a large phase mismatch. Therefore, I conclude that the material properties are changing between the shot locations within one shot/geophone group and that the strike direction isn't in north-south direction.

To test different strike directions I systematically change the shot/geophone groups by shifting the two shot profiles relatively against each other. For *case 2* I use the shot/geophone groups displayed in Fig. V.9(c) and Tab. V.3. In this case the relative shift is 30 m and there are 7 shot/geophone groups. Note that the number of the shot/geophone groups are less than in *case 1* due to a limited number of possible combinations. In Fig. V.10(b) the waveform comparison of *case 2* is displayed. The fit of the waveforms is accurate for all shot/geophone groups. Hence, the material properties aren't changing along the shot locations used within one shot/geophone group. This is a strong indication that the used relative shift is more or

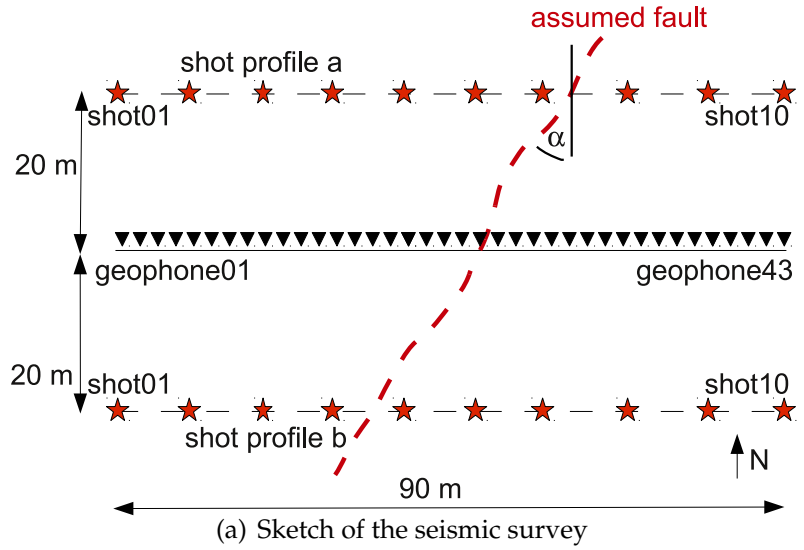

(a) Sketch of the seismic survey

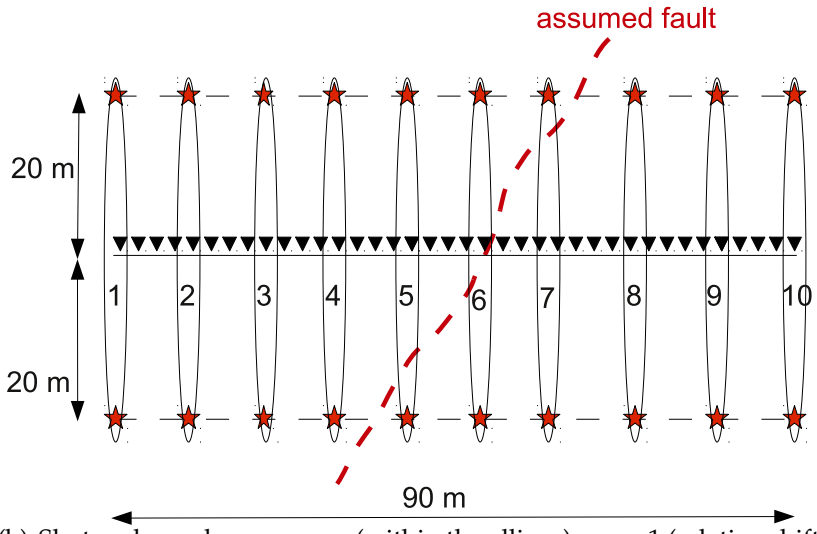

(b) Shot and geophone groups (within the ellipse) - case 1 (relative shift 0 m)

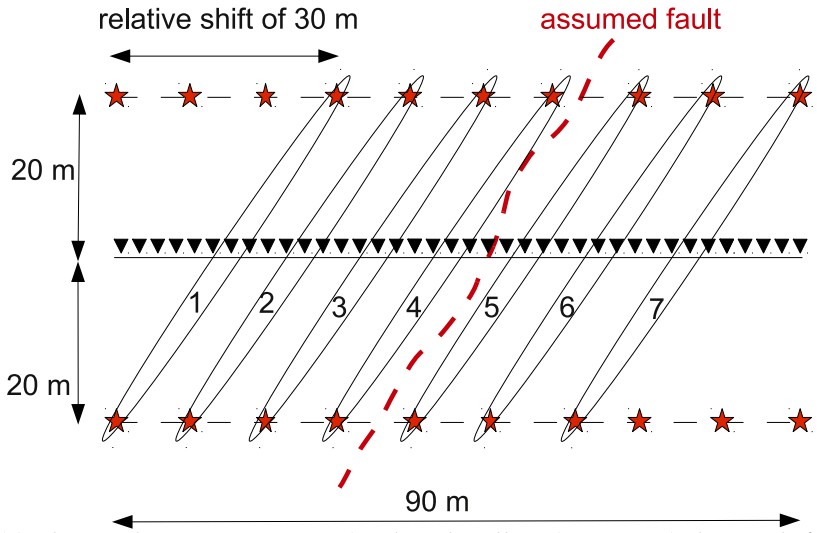

(c) Shot and geopone groups (within the ellipse) - case 2 (relative shift 30 m)

Figure V.9: (a) displays a sketch of the seismic survey for the estimation of the strike direction of the 2D fault. For the analysis different groups of shots and geophones are formed (within the ellipse). (b) shows groups without a relative shift while (c) displays shot and geophone groups with a relative shift of 30 m. Note that not all geophones are displayed.

less parallel to the strike direction. I have also tested other relative shifts like 10 m, 20 m and 40 m and different corner frequency of the low-pass filtering (see Appendix A). Altogether it is not possible to explain all shot/geophone groups and wave types with only one strike direction. Summarizing, a relative shift between 20-30 m is a good compromise. With elementary trigonometry I obtain a strike direction α between

$$\alpha = \arctan\left(\frac{\text{relative shift}}{\text{2x offset (20 m)}}\right) \approx \arctan\left(\frac{20...30\text{ m}}{40\text{ m}}\right) \approx 25^\circ - 36^\circ. \tag{V.3}$$

We use this information for the main shallow-seismic 2D survey in Section V.4.

shot/geophone group	shot profile a	shot profile b	geophone number
1	shot01	shot01	1
2	shot02	shot02	4,5
3	shot03	shot03	9,10
4	shot04	shot04	14,15
5	shot05	shot05	19,20
6	shot06	shot06	24,25
7	shot07	shot07	29,30
8	shot08	shot08	34,35
9	shot09	shot09	39,40
10	shot10	shot10	43

Table V.2: Shot/geophone groups for *case 1* (see Fig. V.9(b)). Waveforms are plotted in Fig. V.10(a).

shot/geophone group	shot profile a	shot profile b	geophone number
1	shot04	shot01	7,8
2	shot05	shot02	12,13
3	shot06	shot03	16,17
4	shot07	shot04	22,23
5	shot08	shot05	27,28
6	shot09	shot06	32,33
7	shot010	shot07	36,37

Table V.3: Shot/geophone groups for *case 2* (see Fig. V.9(c)). Waveforms are plotted in Fig. V.10(b).

V.2.3 Conclusions

The geological formation at the southern rim of the Taunus is a strong indication for a 2D structure of the subsoil at the test-site Mammolshain. This was confirmed by a DC geoelectric investigation of the annual field practical course of the University of Frankfurt. In addition, I have coordinated two shallow-seismic surveys to verify the 2D assumption and to estimate

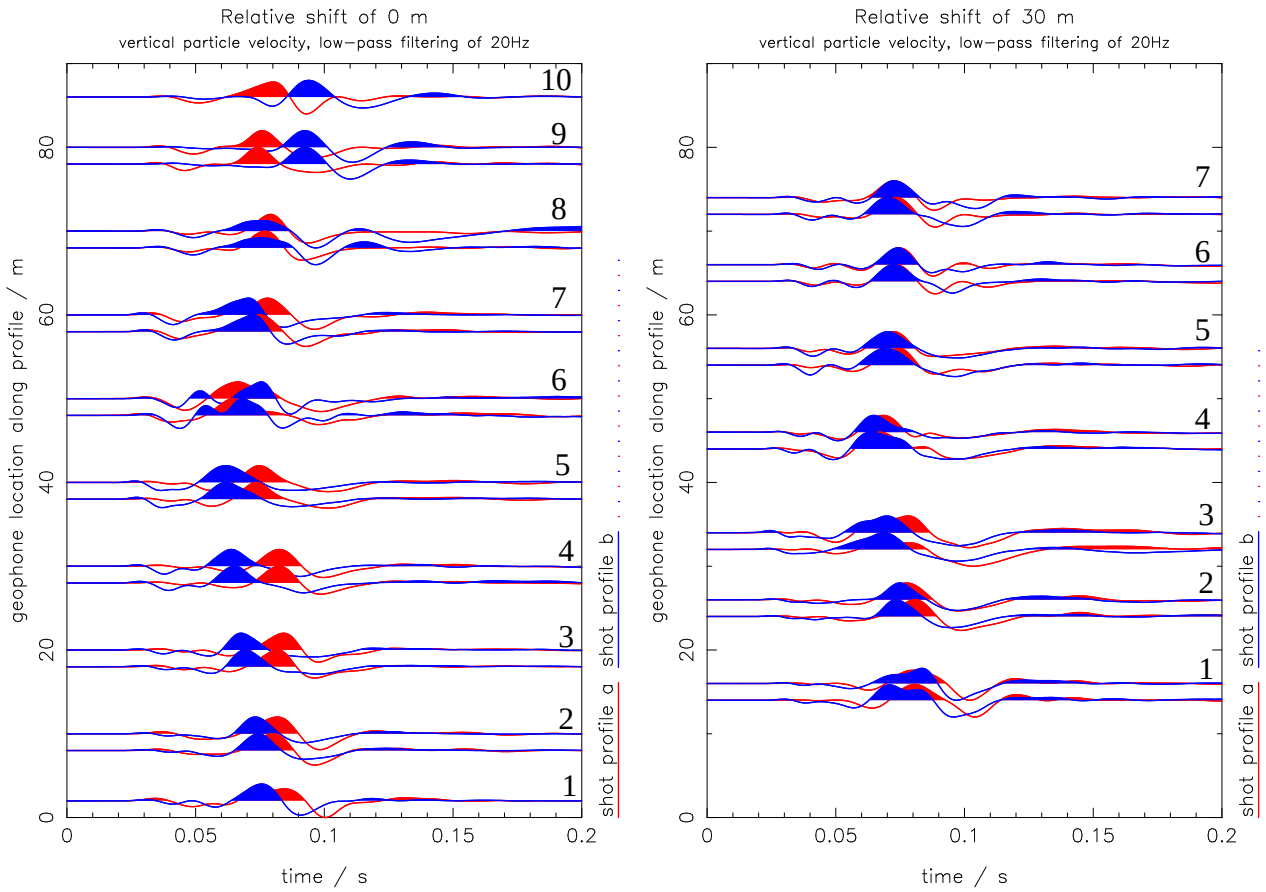

(a) relative shift of 0 m

(b) relative shift of 30 m

Figure V.10: Vertical particle velocity of shot/geophone groups as displayed in Fig.V.9. Red seismograms display shots excited on the shot profile a and blue seismograms of shot profile b. Each trace is normalized to its maximum amplitude. Numbers on the right side indicate shot/geophone groups given in Table V.2 and V.3.

the strike direction of the 2D fault which are essential requirements for the 2D seismic survey. I showed that the material properties mostly change perpendicular and less parallel to the 2D faulting. I estimated a preferred orientation of the fault of $\alpha \approx 25° - 36°$. Finally, I bring the knowledge of these preparatory investigations together for the 2D shallow-seismic field survey in Section V.4.

V.3 Ground truthing

We acquired a dynamic probing light (DPL) investigation in collaboration with the Bauhaus-University Weimar perpendicular to the 2D fault (Section V.3.1). Additionally, they estimated seismic velocities as well as density values by laboratory measurements (Section V.3.2). These collected ground-truth data will be compared to the inversion results obtained by FWI.

V.3.1 Dynamic probing light (DPL) investigation

After Smoltczyk (2002) dynamic probing light (DPL) is an in situ measurement of the penetration resistance from driving a cone vertically into the ground. A given mass (5 kg) at a constant height (0.5 m) of fall is used to drive the cone, while the number of blows N for a penetration depth of 0.1 m is counted. The diameter of the cone is slightly larger than that of the rod to reduce skin fraction and allowing the penetration resistance of the cone to be measured more accurately (Smoltczyk, 2002). I expect that the penetration resistance rapidly increases with depth in the northwestern part of the fault where sericite-gneiss is met at shallow depth and in the southeast of the faulting sedimentary layers generate low penetration resistance in larger depth.

The Bauhaus-University Weimar acquired a DPL investigation at the test-site Mammolshain within the TOAST project. Some impressions of the survey are plotted in Fig. V.11. The measurement progresses from the northwest of the fault to the southeast. In total we acquired 5 single DPLs. The number of blows N for a penetration depth of 0.1 m over the location along the profile is displayed in Fig. V.12. The maximum number of blows was set to $N_{max} = 80$. Material with a higher penetration resistance cannot be investigated with a DPL because the weight of the mass is too less to penetrate the subsoil. This depth may be interpreted as the transition zone between unconsolidated sediments and the upper edge of the weathering zone of the sericite-gneiss. The maximum number N_{max} was achieved in different depths along the profile why I conclude that the transition zone or rather the depth of the first weathering zone changes laterally. At the profile location of 0 m in the northwestern part of the fault N_{max} is reached at a depth of 1.4 m. For profile locations of 20 m and 40 m the weathering zone gets more shallow (0.8 m and 0.4 m, respectively). For larger profile locations it gets deeper (profile location of 80 m $\rightarrow$ 2.4 m) because the weathering zone is covered by sedimentary layers. This investigation emphasizes the geological formation.

V.3.2 Laboratory measurement of shear-wave velocity

The Bauhaus-University Weimar deals additionally with the measurement of seismic velocities of undisturbed samples. The following investigation is prepared by Binod Kafle of Bauhaus-University Weimar[1]. The undisturbed samples for the laboratory tests are obtained from the test-site Mammolshain at the northwest (Pit 1, depth of 0.75 m) and southeast (Pit 2, depth of 0.9 m) of the faulting. In Table V.4 the results of the report are displayed. Binod Kafle concludes that the investigation shows significant variations in water content and in clay content of the subsoil. Variations of specific gravity aren't significant but the water content and the clay content of the soil varies which cause a significant change in the bulk density. For Pit 1 and Pit 2 the bulk density is 2085 kg/m^3 and 2201 kg/m^3, respectively. Although these variations are observed for physical properties, the variations of the S-wave velocity between the northwest and the southeast of the faulting aren't significant. The shear-wave velocities are estimated between 200 m/s and 250 m/s which are common seismic velocities for shallow sediments. We have to keep in mind that this investigation allows only a selective information at the location of sample points and doesn't reflect the lateral variations of the

[1]Faculty of Civil Engineering, Modelling in Geomechanics

(a) upper position of the mass (b) lower position of the mass

Figure V.11: Impressions of dynamic probing light investigation at the test-site Mammolshain. The mass weighs 5 kg and the height of fall is 0.5 m.

S-wave velocities perpendicular to the faulting. Furthermore, the depth of sampling points are almost similar and shallow (< 1 m) why the samples reflect rather the top soil than lateral variations of material properties along the faulting. However, the estimated values are useful for comparing with initial and inferred inversion parameters for the topmost meters of the subsurface models later on.

V.4 2D shallow-seismic field survey

In the summer of 2011 I coordinated a multi-day shallow-seismic 2D survey at the test-site Mammolshain with the TOAST project partners from Ruhr-University of Bochum (RUB), Geophysics and Geotechnique Leipzig GmbH (GGL), German Research Centre for Geosciences of Potsdam (GFZ) and Karlsruhe Institute of Technology (KIT). Since it was a large survey we needed a lot of manpower and plenty of different equipment. We acquired 4 seismic profiles (P1, P2, P3 and P4) which are displayed in Figs V.13 and V.14. The knowledge of the preparatory investigations of Section V.2 are included in the orientation of the profiles especially for Profiles P3 and P4. We used 50 three component and 39 vertical component

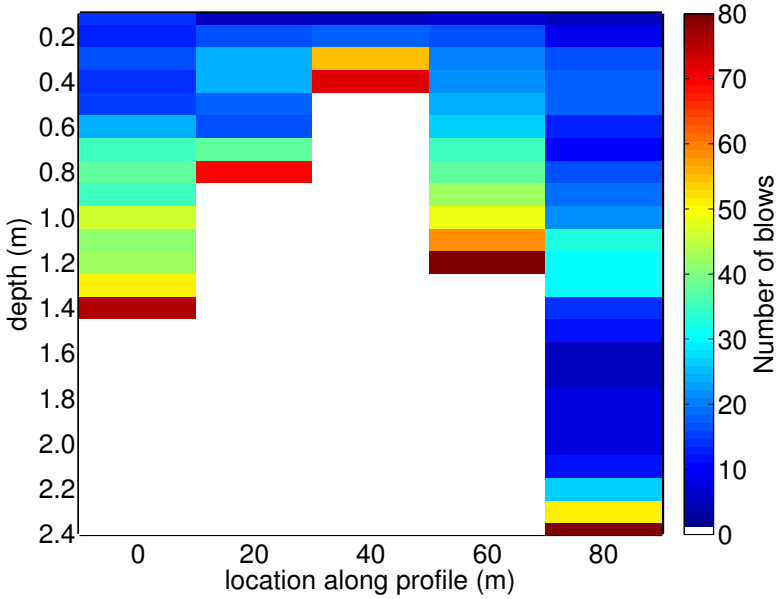

Figure V.12: Dynamic probing light investigation at the test-site Mammolshain. The profile coincides with Profile P3 (see Fig. V.14)

	Pit 1 (northwest)	Pit 2 (southeast)
Type	plastic clay	plastic clay
Clay content	70 %	50 %
Liquid content	30 %	22 %
Bulk density	2085 kg/m^3	2201 kg/m^3
Dry density	1906 kg/m^3	2062 kg/m^3
S-wave velocity	210-250 m/s	200-220 m/s

Table V.4: Laboratory measurements of undisturbed samples at the test-site Mammolshain. The obtained S-wave velocities are related to a depth of 1 m.

geophones (eigenfrequency of 4.5 Hz) and recorded the data with 8 geodes of Geometrics[2]. We chose a sampling rate of 0.25 ms and the record length was 1 s. We used four different sources:

1. pneumatic hammer to generate a strong and repeatable impact signal as vertical source of GFZ (S. Lüth, R. Giese)

2. magnetostrictive vibration source to generate a high resolution signal as vertical source of GFZ (S. Lüth, R. Giese)

3. vertical hammer blow as vertical source

4. SH-source (German: S-Wellen-Egge) to excite horizontally polarized waves with horizontal hammer impacts

[2]http://www.geometrics.com/geometrics-products/seismographs/geode/

For my thesis I focus on the vertical and horizontal hammer impacts. The data of the pneumatic hammer and the magnetostrictive vibration source is partly investigated by Heike Richter of GFZ. For the Profiles P1 and P2 the shot distance for the vertical hammer blow was 10 m and for the SH-source 30 m. For the Profiles P3 and P4 the shot distance was 4 m for both the vertical hammer blow as well as for the SH-source (only acquired for Profile P3!).

Figure V.13: An impression of the test-site Mammolshain. Viewing direction is northwest. The seismic Profile P3 is along the rods of the stadia surveying for the exact location and orientation of the seismic profiles. Photo courtesy of GFZ.

V.5 Comparison of Profile P3 and Profile P4

We set up Profile P3 and P4 with the best of strike direction's knowledge of Section V.2 perpendicular to the faulting and additionally parallel to each other to verify the 2D assumption. If the test-site Mammolshain is, on the one hand, a dominant 2D faulting and, on the other hand, the Profiles P3 and P4 are set up perpendicular to the 2D fault, the acquired wave

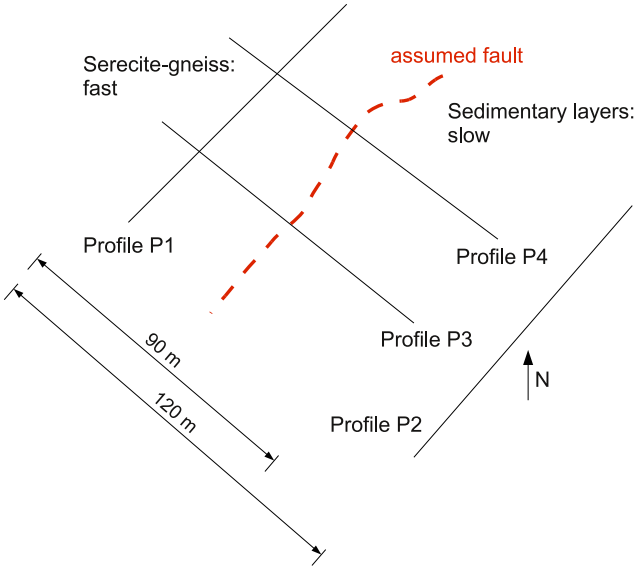

Figure V.14: Sketch of the shallow-seismic 2D survey at the test-site Mammolshain.

fields of Profiles P3 and P4 show similar phase velocities along the profile. Additionally, the location of the faulting has to be similar within both Profiles P3 and P4. To investigate this I show a common-offset gather for an offset of 20 m of Profile P3 and P4 in Fig. V.15 for the vertical hammer blow. For shot locations along the profile between 0 m and 56 m the phase velocities of Profile P3 and P4 change slightly and quite similar to each other. For shot locations between 60 m and 68 m the phase velocities differ clearly. Firstly, I conclude that the lateral variations of the material properties are small and comparable between Profile P3 and P4 for profile meters of 0 - 60 m. Secondly, a change in the material properties at a profile location of 60 m is observable and different for both profiles. Nevertheless, the location of the faulting seems to be at the same profile location for Profile P3 and P4 between 20 and 40 m.

Furthermore, I investigate the similarity of common-shot gathers between Profile P3 and P4 to study the 2D assumption. With the knowledge of the common-offset gather investigation it is confirmed that a comparison of single shots with the same distance to the 2D faulting is approved. In Fig. V.16 I compare shot01 (northwest end of profile; profile meter 0 m) and shot24 (southeast end of profile; profile meter 90 m) of Profile P3 and P4. It is obvious that the excited wave fields of shot01 and shot24 differ clearly, however, the seismograms of Profile P3 and P4 for one shot location are quite similar to each other. Please note that the influence of the different source time functions of the hammer blows aren't removed. Both shots (northwest and southeast of the fault) excited wave fields where the phase velocities change differently along the profile which is a strong indication for a 2D structure in the subsoil.

I expect that the 2D assumption is more fulfilled for strongly low-pass filtered data than for the full bandwidth of the data. For strongly low-pass filtered data long wavelength structures are dominant in the wave field. Small heterogeneity like rock fragments or tiny sediment lenses might corrupt the wave field at higher frequencies with 3D effects. These 3D effects cannot be explain by the 2D forward modeling in our 2D inversion scheme. To check this behavior I filtered the seismograms for all shots (shot01, shot02,...,shot24) of Profile P3 and P4

with different corner frequencies of a fourth-order Butterworth low-pass filter and calculated the normalized misfit function of eq. II.50 between Profile P3 and P4. The result is plotted in Fig. V.17. I observe a kind of minimum in the misfit for low-pass filtered data of 10 - 20 Hz. For higher frequencies the misfit increases dramatically and it seems to stagnate for frequencies larger than 60 Hz.

I conclude from the common-offset investigation that material properties along Profile P3 and P4 are fairly similar for profile meters of 0 - 60 m and slightly different for larger profile meters. The common-shot investigation emphasize the 2D assumption due to the similarity between the wave fields of Profile P3 and P4 and the different change of the phase velocities along the profiles. Nevertheless, I argue from the misfit of different low-pass filtered data that the 2D assumption is probably more fulfilled for strongly low-pass filtered data (10 - 30 Hz) than for higher frequencies (> 50 Hz). This observation may limit the successful inversion for high-frequency data in the FWI in Section V.8.

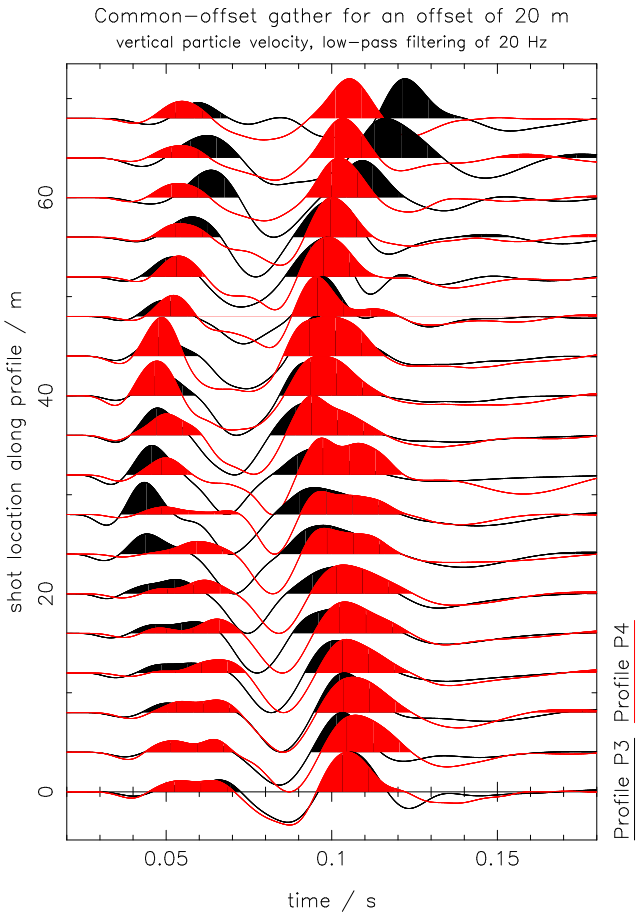

Figure V.15: Common-offset gather for an offset of 20 m of Profile P3 (black traces) and P4 (red traces). Each trace is normalized to its maximum amplitude.

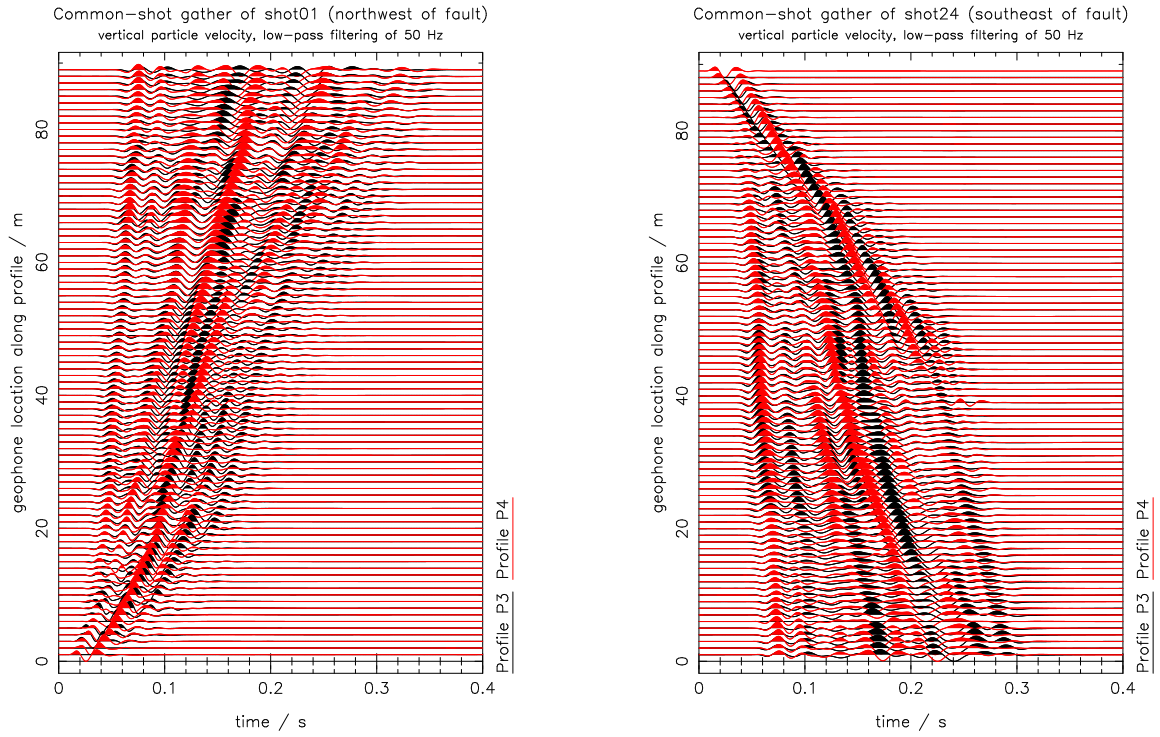

(a) shot01 in the northwest of fault

(b) shot24 in the southeast of fault

Figure V.16: Common-shot gather of shot01 (northwest end of profile; profile meter 0 m) and shot24 (southeast end of profile; profile meter 90 m) for Profile P3 (black traces) and P4 (red traces). Each trace is normalized to its maximum amplitude.

V.6 Preprocessing of the field data

3D/2D transformation

To make 2D FWI applicable to field data, recordings must be preprocessed to simulate the response to a line source (Chapter III). After the point-source wave fields are filtered, the wave fields can be inverted by a 2D full-waveform inversion. I apply the *hybrid* transformation to the original point-source field data to account for the different geometrical spreading of the field data (3D) and the 2D forward simulation in our 2D inversion scheme. As the *hybrid* transformation is a combination of the *single-velocity* and *direct-wave* transformation I have to select the single phase velocity v_{ph} at small offsets and the transition zone from offset r_1 to r_2 between both. The single-phase velocity is estimated from the phase velocity of the Rayleigh waves in the region near to the source. The values of the transition zone are based on the consideration of the dominant wavelength of the Rayleigh waves. For the test-site Mammolshain I choose $v_{ph} = 300\,\mathrm{m/s}$, $r_1 = 10\,\mathrm{m}$ and $r_2 = 20\,\mathrm{m}$ for all shots. Please note that the chosen values of v_{ph}, r_1 and r_2 have only an influence on the amplitude correction for near-offset traces. Later on not all traces are considered during the FWI (trace killing) due

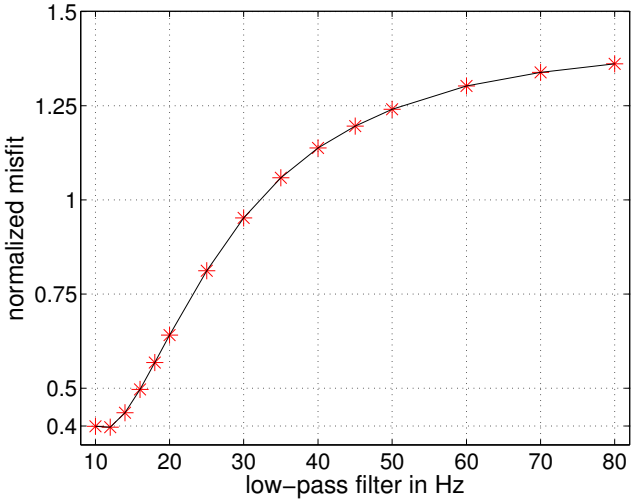

Figure V.17: Normalized misfit over all shots between Profile P3 and P4 (only vertical component) over corner frequency of the low-pass filter.

to clipping or strong ringing of single traces and near-field effects. Therefore, especially near offset traces are concerned of the trace killing why the chosen parameters of the *hybrid* transformation are not significant for the later FWI results. At the bottom line, the *direct-wave* transformation is used effectively.

The phase shift of $\pi/4$ is applied by a convolution with $\sqrt{t^{-1}}$ in the time domain which equals a fractional (half) integration (Forbriger et al., 2014b). This causes strong static offsets for some traces due to low-frequency noise in the field data. To reduce these artifacts I apply a fourth-order Butterworth high-pass filter with a corner frequency of 5 Hz prior to the 3D/2D transformation.

Overview of the preprocessing of 3D/2D transformation:

1. Tapering ensures that the traces are zero before the first arrival of the P-wave and after the fundamental mode of the Rayleigh wave.
2. Usage of fourth-order Butterworth high-pass filter with a corner frequency of 5 Hz to reduce low-frequency noise.
3. Application of 3D/2D transformation with *hybrid* transformation ($v_{ph} = 300\,\mathrm{m/s}$, $r_1 = 10\,\mathrm{m}$ and $r_2 = 20\,\mathrm{m}$).

In Fig. V.18 a comparison of the original point-source field data and the line-source corrected field data with the *hybrid* transformation is plotted. The applied phase shift of $\pi/4$ is observable. The traces are normalized to their maximum why the amplitude-decay with offset cannot be observed.

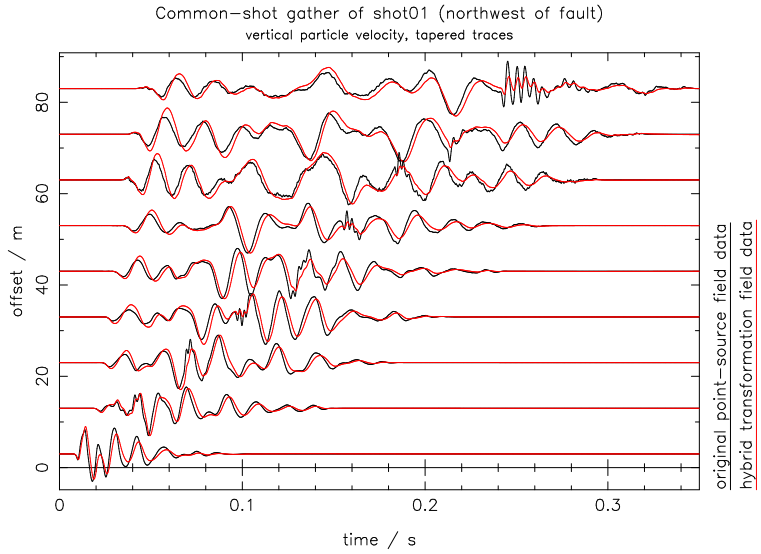

Figure V.18: Exemplary comparison of shot01 (northwest of fault) of original point-source field data and line-source corrected field data with the *hybrid* transformation. The phase shift of $\pi/4$ is observable. Each trace is normalized to its maximum amplitude and only every 10th trace is displayed.

Anelastic damping

Unconsolidated sediments generally have the highest attenuation properties among rocks (Schön, 1996). It is caused by the non compact nature of the grain skeleton. Schön (1996) observes Q values between 5 (e.g. clay), 8 (e.g. sand), 20 (e.g. silt, gravel) and 50-80 e.g. for unconsolidated rocks for shallow sediments. In preparatory investigations towards an application of FWI to field data my colleague Lisa Groos has shown that the effects of anelastic damping are significant in shallow-seismic field data (Groos et al., 2014). I assume constant quality factors as a priori known parameters in the inversion and don't invert for them during inversion. I use $Q_p = Q_s$ where Q_p is the quality factor of P-waves and Q_s is the quality factor of S-waves. As rheological model a generalized standard linear solid (GSLS) is used (Blanch et al., 1995; Bohlen, 1998, 2002).

We recommend a rather high quality factor because the subsequently applied source-wavelet correction filters act as low-pass filters (Groos et al., 2014). Otherwise (too low quality factor) the source-wavelet filters must increase the bandwidth of the simulated data, however, this is limited by the stabilization used in the source-wavelet inversion. Therefore, I choose for the quality factor $Q_p = Q_s \approx 20$. This quality factor is approximated by three relaxation mechanism with the relaxation frequencies $f_1 = 1.48\,\mathrm{Hz}$, $f_2 = 14.98\,\mathrm{Hz}$ and $f_3 = 101.99\,\mathrm{Hz}$ and $\tau = 0.082$. The frequency dependence of the quality factor is displayed in Fig. V.19. This attenuation is fixed during all following inversion tests with the field data set Mammolshain.

Source-wavelet correction filter

For an inversion of field data it is necessary to estimate the unknown source time functions

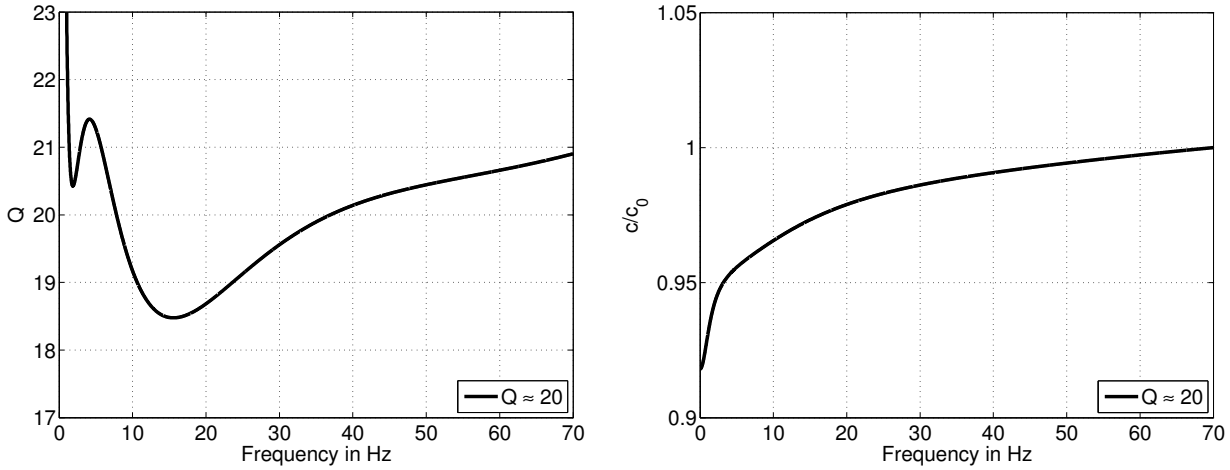

(a) Frequency dependency of Q.

(b) Velocity dispersion caused by damping.

Figure V.19: Rheological model used for forward simulation in the FWI of the field data set Mammolshain. A constant quality factor $Q_p = Q_s \approx 20$ is approximated with three relaxation mechanisms. (a) displays the frequency dependence of the quality factor and (b) the corresponding phase velocity dispersion caused by damping. c is the phase velocity and c_0 is the phase velocity at the used reference frequency of 70 Hz.

of the hammer impacts for each single shot. This is done by a stabilized deconvolution of the recorded wave field with the synthetics (Section II.4.4). The obtained source-wavelet correction filters are unaltered within a frequency interval and they are recalculated for each single shot when the frequency interval is increased. For the estimation of the source-wavelet correction filters only 5 - 10 near-offset traces per shot are used. Offset ranges vary between about 10 - 30 m. Smaller offsets are corrupted by near-field effects. These traces are selected manually due to data quality of each shot. I decided to take only traces with small offsets for the estimation so that the source-wavelet correction filters aren't strongly corrupted by differences in the wave fields due to differences of the true subsoil and the current subsurface models in the inversion. The optimized source wavelets are shown in the Appendix (Figs B.5, B.6, C.2 and C.3).

V.7 Starting models - First-arrival travel-time tomography

We use travel-time tomographies of first arrivals of P- and S-waves to obtain suitable starting models for the subsequent full-waveform inversion. Our TOAST project partner F. Köllner from GGL applied the program Rayfract[3] to calculate travel-time tomographies and A.-S. Reiß from the Geophysical Institute of KIT used ReflexW[4]. Both programs solve the Eikonal equation, however, by a slightly different way. Rayfract applies a first-order Eikonal solver to calculate the travel-time of the fastest wave at any point of a regular grid (Lecomte

[3]http://www.rayfract.com/
[4]http://www.sandmeier-geo.de/

et al., 2000). Within the tool *2D refraction* of ReflexW the curved rays are calculated using a finite-difference approximation of the Eikonal equation (User's guide of ReflexW[5]). Lecomte et al. (2000) confirmed the validity of their approach by comparisons with a finite-difference scheme (Vidale, 1988). Therefore, I suggest that the influence of the way of solving the Eikonal equation is not significant for the calculated travel times. However, the programs use different starting models (partly automatically generated) and number of velocity layers for the inversion which has a big impact on the results. Furthermore, travel-time tomography is based on the picked travel times of users which are subjectively biased. I discuss in the following two different starting models obtained by Rayfract and ReflexW which differ mostly in the S-wave velocity model. We use for the tomographies the vertical and horizontal component of Profile P3 (see Fig. V.14). The P-wave velocity model is derived from the vertical component (39 vertical and 50 three-component geophones) of all shots where a hammer blow was used as vertical source. The S-wave velocity model is inferred from the horizontal component of the 50 three-component geophones where the SH-source was used to excite horizontally polarized waves with horizontal hammer impacts.

V.7.1 Starting model 1 with Rayfract

The first starting model (*starting model 1*) is obtained by our TOAST project partner F. Köllner from GGL with Rayfract. The ray coverage of the P-wave velocity tomography is much higher than for the S-wave velocity inversion due to larger number of receivers and extra far-offset shots (see Fig. V.20). Especially at the southeast end of the profile (right side) there is a lack of rays in the S-wave velocity tomography. This is also reflected in the S-wave tomography result in Fig. V.21(a) where only within the black box reliable S-wave velocities are estimated. Outside of the box I extended the values to the length of the profile and in depth. The S-wave velocity model is characterized by seismic velocities between 350 - 1100 m/s and by small lateral variations along the profile. Please note that all colorbars are adjusted to the global minimum and maximum values within the next figures in this section. The result of the travel-time tomography of the P-wave velocity is displayed in Fig. V.21(b). We obtain values between 800 - 2600 m/s. We observe also small lateral variations along the profile. The results of the travel-time tomography for the P-wave and S-wave come as a surprise to me, because I expected a more step like structure of the subsurface. However, the P-wave velocity model predicts the first arrivals of the P-wave quite well.

After Bachrach et al. (2000) reasonable v_p/v_s ratios are expected for seismic material properties of shallow sediments between 1.56 (i.e., a Poisson number of $\nu = 0.15$) and values larger than 10 (i.e., $\nu > 0.495$). Stümpel et al. (1984) report even $\nu = 0$ (v_p/v_s ratio of 1.41) for dry and partially saturated sand. Material with $\nu < 0$ is physically not intuitive, because the material will actually contract in the transverse direction when compressed or expand when stretched. For shallow-seismic surveys known values lie between (Forbriger, 2003, Part II)

$$0.1 < \nu < 0.49, \tag{V.4}$$

$$1.5 < v_p/v_s < 10. \tag{V.5}$$

[5]Downloadable at http://www.sandmeier-geo.de/downloadguides.html

In Fig. V.21(c) the v_p/v_s ratio of *starting model 1* is shown. The values vary between 1.45 and 2.8 which is reasonable for shallow sediments. Therefore, I conclude that the S-wave and P-wave velocity model are physically feasible.

The density model is obtained about a modified Gardner's relationship. Gardner et al. (1974) determined in empirical studies the following relationship between P-wave velocity and density ρ:

$$\rho(\mathrm{kg/m^3}) = 0.31 \cdot 1000 \cdot v_p^{0.25}. \tag{V.6}$$

This relationship is mostly inferred for sedimentary rocks, especially shales, but it is not completely satisfied for the test-site Mammolshain. Schön (1996) presents detailed density values for unconsolidated sediments. I modified eq. V.6 for density values of lime-free border facies with gravel, sand and clay and the upper edge of the weathering zone of the sericite-gneiss to:

$$\rho(\mathrm{kg/m^3}) = 0.31 \cdot 1000 \cdot v_p^{0.3}. \tag{V.7}$$

The density model in Fig.V.21(d) is obtained with eq. V.7. I obtain density values between 2100 - 3100 $\mathrm{kg/m^3}$ which are reliable for the test-site Mammolshain (Schön, 1996).

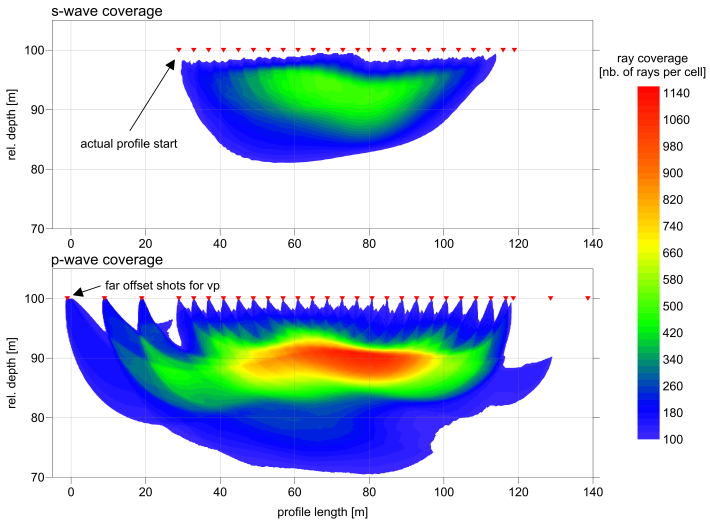

Figure V.20: Ray coverage of S-wave and P-wave tomographies below Profile P3 with Rayfract (courtesy of F. Köllner from GGL).

V.7.2 Starting model 2 with ReflexW

Shallow-seismic Rayleigh waves have a high sensitivity to the S-wave velocities in the topmost meters of the subsoil. Therefore, appropriate starting models of v_s are essential for a successful FWI with Rayleigh waves. In the following, we repeat the S-wave velocity tomography with the program ReflexW to obtain *starting model 2*. The result of the travel-time tomography of the S-wave velocity is displayed in Fig. V.22(a). We observe values of seismic velocities between 350 - 1200 m/s which is almost similar to the S-wave velocities of *starting*

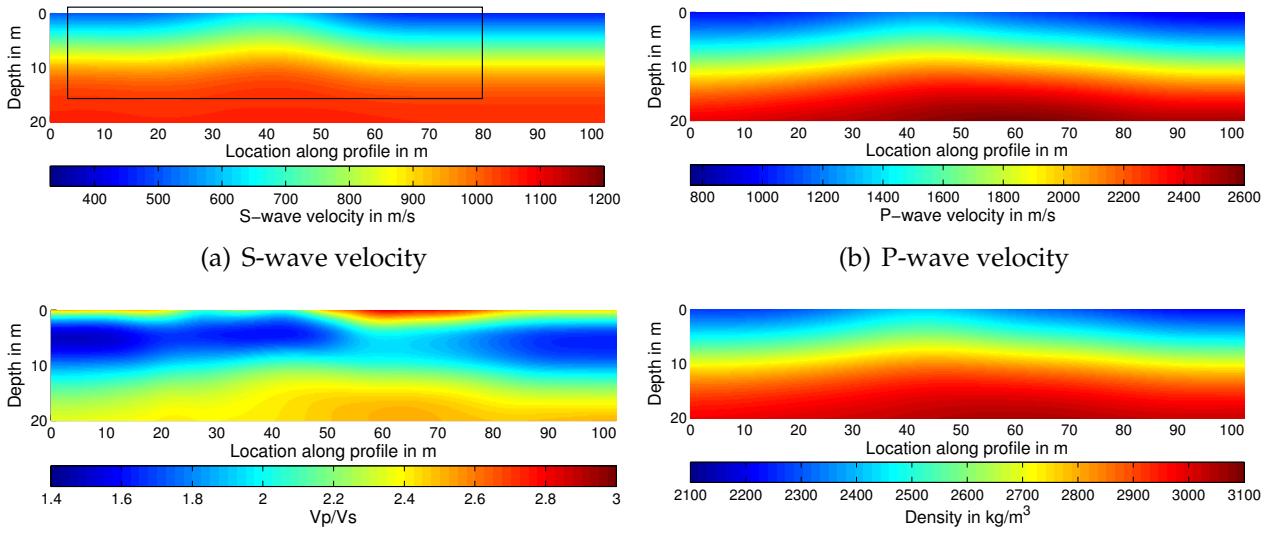

(a) S-wave velocity

(b) P-wave velocity

(c) v_p/v_s ratio

(d) Density model

Figure V.21: Results of first-arrival travel-time tomography with Rayfract as well as v_p/v_s ratio and density obtained by eq. V.7.

model 1. However, the structure of the seismic velocities differs clearly. I observe a step like structure at a profile location of 70 - 90 m. For larger profile locations slow seismic velocities between 400 - 550 m/s are also met in larger depths. Furthermore, higher S-wave velocities are obtained at profile locations of 10 - 70 m in the shallow part of the model (0 - 8 m depth).

In a first step the P-wave velocity model for *starting model 2* is the same as for *starting model 1* (see Fig. V.22(b)). The calculated v_p/v_s ratio of *starting model 2* is displayed in Fig. V.22(c). I observe very small values of 1.2 in the shallow part of the model which corresponds to a negative Poisson numbers. Therefore, this part of the model is physically not reasonable. For this reason I modify the v_p model that I obtain at least a v_p/v_s ratio of 1.5 ($v_p > 1.5\ v_s$). It would be also possible to modify the v_s model but due to the high sensitivity of the Rayleigh waves to shear-wave velocities it seems more appropriate to change the v_p model. This is done by checking the v_p/v_s ratio at every grid point and if it is less than 1.5 the P-wave velocity will be increased. The result is displayed in Fig. V.22(d) for the modified v_p/v_s ratio and in Fig. V.22(e) for the modified v_p model. Please note that the differences between the original and the modified v_p/v_s ratios are small and only apparent in the shallow parts of the subsurface models. The density model in Fig. V.22(f) is calculated with eq. V.7 and the modified v_p model.

In Section V.3.2 we investigated the shear-wave velocity and the bulk density for two shallow samples in laboratory measurements. We obtained shear-wave velocities between 200 m/s and 250 m/s as well as 2085 - 2200 kg/m^3 for density. The calculated S-wave velocities for the travel-time tomography results are for shallow depth slightly higher (around 350 m/s), however, the density values are within the same range. I conclude that the starting models are physically feasible in respect to the laboratory measurements of Bauhaus-University Weimar.

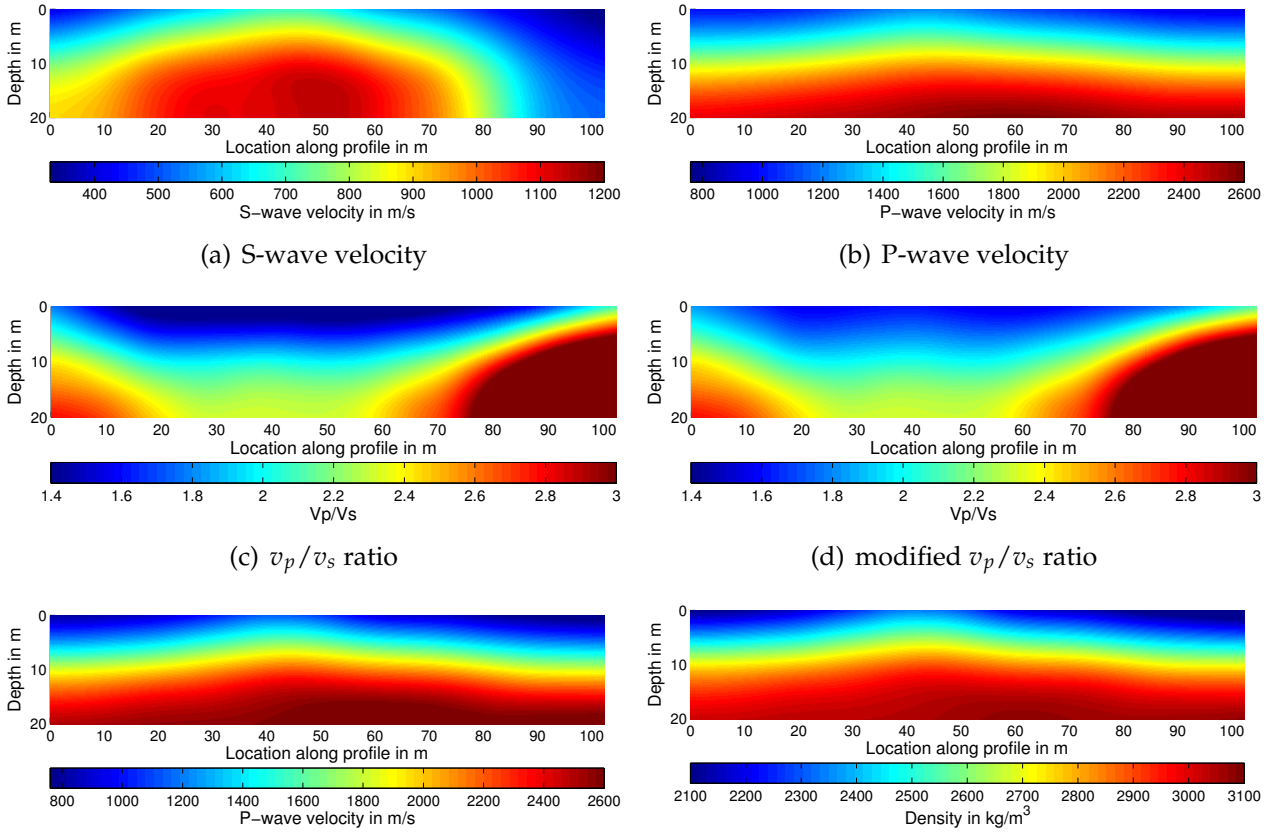

(a) S-wave velocity

(b) P-wave velocity

(c) v_p/v_s ratio

(d) modified v_p/v_s ratio

(e) modified P-wave velocity

(f) density model

Figure V.22: Results of first-arrival travel-time tomography with ReflexW as well as v_p/v_s ratio and density obtained by eq. V.7.

Figs V.23(a) and V.23(b) show a comparison of field data and synthetics generated with *starting model 1* and *starting model 2*, respectively, for the first frequency interval (low-pass filter of 10 Hz) used in the subsequent field-data inversion (Section V.8). For both starting models individual source-wavelet correction filters are estimated with near-offset traces. Obviously there aren't any problems with cycle skipping. Residuals are rather small for near offsets due to the source-wavelet correction but for far-offset traces the differences of both starting models are observable. It seems that both subsurface models are appropriate starting models for the field-data inversion. Therefore, I use both *starting models 1* and *2* for the application of FWI to the field data set Mammolshain in Section V.8.

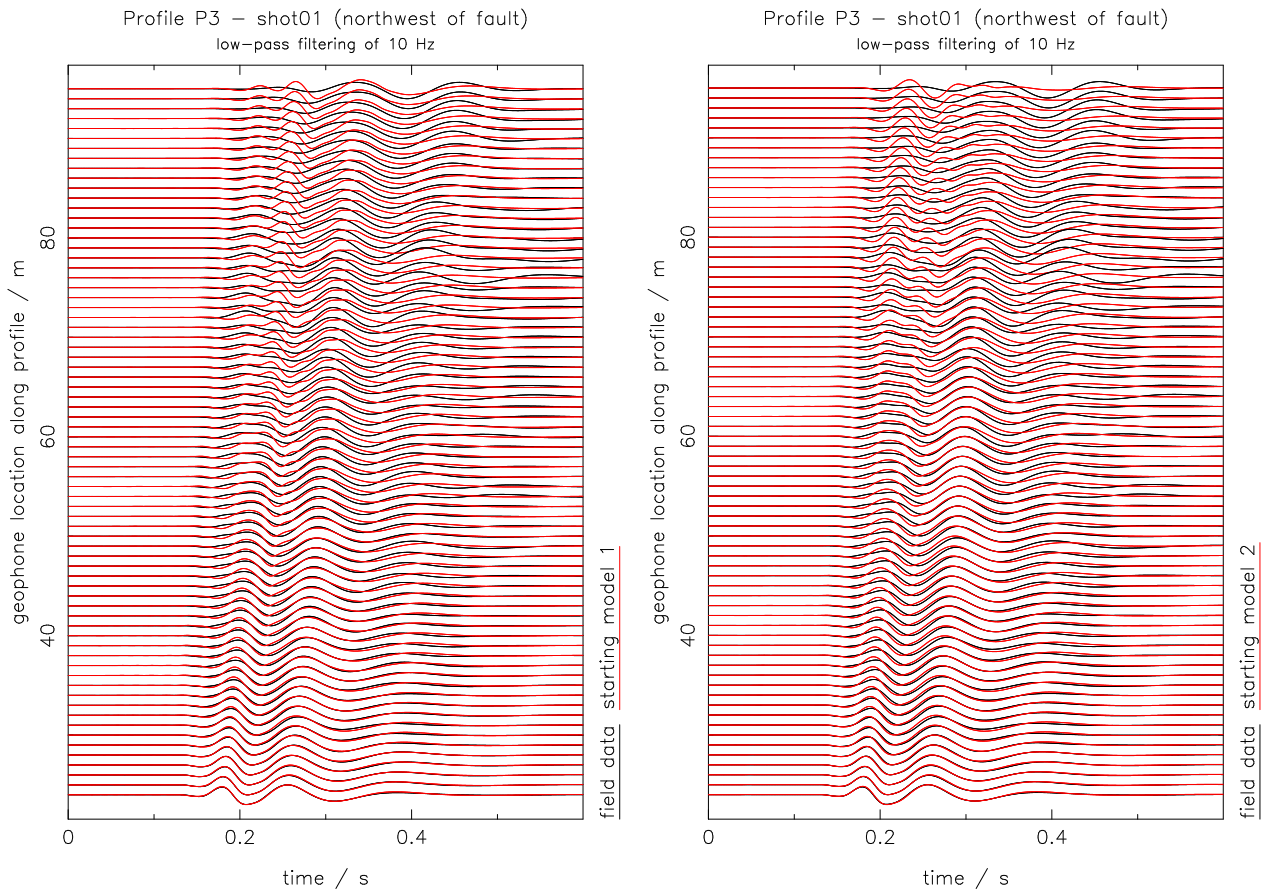

(a) *starting model 1* (b) *starting model 2*

Figure V.23: Common-shot gather of shot01 (northwest of fault, profile meter 0 m) of field data and synthetics generated with (a) *starting model 1* and (b) *starting model 2* for low-pass filtered data of 10 Hz. Individual source-wavelet correction filters are estimated with near-offset traces.

V.8 Application of FWI to Mammolshain field data

Finally, I apply the 2D elastic full-waveform inversion to the shallow-seismic Rayleigh waves recorded at the test-site Mammolshain. I focus on the Profile P3 and Profile P4 because they were set up perpendicular to the faulting and can be considered as 2D data sets. In Section V.8.1 I explain the inversion setup used for all inversion tests of the field data. Sections V.8.2, V.8.3 and V.8.4 focus on the field-data inversion results of Profile P3. In Section V.8.5 I present the inferred subsurface models of Profile P4. Subsequently, the inversion results of both profiles are compared in Section V.8.6. In the last section I discuss identified problems and future work of the inversion with field data (Section V.8.7).

V.8.1 Inversion setup

Our FWI method is based on the adjoint method where the parallelized viscoelastic finite-difference forward modeling and the gradient calculation are performed in the time domain (Chapter II). To increase the convergence speed we use the conjugate gradient direction. Furthermore, I apply preconditioning to the gradients where semi-circular tapers (radius of 2 m) are used at the source locations to avoid strong artifacts. The misfit function is defined by the L2 norm of normalized seismograms in eq. II.50. As this objective function contains normalized seismograms near and far-offset traces contribute equally to the misfit and it is not sensitive to residuals in the amplitude decay with offset. It is, however, sensitive to relative amplitude differences within one seismogram. The relevant parameters for the FD-modeling are given in Table D.3 in the Appendix D. I invert independently for the P-wave and S-wave velocity as well as for density. I use 24 vertical hammer blows as vertical sources and the vertical component of 89 receivers (see Section V.4). Please note that not all traces of every shot are used due to less data quality. Especially near-offset traces are corrupted by clipping and near-field effects.

I apply a multi-scale inversion with frequency filtering (Section II.4.3). Starting with the inversion of strongly low-pass filtered data establishes the long wavelength components of the subsurface model first. Gradually higher frequencies are added to deduce the smaller scale distribution of the material properties in the subsurface subsequently. Actually the data is band-pass filtered using a high-pass filter of 5 Hz applied by the 3D/2D transformation prior to the inversion. This is clearly observable in the amplitude spectrum of Profile P3 displayed in Fig. V.24. Largest amplitudes occur for 8 - 12 Hz. For higher frequencies the amplitudes decrease. Therefore, I start with a fourth-order Butterworth low-pass filter with a corner frequency of 10 Hz and increase the frequency interval in steps of 2 Hz (5 - 10 Hz, 5 - 12 Hz, 5 - 14 Hz,..., 5 - 40 Hz) sequentially. The frequency interval is increased when the relative misfit change in the inversion is less than 0.5 % between the current iteration and the second to last iterations. The minimum number of iterations per frequency interval is 5. The largest frequency interval includes 5 - 40 Hz. All inversion parameters are summed up in Table D.4 in Appendix D.

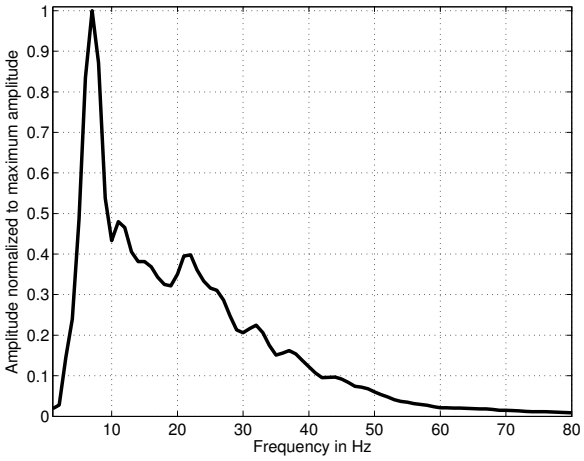

Figure V.24: Mean amplitude spectrum of Profile P3 for all shots and receivers.

Regularization of inversion parameters
1) For all inversion tests I require a minimum v_p/v_s ratio of 1.5 which is checked after every model update to ensure physically feasible subsurface models. This is done by checking the v_p/v_s ratio at every grid point after every model update and if it is less than 1.5 the P-wave velocity will be increased so that $v_p/v_s = 1.5$.

2) The gradients and the models are smoothed with a 2D median filter. I chose a filter length which is unaltered during the inversion. The filter length should be chosen to reduce artifacts smaller than half of the minimum wavelength caused by the ambiguity of the inversion. For all inversions of the field data from the test-site Mammolshain the filter length of the 2D median filter amounts 1 m.

3) The parameter range of density is limited between 1200 kg/m^3 and 3100 kg/m^3 to avoid unrealistic density values (in particular, $\rho < 1000\,\mathrm{kg/m^3}$). Furthermore, I observe large variations in the density model which haven't an influence to the waveforms at all. Therefore, I constrain the density update by scaling the step length α_ρ of the density parameter with a scalar factor of 30 % (Section II.4.2). This approach hasn't neither an influence on the convergence properties nor on the total data misfit. However, it ensures that the density model keeps closer to the initial values which is a reasonable assumption.

V.8.2 Profile P3 - *starting model 2*

In this section I present the inversion results from the test-site Mammolshain of shallow-seismic field data recorded on the Profile P3. As our inversion scheme is based on a local optimization principle the starting model is one of the most crucial points for a successful inversion. Therefore, I have used two starting models to investigate different convergence properties. Both initial P-wave and S-wave velocity models are derived from a travel-time tomography of the first arrivals of P-waves and S-waves, respectively (see Section V.7). *Starting model 2* shows a stronger convergence than *starting model 1* and the inferred subsurface models predict the field data slightly better. It seems that *starting model 2* is more reliable than

starting model 1 for the inversion of the field data recorded on Profile P3. I will describe the differences in detail later on. Therefore, I firstly present the inversion results with *starting model 2* and the results with *starting model 1* subsequently.

In Fig. V.25 the *starting model 2* is plotted. The models are in comparison to Fig. V.22 extended up to a depth of 100 m, but only the topmost 40 m are displayed. I started inversion tests with shallow models up to a depth of 20 m. This ended up in strong artifacts and a poor convergence. For this reason I extended the models to larger depths and I observe a penetration depth of the Rayleigh waves up to 40 m depth during the inversion.

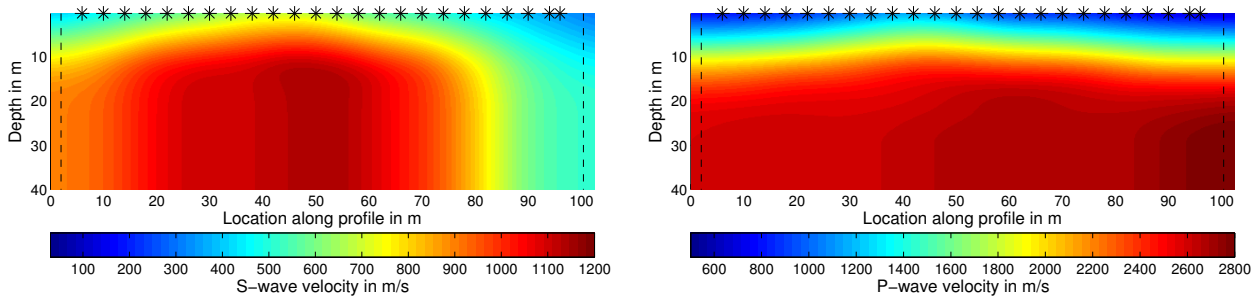

(a) S-wave velocity

(b) P-wave velocity

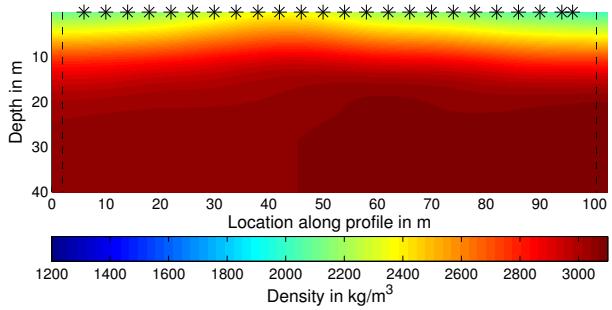

(c) Density

Figure V.25: *Starting model 2* which is extended to a total depth of 100 m. Only the topmost meters up to a depth of 40 m are displayed. Black stars denote the source locations and black dashed lines indicate the absorbing boundaries realized by CPML.

I start the inversion with strongly low-pass filtered data of 10 Hz and increase the frequency interval sequentially in steps of 2 Hz. The evolution of the misfit is shown in Fig. V.26(a). I observe a strong convergence for low frequencies up to 20 Hz. Subsequent the misfit increases with higher frequencies and ends up with the highest misfit value at the highest frequency of 40 Hz used in the inversion. The frequency interval is increased when the relative misfit change in the inversion is less than 0.5 % between the current iteration and the second to last iteration. This unaltered criteria is valid for every frequency interval. However, the number of iteration within one frequency interval can differ due to different convergence properties.

It seems that the misfit cannot be reduced significantly (less than 1-2 % of total signal energy) for higher frequencies (> 20 Hz) and additionally that the inferred subsurface models of the lower frequencies cannot predict the waveforms of higher frequencies. Possible reasons are non-linearities of the objective function at higher frequencies and small-scale heterogeneities

which violate the 2D assumption (see comparison of low-pass filtered data of Profile P3 and P4 in Fig. V.17). In Fig. V.26(b) the evolution of model changes is plotted. RMS values are calculated between the starting model and the current model of each iteration step. The updated models for P-wave velocity and density aren't changing much. For the S-wave velocity a strong change for lower frequencies is observable. For higher frequencies almost no changes are visible. Fig. V.26(c) shows a zoomed in view of evolution of model changes between iteration 60 and 150 for the S-wave velocity. It seems that the model changes are fluctuating and this probably means that the inversion do and undo updates from one iteration to the other iteration. This is also emphasized by strong jumps of used step lengths between iteration 60 and 150. The inversion fails and is trapped in a local minimum.

In Fig. V.27 data misfits of single shots and single receivers for different frequency intervals are shown color-coded. Blue color indicates low misfit values whereas red color shows high misfit values. The colorbar is adapted for all three frequency intervals. The sum of each misfit value results in the total misfit. For the low-pass filtered data of 20 Hz I observe for almost all shots and receivers a small misfit value (see Fig. V.27(a)). Only for shot06 and shot07 for far-offsets trace numbers of 60-89 slightly higher misfit values appear. The total misfit amounts 20 % of total signal energy. The misfits for higher frequencies accumulate with increasing frequency interval in Fig. V.27(b) for 30 Hz and in Fig. V.27(c) for 40 Hz. The total misfit amounts 32 % for the 30 Hz low-pass filtered data and 48 % for the 40 Hz low-pass filter. If I regard the misfit as a measure of how successful an inversion is, it is clear that the inversion of the low-pass filtered data of 20 Hz should be more reliable than the inversion with low-pass filtered data of 30 Hz and 40 Hz. Fig. V.28 shows the comparison of seismograms of the field data and of the inferred subsurface model for three exemplary shots (profile location of 6 m, 50 m and 96 m) of the low-pass filtered data of 20 Hz. Residuals are small along the geophone locations for all shots and receivers. However, there are phases in the synthetics e.g. for shot24 (geophone location: 30 - 65 m, approximately at a recording time of 0.2 s) which aren't present in the field data. Nevertheless, judging from the waveform only we apparently have estimated an appropriate subsurface model during inversion. The misfit is reduced from an initial error of 44 % to 20 % of total signal energy. Comparison for the low-pass filtered data of 30 Hz and 40 Hz are plotted in the Appendix B.1 and B.2. The above addressed phases in the synthetics which aren't present in the field data seems to be amplified and might be a strong indication that the inversion is trapped within a local minimum for higher frequencies.

Judging from the evolution of the misfit and model changes as well as from the waveform residuals I conclude that only the inferred subsurface models up to 20 Hz are appropriate inversions results. For higher frequencies known problems like higher non-linearities of the misfit function and violation of the 2D assumption occur and corrupt a successful full-waveform inversion. These problems of higher frequencies are also observable with *starting model 1* and for the inversion of the field data recorded on Profile P4. Therefore, I discuss in the following only inversion results up to a low-pass frequency of 20 Hz.

In Fig. V.29 the FWI results for the S-velocity, P-velocity and density, respectively, are plotted with the some colorbar as for the starting model in Fig. V.25. The corresponding seismograms of field data and the synthetics for 20 Hz low-pass filtered data are shown in Fig. V.28. As seen in Fig. V.26(b) the largest changes are observable for the S-wave velocity. The changes for P-wave velocity and density are rather small and they don't have a strong impact on the

waveform of the dominant Rayleigh waves present in the field data. This is investigated by a synthetic forward simulation study where I have used combinations of inferred subsurface models and starting models.

The inferred subsurface model for the S-wave velocity shows a dominant 2D structure of the subsurface. On the left side of the profile (0 - 50 m) I observe a heterogeneous model which is characterized by shallow small-scale structures and comparative slow seismic velocities. The penetration depth of the Rayleigh waves is obviously around 40 m. For larger depths the inferred subsurface model is not changed relative to the starting model. A significant horizon of the upper edge of the weathering zone of the sericite-gneiss isn't observable. The transition from sediments to sericite-gneiss is more characterized by larger velocities in larger depths, but a high contrast structure isn't present. At profile locations of 50 - 80 m also high S-velocities are observable in shallow depth. For the right side of the profile I observe similar S-velocities for the half space in comparison to the left side of the profile, however, in shallow depth of 0 - 20 m very slow S-velocities are inferred by the inversion.

To investigate the process of the inversion with frequency filtering I show in Fig. V.30 the inferred subsurface models for the S-wave velocity of 10 Hz and 20 Hz low-pass filtered data. The inferred subsurface model for 10 Hz low-pass filtered data shows already the gross features of the final subsurface model which clearly proves the expectations for starting with low frequencies. By adding higher frequencies to the inversion small-scale heterogeneities are deduced, however, the gross 2D structure is established, too.

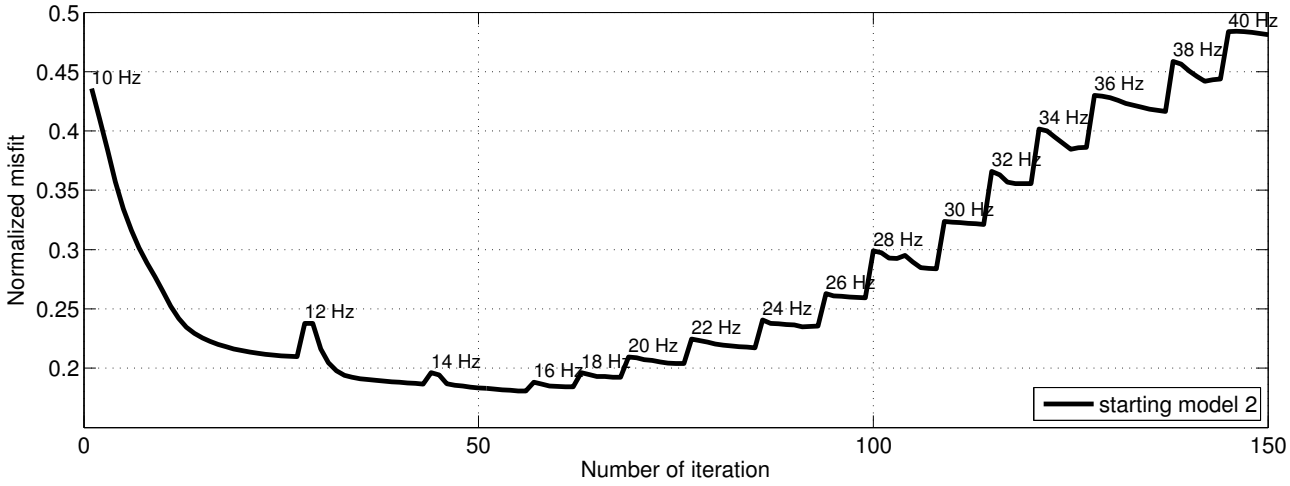

(a) Data misfit evolution.

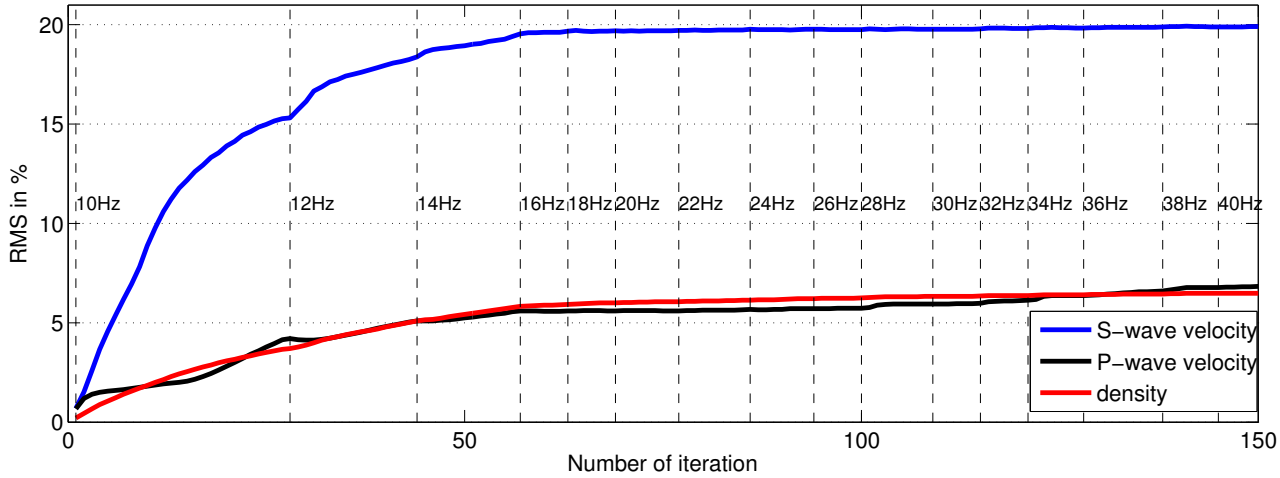

(b) Model change evolution

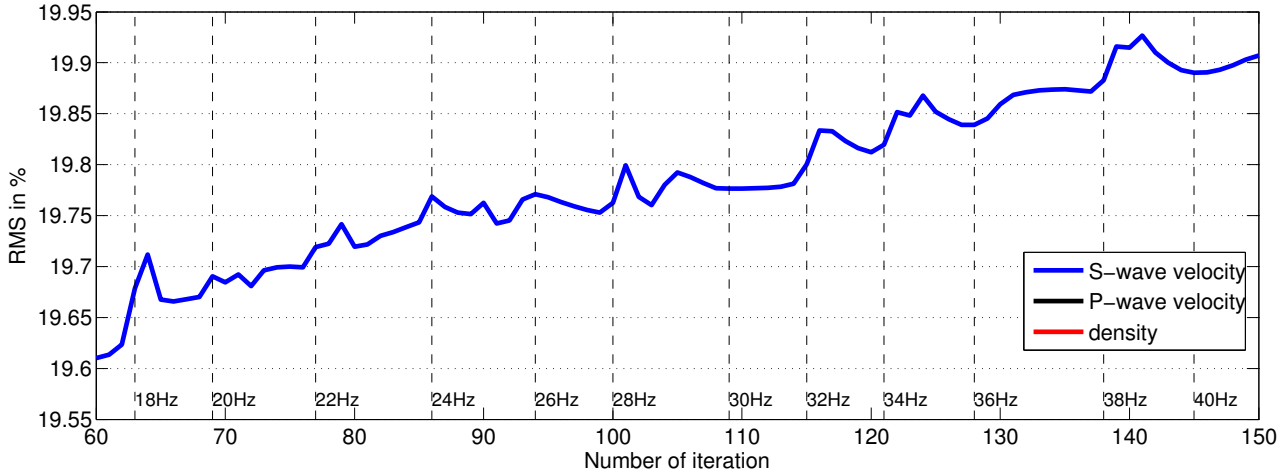

(c) Zoomed in evolution of model change between iteration 60 and 150

Figure V.26: (a) displays the evolution of data misfit calculated with eq. II.50 during FWI of Profile P3 with *starting model 2*. (b) displays the RMS value between the starting model and the current model of each iteration. (c) shows a zoomed view of evolution of model change between iteration 60 and 150. The numbers within the figures show the upper corner frequency of the frequency interval. For each frequency bandwidth a new source-wavelet correction filter per shot is estimated.

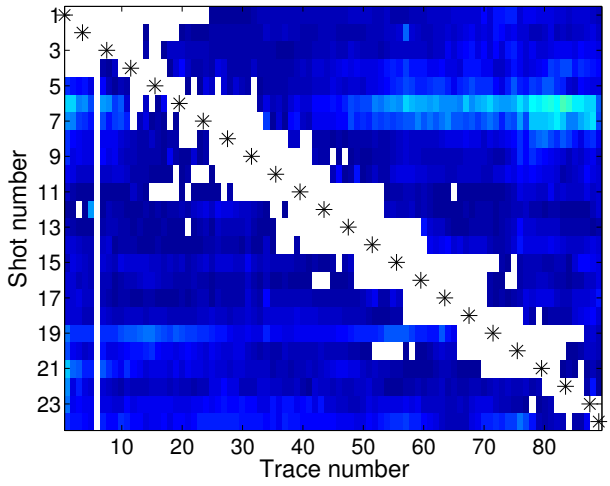

(a) Low-pass filter of 20 Hz

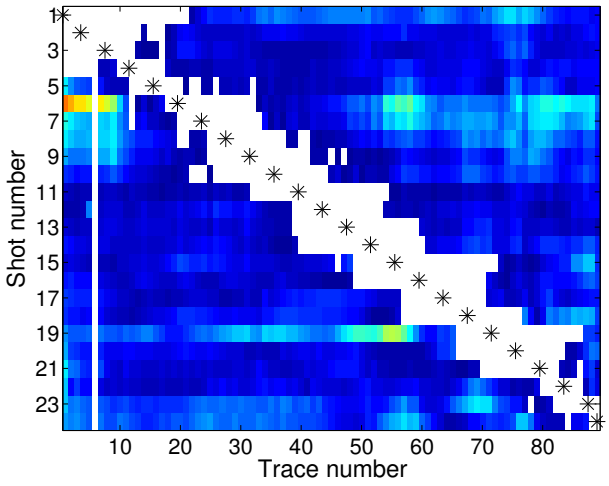

(b) Low-pass filter of 30 Hz

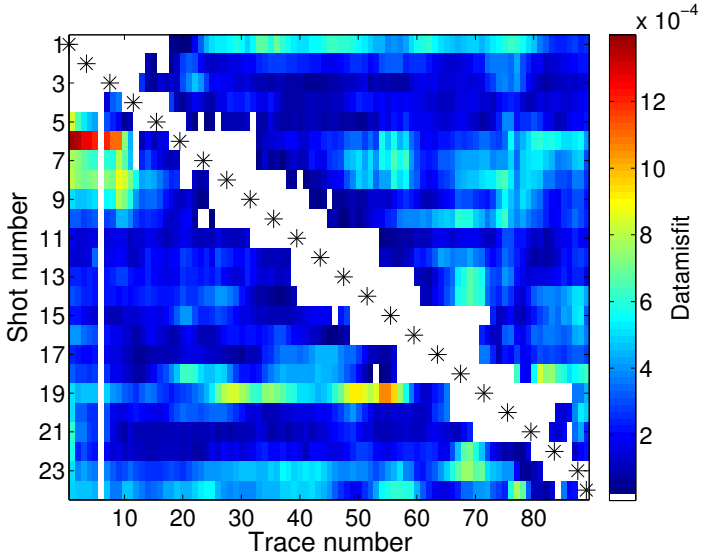

(c) Low-pass filter of 40 Hz

Figure V.27: Data misfit of single shots and single receivers for different frequency intervals with *starting model 2* after FWI. The sum of each misfit value results in the total misfit: (a) low-pass filter of 20 Hz - The total misfit amounts to 20 % of total signal energy, (b) low-pass filter of 30 Hz - 32 % of total signal energy and (c) low-pass filter of 40 Hz - 48 % of total signal energy. Source locations are marked with black stars. Clipped or corrupted traces (in particular near-field effects) are plotted in white and aren't considered within the misfit calculation as well as in the inversion.

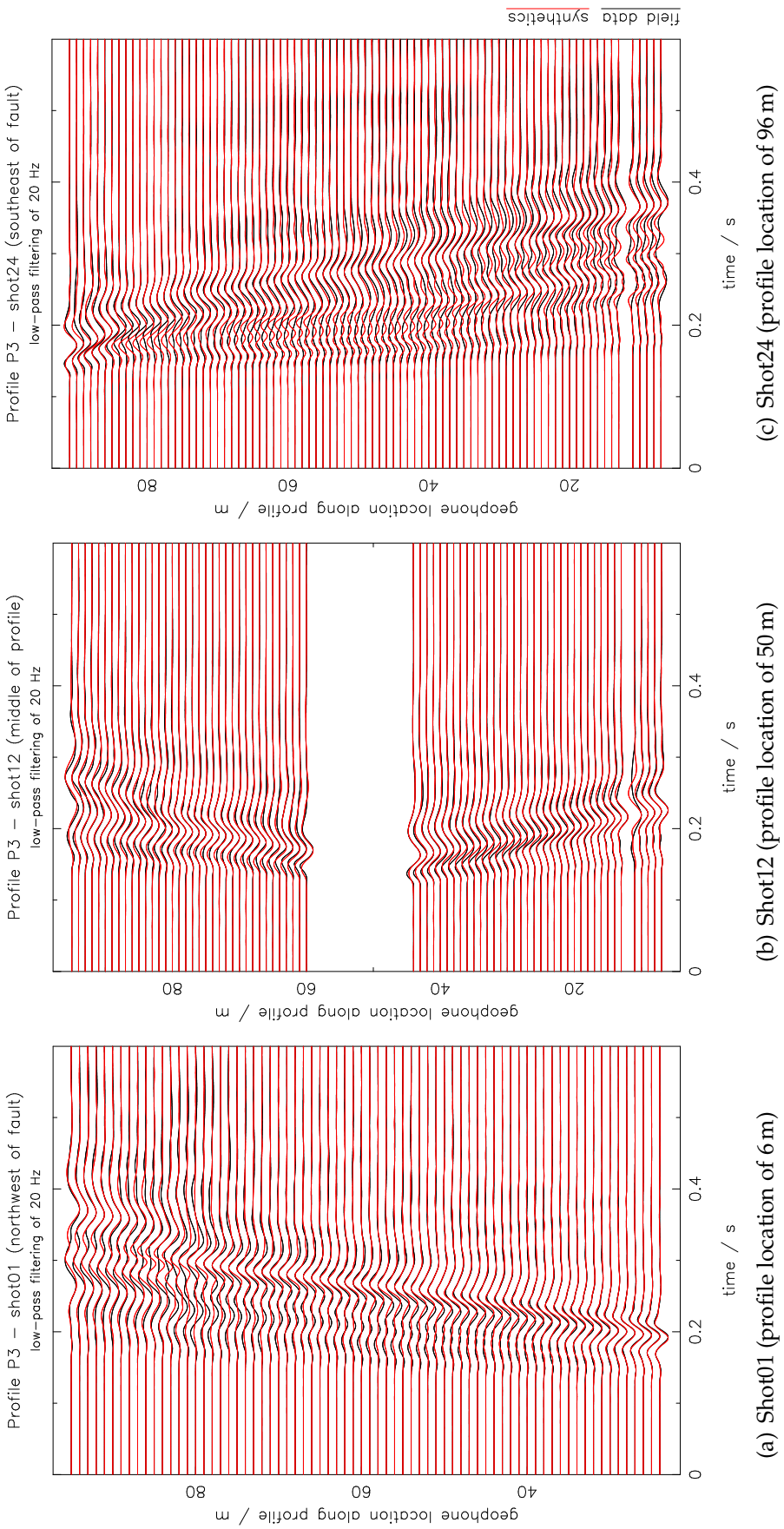

(a) Shot01 (profile location of 6 m) (b) Shot12 (profile location of 50 m) (c) Shot24 (profile location of 96 m)

Figure V.28: Comparison of field data (black solid line) and synthetics (red solid line) for low-pass filtered data of 20 Hz of Profile P3 with *starting model 2* after FWI. Displayed are vertical particle displacement seismograms. The corresponding inversion result is shown in Fig. V.29. Each trace is normalized to its maximum amplitude.

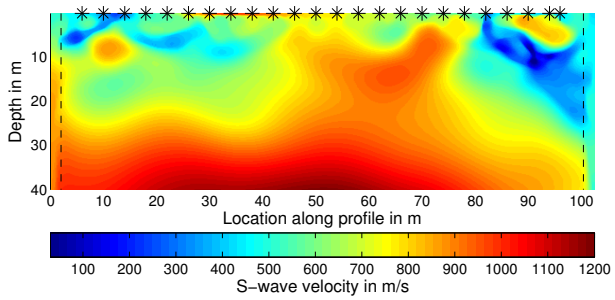

(a) S-wave velocity

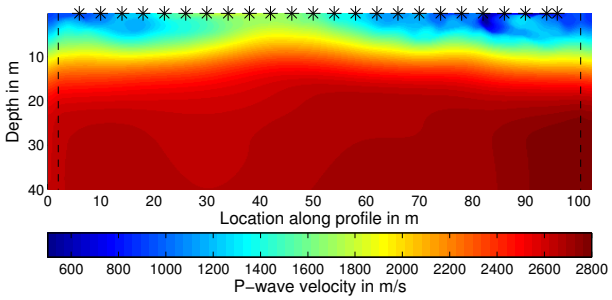

(b) P-wave velocity

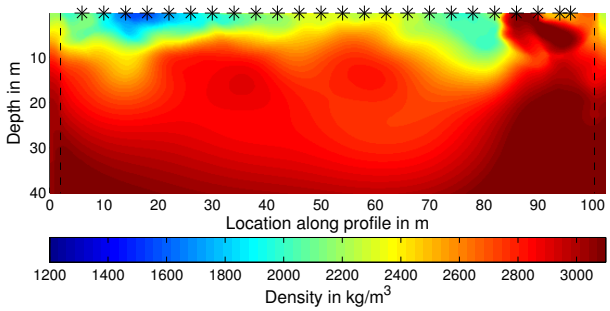

(c) Density

Figure V.29: FWI result of (a) S-wave velocity model, (b) P-wave velocity model and (c) density model of Profile P3 for *starting model 2* and for low-pass filtered data of 20 Hz. Black stars denote the source locations and black dashed lines indicate the absorbing boundaries with CPML.

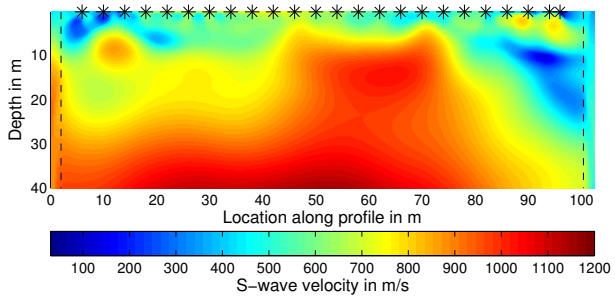

(a) Low-pass filter of 10 Hz

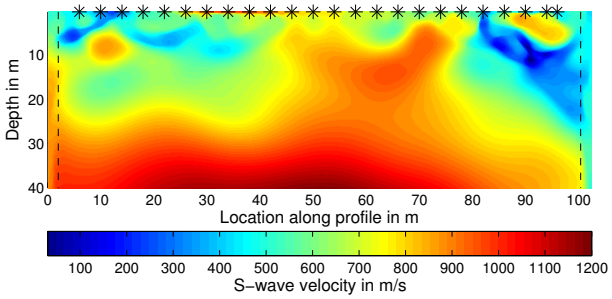

(b) Low-pass filter of 20 Hz

Figure V.30: Evolution of model change with frequency filtering for the S-wave velocity model between 10 Hz and 20 Hz for Profile P3 and with *starting model 2*.

V.8.3 Profile P3 - *starting model 1*

In this section I deal again with the shallow-seismic field data from Mammolshain recorded on Profile P3. This time I present the 2D FWI results with *starting model 1*. The following inversions run with the same parameter settings like frequency filtering, smoothing, minimum v_p/v_s ratio and so on as used in the previous section. The number of iterations can differ due to different convergence properties. The discussed problems of higher frequencies (> 20 Hz) in the inversion are also observable with *starting model 1*. Therefore, I discuss only the inversion results up to 20 Hz.

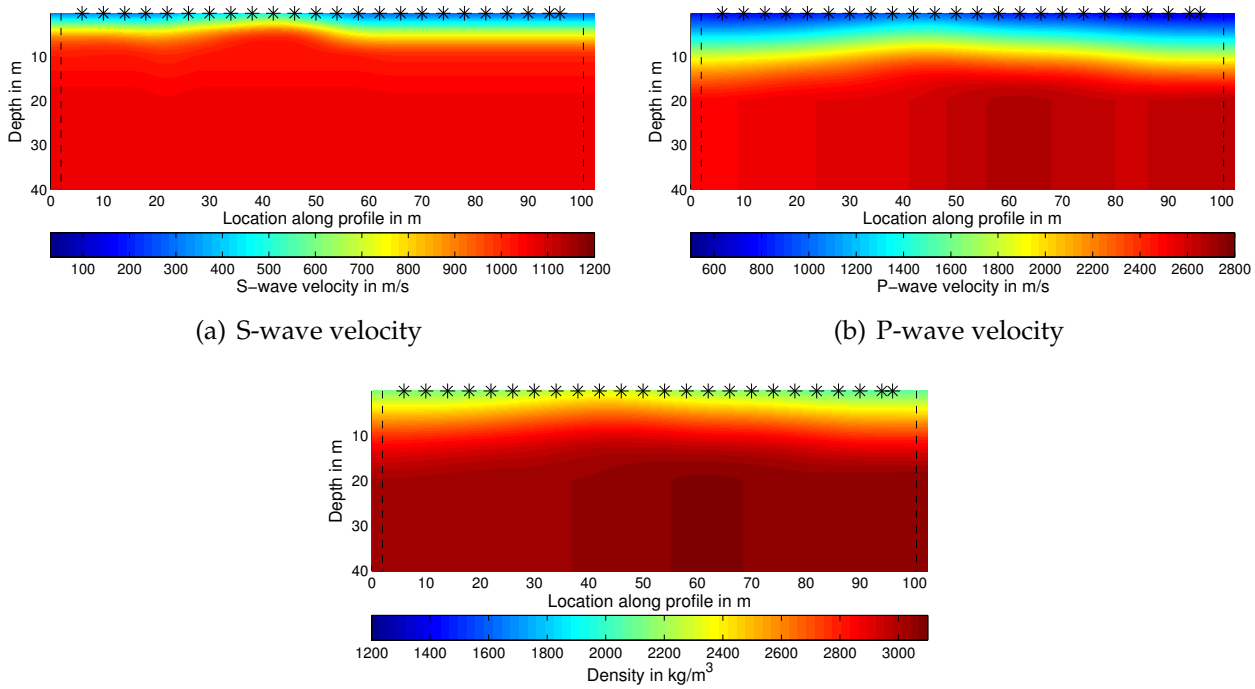

(a) S-wave velocity

(b) P-wave velocity

(c) Density

Figure V.31: *Starting model 1* which is extended to a total depth of 100 m. Only the topmost meters up to a depth of 40 m are displayed. Black stars denote the source locations and black dashed lines indicate the absorbing boundaries with CPML.

In Fig. V.31 the starting models for S-velocity, P-velocity as well as density are plotted. The starting models are extended up to a depth of 100 m in the same way as for *starting model 2* but only the topmost 40 m are displayed due to the limited penetration depth of the Rayleigh waves. Fig. V.32 shows the evolution of data misfit during FWI with *starting model 1*. The misfit is reduced from an initial error of 40 % to around 30 % of total signal energy. Additionally, I have added the misfit history of the inversion with *starting model 2* for comparison. The final data misfit is around 10 % larger than for *starting model 2* at the end of the inversion. Furthermore, the convergence is obviously less because the inversion calculates 32 iteration steps more than with *starting model 2* for the same frequency intervals.

Fig. V.33 shows data misfits of single shots and single receivers color-coded. Blue color indicates low misfit values whereas red color shows high misfit values. For comparison the

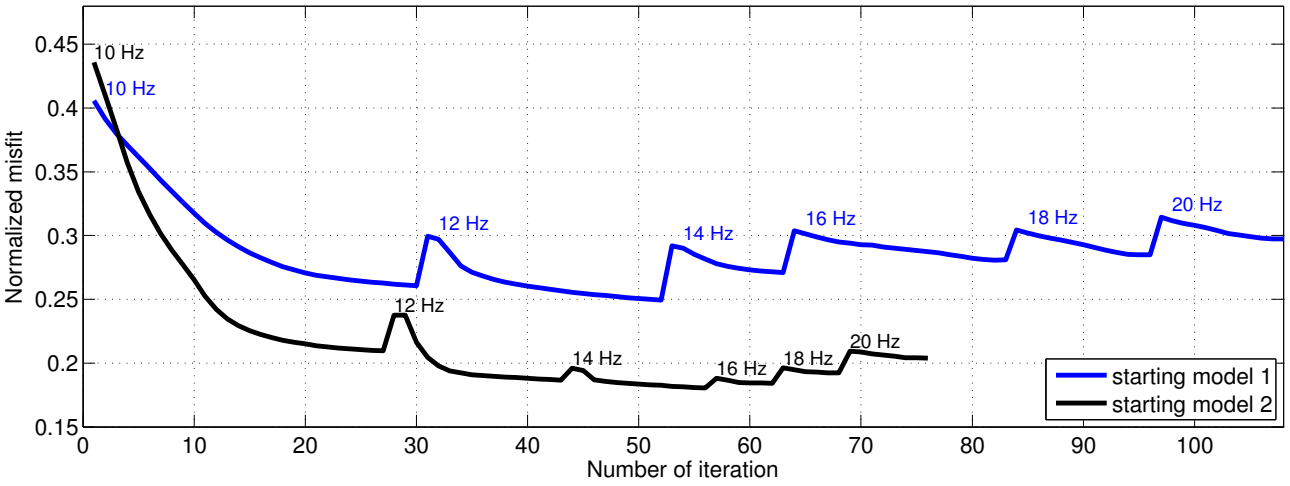

Figure V.32: Comparison of evolution of data misfit calculated with eq. II.50 during FWI of Profile P3 with *starting model 1* and *starting model 2* up to a low-pass frequency of 20 Hz. For each frequency interval a new source-wavelet correction filter per shot is estimated.

colorbar is adapted to Fig. V.27. The sum of each misfit value results in the total misfit. The misfit values are for all shots and receivers slightly larger in comparison to *starting model 2* (Fig. V.27(a)) which is also reflected in the total misfit. Fig. V.34 shows the comparison of seismograms of the field data and of the inferred subsurface model for three exemplary shots (profile location of 6 m, 50 m and 96 m) of 20 Hz low-pass filtered data. Clear residuals are observable along the geophone locations for all shots and receivers. However, the main phases are well predicted by the inferred subsurface model, but there are obvious phases which aren't present in the field data. Shot12 in the middle of the profile shows quite small residuals in comparison to shot01 and shot24. A consistent observation that shots within the profile are better predicted than shots at the end of the profile isn't apparent (compare Fig. V.33).

Judging from the data misfit and the waveform residuals the inversion apparently has estimated a subsurface model which indeed predicts the main phases of field data quite well but also produces significant artifacts along the geophone locations. In Fig. V.35 the FWI results for the S-velocity, P-velocity and density, respectively, are plotted with the same colorbar as for the starting model in Fig. V.31 and the inversion results with *starting model 2* (Fig. V.29). The gross features of the inversion results for S-wave velocity, the P-wave velocity and the density look quite similar to the inversion results inferred with *starting model 2*. A detailed discussion about the differences is shown in the following section.

V.8.4 Discussion - Profile P3

In the two previous sections I presented two individual 2D FWI results of the field data Mammolshain recorded on the Profile P3 with two different starting models. Both inversions show different convergence properties: *starting model 1* calculates 32 iterations more and ends up in a significantly larger (10 %) data misfit. For higher frequencies (> 20 Hz) both inversions fail and there are strong indications that the inversions are trapped in a local

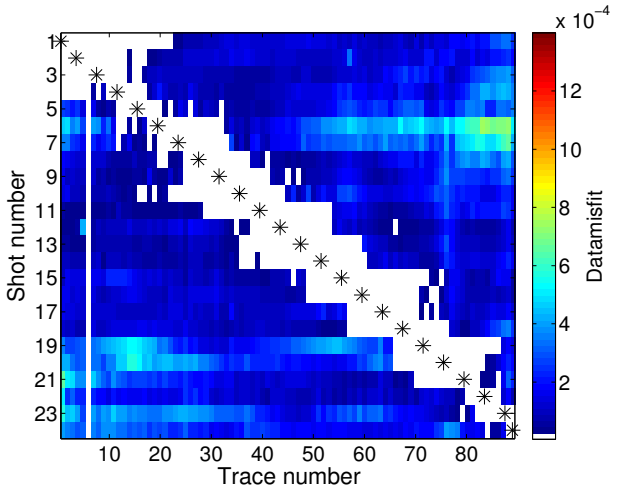

Figure V.33: Data misfit of single shots and single receivers for Profile P3 with *starting model 1* for 20 Hz low-pass filtered data after FWI. The sum of each misfit value results in the total misfit (29 % of total signal energy). Source locations are marked with black stars. Clipped or corrupted traces (e.g. near-field effects) are plotted in white and aren't considered within the misfit calculation as well as in the inversion. For comparison the colorbar is adapted to Fig. V.27.

minimum. The gross features of the inversion results for P-wave velocity and density look quite similar to each other. Indeed this is also the case for S-wave velocity, however, they differ in some details. As I mentioned in Section V.8.2 the P-wave velocity and the density aren't constrained strongly by the waveform of the dominant Rayleigh waves present in the field data. Therefore, the small differences between the S-velocity models are mainly responsible for the significant data residuals present at the end of the inversion with *starting model 1*. To investigate the differences of the S-velocity models in more detail I plotted in Fig. V.36 both starting models and FWI results and additionally three vertical velocity profiles at profile locations of 11 m, 33 m and 60 m. Surprisingly the velocity profiles of the left side (profile location of 11 m) show nearly the same velocity distribution with depth for both inversions. There exists a small high-velocity anomaly in both FWI results. For profile location of 33 m the profiles differ mainly in the shallow depth of 0 - 4 m. Both FWI results of these two profiles differ clearly from their initial velocities of the starting models. For profile locations between 50 m and 80 m the FWI results differ mostly (besides on the right boundary of the models). FWI result of *starting model 1* for profile location of 60 m is nearly the same as the starting model itself. Only in the shallow depth it differs from it. The final model 2 of *starting model 2* is changed during the inversion significantly which is observable at the vertical velocity profile of 60 m. The differences at the right boundary (85 m - 100 m) of both models can be hardly interpreted. For both FWI results slow seismic S-velocities are deduced up to a depth of 30 m. But there are also a lot of discrepancies between both. An additional field survey with an extension of the profile lengths could improve the wave path coverage in this region of interest. Finally, it is difficult to access why the final model 2 predicts the field data in some way better than final model 1. In total they show both the same gross features of the subsurface and therefore, support each other for a more reliable FWI result of Profile P3.

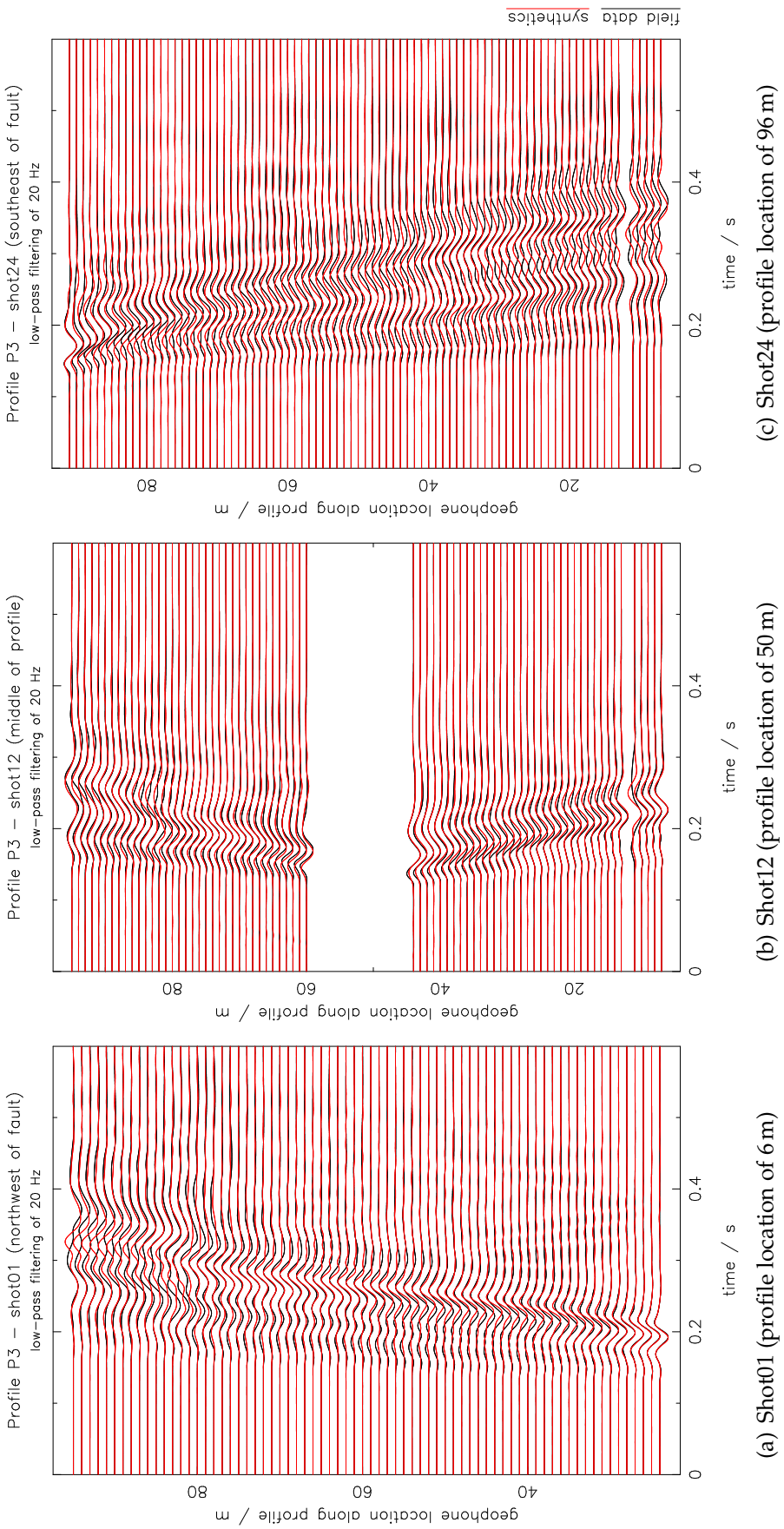

(a) Shot01 (profile location of 6 m)

(b) Shot12 (profile location of 50 m)

(c) Shot24 (profile location of 96 m)

Figure V.34: Comparison of field data (black solid line) and synthetics (red solid line) for low-pass filtered data of 20 Hz of Profile P3 with *starting model 1* after FWI. Displayed are vertical particle displacement seismograms. The corresponding inversion result is shown in Fig. V.35. Each trace is normalized to its maximum amplitude.

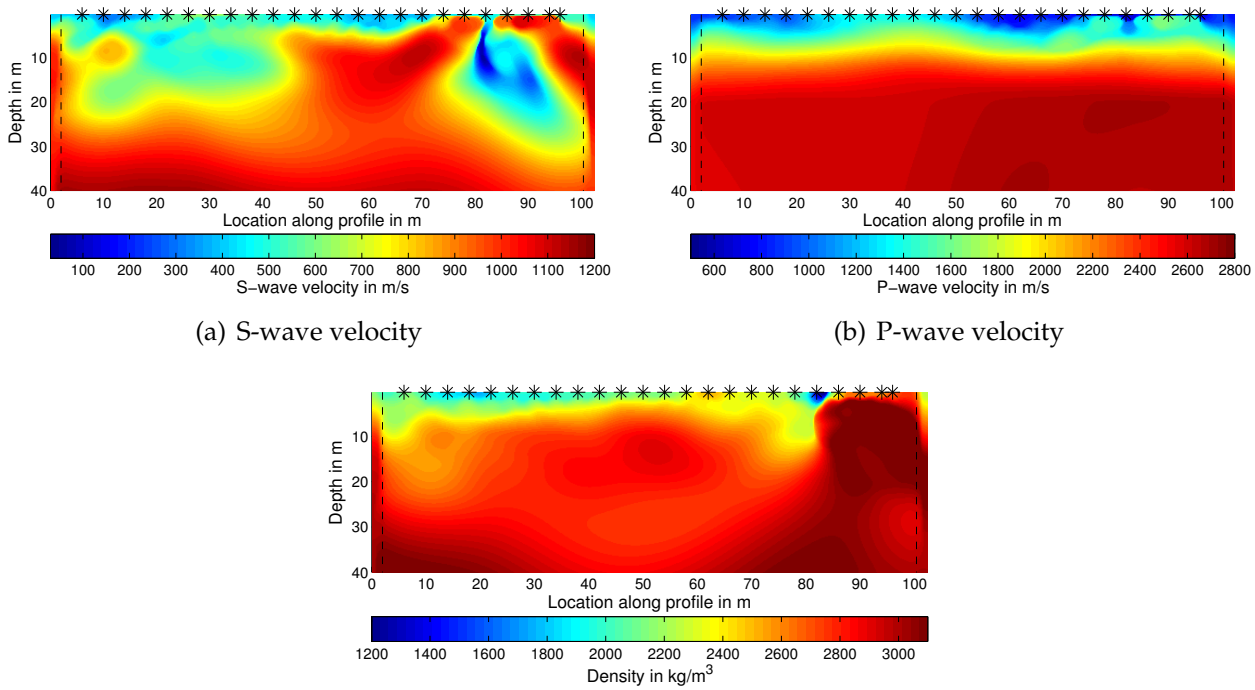

(a) S-wave velocity

(b) P-wave velocity

(c) Density

Figure V.35: FWI result of (a) S-wave velocity model, (b) P-wave velocity model and (c) density model of Profile P3 for *starting model 1* and for low-pass filtered data of 20 Hz. Black stars denote the source locations and black dashed lines indicate the absorbing boundaries with CPML.

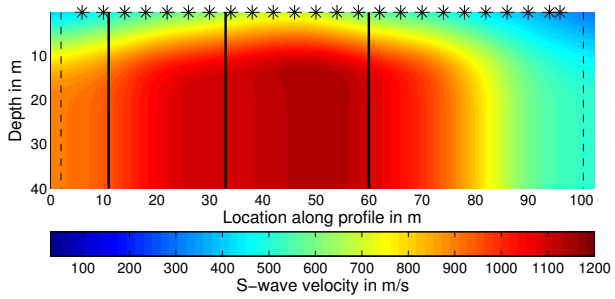

(a) *starting model 2*

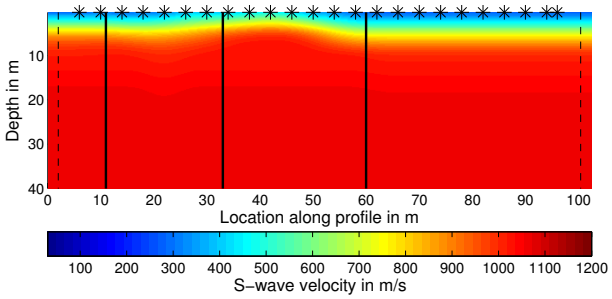

(b) *starting model 1*

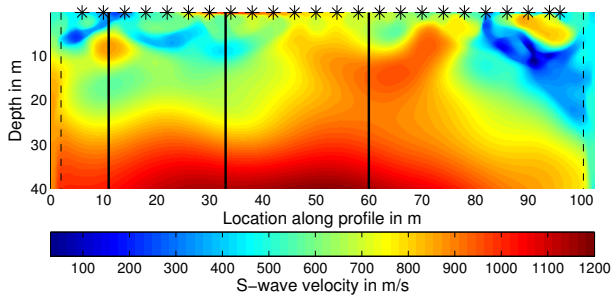

(c) final model 2

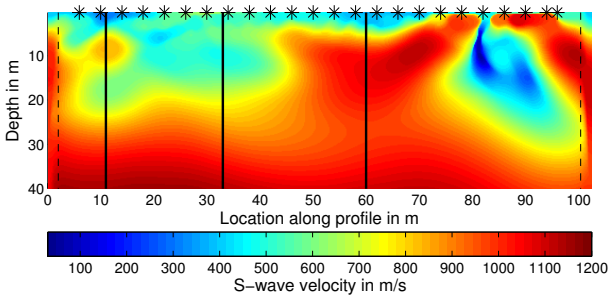

(d) final model 1

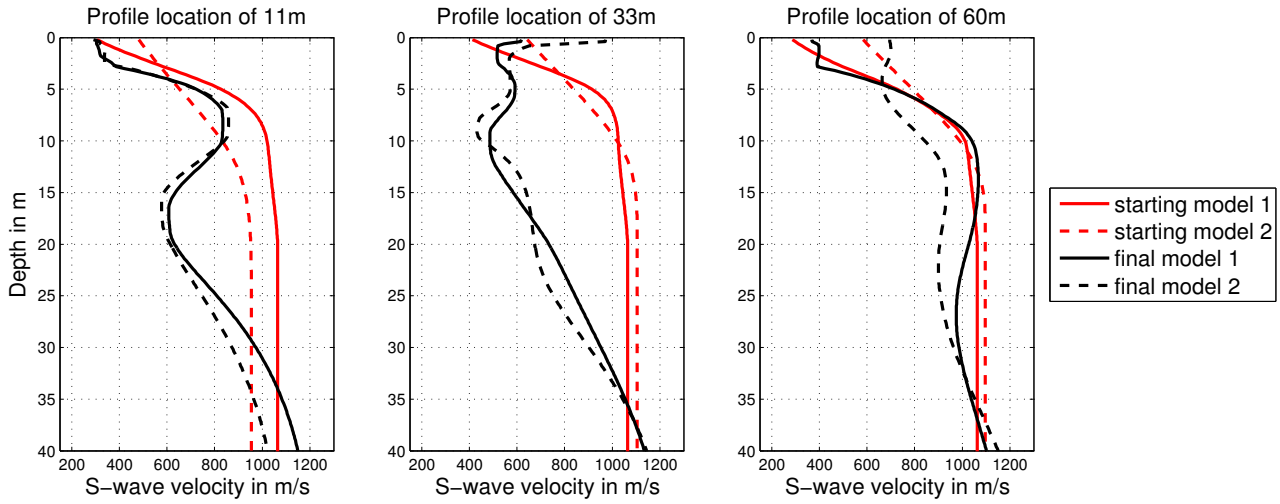

(e) vertical velocity profiles

Figure V.36: Starting models and FWI results of Profile P3 for the S-wave velocity. (a) displays *starting model 2* and (b) *starting model 1*. (c) shows the inversion result with *starting model 2* and (d) with *starting model 1*. Three vertical velocity profiles are plotted in (e). Red lines indicate the starting models and black lines the final models. Black stars in (a) to (d) denote the source locations and black dashed lines indicate the absorbing boundaries with CPML.

V.8.5 Profile P4 - *starting model 1* and *2*

In this section I present the full-waveform inversion results from the test-site Mammolshain of shallow-seismic field data recorded on the Profile P4 (see Fig. V.14). The following inversions run with the same parameter settings like frequency filtering, smoothing and so on. Furthermore, the *starting models 1* and *2* are exactly the same as for Profile P3. However, due to different data quality the trace killing differs from that applied for Profile P3 slightly. For higher frequencies than 20 Hz I observe the same described problems than for Profile P3. Therefore, I discuss only the FWI results up to 20 Hz.

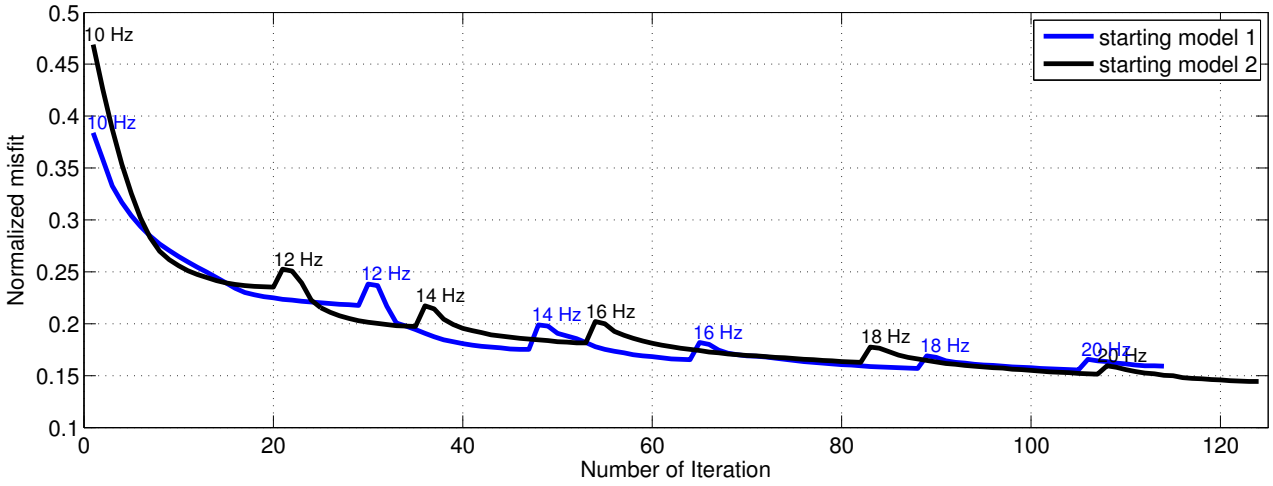

Figure V.37: Comparison of evolution of data misfit calculated with eq. II.50 during FWI of Profile P4 with *starting model 1* and *starting model 2* up to a low-pass frequency of 20 Hz. For each frequency interval a new source-wavelet correction filter per shot is estimated.

In Fig. V.37 the misfit evolution of the inversion with *starting model 1* and *2* is displayed. Surprisingly the inversions for both starting models show almost the same convergence properties why I discuss both results within one section. The misfit is reduced from an initial error of 38 % and 47 % to around 16 % and 14 % of total signal energy for *starting model 1* and *2*, respectively.

Fig. V.38 shows data misfits of single shots and single receivers color-coded. Blue color indicates low misfit values whereas red color shows high misfit values. For comparison the colorbar is adapted to the global minimum and maximum value of each other. The sum of each misfit value results in the total misfit. The misfit values for some shots and receivers are slightly larger of *starting model 1* (e.g. shot08) in comparison to *starting model 2* which is also reflected in the total data-misfit difference of 2 %. Fig. V.39 and Fig. V.40 show the comparison of seismograms of the field data and of the inferred subsurface model for three exemplary shots (profile location of 6 m, 50 m and 96 m) of 20 Hz low-pass filtered data with *starting model 1* and *starting model 2*, respectively. The residuals for both starting models are small for all geophone and shot locations. Obviously the two inferred subsurface models predict the field data equally well. This is emphasized by a comparison of waveforms produced by these two inferred subsurface models in the Appendix C.1.

Judging from the final data misfit and the waveform residuals FWI has apparently inferred

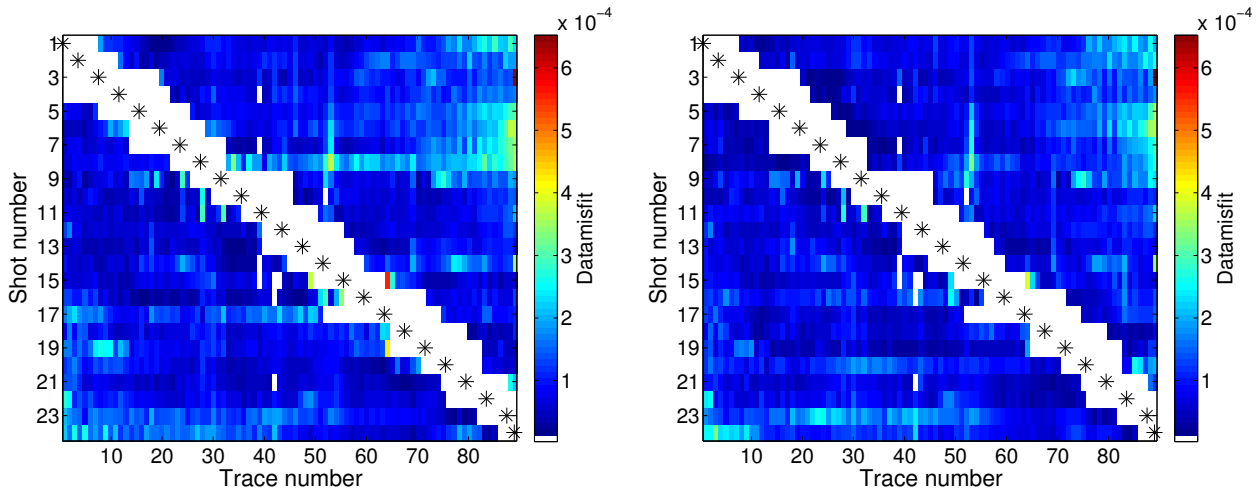

(a) *starting model 1* (b) *starting model 2*

Figure V.38: Data misfit of single shots and single receivers for Profile P4 with (a) *starting model 1* and (b) *starting model 2* for 20 Hz low-pass filtered data after FWI. The sum of each misfit value results in the total misfit: 16 % of total signal energy for *starting model 1* and 14 % for *starting model 2*. Source locations are marked with black stars. Clipped or corrupted traces (e.g. near-field effects) are plotted in white and aren't considered within the misfit calculation as well as in the inversion. For comparison the colorbar is adapted to the global minimum and maximum value of each other.

two appropriate subsurface models which both predict the field data equally well. Figs V.41 and V.42 display the starting and inferred subsurface models with *starting model 1* and *2*, respectively. The inferred subsurface models for all inversion parameters resemble each other in the gross features. Nevertheless, this emphasizes that our inversion scheme is based on a local optimization principle and shows the ambiguity of the inversion problem. It seems that both inversions end up in local minima which are close to each other. The inferred P-wave velocity models differ only slightly from their inital models which emphasizes that the P-wave velocity isn't constrained strongly by the Rayleigh waves present in field data. In spite of the regularized update of density the inferred subsurface model shows large variations. Regions of low and high density values correlate with slow and high S-wave velocities in the shallow depth for both starting models, respectively. The inferred S-wave velocity models are quite similar to each other in spite of the different starting models. The largest differences are observable in the vicinity of the model boundaries. The wave path coverage is expected to be low at the boundaries and shows the ambiguity of the inversion in this part of the subsurface models.

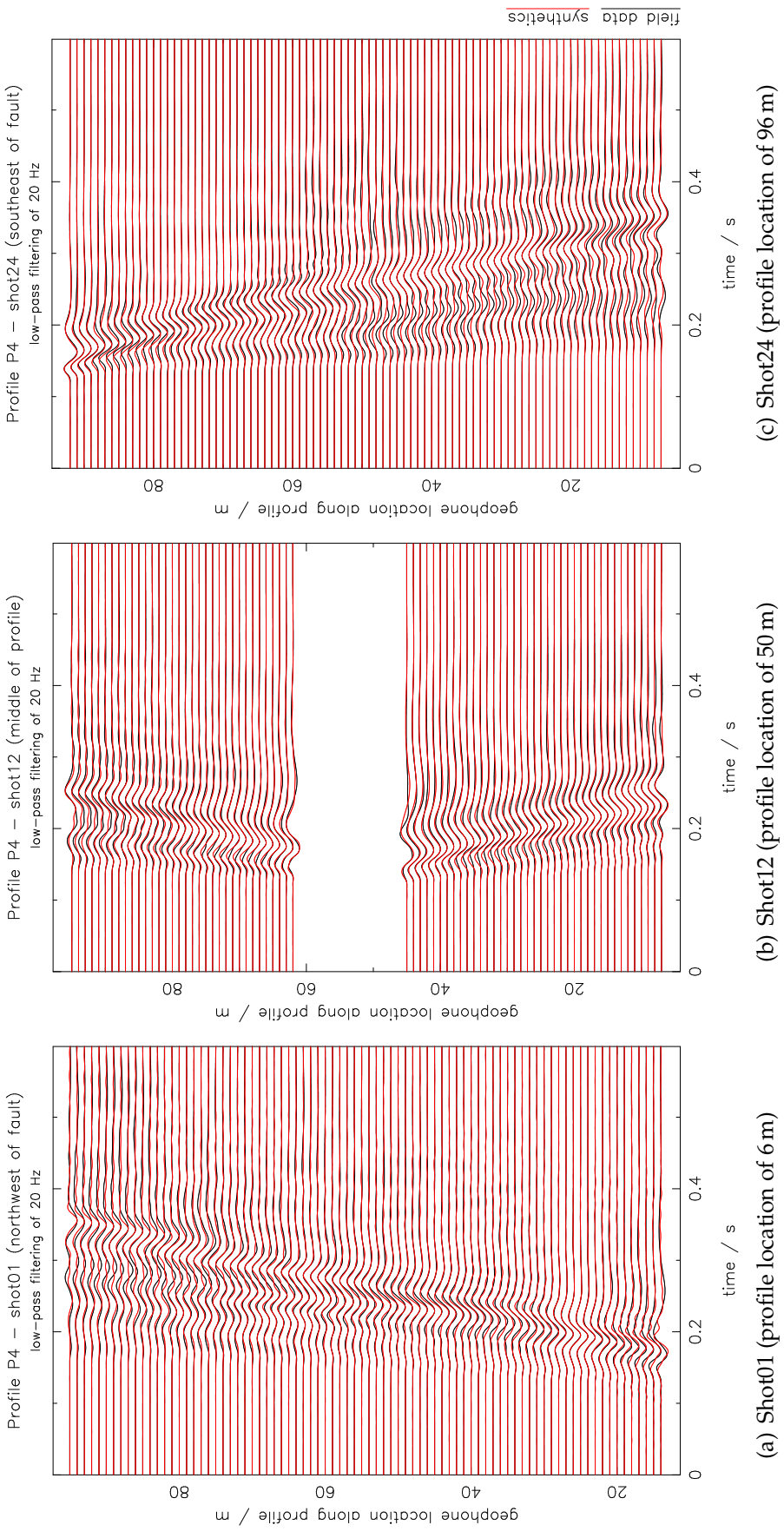

(a) Shot01 (profile location of 6 m) (b) Shot12 (profile location of 50 m) (c) Shot24 (profile location of 96 m)

Figure V.39: Comparison of field data (black solid line) and synthetics (red solid line) for low-pass filtered data of 20 Hz of Profile P4 with *starting model 1* after FWI. Displayed are vertical particle displacement seismograms. The corresponding inversion result is shown in Fig. V.41. Each trace is normalized to its maximum amplitude.

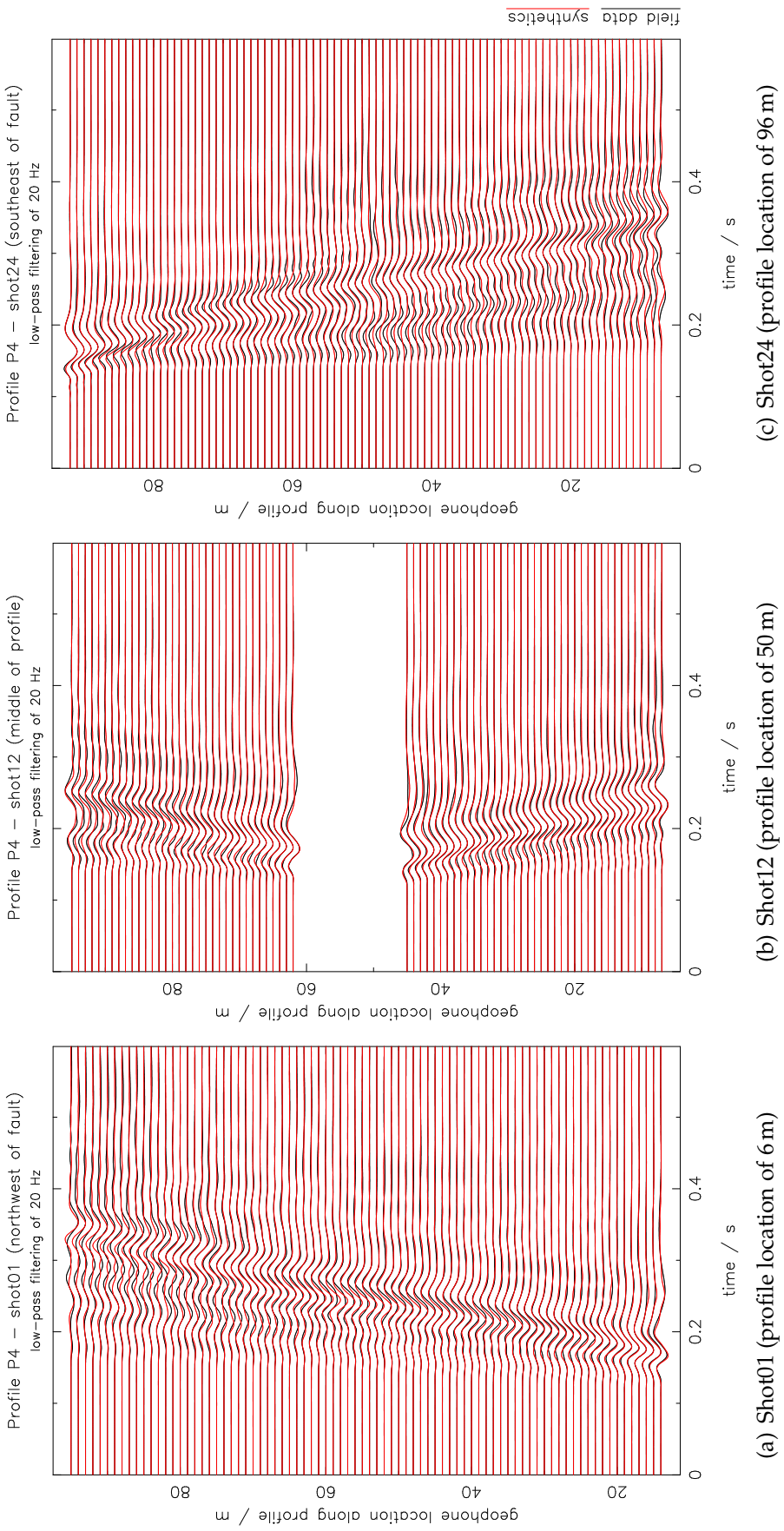

(a) Shot01 (profile location of 6 m)

(b) Shot12 (profile location of 50 m)

(c) Shot24 (profile location of 96 m)

Figure V.40: Comparison of field data (black solid line) and synthetics (red solid line) for low-pass filtered data of 20 Hz of Profile P4 with *starting model 2* after FWI. Displayed are vertical particle displacement seismograms. The corresponding inversion result is shown in Fig. V.42. Each trace is normalized to its maximum amplitude.

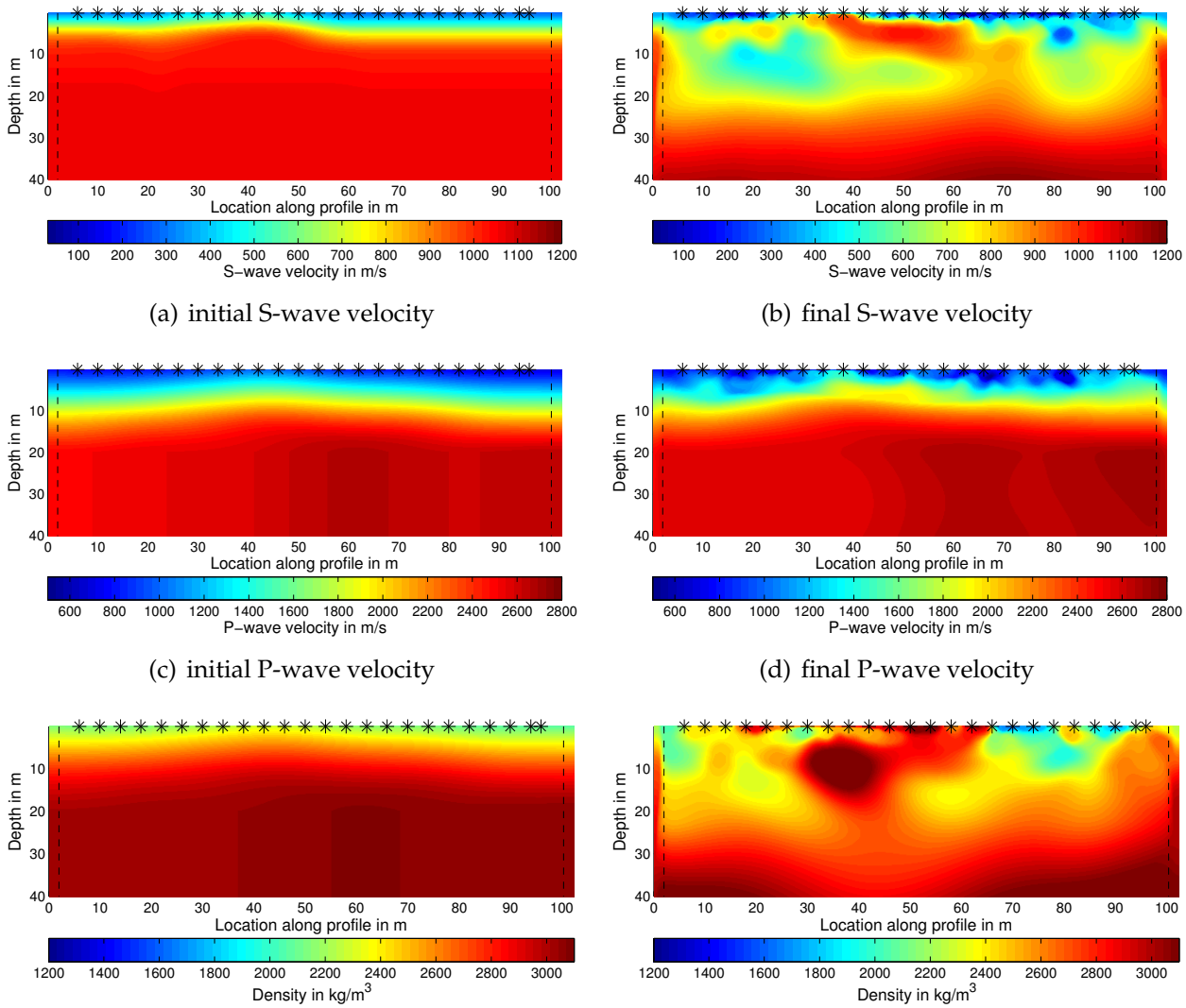

(a) initial S-wave velocity

(b) final S-wave velocity

(c) initial P-wave velocity

(d) final P-wave velocity

(e) inital density model

(f) final density model

Figure V.41: *Starting model 1* and inferred models by 2D FWI of Profile P4 for low-pass filtered data of 20 Hz. (a,b) display the S-wave velocity models, (c,d) the P-wave velocity models and (e,f) the density models. Black stars denote the source locations and black dashed lines indicate the absorbing boundaries with CPML.

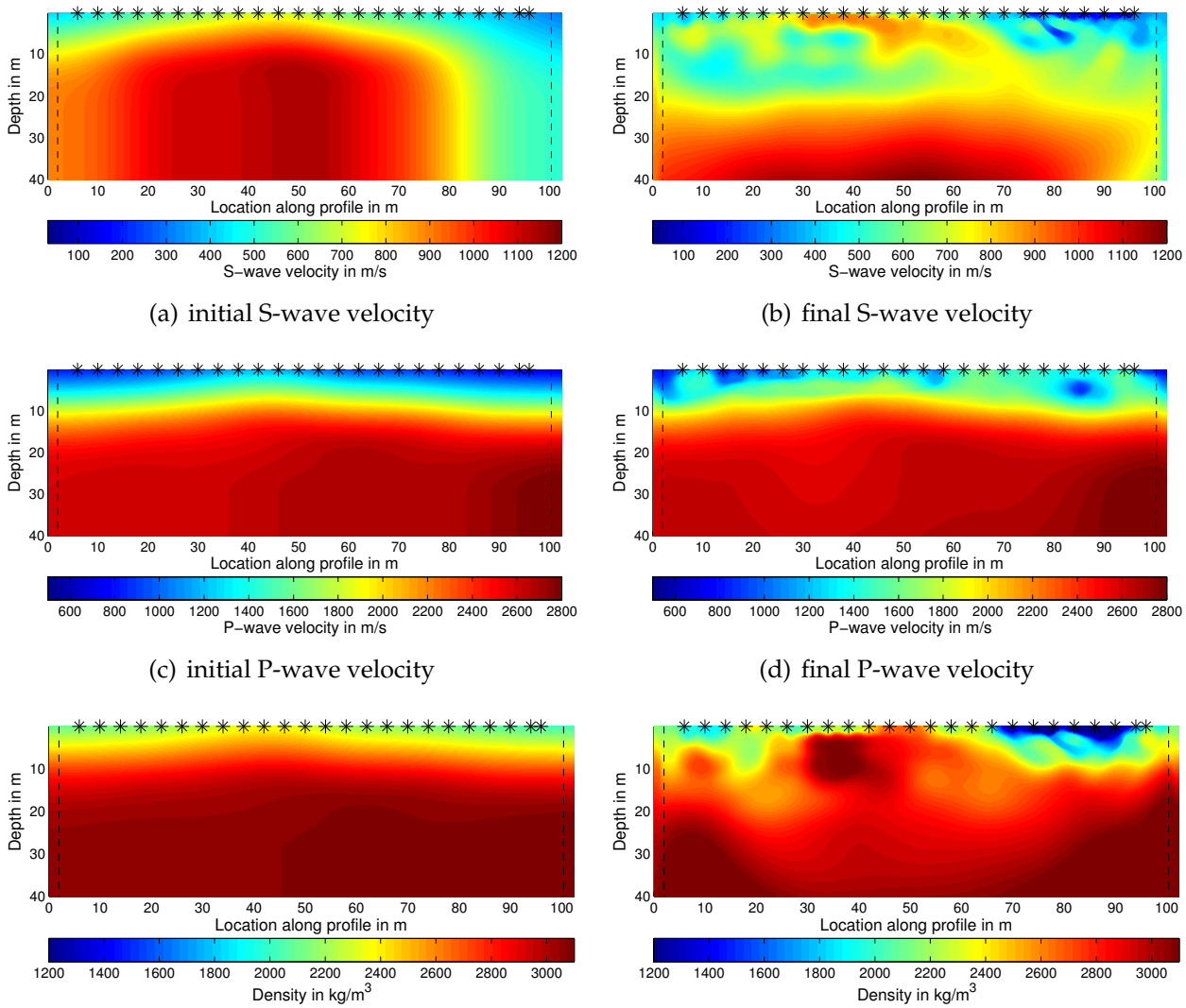

(a) initial S-wave velocity

(b) final S-wave velocity

(c) initial P-wave velocity

(d) final P-wave velocity

(e) inital density model

(f) final density model

Figure V.42: *Starting model 2* and inferred models by 2D FWI of Profile P4 for low-pass filtered data of 20 Hz. (a,b) display the S-wave velocity models, (c,d) the P-wave velocity models and (e,f) the density models. Black stars denote the source locations and black dashed lines indicate the absorbing boundaries with CPML.

V.8.6 Comparison of Profile P3 and Profile P4

2D FWI of Profile P3 and Profile P4 show similar convergence properties. However, it seems that *starting model 2* is for both profiles slightly more appropriate than *starting model 1*. For this reason I compare in the following the inferred subsurface models of Profile P3 and P4 with *starting model 2* in more detail. Fig. V.43 shows the two field-data inversion results as well as vertical velocity profiles of the shear-wave velocity. The gross features in the left and right part of the model are quite similar to each other (at least in larger depths). The largest differences of the velocity structure occur at profile location of 50 - 80 m. The large-scale feature of this high velocity region of Profile P3 isn't observable for Profile P4. Nevertheless, high seismic velocities are observable at shallow depth in both subsurface models at this part. Furthermore, the inferred subsurface models show more similarities in the depth (> 20 m) while they differ significantly in the shallow parts of the models. For profile locations between 10 m and 70 m the deduced seismic velocities are rather smaller than their initial values. However, for the vertical velocity profile located at 85 m higher shear-wave velocities are inferred in comparison to the starting model. So both inversion results show resemblance to each other, but obviously the assumption of a 2D structure isn't completely fulfilled.

V.8.7 Identified problems and future work

Model size
Forbriger (2001, 2003), Hippel (2006), Tran and McVay (2012), Tran et al. (2013) and Groos (2013) observe penetration depths of recorded shallow-seismic Rayleigh waves between 6 m and 20 m. Romdhane et al. (2011) show for their synthetic study even reliable reconstructions in depths up to 50-60 m. However, they use a quite long profile of about 200 m and benefit from reflected body waves for higher frequencies. Nevertheless, I expected from the experience of my colleagues Lisa Groos, Thomas Forbriger and myself that a penetration depth of the Rayleigh waves up to 20 m is realistic in the case of the shallow-seismic survey in Mammolshain with a profile length of 90 m. Because of this I started with shallow subsurface models of 25 m depth. The inversion failed for the same inversion strategy described above. Strong artifacts occur and it wasn't possible to explain all waveforms of single shots with the inferred subsurface models. The inversion was obviously trapped in a local minimum. I tried to overcome these problems by using only single shots in the inversion and studied calculated gradients of single shots in detail. I observed for these inversion tests that the model updates get very close to the bottom boundary of the models and decided to extend the models up to a depth of 100 m. Subsequently, the misfit could be reduced during inversion and the initial models are changed up to 40 m depth. I conclude that this correlates with the penetration depth of the Rayleigh waves.

Smoothing
Appropriate smoothing of gradients and models is a key point for successful full-waveform inversions. On the one hand, I observe instabilities during forward simulations due to very small-scale heterogeneities in the subsurface models inferred by the inversion. To avoid these artifacts very small filter lengths (around 0.5 m) are required. The filter lengths are still smaller than half of the minimum wavelength λ_{min}. On the other hand, a smooth inferred

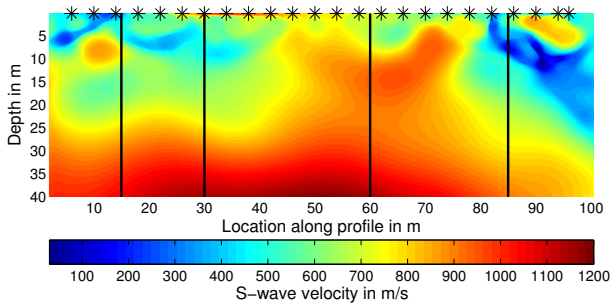

(a) Profile P3

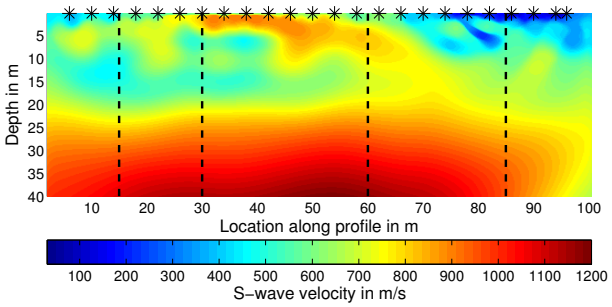

(b) Profile P4

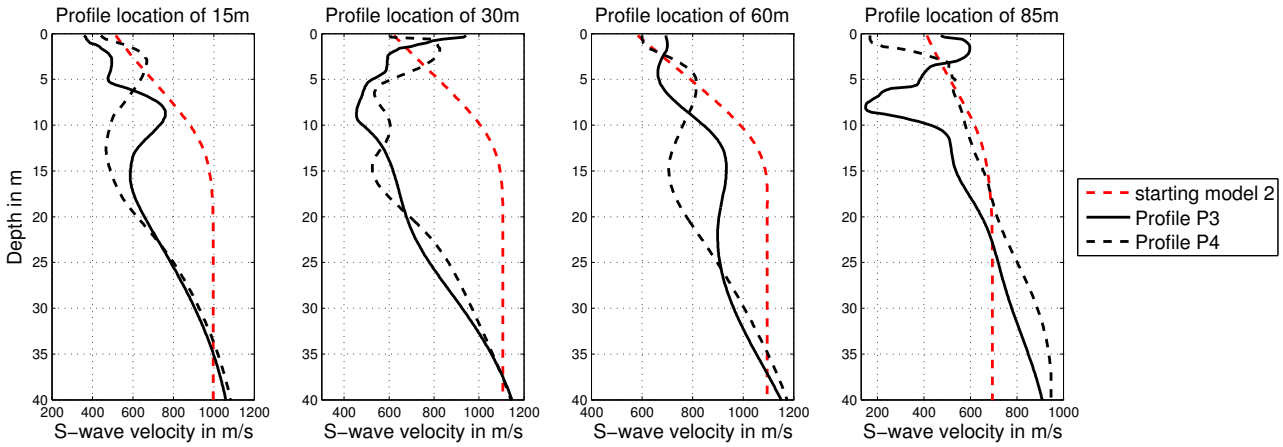

(c) Vertical velocity profiles

Figure V.43: 2D FWI result of (a) Profile P3 and (b) Profile P4 with *starting model 2* as well as four vertical velocity profiles in (c). Black solid and dashed lines indicate vertical velocity profiles of Profile P3 and P4, respectively. Dashed red lines display *starting model 2* for comparison. Black stars in (a) to (b) denote the source locations. Model boundaries with CPML are cut off.

subsurface model is preferred over a rather rough model as long as the waveform fit is similar. Because it shows the ambiguity of the inversion problem and the inferred small-scale structures of the rough model aren't reliable. Therefore, I tested different smoothing strategies to infer an appropriate smooth subsurface model. I tested to correlate the filter length of the 2D median filter with the smallest present wavelength λ_{min} in the data set. The filter length was set to half the length of the smallest wavelength λ_{min}. E.g. for the 10 Hz low-pass filtered data the smallest wavelength is about $\lambda_{min} \approx 20$ m. Therefore, I used a 2D median filter with a filter length of 10 m to smooth the gradients (filter length for model smoothing is still around 0.5 m). Subsequently, the filter length was recalculated for every frequency interval. Unfortunately this approach provided too large filter lengths which undo updated velocity structures inferred by the inversion. Therefore, I chose a filter length which is unaltered during the inversion. The filter length should be chosen that small-scale artifacts are reduced. I tested two filter lengths of 1 m and 5 m. But even the filter length of 5 m was chosen too large why the inversion failed. It seems that the field-data inversion is very sensitive to the used filter length of the 2D median filter. Finally, the filter length of the 2D median filter amounts 1 m for all inversions of the field data from the test-site Mammolshain.

Starting models

For inversion tests with synthetic observed data I have good experiences with linear gradients for each inversion parameter as initial models. The parameter values of the starting model should comprise the parameter range of the true model (known for reconstruction tests) which turned out to be essential for the inversion not to get stuck in a local minimum. I varied the parameter range of the linear gradients as well as the depth of the transition zone of the linear gradient and the half space to obtain different starting models (e.g. strong and weak linear gradients) for the field data inversion. Unfortunately the inversion failed for all linear gradients I have generated so far. This emphasizes how crucial the choice of an appropriate starting model is. Small variations may yield that the inversion gets stuck in a local minimum. This also reflects the non-linearity between inversion parameters and the data.

Frequency intervals

I apply a multi-scale inversion with frequency filtering. On the one hand, the long wavelength components of the subsurface model should be established first. Small-scale structures are not significant due to the ambiguity of the inversion problem. On the other hand, the risk to get stucked in a local minimum can be reduced significantly by using strongly low-pass filtered data in the beginning of the inversion (Bunks et al., 1995). However, there is usually a lack of low frequency content in field data caused by acquisition geometry, sources and the transfer characteristics of the recording equipment (e.g. eigenfrequency of geophones). For shallow-seismic field data this effect is increased due to the applied 5 Hz high-pass filter in the 3D/2D transformation prior to the inversion (see Fig. V.24). The smallest frequency and the steps of increasing the frequency intervals have to be chosen carefully. For the field-data inversion of Mammolshain the lowest frequency of 10 Hz is feasible. I tested also to start with 15 Hz low-pass filtered data, but this ended up in a local minimum. I increase the bandwidth in steps of 2 Hz which seems to be quite small but essential for a successful inversion. For larger frequency intervals (e.g. steps of 5 Hz) the inversion failed.

Density
For acoustic full-waveform inversions, which are mainly performed in marine environments, Barner and Charara (2009) showed that a constant-density acoustic inversion produces worse inversion results. However, as density is a difficult inversion parameter to reconstruct, in most of the case studies the authors only invert for the P-wave velocity (Przebindowska, 2013). Density is commonly obtained using an empirical formula like the Gardner's relationship (see eq. V.6) or density is fixed at a constant value. Przebindowska (2013) reported for marine seismics that a constant density assumption leads to artifacts in the reconstructed velocity models and recommends rather to allow for density inversion than use a fixed relationship between velocity and density.

For elastic full-waveform inversion of shallow-seismic Rayleigh waves many authors (Tran and McVay, 2012; Tran et al., 2013; Bretaudeau et al., 2013; Romdhane et al., 2011) demonstrated successful applications whereas density is fixed at a constant value. Köhn (2011) and Groos (2013) show elastic applications with density inversion with reflected waves and Rayleigh waves, respectively. They report that density is difficult to infer and that a successful reconstruction of density requires very good starting models or a priori known informations which are hardly present for field data sets. In Chapter III I show for a shallow-seismic 2D subsurface structure with Rayleigh waves that elastic full-waveform inversion isn't significantly sensitive to infer the density model appropriate.

Finally, it isn't obvious from the literature how to deal with the density parameter in a field-data inversion of shallow-seismic Rayleigh waves. For this reason I run four inversion tests assuming different density information and strategies for density updates during inversion to study the role of density on the elastic full-waveform inversion of shallow-seismic field data.

1. Fixed density model obtained by Gardner's relationship with P-wave velocity (see eq. V.6)

2. Density update at each iteration step using Gardner's relationship modified for unconsolidated sediments with P-wave velocity

3. Density update at each iteration step using Gardner's relationship modified for unconsolidated sediments with S-wave velocity

4. Density inversion (initial model obtained by Gardner's relationship modified for unconsolidated sediments with P-wave velocity, Section V.7)

First three inversion tests showed strong artifacts as well as weak convergence properties. The inversions already failed for the lowest frequency interval of low-pass filtered data of 10 Hz because the waveform residuals couldn't be reduced. One possible cause of failure could be that the empirical formula is only adapted for certain rock types and that this isn't appropriate for shallow seismics. The inversion results of the fourth case are discussed in Section V.8 and show obviously a successful field-data inversion. From this point of view I can emphasize the statement of Przebindowska (2013): allow for density inversion, rather than to use a fixed relationship between velocity and density.

The used misfit function of FWI is defined by the L2 norm of normalized seismograms. As this objective function contains normalized seismograms near and far-offset traces contribute equally to the misfit and therefore it is not sensitive to residuals in the amplitude decay with offset. After the successful inversion of the field data it may be of interest to use the inferred subsurface models as starting models for a subsequent inversion with the classical L2 norm as measure of misfit. As density is considered to be sensitive to absolute amplitudes, this could improve the density model as well as the velocity models.

2D assumption
In Section V.5 I showed the similarity of Profile P3 and P4 to discuss the 2D assumption of the subsurface. A lot of investigations like the common-offset and common-shot gathers reflect the 2D assumption, however, it also emphasizes that it is more fulfilled for strongly low-pass filtered data. This might be a reason why the full-waveform inversion fails for higher frequencies. The long wavelength component of the subsoil might be considered as a dominant 2D structure. Small heterogeneity like rock fragments or tiny sediment lenses might corrupt the wave field at higher frequencies with 3D effects. These 3D effects cannot be explain by the 2D forward modeling in our 2D inversion scheme why the inversion fails. Furthermore, inversion results of Profile P3 and P4 show resemblance to each other, but obviously the assumed dominant 2D structure isn't present in the subsurface.

Viscoelasticity
The field-data inversions failed for higher frequencies than 20 Hz. For higher frequencies the non-linearity of model parameters and data increases. Therefore, a physical correct simulation of synthetics is essential for the success of the method. Effects of anelastic damping are significant to waveforms in shallow-seismics. Viscoelasticity causes a distance and frequency dependent damping (Groos et al., 2014). We have to keep in mind that the used Q values are estimated empirically from literature. Furthermore, I'm using constant Q models as well as $Q_p = Q_s$ and thus pose a potential source of quality degradation. For now this assumption is feasible (at least for low frequencies), however, for future work different strategies for a better Q estimation and more realistic Q models should be considered.

Three-component geophones
We used at the test-site Mammolshain 50 three-component geophones (eigenfrequency of 4.5 Hz). Up to now I only consider the horizontal (perpendicular to the profile) and the vertical component. The former is used for the travel-time tomography of the S-wave velocity, while the latter is used for the starting model of P-wave velocity as well as for the full-waveform inversion. Since I apply a 2D FWI it is also possible to take the radial (parallel to the profile) component into account to add more information to the inversion. Indeed Romdhane et al. (2011) report that the most information is provided by the vertical component, however, inferred subsurface models bias from lower resolution capability of deeper layers compared to the results where radial and vertical component data is used together. This isn't done so far for the Mammolshain data set and should be considered in future work.

Envelope-based misfit definition
The envelope-based misfit is defined as the difference between envelopes of recorded and synthetic data (see eq. II.56). Such a misfit definition might reduce the non-linearity of the misfit function. The envelope of a seismogram is less sensitive to the oscillating waveform and therefore the risk of cycle-skipping can be reduced dramatically. Furthermore, the long wavelength components are amplified (remember lack of low frequencies in field data). Bozdag et al. (2011) and Chi et al. (2013) show a successful application for seismological scale and a reflection case study, respectively. I implemented the misfit definition after Bozdag et al. (2011) and Chi et al. (2013) in our inversion scheme (Section II.3.3). Unfortunately the misfit couldn't be reduced in the inversion. Obviously the approach is more complex in the presence of shallow-seismic Rayleigh waves and requires a more detailed investigation in future work. In Fig. B.3 field data and the corresponding envelope of shot24 are displayed.

V.9 Discussion and conclusion

I presented applications of 2D FWI to two shallow-seismic field data sets which were acquired at the test-site Mammolshain (Taunus). The misfit is reduced significantly (e.g. Profile P4, *starting model 2*: 47 % to 14 % of total signal energy) in the full-waveform inversion and the inferred subsurface models predict the field data well. In particular, the S-wave velocity models show significant 2D structures of the subsoil. The initial models are changed up to 40 m depth and therefore I conclude that this correlates with the penetration depth of the Rayleigh waves.

I have chosen the test-site Mammolshain because a lot of strong indications support the idea of a predominantly 2D structure in the subsoil (Section V.2). After the inversion of the field data I can confirm some of them but I also have to mitigate the idea of a dominant 2D structure.

The exploration drillings identify the sericite-gneiss in 9 m depth (Fig. V.3), however, there exists a vertical difference in altitude of around 40 m between the drilling site and the test-site Mammolshain. Probably the penetration depth of the Rayleigh waves is too small to be sensitive to the upper edge of the sericite-gneiss. Furthermore, the S-wave velocities of quartzite, gneiss and schist are approximately 1500 - 3100 m/s (see Table V.1). The fastest inferred S-wave velocities in the full-waveform inversion of around 1200 m/s (Fig V.43) emphasize that the inferred seismic properties reflect rather the weathering zone of the upper edge of the sericite-gneiss. This is observable for the P-wave velocities in a similar way. Nevertheless, the S-wave velocities measured by laboratory for shallow depths can be identified in the inferred seismic velocities (Table V.4).

The DPL investigation showed in Fig. V.12 reflects a significant lateral variation of the penetration resistance of the subsoil in the topmost meters (< 2 m depth). The DPL profile coincides with Profile P3 (see Fig. V.14). This observation is mainly reflected in the inferred S- and P-wave velocity model. Fig. B.4 in the Appendix B shows a zoomed view of the inferred seismic velocities of shallow depth. For the left side of the model low seismic velocities indicate low penetration resistances whereas in the middle of the profile high seismic velocities are observable (→ higher penetration resistance). For the right side of

the model the P-wave velocity model confirm the DPL investigation, however, the S-wave velocity model differs from the ground-truth data in this part of the model.

The 2D assumption is one of the most crucial requirements for a successful 2D full-waveform inversion. I studied with many preparatory investigations the predominant 2D structure of the subsoil (Section V.2). Not only the 2D assumption itself was investigated (Section V.2.1), but also the strike direction α of the fault (Section V.2.2). Nevertheless, the comparison of Profile P3 and P4 shows that in particular the right side of the profile differs (Fig. V.15) as well as that the conformance to the 2D assumption is only fulfilled for strongly low-pass filtered data (Fig. V.17). This is also reflected in the convergence properties of the inversion (Fig. V.26) which fails for higher frequencies (> 20 Hz).

The travel-time tomographies of first arrivals of P- and S-waves are appropriate to obtain suitable starting models for the full-waveform inversion with shallow-seismic Rayleigh waves (Section V.7). Both used starting models show almost similar convergence properties (e.g. Fig. V.37). Using linear gradients as starting models yields to strong artifacts and the inversion is obviously trapped in a local minimum.

I obtained 2D FWI results for the field-data inversion with Profile P3 and P4 (Section V.8.3, V.8.2 and V.8.5). The misfit is significantly reduced in the inversion and the deduced subsurface structures predict the field data well. Up to now the inversion is only successful for low-pass filtered data of 20 Hz. For higher frequencies I observe that the model changes between adjacent iteration steps stagnate accompanied by an increase of data misfit (Fig. V.26). Problems for higher frequencies are stronger non-linearities (Section V.8.7) and violation of the 2D assumption (Fig. V.17). Nevertheless, I conclude that elastic full-waveform inversion of recorded shallow-seismic Rayleigh waves is able to image lateral variations of subsurface elastic properties.

Chapter VI

Summary and conclusion

The main objective of my thesis was the application of 2D elastic full-waveform inversion (FWI) to shallow-seismic Rayleigh waves recorded on 2D structures. Therefore, I focused on the implementation of accurate spreading transformations for 2D media as the most important prerequisite. Finally, I applied the 2D adjoint FWI scheme to a field data set recorded on a significant 2D subsurface structure.

Established methods to invert surface waves are the inversion of dispersion curves (Wathelet et al., 2004) or wave-field expansion coefficients (Forbriger, 2003, Part I and II). However, these concepts are only applicable for depth dependent or rather smooth lateral variations of elastic material properties. For strong lateral variations or even 3D structures (e.g. sediment lenses) the concept breaks down because no continuous dispersion curves can be extracted (Forbriger, 2001). To overcome the 1D limitation elastic full-waveform inversion can be applied to infer 2D and 3D structural earth models from shallow-seismic surface waves. The aim of full-waveform inversion is to extract information from observed seismograms on model parameters describing the Earth's interior. An adjoint approach is applied and the elastic finite-difference forward modeling as well as the gradient calculation are performed in the time domain.

My thesis predominantly focused on

- methodology improvements in preparation for shallow-seismic applications,
- investigation of line-source implementation in order to consider 3D wave propagation effects in a 2D FWI,
- application to (multi-component) field data recorded on 2D structure.

Methodology improvements and inversion strategies

A preconditioned conjugate gradient method is used to solve the non-linear inverse problem iteratively. The application of preconditioning to the gradients in elastic full-waveform inversion is a basic prerequisite. In the presence of shallow-seismic Rayleigh waves I observed

high gradient amplitudes in the vicinity of the source locations. Therefore, I tapered the gradients per shot semi-circularly at the source locations. Furthermore, these artifacts can be mitigated by the preconditioning with the approximated Hessian matrix. Additionally, the Hessian acts as a depth-dependent amplifier and yields to stronger convergence rates. To avoid instabilities during forward simulations due to very small-scale heterogeneities I smoothed the gradients with filter lengths smaller than half of the minimum wavelength. These approaches have evolved as best strategies for successful inversions and stronger convergence rates. Furthermore, I implemented an automatic application of multi-scale inversion with frequency filtering and estimation of the unknown source time functions of the hammer impacts for each single shot and each frequency interval. First is applied to avoid cycle skipping or rather local minima during the inversion. In addition, I introduced further inversion strategies, such as checking the v_p/v_s ratio to ensure physically feasible subsurface models and regularization of the density update. These approaches are proved to be meaningful and consistent for inversion tests with synthetic observed data as well as for field data application.

Line-source simulation for shallow-seismic data

Full-waveform inversion of shallow-seismic surface waves is able to image lateral variations of subsurface elastic properties. Line-source simulation for point-source data is required when applying algorithms of 2D adjoint FWI to recorded shallow-seismic field data. Equivalent line-source response for point-source data can be obtained by convolving the waveforms with $\sqrt{t^{-1}}$ (t: travel time), which produces a phase shift of $\pi/4$. Subsequently, an amplitude correction must be applied. In this work I recommend to scale the seismograms with $\sqrt{2rv_{ph}}$ at small receiver offsets r, where v_{ph} is the phase velocity, and gradually shift to applying a $\sqrt{t^{-1}}$ time-domain taper and scaling the waveforms with $r\sqrt{2}$ for larger receiver offsets r. This line-source simulation is called the *hybrid* transformation and I demonstrate its outstanding performance on a 2D heterogeneous structure. The fit of the phases as well as the amplitudes for all shot locations and components (vertical and radial) is excellent with respect to the reference line-source data. An approach for 1D media based on Fourier-Bessel integral transformation generates strong artifacts for waves produced by 2D structures. The theoretical background for both approaches is briefly introduced. In Chapter III I studied their performance when applied to waves propagating in a significantly 2D-heterogeneous structure. I calculated synthetic seismograms for 2D structure for line sources as well as point sources. Line-source simulations obtained from the point-source seismograms by different approaches are then compared to the corresponding line-source reference waveforms. Although being derived by an approximation, the *hybrid* transformation performs excellently except for explicitly back-scattered waves. In reconstruction tests I further invert point-source synthetic seismograms by a 2D full-waveform inversion and evaluate its ability to reproduce the original structural model in comparison to the inversion of line-source synthetic data. Even when applying no explicit correction to the point-source waveforms prior to inversion only moderate artifacts appear in the results. However, the overall performance is best in terms of model reproduction and ability to reproduce the original data in a 3D simulation if inverted waveforms are obtained by the *hybrid* transformation.

Feasibility study of a line-source simulation in the field

Among the numerical 3D/2D transformation techniques I present in Chapter IV the approach for simulating a line source in the field by superposition of single point sources perpendicular to the receiver profile. For a vast number of point sources I show for a synthetic case study that the approach is in principle applicable for a simulation of a line source in the field. Furthermore, I present that the approach is also valid for field data within the expected limits of an appropriate line-source simulation which depend on the line-source profile length and the offset of the receiver. I conclude that a simulation of a line source in the field survey is meaningful, however, it is inefficient due to the vast number of required point sources in particular for far-offset traces. In the framework of FWI where several source locations are required the effort will be dramatically increased. Therefore, I conclude that the numerical transformations presented in Chapter III are superior to the approach introduced here.

Inversion of field data on a 2D structure – test-site Mammolshain

2D FWI is reasonably applicable to field data acquired on 2D structures since scattering at 3D structures cannot be explained by 2D forward solver within the inversion scheme. However, it is a challenging task to find a dominant 2D nature of the subsoil. I selected a 2D test-site on a fault system of the southern rim of the Taunus. We acquired two shallow-seismic field data sets for preparatory investigations. I studied and verified the predominant 2D assumption itself and the strike direction of the fault, so that the receiver profiles for the later main survey can be set up perpendicularly to the fault direction. Subsequently, we acquired a shallow-seismic 2D survey at the test-site Mammolshain. We recorded two profiles perpendicular (Profile P3 and P4) and additionally two profiles parallel (Profile P1 and P2) to the fault. The comparison of Profile P3 and P4 shows that in particular the wave fields on the right side of the profile differ as well as that the conformance to the 2D assumption is only fulfilled for strongly low-pass filtered data. This is also reflected in the convergence properties of the inversion which fails for higher frequencies (> 20 Hz). I use two starting models which are obtained by travel-time tomographies of first arrivals of P- and S-waves, respectively, with the programs Rayfract and ReflexW. Both are appropriate for elastic full-waveform inversion of shallow-seismic Rayleigh waves and result in FWI with almost similar convergence properties. Homogeneous and linear-gradient starting models yield the inversion to get stuck in local minima. In the successful FWI tests the misfit is reduced significantly for both seismic profiles (P3 and P4) in the inversion and the inferred subsurface models predict the field data well. The initial models are changed up to 40 m depth. I conclude that this correlates with the penetration depth of the Rayleigh waves. In particular, the S-wave velocity models show significant 2D structures of the subsoil. The inversion results can be partly compared to ground truthing measurements. The deduced shallow subsurface models seem to be consistent to the laboratory measurements. Both inversion results (Profile P3 and P4) show resemblance to each other, but obviously the assumption of a 2D structure isn't completely fulfilled. Finally, I conclude that elastic full-waveform inversion is applicable to shallow-seismic Rayleigh waves recorded on a 2D-heterogeneous structure.

Concluding, the approach of 2D elastic full-waveform inversion applied to shallow-seismic Rayleigh waves has the potential to image 2D structures of the subsoil. This is shown for a synthetic case study as well as for a field data application. I considered effects on wave propagation, such as anelastic damping, source-wavelet inversion and geometrical spreading, in order to simulate waveforms as accurately as possible. However, the potential neglect of 3D structures violates the 2D assumption and might result in corrupted subsurface structures. Therefore, 3D elastic FWI may be considered for prospective work to check the feasibility of the inferred 2D subsurface models. Besides appropriately physical simulation of waveforms, other misfit definitions should be taken into account to mitigate the problem of local minima and the influence of the initial model for future inversion tests. Further investigations, such as regularization, are required for a more robust inversion procedure. However, in contrast to other conventional imaging methods of shallow-seismic surface waves, elastic FWI is able to take the complete waveforms of 2D modeling into account and therefore to image 2D subsurface structures appropriately.

Bibliography

Aki, K. and Richards, P. (1980). Quantitative seismology. W. H. Freeman and Co.

Amundsen, L. and Reitan, A. (1994). Transformation from 2-D to 3-D wave propagation for horizontally layered media. Geophysics, 59(12):1920–1926.

Auer, L., Nuber, A., Greenhalgh, S., Maurer, H., and Marelli, S. (2013). A critical appraisal of asymptotic 3D-to-2D data transformation in full-waveform seismic crosshole tomography. Geophysics, 78(6):R235–R247.

Bachrach, R., Dvorkin, J., and Nur, A. M. (2000). Seismic velocities and poisson's ratio of shallow unconsolidated sands. Geophysics, 65(2):559–564.

Barner, C. and Charara, M. (2009). The domain of applicability of acoustic full-waveform inversion for marine seismic data. Geophysics, 74(6):WCC91–WCC103.

Blanch, J. O., Robertsson, J. O. A., and Symes, W. W. (1995). Modeling of a constant Q: Methodology and algorithm for an efficient and optimally inexpensive viscoelastic technique. Geophysics, 60(1):176–184.

Bleibstein, N. (1986). Two-and-one-half dimensional in-plane wave propagation. Geophysical Prospecting, 34:686–703.

Bohlen, T. (1998). Viskoelastische FD-Modellierung seismischer Wellen zur Interpretation gemessener Seismogramme. PhD thesis, Christian-Albrechts-Universität zu Kiel.

Bohlen, T. (2002). Parallel 3-D viscoelastic finite difference seismic modelling. Comput. Geosci., 28:887–899.

Bohlen, T., Kugler, S., Klein, G., and Theilen, F. (2004). 1.5D inversion of lateral variation of Scholte-wave dispersion. Geophysics, 69(2):330–344.

Bozdag, E., Trampert, J., and Tromp, J. (2011). Misfit functions for full waveform inversion based on instantaneous phase and envelope measurements. Geophys. J. Int., 185:845–870.

Bretaudeau, F., Brossier, R., Leparoux, D., Abraham, O., and Virieux, J. (2013). 2D elastic full-waveform imaging of the near-surface: application to synthetic and physical modelling data sets. Near Surface Geophysics.

Bunks, C., Saleck, F. M., Zaleski, S., and Chavent, G. (1995). Multiscale seismic waveform inversion. Geophysics, 60(5):1457–1473.

Butzer, S., Kurzmann, A., and Bohlen, T. (2013). 3D elastic full waveform inversion of small-scale heterogeneities in transmission geometry. Geophysical Prospecting, 61(6):1238–1251.

Carcione, J. M., Kosloff, D., and Kosloff, R. (1988). Wave propagation simulation in a linear viscoacoustic medium. Geophysical Journal of the Royal Astronomical Society, 93(2):393–407.

Cerjan, C., Kosloff, D., Kosloff, R., and Reshef, M. (1985). A nonreflecting boundary condition for discrete acoustic and elastic wave equations. Geophysics, 50(4):705–708.

Chi, B., Dong, L., and Liu, Y. (2013). Full waveform inversion based on envelope objective function. In Extended Abstracts, 75th EAGE Conference and Exhibition, London. EAGE.

Choi, Y. and Alkhalifah, T. (2012). Application of multi-source waveform inversion to marine streamer data using the global correlation norm. Geophysical Prospecting, 60:748–758.

Courant, R., Friedrichs, K., and Lewy, H. (1928). Über die partiellen Differenzengleichungen der mathematischen Physik. Mathematische Annalen, 100:32–74.

Courant, R., Friedrichs, K., and Lewy, H. (1967). On the partial differential equations of mathematical physics. IBM Journal, pages 215–234.

Crase, E., Pica, A., Noble, M., McDonald, J., and Tarantola, A. (1990). Robust elastic nonlinear waveform inversion: Application to real data. Geophysics, 55(5):527–538.

Doblain, M. (1986). The application of high-order differencing to the scalar wave equation. Geophysics, 51:54–66.

Forbriger, T. (2001). Inversion flachseismischer Wellenfeldspektren. PhD thesis, Institut für Geophysik, Universität Stuttgart.

Forbriger, T. (2003). Inversion of shallow-seismic wavefields: Part I and II. Geophys. J. Int., 153(3):719–752.

Forbriger, T., Auras, M., Bilgili, F., Bohlen, T., Butzer, S., Christen, S., Cristiano, L., Friederich, W., Giese, R., Groos, L., Igel, H., Köllner, F., Krompholz, R., Lüth, S., Mauerberger, S., Meier, T., Mosca, I., Niehoff, D., Richter, H., Schäfer, M., Schuck, A., Schumacher, F., Sigloch, K., Vormbaum, M., and Wuttke, F. (2014a). Tomography of the Earth's Crust: From Geophysical Sounding to Real-Time Monitoring. Springer International in Earth Sciences.

Forbriger, T., Groos, L., and Schäfer, M. (2014b). Line-source simulation for shallow-seismic data. Part 1: Theoretical background. Geophys. J. Int., 198(3):1387–1404.

Fuchs, K. and Müller, G. (1971). Computation of synthetic seismograms with the reflectivity method and comparison with observations. Geophys. J.R. astr. Soc., 23(4):417–433.

Gardner, G., Gardner, L., and Gregory, A. (1974). Formation velocity and density - the diagnostic basics for stratigraphic traps. Geophysics, 39:770–780.

Groos, L. (2013). 2D full waveform inversion of shallow seismic Rayleigh waves. PhD thesis, Karlsruhe Institute of Technology (KIT).

Groos, L., Schäfer, M., Forbriger, T., and Bohlen, T. (2014). The role of attenuation in 2D full-waveform inversion of shallow-seismic body and Rayleigh waves. Geophysics GEO-2013-0462.

Hippel, A. (2006). Anwendung flachseismischer Oberflächenwellenmessungen zur Charakteriserung des Untergrundes. Master's thesis, Geophysikalisches Institut, Universität Karlsruhe (TH).

Hudson, J. (1977). Scattered waves in the coda of P. J. Geophys., 43:359–374.

Hüttner, R., Konrad, H.-J., and Zitzmann, A. (1986). Geologische Übersichtskarte 1:200.000, Blatt CC7110 Mannheim. Bundesanstalt für Geowissenschaften und Rohstoffe.

Köhn, D. (2011). Time domain 2D elastic full waveform tomography. PhD thesis, Christian-Albrechts-Universität zu Kiel.

Köhn, D., De Nil, D., Kurzmann, A., Groos, L., Schäfer, M., and Heider, S. (2013). DENISE - User manual. Christian-Albrechts-Universität zu Kiel und Karlsruher Institut für Technologie, `http://www.gpi.kit.edu/downloads/manual_DENISE.pdf` (last acces: April 2014).

Köhn, D., De Nil, D., Kurzmann, A., Przebindowska, A., and Bohlen, T. (2012). On the influence of model parametrization in elastic full waveform tomography. Geophysical Journal International, 191(1):325–345.

Komatitsch, D. and Martin, R. (2007). An unsplit convolutional perfectly matched layer improved at grazing incidence for the seismic wave equation. Geophysics, 72(5,S):SM155–SM167.

Kümmerle, E. and Seidenschwann, G. (2009). Erläuterungen zur Geologischen Karte von Hessen 1:25000 Blatt Nr. 5817 Frankfurt a.M. West. Hess. Landesamt für Umwelt und Geologie, Wiesbaden.

Lecomte, I., Gjøystdal, H., Dahle, A., and Pedersen, O. (2000). Improving modelling and inversion in refraction seismics with a first-order eikonal solver. Geophysical Prospecting, 48(3):437–454.

Levander, A. R. (1988). Fourth-order finite-difference P-SV seismograms. Geophysics, 53(11):1425–1436.

Liu, H. P., Anderson, D. L., and Kanamori, H. (1976). Velocity dispersion due to anelasticity: implications for seismology and mantle composition. Geophysical Journal of the Royal Astronomical Society, 47(1):41–58.

Martin, R. and Komatitsch, D. (2009). An unsplit convolutional perfectly matched layer technique improved at grazing incidence for the viscoelastic wave equation. Geophys. J. Int., 179(1):333–344.

Miller, R.D.and Xia, J., Park, C., and Ivanov, J. (1999). Multichannel analysis of surface waves to map bedrock. The Leading Edge, December:1392–1396.

Mora, P. (1987). Nonlinear two-dimensional elastic inversion of multioffset seismic data. Geophysics, 52(9):1211–1228.

Müller, G. (2007). Theory of elastic waves. Samizdat Press.

Nocedal, J. and Wright, S. J. (1999). Numerical Optimization. Springer, New York.

Pica, A., Diet, J. P., and Tarantola, A. (1990). Nonlinear inversion of seismic reflection data in a laterally invariant medium. Geophysics, 55(3):284–292.

Pratt, R. G. (1990). Inverse theory applied to multi-source cross-hole tomography. Part II: Elastic wave-equation method. Geophysical Prospecting, 38:311–330.

Pratt, R. G. (1999). Seismic waveform inversion in the frequency domain, part 1: Theory and verification in a physical scale model. Geophysics, 64:888–901.

Pratt, R. G., Shin, C., and Hicks, G. J. (1998). Gauss-Newton and Full-Newton methods in frequency-domain seismic waveform inversion. Geophysical Journal International, 133:341–362.

Pratt, R. G. and Worthington, M. H. (1990). Inverse theory applied to multi-source cross-hole tomography, Part I: Acoustic wave-equation method. Geophysical Prospecting, 38:287–310.

Przebindowska, A. (2013). Acoustic Full Waveform Inversion of Marine Reflection Seismic Data. PhD thesis, Karlsruhe Institute of Technology (KIT).

Robertsson, J. O. A., Blanch, J. O., and Symes, W. W. (1994). Viscoelastic finite-difference modeling. Geophysics, 59(9):1444–1456.

Romdhane, G., Grandjean, G., Brossier, R., Rejiba, F., Operto, S., and Virieux, J. (2011). Shallow-structure characterization by 2D elastic full-waveform inversion. Geophysics, 76(3):R81–R93.

Schäfer, M., Groos, L., Forbriger, T., and Bohlen, T. (2012). On the effects of geometrical spreading corrections for a 2D full waveform inversion of recorded shallow seismic surface waves. In Extended Abstracts, 74th EAGE Conference and Exhibition, Copenhagen. EAGE.

Schäfer, M., Groos, L., Forbriger, T., and Bohlen, T. (2014). Line-source simulation for shallow-seismic data. Part 2: Full-waveform inversion - a 2D synthetic case study. Geophys. J. Int., 198(3):1405–1418.

Schön, J. (1996). Physical Properties of Rocks: Fundamentals and Principles of Petrophysics. Pergamon.

Sheen, D.-H., Tuncay, K., Baag, C.-E., and Ortoleva, P. J. (2006). Time domain gauss-newton seismic waveform inversion in elastic media. Geophys. J. Int., 167(3):1373–1384.

Sirgue, L. and Pratt, R. G. (2004). Efficient waveform inversion and imaging: A strategy for selecting temporal frequencies. Geophysics, 69(1):231–248.

Smoltczyk, U. (2002). Geotechnical Engineering Handbook, Volume 1, Fundamentals. Ernst and Sohn.

Socco, L., Foti, S., and Boiero, D. (2010). Surface-wave analysis for building near-surface velocity models - Established approaches and new perspectives. Geophysics, 75(5):75A83–75A102.

Stelzer, Z. (2010). Akquisition und Interpretation von Oberflächenwellen für die Wellenforminversion. diploma thesis, Karlsruhe Institute of Technology.

Stümpel, H., Kähler, S., Meissner, R., and Milkereit, B. (1984). The use of seismic shear waves and compressional waves for lithological problems of shallow sediments. Geophysical Prospecting, 32:662–675.

Tarantola, A. (1984). Inversion of seismic reflection data in the acoustic approximation. Geophysics, 49(8):1259–1266.

Tarantola, A. (1986). Theoretical Background for the Inversion of Seismic Waveforms, Including Elasticity and Attenuation. Pure and Applied Geophysics, 128(1/2):365–399.

Tarantola, A. (1987). Inverse Problem Theory: Methods for Data Fitting and Parameter Estimations. Elsevier Science Publ. Co, New York.

Tarantola, A. (1988). Theoretical background for the inversion of seismic waveforms, including elasticity and attenuation. Pure Appl. Geophys., 128(1-2):365–399.

Tran, K. T. and McVay, M. (2012). Site characterization using Gauss-Newton inversion of 2-D full seismic waveform in the time domain. Soil Dyn. Earthq. Eng., 43:16–24.

Tran, K. T., McVay, M., Faraone, M., and Horhota, D. (2013). Sinkhole detection using 2D full seismic waveform tomography. Geophysics, 78:R175–R183.

Tromp, J., Tape, C., and Liu, Q. (2005). Seismic tomography, adjoint methods, time reversal and banana-doughnut kernels. Geophys. J. Int., 160(1):195–216.

Ungerer, J. (1990). Berechnung von Nahfeldseismogrammen mit der Reflektivitätsmethode. diploma thesis, Institut für Geophysik, Universität Stuttgart.

Vidale, J. (1988). Finite-difference calculation of travel times. Bulletin of the Seismological Society of America, 78:2062–2076.

Virieux, J. (1986). P-SV wave propagation in heterogeneous media: velocity-stress finite-difference method. Geophysics, 54(4):889–901.

Virieux, J. and Operto, S. (2009). An overview of full-waveform inversion in exploration geophysics. Geophysics, 74(6):WCC1–WCC26.

Wapenaar, C. P. A., Verschuur, D. J., and Herrmann, P. (1992). Amplitude preprocessing of single and multicomponent seismic data. Geophysics, 57(9):1178–1188.

Wathelet, M., Jongmans, D., and Ohrnberger, M. (2004). Surface-wave inversion using a direct search algorithm and its application to ambient vibration measurements. Near Surface Geophysics, 2(4):211–221.

Winkelmann, M. (1997). Palynostratigraphische Untersuchungen am Südrand des Rheinischen Schiefergebirges (Südtaunus, Südhunsrück). Herbert Utz Verlag.

Wu, R. and Aki, K. (1985). Scattering characteristics of elastic waves by an elastic heterogeneity. Geophysics, 50:582–595.

List of Tables

List of Figures

Appendix A

Estimation of the strike direction of the 2D fault

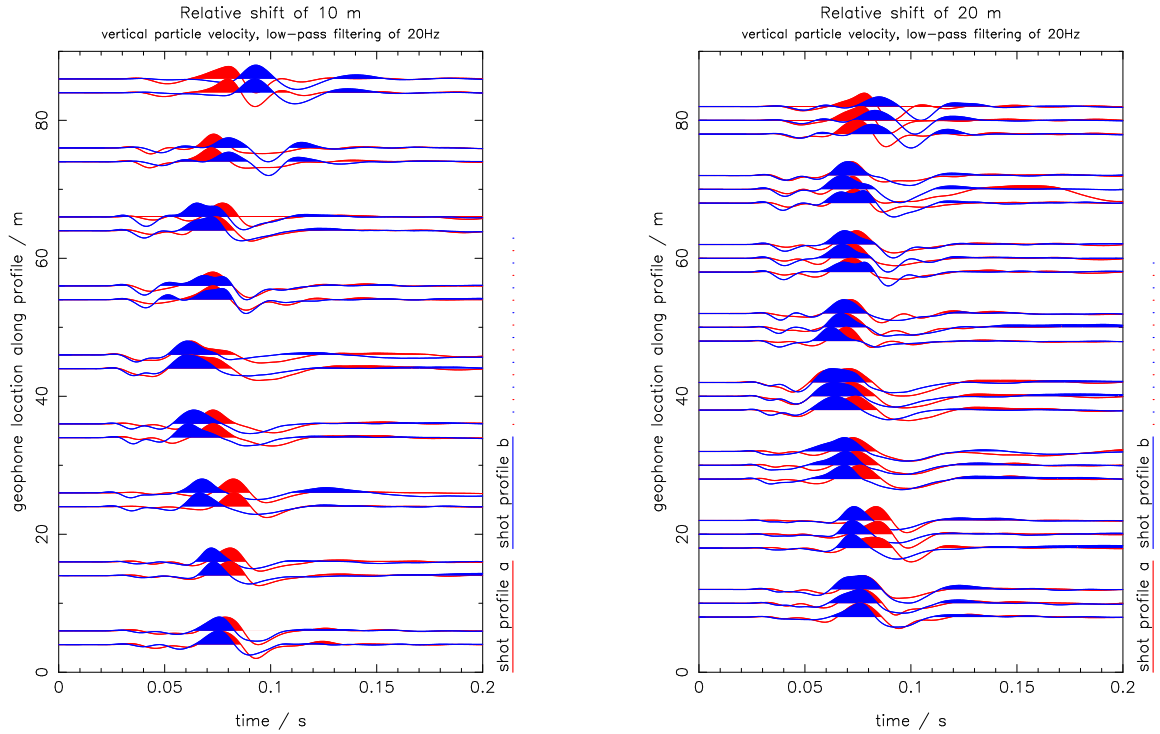

(a) relative shift of 10 m

(b) relative shift of 20 m

Figure A.1: Vertical particle velocity of shot and geophone groups as displayed in Fig.V.9. Red seismograms display shots excited on the shot profile a and blue seismograms of shot profile b. Each trace is normalized to its maximum amplitude.

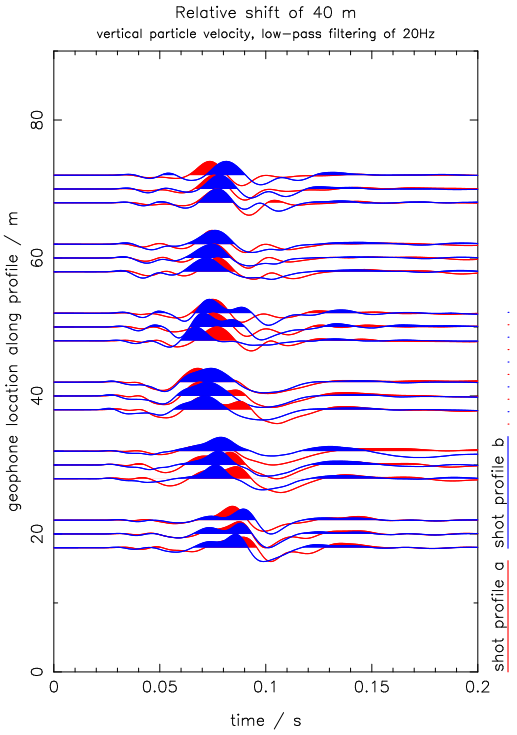

(a) relative shift of 40 m

Figure A.2: Vertical particle velocity of shot and geophone groups as displayed in Fig.V.9. Red seismograms display shots excited on the shot profile a and blue seismograms of shot profile b. Each trace is normalized to its maximum amplitude.

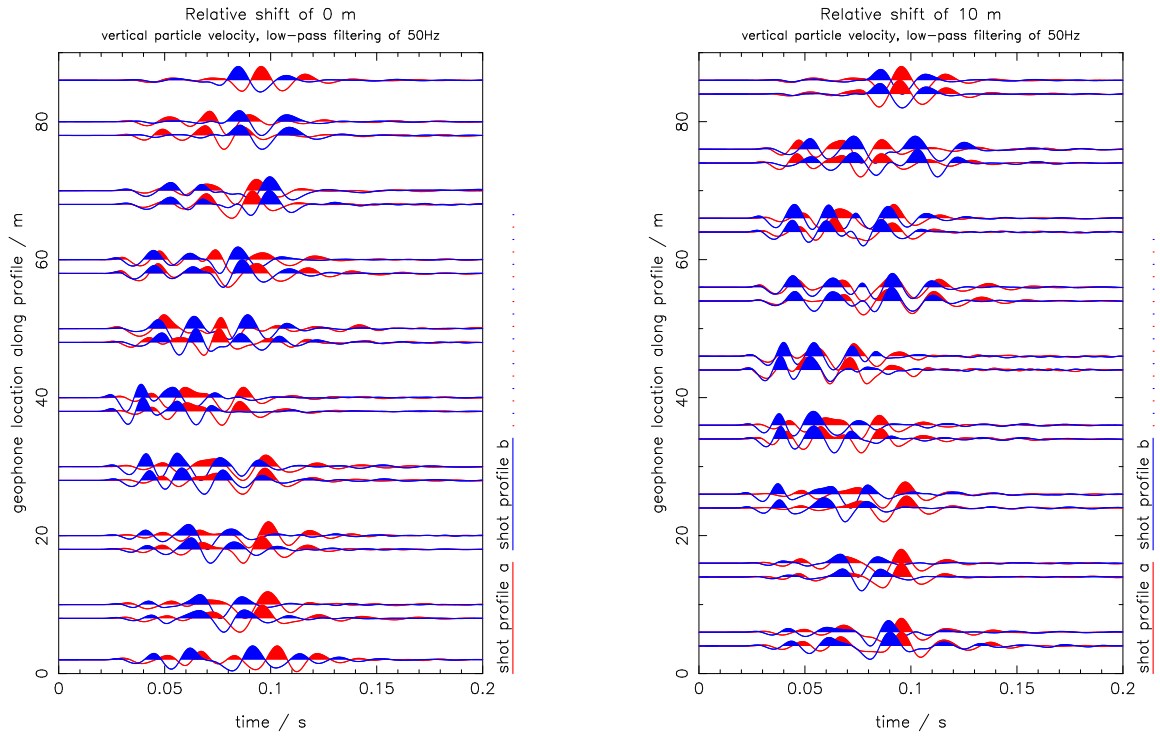

(a) relative shift of 0 m

(b) relative shift of 10 m

Figure A.3: Vertical particle velocity of shot and geophone groups as displayed in Fig.V.9. Red seismograms display shots excited on the shot profile a and blue seismograms of shot profile b. Each trace is normalized to its maximum amplitude.

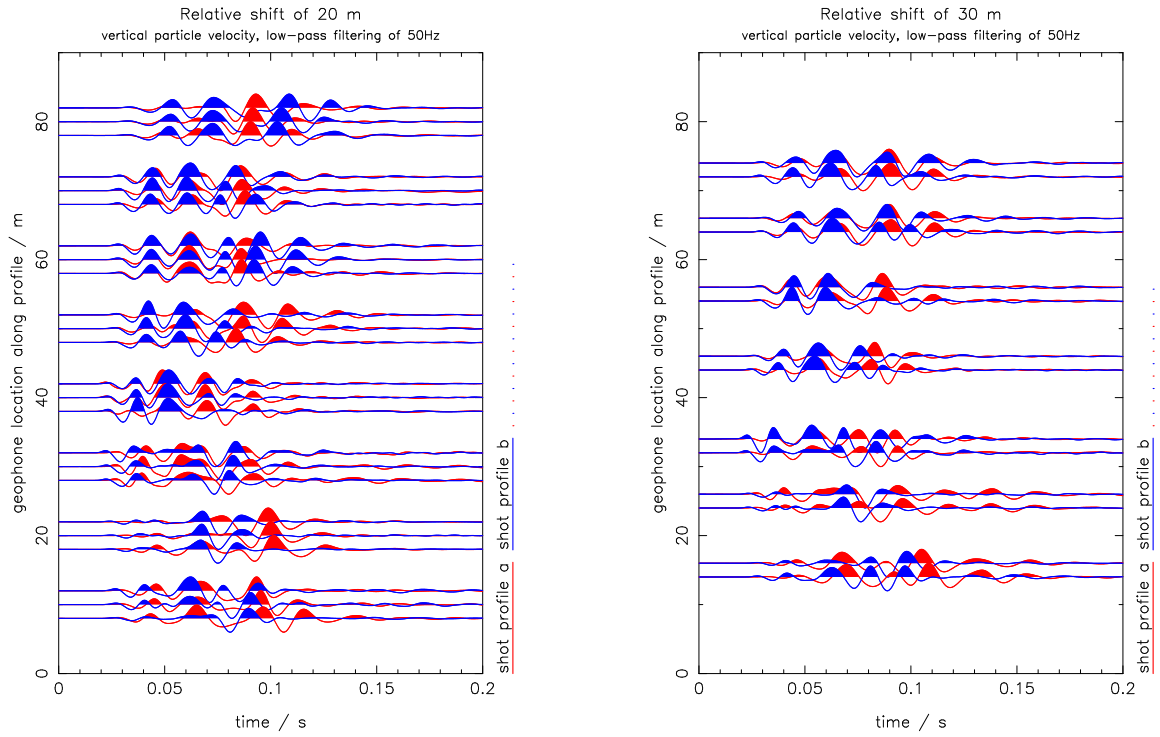

(a) relative shift of 20 m

(b) relative shift of 30 m

Figure A.4: Vertical particle velocity of shot and geophone groups as displayed in Fig.V.9. Red seismograms display shots excited on the shot profile a and blue seismograms of shot profile b. Each trace is normalized to its maximum amplitude.

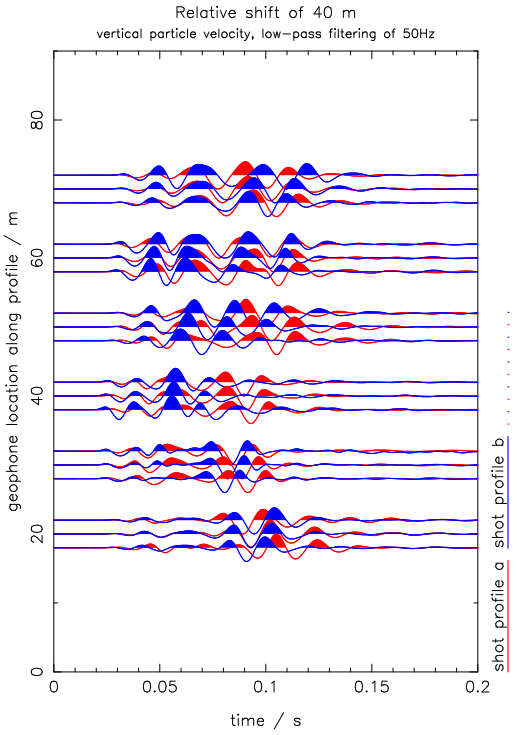

(a) relative shift of 40 m

Figure A.5: Vertical particle velocity of shot and geophone groups as displayed in Fig.V.9. Red seismograms display shots excited on the shot profile a and blue seismograms of shot profile b. Each trace is normalized to its maximum amplitude.

Appendix B

FWI of Profile P3

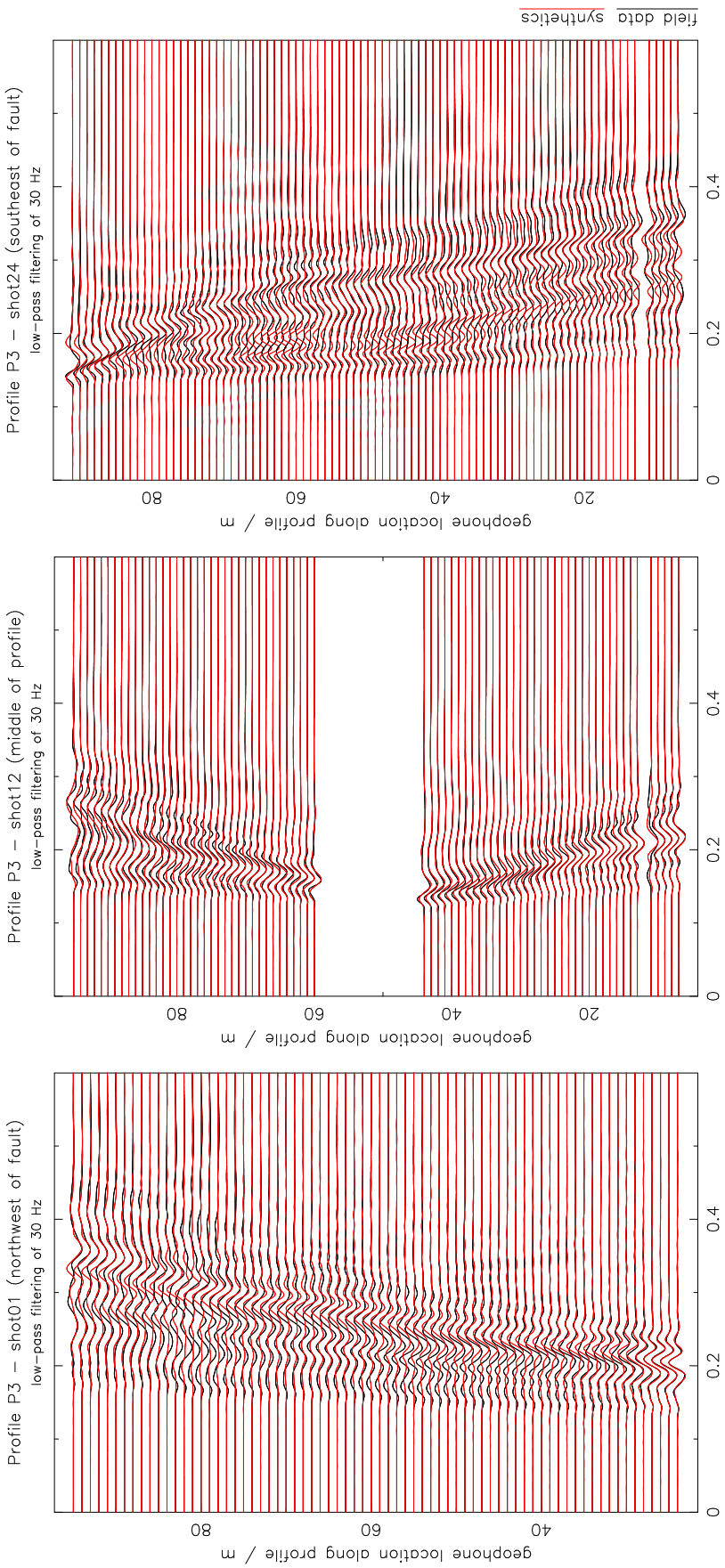

(a) Shot 01 (profile location of 6 m)

(b) Shot 12 (profile location of 50 m)

(c) Shot 24 (profile location of 96 m)

Figure B.1: Comparison of field data (black solid line) and synthetics (red solid line) for low-pass filtered data of 30 Hz of Profile P3 with *starting model 2* after FWI. Displayed are vertical particle displacement seismograms. Each trace is normalized to its maximum amplitude.

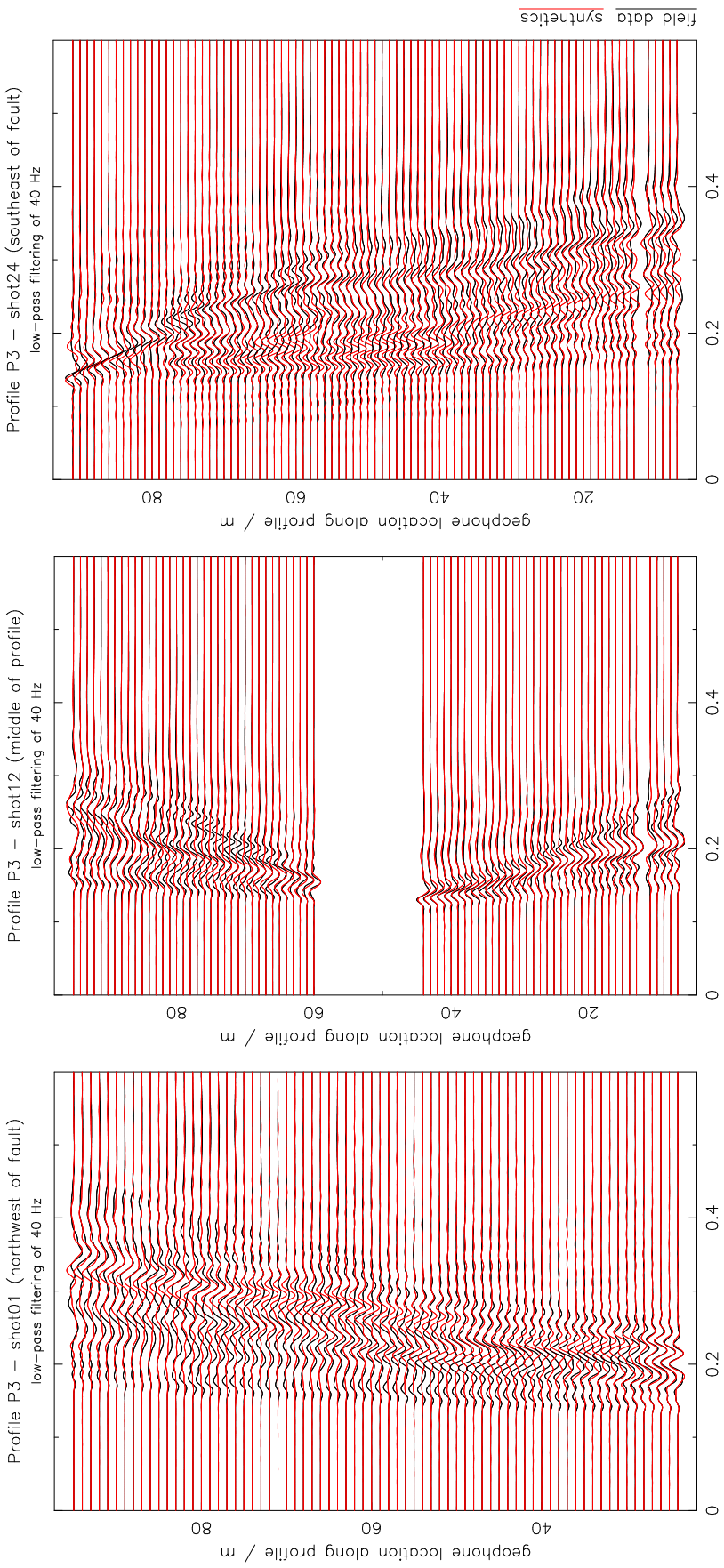

(a) Shot 01 (profile location of 6 m)

(b) Shot 12 (profile location of 50 m)

(c) Shot 24 (profile location of 96 m)

Figure B.2: Comparison of field data (black solid line) and synthetics (red solid line) for low-pass filtered data of 40 Hz of Profile P3 with *starting model 2* after FWI. Displayed are vertical particle displacement seismograms. Each trace is normalized to its maximum amplitude.

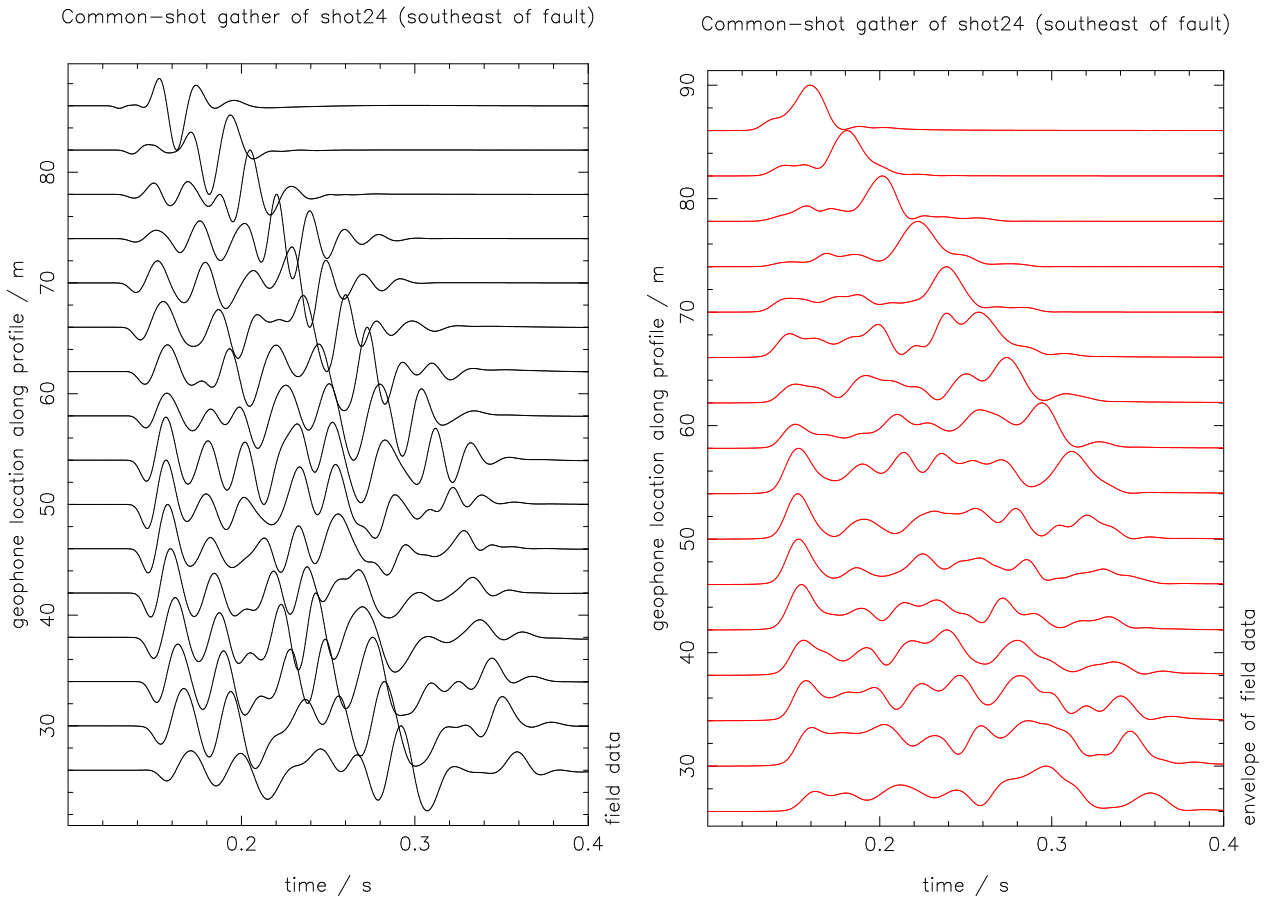

(a) Field data

(b) Envelope of field data

Figure B.3: Comparison of field data (black solid line) and the envelope of field data (red solid line) for low-pass filtered data of 50 Hz of Profile P3. Each trace is normalized to its maximum amplitude.

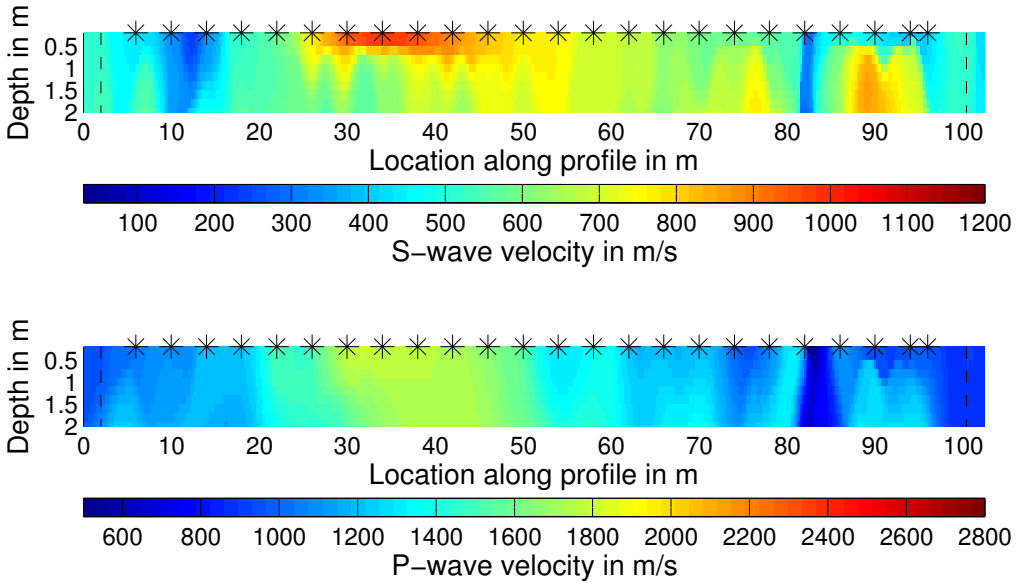

Figure B.4: Shallow part (0-2 m depth) of S- and P-wave velocity results of Profile P3 obtained by using *starting model 2*.

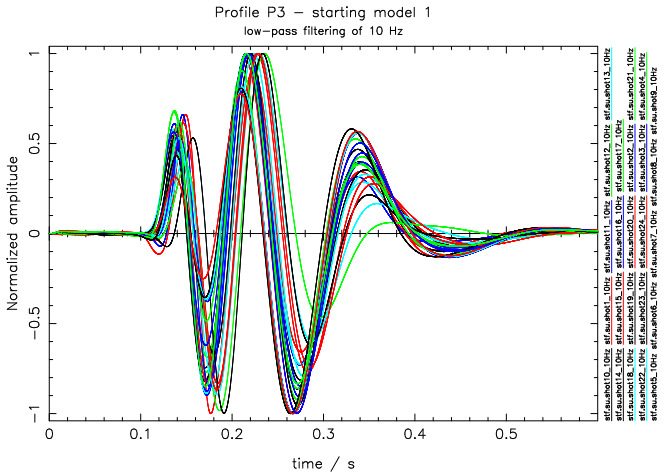

(a) Low-pass filter of 10 Hz.

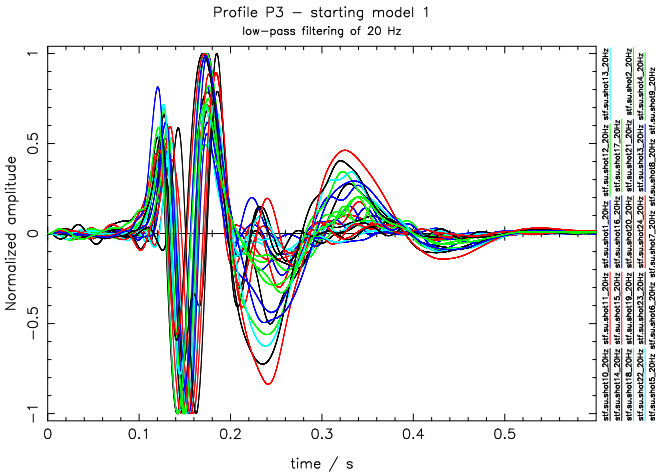

(b) Low-pass filter of 20 Hz.

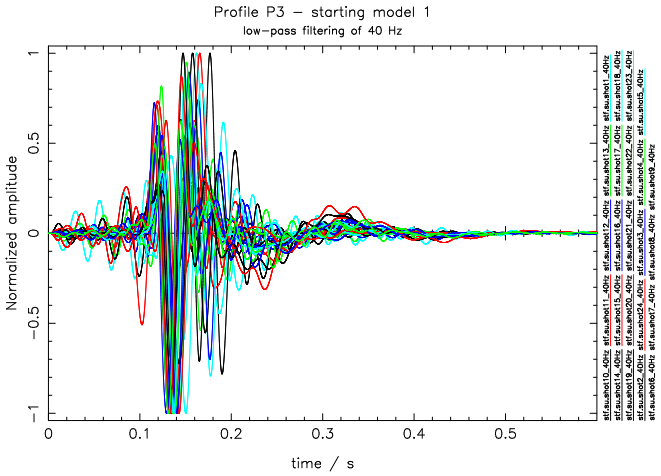

(c) Low-pass filter of 40 Hz.

Figure B.5: Profile P3: Optimized source time functions of the hammer impacts for each single shot during inversion with *starting model 1*. The wavelet is shifted by 0.1 s to consider acausal parts of it.

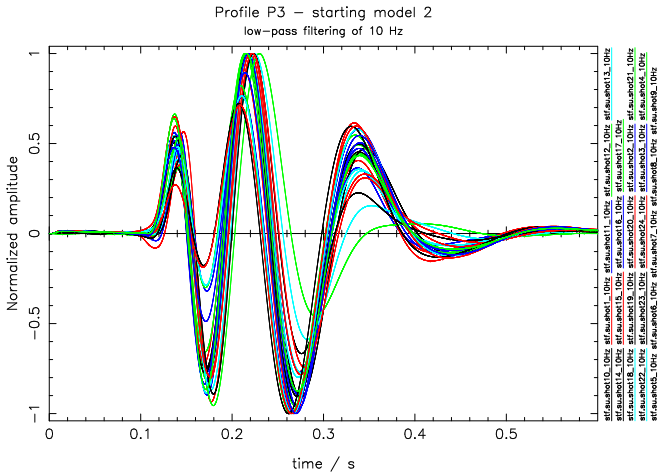

(a) Low-pass filter of 10 Hz.

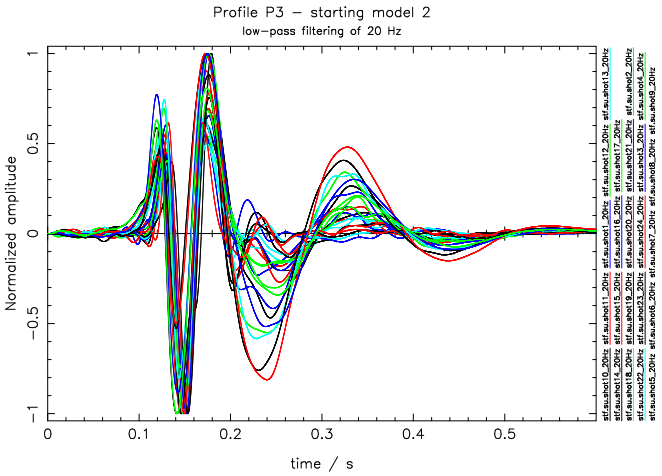

(b) Low-pass filter of 20 Hz.

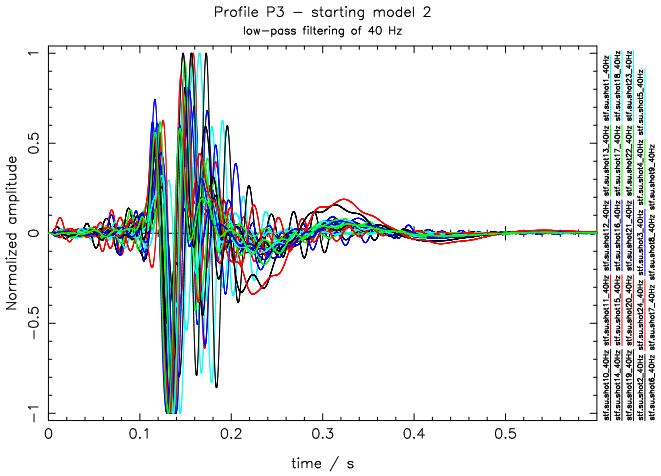

(c) Low-pass filter of 40 Hz.

Figure B.6: Profile P3: Optimized source time functions of the hammer impacts for each single shot during inversion with *starting model 2*. The wavelet is shifted by 0.1 s to consider acausal parts of it.

Appendix C

FWI of Profile P4

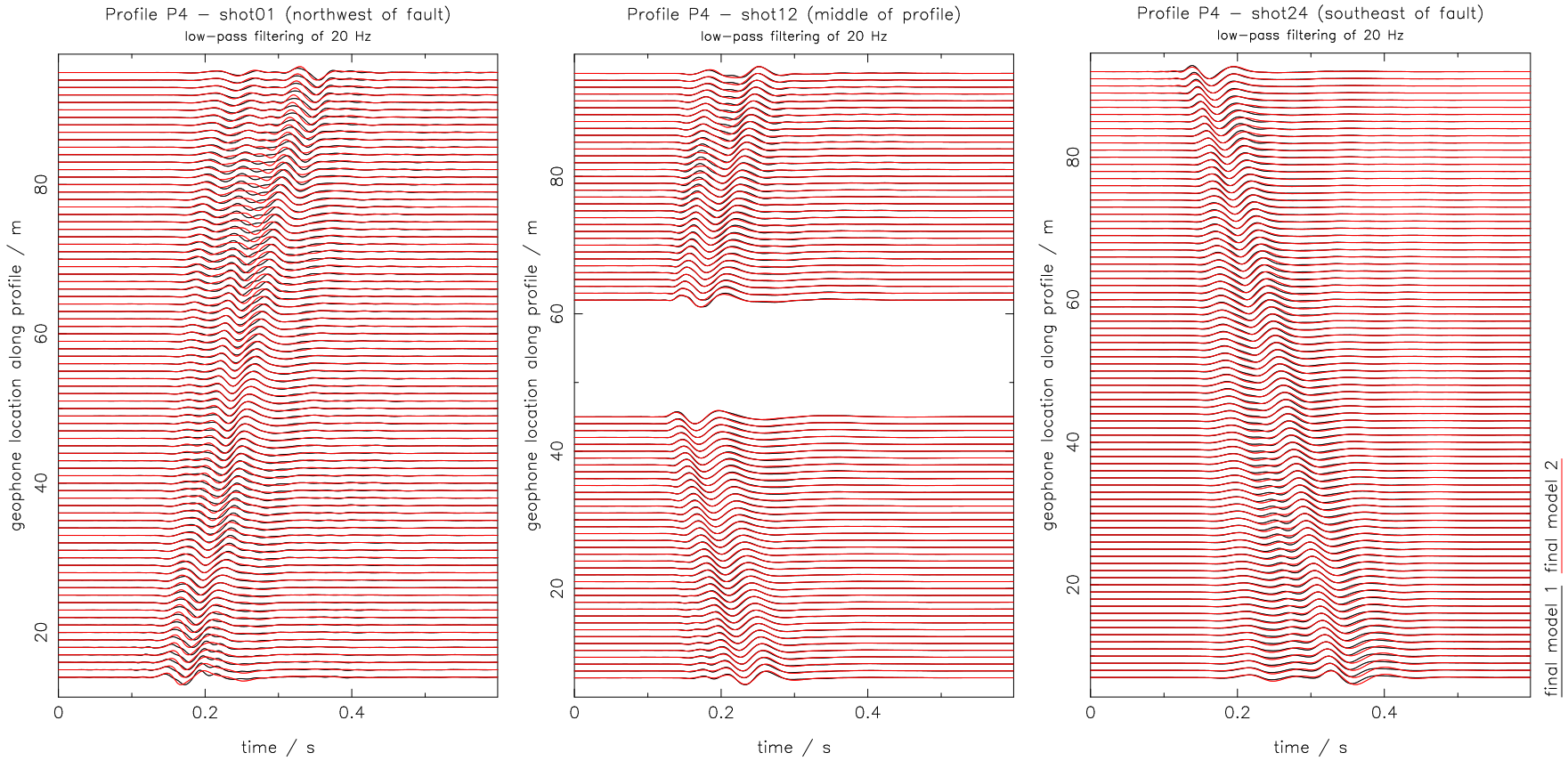

(a) Shot 01 (profile location of 6 m) (b) Shot 12 (profile location of 50 m) (c) Shot 24 (profile location of 96 m)

Figure C.1: Comparison of synthetics of final model 1 (black solid line) and synthetics of final model 2 (red solid line) for low-pass filtered data of 20 Hz. Displayed are vertical particle displacement seismograms. Final model 1 is obtained by using *starting model 1* in the inversion and final model 2 is obtained by using *starting model 2*. The corresponding inversion results are shown in Figs V.41 and V.42. Each trace is normalized to its maximum amplitude.

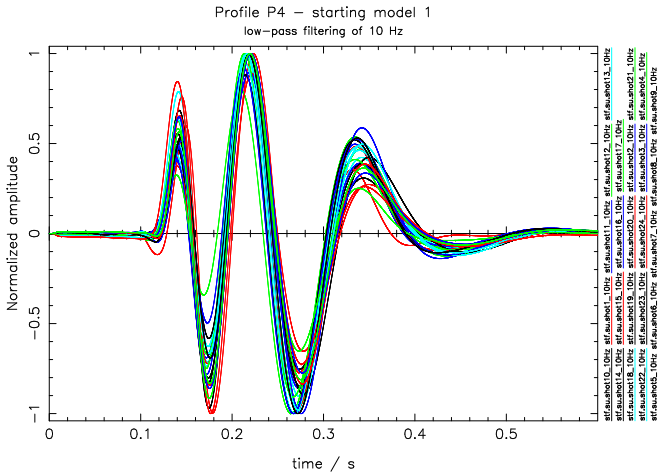

(a) Low-pass filter of 10 Hz.

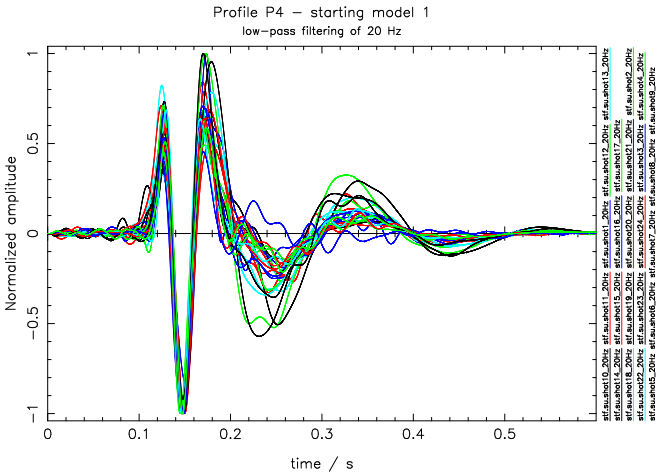

(b) Low-pass filter of 20 Hz.

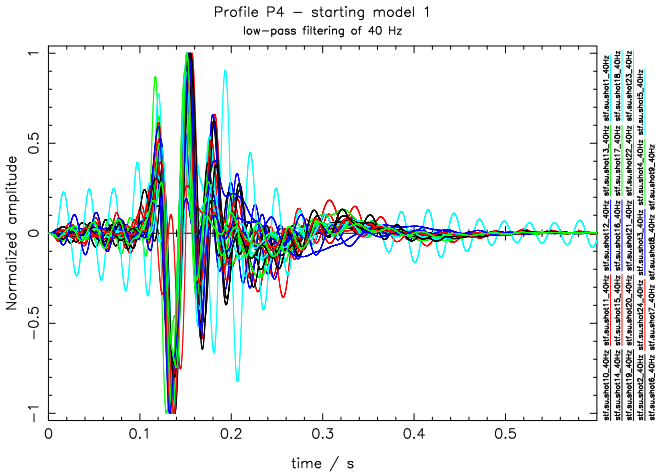

(c) Low-pass filter of 40 Hz.

Figure C.2: Profile P4: Optimized source time functions of the hammer impacts for each single shot during inversion with *starting model 1*. The wavelet is shifted by 0.1 s to consider acausal parts of it.

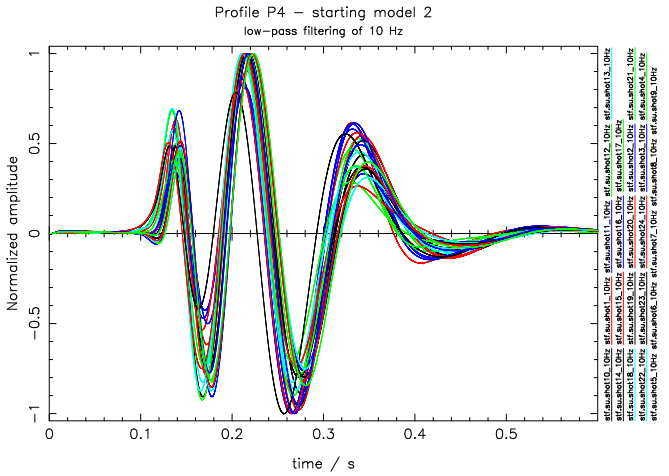

(a) Low-pass filter of 10 Hz.

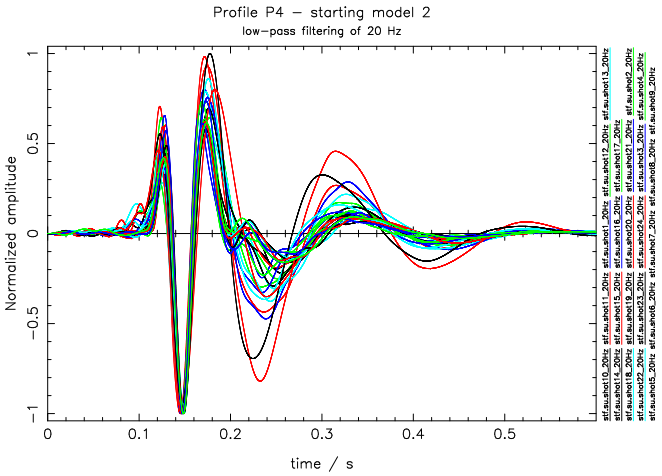

(b) Low-pass filter of 20 Hz.

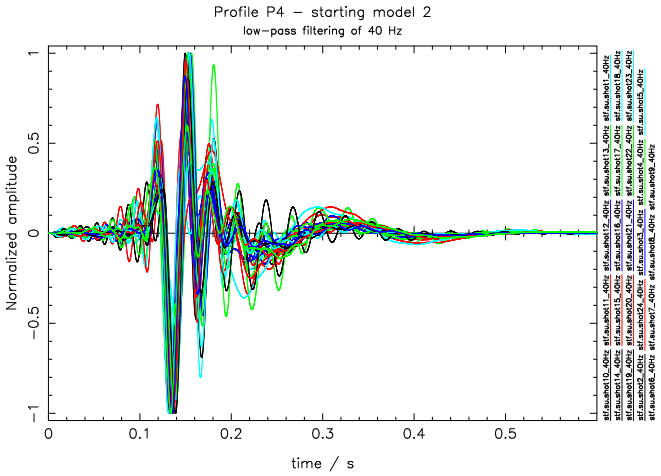

(c) Low-pass filter of 40 Hz.

Figure C.3: Profile P4: Optimized source time functions of the hammer impacts for each single shot during inversion with *starting model 2*. The wavelet is shifted by 0.1 s to consider acausal parts of it.

Appendix D

Parameters for FD-modeling and FWI

Model size (N_x x N_y)	N_x: 500 grid points, N_y: 100 grid points, grid spacing: 0.2 m
Propagation time	10000 time steps, time discretization: $5 \cdot 10^{-5}$ s
CPML boundary	width: 4 m (at left, right and bottom boundaries) free surface: yes
Order of spatial FD operator	2
Number of CPUs	x-direction: 4, y-direction: 2
Computing time for 20 shots	0.31 h

Table D.1: Numerical parameters of 2D finite-difference forward modeling for the 3D/2D transformation in Chapter III. All calculations are carried out on a workstation [8 CPU cores in an Intel(R) Core(TM) i7 CPU 950 @ 3.07 GHz with 12 GiB memory].

Model size (N_x x N_y x N_z)	N_x: 500 grid points, N_y: 100 grid points, N_z: 200; grid spacing: 0.2 m
Propagation time	10000 time steps, time discretization: $5 \cdot 10^{-5}$ s
CPML boundary	width: 4 m (at left, right and bottom boundaries) free surface: yes
Order of spatial FD operator	2
Number of CPUs	x-direction: 4, y-direction: 2
Computing time for 20 shots	96 h

Table D.2: Numerical parameters of 3D finite-difference forward modeling for the 3D/2D transformation in Chapter III. All calculations are carried out on a workstation [8 CPU cores in an Intel(R) Core(TM) i7 CPU 950 @ 3.07 GHz with 12 GiB memory].

Model size (N_x x N_y)	N_x: 512 grid points, N_y: 512 grid points, grid spacing: 0.2 m
Propagation time	15000 time steps, time discretization: $4 \cdot 10^{-5}$ s
CPML boundary	width: 4 m (at left, right and bottom boundaries) free surface: yes
Order of spatial FD operator	4
Number of CPUs	x-direction: 16, y-direction: 16

Table D.3: Numerical parameters of 2D finite-difference forward modeling for FWI of field dataset Mammolshain in Chapter V. All calculations are carried out on the high-performance computer InstitutsCluster II (IC2) at Steinbuch Centre for Computing of Karlsruhe Institute of Technology. For more information visit `http://www.scc.kit.edu/dienste/ic2.php`.

3D/2D transformation	*Hybrid* transformation (v_{ph} = 300 m/s, r_1 = 10 m and r_2 = 20 m)
Anelastic damping	$Q_p = Q_s = 20$
Starting models	Travel-time tomography independent for v_p and v_s
Preconditioning of gradients	Semi-circular taper (radius of 2 m) at source locations
Misfit definition	Normalized L2-norm (eq. II.46)
Shots	24 vertical hammer blows (shot distance 4 m)
Receivers	89 vertical geophones with an eigenfrequency of 4.5 Hz (equidistant geophone spacing of 1 m)
Multiscale strategy	5-10 Hz, 5-12 Hz, 5-14 Hz, ..., 5-40 Hz
v_p/v_s ratio	1.5
Model smoothing	2D median filter of 1 m length
Parameter range of density	1200 - 3100 kg/m^3
Constraint of the density update	Scaling the step length α_ρ with a scalar factor of 30 %

Table D.4: Inversion parameters of 2D FWI described in Chapter V for all inversions of the field dataset Mammolshain.

Appendix E

Used soft- and hardware

Software
The 2D elastic FWI code `DENISE` was originally developed by Daniel Köhn. The code is freely available under the terms of GNU public license and references to the source code are provided at `http://www.opentoast.de`. It has been developed further by Lisa Groos, Sven Heider and myself at the Geophysical Institute (GPI) of Karlsruhe Institute of Technology.

For preprocessing, visualization, tools for filtering and tapering of seismic data as well as calculation of Fourier-Bessel expansion coefficients, estimation of an optimal source wavelet correction filter, application of 3D/2D spreading transformations and so on the software package `TFSoftware` is used. It is maintained and mainly developed by Thomas Forbriger. The software package is also partly available at `http://www.opentoast.de` under the terms of GNU public license. For visualization `PGPLOT` written by Tim Pearson is used.

Furthermore, I used `Matlab for Linux` (`The Mathworks`) and `Seismic Un*x` for creating the figures, analysis of FWI results and conversion of seismic data.

This thesis is written in LaTeX 2_ε.

Hardware
The synthetic reconstruction tests are carried out on a personal workstation [8 CPU cores in an Intel(R) Core(TM) i7 CPU 950 @ 3.07 GHz with 12 GiB memory] with a Linux operating system. The field data inversion is computed on the high-performance computer InstitutsCluster II (IC2) at Steinbuch Centre for Computing of Karlsruhe Institute of Technology. For more information visit `http://www.scc.kit.edu/dienste/ic2.php`.

Danksagung

Allen voran möchte ich meiner Familie danken, insbesondere meine Eltern, die mich stets liebevoll in allen Lebenslagen unterstützen und mir immer mit Rat und Tat zur Seite stehen.

Thomas Bohlen danke ich für die Übernahme des Hauptreferats dieser Arbeit, für sein Vertrauen sowie für die vielen Freiheiten, die ich während meiner Promotion genießen durfte.

Von der Universität Kiel gilt mein Dank Wolfgang Rabbel für die Übernahme des Korreferats und für seine konstruktive Kritik an meiner Arbeit. Daniel Köhn hat mit seinem 2D FWI Code DENISE den Grundstein für diese Arbeit gelegt – vielen Dank dafür.

Bei allen TOAST-Projektpartner möchte ich mich bedanken, vor allem bei denen, die mich bei unserer großen Feldkampagne in Mammolshain unterstützt haben. Ein besonderer Dank gilt Florian Köllner für die vielen Gespräche und die fachliche Unterstützung.

Liebe Arbeitsgruppe der Angewandten Seismik, die letzten dreieinhalb Jahre sind wie im Fluge vergangen. Das lag nicht nur an den vielen spannenden Aufgaben und Herausforderungen, die wir uns geteilt haben, sondern auch an den vielen entstandenen Freundschaften in dieser Zeit. Ohne euch wäre ich wahrscheinlich nach einem meiner (zahlreichen) Kajakausflüge nicht an meinen Schreibtisch zurück gekehrt ;) – danke Anna, Ines, Stefan, André, Anja, Sven, Simone und Lisa! Simone, vielen Dank für die super Atmosphäre in unserem gemeinsamen Büro.

Lisa möchte ich danken für die großartige Zusammenarbeit wie unsere zahllosen kleineren und größeren Diskussionen, spannende Konferenzbesuche und dass sie immer ein offenes Ohr für mich hatte. Ich habe es jeden Tag sehr genossen, dass ich eine Mitstreiterin bei diesem "S"chönen Thema hatte.

Thomas Forbriger gilt ein ganz besonderer Dank für sein Vertrauen, seine Geduld und seine Mühen. Seine konstante, enthusiastische und konzentrierte Arbeitsweise haben mich und die vorliegende Arbeit stark geprägt. Ohne ihn würde diese Arbeit ganz sicher nicht in dieser Form existieren.

Acknowledgment

The study was carried out within the GEOTECHNOLOGIEN program, funded by the German Ministry of Education and Research (BMBF), Grant 03G0752. It was also kindly supported by the sponsors of the *Wave Inversion Technology (WIT) Consortium*, Germany.